Low-Mass Dark Matter Search in SuperCDMS: Sub-keV Calibration and Constraints on ALPs and Dark Photons, with Neutrino Floor Studies

By

SUDIPTA DAS

PHYS11201905005

National Institute of Science Education and Research, Bhubaneswar

A thesis submitted to the Board of Studies in School of Physical Sciences

In partial fulfillment of requirements For the Degree of

DOCTOR OF PHILOSOPHY

of

HOMI BHABHA NATIONAL INSTITUTE

April, 2026

Homi Bhabha National Institute

Recommendations of the Viva Voce Committee

As members of the Viva Voce Committee, we certify that we have read the dissertation prepared by **Sudipta Das** entitled **"Low-Mass Dark Matter Search in SuperCDMS: Sub-keV Calibration and Constraints on ALPs and Dark Photons, with Neutrino Floor Studies"** and recommend that it may be accepted as fulfilling the thesis requirement for the award of Degree of Doctor of Philosophy.

Chairman - Prof. Sanjay Kumar Swain Sanjay Swain **Date:** 13/8/2026

Guide / Convener - Prof. Bedangadas Mohanty BMohanty **Date:** 13/08/2026

Examiner - Prof. Rupak Mahapatra Rupak Kumar Mahapatra **Date:** 13/08/2026

Member 1 - Dr. Kartikeswar Senapati K. Senapati **Date:** 13/08/2026

Member 2 - Dr. Nishikanta Khandai NKhandai **Date:** 13/08/2026.

Member 3 - Dr. Seema Bahinipati Seema Bahinipati **Date:** 13/08/2026

Final approval and acceptance of this thesis is contingent upon the candidate's submission of the final copies of the thesis to HBNI.

I hereby certify that I have read this thesis prepared under my direction and recommend that it may be accepted as fulfilling the thesis requirement.

Date : August 9, 2026
Place : NISER, JATNI

BMohanty
(Guide)

STATEMENT BY THE AUTHOR

This dissertation has been submitted in partial fulfillment of requirements for an advanced degree at Homi Bhabha National Institute (HBNI) and is deposited in the library to be made available to borrowers under rules of the HBNI.

Brief quotations from this dissertation are allowable without special permission, provided that accurate acknowledgement of source is made. Requests for permission for extended quotation from or reproduction of this manuscript in whole or in part may be granted by the Competent Authority of HBNI when in his or her judgment the proposed use of the material is in the interests of scholarship. In all other instances, however, permission must be obtained from the author.

Date : August 13, 2026
Place : NISER, JATNI

Sudipta Das
13/08/2026

(AUTHOR)

DECLARATION

I hereby declare that the investigation presented in the thesis has been carried out by me. The work is original and has not been submitted earlier as a whole or in part for a degree/diploma at this or any other Institution/University.

Date : August 13, 2026
Place : NISER, JATNI

Sudipta Das
13/08/2026
(AUTHOR)

CERTIFICATION OF ACADEMIC INTEGRITY

Undertaking by the student

1. I **Sudipta Das**, HBNI Enrolment No. **PHYS11201905005** hereby undertake that the thesis titled "**Low-Mass Dark Matter Search in SuperCDMS: Sub-keV Calibration and Constraints on ALPs and Dark Photons, with Neutrino Floor Studies**" is prepared by me and is the original work undertaken by me.
2. I also hereby undertake that this document has been duly checked through a plagiarism detection tool and the document is found to be plagiarism free as per the guidelines of the Institute/UGC.
3. I am aware and undertake that if plagiarism is detected in my thesis at any stage in the future, suitable penalty will be imposed as applicable as per the guidelines of the Institute/UGC.

Sudipta Das 13/08/2026

Signature of the Student with date

Endorsed by the thesis supervisor

I certify that the thesis written by the student is plagiarism free as mentioned above.

Signature of the thesis supervisor with date 13/08/2026

Name	:	Prof. Bedangadas Mohanty
Designation	:	Senior Professor
Department / Centre	:	School of Physical Sciences
Name of the CI / OCC	:	National Institute of Science Education and Research (NISER)

List of Publications arising from the thesis

Journal Publications

Publications related to this thesis

1. **S. Das**, V. K. S. Kashyap, and B. Mohanty. "Energy calibration of EJ-301 scintillation detector using unfolding methods for fast neutron measurement". *Nuclear Instruments and Methods in Physics Research Section A: Accelerators, Spectrometers, Detectors and Associated Equipment* 1042 (2022), p. 167405. eprint: https://www.sciencedirect.com/science/article/pii/S016890022200701X.

2. M. F. Albakry, I. Alkhatib, D. Alonso-González, D. W. P. Amaral, J. Anczarski, T. Aralis, T. Aramaki, I. Ataee Langroudy, C. Bathurst, R. Bhattacharyya, et al. "Low-energy calibration of SuperCDMS HVeV cryogenic silicon calorimeters using Compton steps". *Phys. Rev. D* 112 (9 2025), p. 092014. eprint: https://link.aps.org/doi/10.1103/jj7w-gkgg. (SuperCDMS collaboration), Primary Analysers: **S. Das**, A. Sattati.

3. **S. Das**, V. K. S. Kashyap, and B. Mohanty. "Impact of reactor antineutrinos on the neutrino floor in low-mass WIMP-like dark matter searches". *Phys. Rev. D* 113 (6 2026), p. 063046. eprint: https://link.aps.org/doi/10.1103/v3lh-r6q2.

4. **S. Das**, R. Dey, V. K. S. Kashyap, B. Mohanty, D. Mondal, S. Banik, M. Chaudhuri, and V. Iyer. “Rare event searches using cryogenic detectors via direct detection methods”. *Modern Physics Letters A* 41.12n13 (2026), p. 2630002. eprint: https://doi.org/10.1142/S0217732326300028.

Other Publications

1. R. Dey, D. Mondal, **S. Das**, V. K. S. Kashyap, and B. Mohanty. “Measurement of cosmic muon-induced events in an HPGe detector using time-coincidence technique”. *Eur. Phys. J. Plus* 140.12 (2025), p. 1191. arXiv: 2505.20317 [physics.ins-det].
2. M. F. Albakry et al. “Search for low-mass electron-recoil dark matter using a single-charge sensitive SuperCDMS-HVeV detector”. *Phys. Rev. D* 113.3 (2026), p. 032001. arXiv: 2509.03608 [hep-ex].

SuperCDMS Analysis notes

1. **S. Das**, V. K. S. Kashyap, and B. Mohanty. *ALP and Dark Photon Search Using Profile Likelihood Ratio Methods in SuperCDMS Soudan*. SuperCDMS Internal Analysis Note. https://confluence.slac.stanford.edu/spaces/CDMS/pages/587619095/Internal+Documentation+Dark+Absorption+in+SuperCDMS+Soudan+using+PLR+method.
2. **S. Das**, V. K. S. Kashyap, and B. Mohanty. *NEXUS Run 13 Trigger Threshold Energy Study at 0 V Detector Bias*. SuperCDMS Internal Analysis Note. https://confluence.slac.stanford.edu/spaces/CDMS/pages/456197186/NEXUS+Run+13+trigger+threshold+energy+0V+calibration.
3. **S. Das**, V. K. S. Kashyap, and B. Mohanty. *NEXUS Run 13 Compton Step Calibration Study at 0 V Detector Bias*. SuperCDMS Internal Analysis Note. https://confluence.slac.stanford.edu/spaces/CDMS/pages/353759544/Compton+step+calibration+analysis+Analyzing+the+0V+data.

4. **S. Das**, V. K. S. Kashyap, and B. Mohanty. *NEXUS Run 13 Compton Step Calibration Study at 100 V Detector Bias*. SuperCDMS Internal Analysis Note. https://confluence.slac.stanford.edu/spaces/CDMS/pages/368331679/Compton+step+calibration+analysis+Analyzing+the+100V+Cs+data.

5. **S. Das**, V. K. S. Kashyap, and B. Mohanty. *NEXUS Run 14 LED Calibration at 150 V Detector Bias and Comparison of 0 V and High-Voltage Detector Responses*. SuperCDMS Internal Analysis Note. https://confluence.slac.stanford.edu/spaces/CDMS/pages/377741983/Calibration+with+150V+LED+data+and+extending+it+to+high+energy+region+using+Cs+data.

6. **S. Das**, V. K. S. Kashyap, and B. Mohanty. *Baseline Gain Correction for LED Calibration at 150 V Detector Bias (NEXUS Run 14)*. SuperCDMS Internal Analysis Note. https://confluence.slac.stanford.edu/spaces/CDMS/pages/440043268/Baseline+gain+correction+for+LED+data+150V.

7. **S. Das** and A. Sattari. *Energy Calibration Study Using Compton Steps in SuperCDMS HVeV Detectors*. SuperCDMS Internal Analysis Note. https://confluence.slac.stanford.edu/spaces/CDMS/pages/407260186/HVeV-R4+Compton+calibration+study.

Conference proceedings

1. **S. Das** (on behalf of SuperCDMS Collaboration). "Calibrating SuperCDMS Si HVeV Detectors Using Compton Steps for Low Mass Dark Matter Searches". In: *Proceedings of the DAE Symposium on Nuclear Physics*. Vol. 67. On behalf of the SuperCDMS Collaboration. 2023.

2. **S. Das,** Varchaswi K. S. Kashyap, and Bedangadas Mohanty. "Simulating Response of a Liquid Scintillation Detector to Gamma and Neutrons". In: *Springer Proceedings in Physics*. Vol. 282. 2023, pp. 55–60.

3. **S. Das** (on behalf of SuperCDMS Collaboration). “Calibrating Energy Scale of SuperCDMS Si HVeV Detectors in keV Range and Study the Compton Steps”. In: *Springer Proceedings in Physics*. Vol. 304. On behalf of the SuperCDMS Collaboration. 2024, pp. 980–982.

4. **S. Das** (on behalf of SuperCDMS Collaboration). “Investigating Compton Steps in SuperCDMS Si HVeV Detectors”. In: *Proceedings of Science (TAUP2023)*. PoS(TAUP2023)077; On behalf of the SuperCDMS Collaboration. 2023, p. 077.

5. **S. Das**, Roni Dey, Dipanwita Mondal, Varchaswi K. S. Kashyap, and Bedangadas Mohanty. “Feasibility of CEνNS Search at APSARA-U”. In: *Proceedings of the XXVI DAE-BRNS High Energy Physics (HEP) Symposium 2024*. Vol. 432. Springer Proceedings in Physics. 2025.

Conferences/Workshop presentations

1. **Sudipta Das**, Varchaswi K. S. Kashyap, and Bedangadas Mohanty. *Impact of Reactor Anti-Neutrinos on the Neutrino Floor for Low-Mass Dark Matter Searches*. NuPhys2026: Prospects in Neutrino Physics, King’s College London, United Kingdom. Oral presentation. 2026.

2. **Sudipta Das**, Roni Dey, Dipanwita Mondal, Varchaswi K. S. Kashyap, and Bedangadas Mohanty. *Feasibility of CEvNS Search at APSARA-U*. XXVI DAE–BRNS High Energy Physics Symposium (HEP 2024), Banaras Hindu University (BHU), Varanasi, India. Oral presentation. 2024.

3. **Sudipta Das**, Roni Dey, Kashyap Varchaswi K. S. Mondal Dipanwita, and Bedangadas Mohanty. *Overview of Dark Matter and CEvNS Search at NISER*. 1st DAE Conclave, NISER, Bhubaneswar, India. Poster presentation. 2024.

4. **Sudipta Das** (on behalf of SuperCDMS Collaboration). *Investigating Compton Steps in SuperCDMS Si HVeV Detectors*. XVIII International Conference on Topics in Astroparticle and Underground Physics (TAUP 2023), Vienna, Austria. Oral presentation. 2023.

5. **Sudipta Das** (on behalf of SuperCDMS Collaboration). *Calibrating SuperCDMS Si HVeV Detectors using Compton Steps*. 67th DAE Symposium on Nuclear Physics (2023), IIT Indore, India. Poster presentation. 2023.

6. **Sudipta Das** (on behalf of SuperCDMS Collaboration). *Calibrating Energy Scale of SuperCDMS Si HVeV Detectors in keV Range and Study of Compton Steps*. XXV DAE–BRNS High Energy Physics Symposium (DAE–HEP 2022), IISER Mohali, India. Poster presentation. 2022.

7. **Sudipta Das**, Varchaswi K. S. Kashyap, and Bedangadas Mohanty. *Simulating Response of a Liquid Scintillation Detector to Gamma and Neutrons*. Advanced Radiation Detector and Instrumentation in Nuclear and Particle Physics (RAPID 2021), University of Jammu, India. Oral presentation. 2021.

Date : August 13, 2026
Place : NISER, Jatni

Sudipta Das
13/08/2026

(AUTHOR)

DEDICATED TO

my Family

ACKNOWLEDGEMENTS

I would like to express my deepest gratitude to my supervisor, Prof. Bedangadas Mohanty, for his constant guidance, encouragement, and insightful mentorship throughout my academic journey. His unwavering faith in me has been a continuous source of motivation. I feel truly fortunate to have been under his supervision for the past five years, beginning with my Master's thesis. His scientific rigor, clarity of thought, and disciplined approach to research have profoundly shaped my development as a researcher. I am especially grateful for the opportunity to work in this field under his guidance, which has significantly influenced my academic direction. His exceptional time management and efficiency are qualities I deeply admire and continually aspire to incorporate into my own personal and professional life. I sincerely thank him for the trust, support, and opportunities he has extended to me, all of which have played a crucial role in my academic growth and in shaping my research career.

I am equally grateful to Dr. Varchaswi Kashyap for his continuous guidance and support, both academically and personally. Despite his demanding schedule, he was always approachable and generous with his time. His encouragement, patience, and thoughtful advice made my research journey both enriching and enjoyable. His support during this research journey gave me confidence and helped me stay focused and motivated.

I sincerely acknowledge my collaborators in the SuperCDMS collaboration, whose contributions were central to two key chapters of this thesis.

I am especially grateful for the collaborative work and support related to the Compton step calibration analysis using HVeV detectors at the SuperCDMS NEXUS facility. Firstly, I would like to thank Dr. Valentina Novati for providing me the opportunity to be involved in the NEXUS HVeV program and for her guidance during the initial phase of this work.

I am also grateful to Dr. Ata Sattari, who co-led this analysis with me, for the extensive discussions, shared effort, and close collaboration that were essential to its successful completion. I sincerely acknowledge Dr. Stefan Zatschler, Prof. Ziqing Hong, Prof. Miriam Diamond, Prof. Wolfgang Rau, Prof. Pekka Sinervo, Dr. Matt Wilson, Dr. Imran Alkhatib and Dr. Enze Zhang for their valuable feedback, constructive suggestions, and insightful discussions, which significantly improved the quality of this work. I also acknowledge Prof. Wolfgang Rau, Dr. Osmond Wen, Dr. Jon Leyva, and Dr. Andy Kubik for serving as analysis reviewers and for their careful evaluation of the analysis, and Prof. Yan Liu for chairing the analysis review committee and overseeing the review process. I extend my thanks to Prof. Scott Oser, Dr. Madeleine Zurowski, and Dr. David Sadek for serving as ORC members for the paper review, and to Dr. Emanuele Michielin and Dr. Stefan Zatschler for their roles as Publication Committee Chairs for their time, effort, and thorough review.

I also sincerely acknowledge the collaborative efforts associated with the low-mass dark matter search using SuperCDMS Soudan data using Profile Likelihood Ratio methods. I would like to thank Dr. Matt Wilson for facilitating the opportunity to present this work in the SuperCDMS Stat Tools and Methods (ST&M) meetings and for enabling valuable discussions that contributed to its development. I am also grateful for the review and approval of my contribution to the dark matter absorption modeling in the "dmmodeling" package, which was subsequently made publicly available by SuperCDMS. I sincerely thank Prof. Wolfgang Rau, Prof. Anthony Villano, Prof. Belina von Krosigk, Prof. Pekka Sinervo, Dr. Stefan Zatschler, and Dr. Rob Calkins for their valuable discussions, guidance, and inputs during the development and completion of this analysis.

I am grateful to my doctoral committee members, Prof. Sanjay Kumar Swain, Prof. Kartikeshwar Senapati, Prof. Nishikanta Khandai, and Prof. Seema Bahinipati, for their careful evaluation of my work and for their valuable comments and suggestions, which helped refine and strengthen my doctoral research.

I sincerely acknowledge Dr. Vijay Iyer, Dr. Samir Banik, and Dr. Mouli Chowdhuri for their mentorship during the early stages of my PhD research. They introduced me to dark matter search experiments within SuperCDMS and laid a strong foundation for my work in this field. Their guidance was instrumental in shaping my initial understanding and approach to research.

I also extend my heartfelt gratitude to Dr. Debashish Mallick, Dr. Ashish Pandav, Dr. Dukhishyam Mallick, Dr. Roni Dey, Dr. Prottay Das, and Dr. Swati Saha for their constant support and encouragement throughout my journey. I would like to especially thank Dr. Swati Saha for her unwavering support, empathy, and encouragement. Her kindness, patience, and quiet strength have been a constant source of comfort. She has always been there to listen and offer thoughtful perspective, providing support in ways that often went beyond the academic. Her belief in me has often been stronger than my own.

I am grateful to my labmates, Sawan, Sarjeeta Gami, Bappaditya Mondal, Dipanwita Mondal, Subhadeep Mandal, and Aritra Ghosh, for their friendship, support, and for fostering a collaborative and positive work environment. The many discussions and shared experiences made my time in the group truly memorable.

I also acknowledge Dr. Ranbir Singh, Dr. Shuddha Shankar Dasgupta, Dr. Raveendrababu Karnam, and Dr. Ganesh Tambave for their encouragement and support, which have been truly uplifting.

I would like to acknowledge the support and facilities provided by my institute, which created an excellent environment for research and learning. I especially thank the Garuda and Kanad high-performance computing cluster facilities, which I utilized at various stages of my academic work. I am also grateful to the administrative and technical staff, whose efforts ensured the smooth functioning of day-to-day academic activities.

Finally, I express my deepest gratitude to my family. My parents have been my constant source of strength, offering unconditional love, positivity, encouragement, and countless sacrifices that made this journey possible. I am especially inspired by my sister, the first in our family to earn a doctorate degree (in Physiology). Her dedication, perseverance, and achievements have continually motivated me to strive for excellence. I am deeply grateful for their unwavering belief in me, which has been central to all that I have accomplished.

Contents

Summary

Astrophysical and cosmological observations provide overwhelming evidence for the existence of non-baryonic dark matter, yet its fundamental particle nature remains one of the most profound open questions in physics. The absence of signals in conventional GeV/c^2–TeV/c^2 WIMP searches has driven the field toward unexplored territory: low-mass dark matter candidates, including sub-GeV/c^2 WIMPs and light bosonic particles such as axion-like particles and dark photons. Exploring this regime demands ultra-low-threshold detectors, precise sub-keV calibration, rigorous statistical methods, and unprecedented control of backgrounds.

This thesis presents experimental and phenomenological advances that strengthen the scientific reach of low-mass dark matter searches, centered on the Super Cryogenic Dark Matter Search (SuperCDMS) program.

The first part develops a novel sub-keV energy calibration technique for SuperCDMS silicon high-voltage eV-resolution (HVeV) detectors. Using Compton steps arising from gamma-ray scattering on bound atomic electrons, distinct spectral features at known atomic binding energies provide a direct and robust mapping between deposited energy and de-

tector response at zero bias voltage. A comparison with an independent optical photon calibration under high bias reveals an approximately 30% difference in response, offering new insight into low-energy phonon production mechanisms. This improved calibration directly enhances sensitivity to light dark matter interactions and refines our understanding of detector physics at the eV scale.

The second part presents statistically rigorous searches for bosonic dark matter candidates, axion-like particles and dark photons, using SuperCDMS Soudan data. A profile likelihood ratio framework incorporating detector response modeling, background parameterization, signal efficiencies, and systematic uncertainties is employed to constrain the axion–electron coupling (g_{ae}) and dark photon kinetic mixing parameter (ϵ). The resulting limits improve upon previous SuperCDMS constraints by up to a factor of five across the mass range 40 eV$/c^2$ to 25 keV$/c^2$, advancing the exploration of light dark sectors.

The third part investigates neutrino-induced nuclear recoils as an irreducible background for low-mass WIMP searches. A detailed phenomenological study of reactor antineutrino–induced coherent elastic neutrino–nucleus scattering is performed using Monte Carlo simulations tailored to SuperCDMS-like ultra-low-threshold detectors, with reactor spectra validated against CONUS+ measurements. A profile likelihood analysis demonstrates that a gigawatt-scale nuclear reactor within approximately 10 km can substantially elevate the neutrino floor, degrading sensitivity to WIMPs below approximately 10 GeV$/c^2$. In contrast, the impact becomes negligible at baselines of order 100 km, identifying reactor proximity as a critical factor in site selection for next-generation experiments.

The fourth part addresses fast neutrons as a dominant environmental background for nuclear-recoil-based dark matter searches. EJ-301 liquid scintillation detectors are calibrated using gamma-ray and Am–Be neutron sources and modeled with detailed Geant4 simulations that incorporate optical photon production, transport, and scintillation quenching. The Birks constant is extracted from proton-recoil data, enabling the construction of a validated neutron response matrix. Unfolding of measured spectra successfully reproduces the known source distribution, establishing a robust and experimentally validated framework for fast-neutron background characterization at underground laboratories.

Together, these studies form a comprehensive framework that integrates detector calibration at the sub-keV scale, advanced statistical dark matter searches, and precise background characterization. By strengthening both experimental sensitivity and theoretical interpretation, this work enhances the discovery potential of next-generation ultra-low-threshold dark matter experiments and advances the global effort to uncover the particle nature of dark matter.

List of Figures

List of Tables

List of Abbreviations

ALPs Axion Like Particles

CCDs Charge-Coupled Devices

CEνNS Coherent Elastic Neutrino–nucleus Scattering

CJPL China Jinping Underground Laboratory

CL Confidence Level

CMB Cosmic Microwave Background

CP Charge–Parity

CTA Cross Talk Amplitude

DM Dark Matter

DPP Digital Pulse Processing

DSF Dynamic Structure Factor

DSNB Diffuse Supernova Neutrino Background

EC Electron-capture

FOM Figure of Merit

FWHM	Full Widths at Half Maximum
GDF	Gaussian Derivative Filter
GF	Gaussian Filter
HV	High Voltage
HVeV	High Voltage eV-resolution)
iZIP	interleaved Z-sensitive Ionization and Phonon
KS	Kolmogorov–Smirnov
LEE	Low Energy Excess
LEU	low-enriched uranium
LFN	Low Frequency Noise
MB	Mean Baseline
MC	Mixing Chamber
NEXUS	Northwestern Experimental Underground Site
NF	NEXUS-Fermilab
NFW	Navarro–Frenk–White
NTL	Neganov–Trofimov–Luke
OF	Optimal Filter
OFL	Optimal Filter Limited
PCB	printed-circuit-board
PDF	Probability Density Function
PLR	Profile likelihood ratio
PMT	Photomultipliertube

PSD Power Spectral Density

PSD Pulse Shape Discrimination

QCD quantum chromodynamics

QE quantumefficiency

QET) Quasiparticle-trap-assisted Electrothermal-feedback Transition-edge sensor

RF Radio-frequency

RIA Relativistic Impulse Approximation

RQ Reduced Quantities

SD Spin-dependent

SI Spin-Independent

SM Standard Model

SQUID Superconducting Quantum Interference Device

SUL Soudan Underground Laboratory

SuperCDMS Super Cryogenic Dark Matter Search

TES Transition Edge Sensors

WIMPs Weakly Interacting Massive Particles

WP Working Point

CHAPTER 1

Introduction

Contents

1.1 The Missing Mass Problem

The current understanding of the Universe relies on the existence of a dominant, non-luminous component of matter known as *dark matter*. The necessity for such a component arises from a persistent and well-established discrepancy between the gravitational mass inferred from astrophysical observations and the mass accounted for by luminous baryonic matter. This discrepancy, commonly referred to as the *missing mass problem*, manifests across a wide range of physical scales, from individual galaxies to the largest observable structures in the Universe.

Early quantitative evidence for this missing mass emerged from studies of galaxy clusters, where application of the virial theorem showed that the observed velocity dispersion of galaxies could not be explained by the gravitational potential of visible matter alone [1, 2]. Subsequent observations across multiple independent probes have consistently reinforced this conclusion. Galaxy rotation curves reveal flat velocity profiles at large radii, implying the presence of extended dark matter halos [3, 4]. Gravitational lensing measurements provide direct evidence of excess mass through relativistic light deflection, most strikingly in merging galaxy clusters such as the Bullet Cluster [5]. On cosmological scales, observations of the cosmic microwave background (CMB) anisotropies and large-scale structure formation further confirm the existence of a non-baryonic matter component [6].

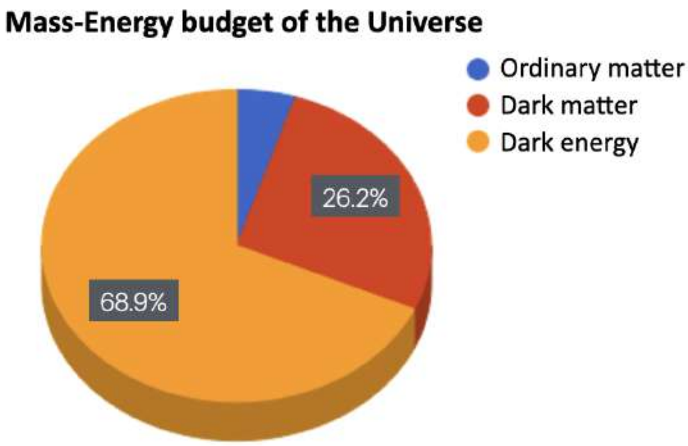

FIGURE 1.1: Energy budget of the Universe as measured by the *Planck* satellite. The composition is approximately 5% baryonic matter, 26% dark matter, and 69% dark energy. The dark matter component exceeds the baryonic matter content by more than a factor of five [6].

Precise measurements from the *Planck* satellite indicate that the energy budget of the Universe (Fig. 1.1) consists of approximately 4.9% baryonic matter, 26.2% dark matter, and

68.9% dark energy [6], as shown in Fig. 1.1. Dark matter, by definition, does not belong to the Standard Model of particle physics and interacts predominantly through gravity, with at most very weak non-gravitational interactions. Despite its elusive nature, the remarkable agreement among diverse observational probes, ranging from stellar dynamics to early-Universe plasma oscillations, strongly supports a consistent cosmological framework in which dark matter constitutes the majority of matter in the Universe. These observations not only highlight the inadequacy of baryonic matter in explaining gravitational phenomena but also provide stringent constraints on the distribution and properties of the dark matter component.

1.1.1 Galaxy Rotation Curves

One of the most direct and compelling pieces of evidence for dark matter arises from the study of galaxy rotation curves. Early indications of missing mass in galaxies can be traced back to the work of Kapteyn in the 1920s, while later studies by Zwicky on galaxy clusters using the virial theorem further strengthened the case for unseen matter [1, 2]. Modern observations of individual galaxies provide even more striking and direct evidence.

In a gravitationally bound system governed by Newtonian dynamics, the rotational velocity $v(r)$ of a star orbiting at a distance r from the galactic center is determined by the enclosed mass $M(r)$ as

$$v(r) = \sqrt{\frac{GM(r)}{r}}\,, \tag{1.1}$$

where G is the gravitational constant. If the mass distribution were dominated solely by luminous matter, primarily stars and gas, then $M(r)$ would approach a constant value beyond the visible extent of the galaxy. In that case, the rotational velocity is expected to decrease as $v(r) \propto r^{-1/2}$ at large radii.

However, observations of spiral galaxies, obtained through Doppler measurements of spectral lines from stars and gas, show a striking deviation from this expectation, as shown in Fig. 1.2. Instead of declining, the rotation curves remain approximately flat even far beyond the optical disk of the galaxy [3, 4]. This behavior implies that the enclosed mass continues to increase with radius.

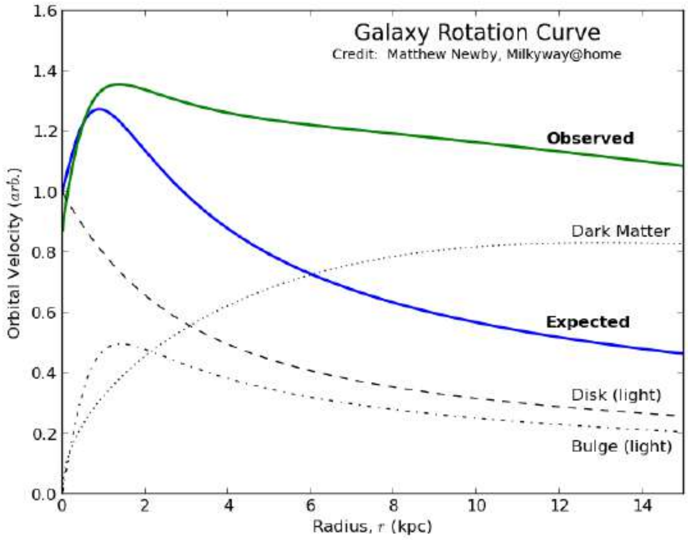

FIGURE 1.2: Observed galaxy rotation curves compared to the expectation from luminous matter alone. The flat behavior at large radii indicates the presence of an extended dark matter halo. Adapted from [7].

A constant rotational velocity at large radii ($v \approx$ const.) directly implies

$$\begin{aligned} v = \sqrt{\frac{GM(r)}{r}} &= \text{const.} \\ \Rightarrow M(r) &\propto r \\ \Rightarrow \rho(r) &\propto \frac{1}{r^2}, \end{aligned} \tag{1.2}$$

where $\rho(r)$ represents the mass density profile. This scaling behavior cannot be explained by the observed distribution of baryonic matter alone and instead points to the presence of an additional, non-luminous mass component.

This discrepancy is naturally resolved by postulating that galaxies are embedded within extended, approximately spherical dark matter halos that extend well beyond the visible disk. Empirical and simulation-motivated profiles, such as the Navarro–Frenk–White (NFW) profile [8], successfully reproduce the observed kinematic behavior of galaxies.

1.1.2 Gravitational Lensing

Gravitational lensing provides a direct and model-independent probe of the total mass distribution in astrophysical systems, irrespective of the nature or composition of the matter involved. According to General Relativity, mass and energy curve spacetime, leading to the deflection of light rays passing near massive objects. When a massive foreground object (the lens), such as a galaxy or galaxy cluster, lies along the line of sight to a distant background source, it can bend the light and produce distorted, magnified, or multiple images of the source [9], as shown in Fig. 1.3.

For a point mass, the deflection angle of a light ray passing at an impact parameter b is given by

$$\alpha = \frac{4GM}{bc^2}, \tag{1.3}$$

where G is the gravitational constant, M is the mass of the lens, b is the impact parameter, and c is the speed of light. In realistic astrophysical systems, the deflection is determined by the projected mass distribution of the lens, and lensing observables can be used to reconstruct the underlying mass profile [10].

A key result from gravitational lensing studies is that the inferred total mass in galaxies and galaxy clusters significantly exceeds the mass attributable to luminous baryonic matter alone. In particular, lensing-derived mass distributions are typically more extended and massive than those inferred from stars and gas, indicating the presence of an additional, non-luminous component. Observations of systems such as merging galaxy clusters further

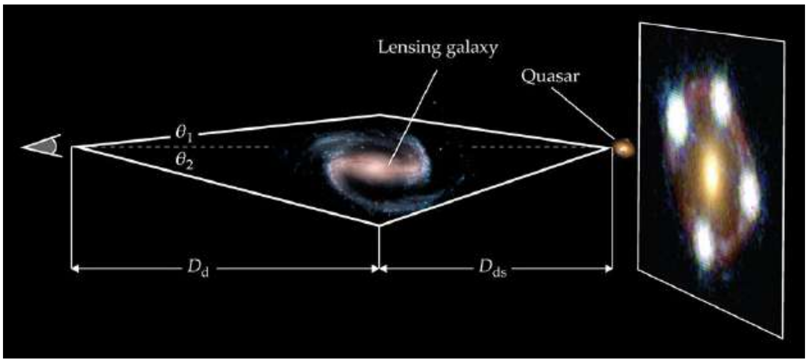

FIGURE 1.3: Schematic illustration of gravitational lensing. Light from a distant background galaxy is deflected by the gravitational field of an intervening massive object (lens), such as a galaxy cluster, producing distorted or multiple images. Analysis of these lensing distortions allows reconstruction of the total mass distribution of the lens, including contributions from non-luminous dark matter. Adapted from [11].

demonstrate that this dominant mass component is spatially distinct from baryonic matter, providing strong and independent evidence for the existence of dark matter [5].

1.1.3 The Bullet Cluster

A particularly striking and direct demonstration of dark matter comes from observations of merging galaxy clusters, most notably the Bullet Cluster (1E 0657−558) [5]. This system formed from the collision of two galaxy clusters approximately 10^8 years ago, resulting in a clear spatial separation between different matter components.

During the collision, the majority of the galactic mass behaves approximately as collisionless particles, passing through one another with minimal interaction, as inferred from gravitational lensing. In contrast, the dominant baryonic component, hot intracluster gas, interacts electromagnetically and experiences ram-pressure drag, slowing it down and causing it to accumulate near the collision center. This gas is observed via its X-ray emission, which traces the distribution of baryonic matter (Fig. 1.4).

The centers of the total mass distribution, obtained from gravitational lensing, and the baryonic mass distribution, obtained from Chandra X-ray imaging, do not coincide [5]. This indicates that most of the mass is associated with a component that does not interact electromagnetically and is effectively collisionless.

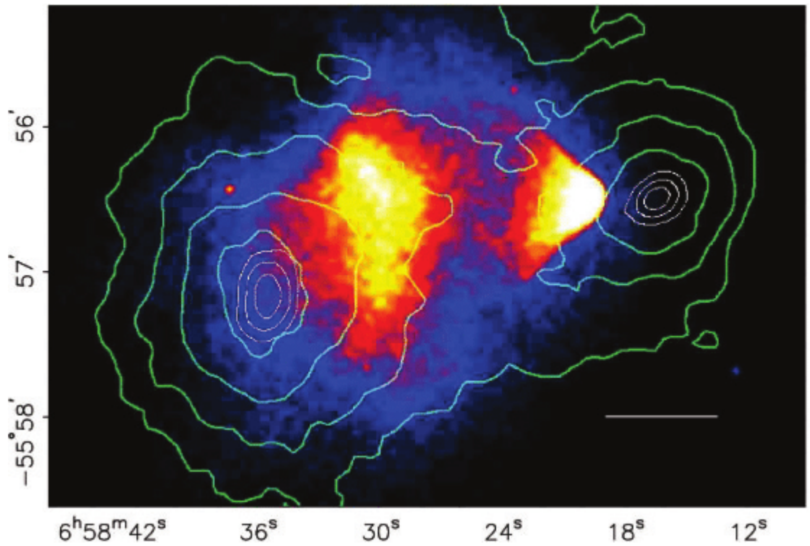

FIGURE 1.4: Composite image of the Bullet Cluster (1E 0657−558). X-ray emission (heat map) traces the hot intracluster gas, which contains the majority of baryonic matter and is slowed during the collision. Green contours represent the total mass distribution reconstructed from weak gravitational lensing. The spatial offset between the gas and total mass provides direct evidence for a dominant, collisionless dark matter component. Adapted from [5].

The observed separation between centres of baryonic gas (traced by X-ray emission) and total gravitational mass (traced by lensing) provides compelling evidence that the dominant matter component is non-luminous and collisionless. This cannot be explained by baryonic matter alone and challenges modified gravity theories that do not invoke additional matter components. The Bullet Cluster thus serves as one of the most direct and robust empirical confirmations of dark matter.

1.1.4 Large-Scale Structure Formation

The large-scale distribution of matter in the Universe provides a key line of evidence for the existence of dark matter. On scales larger than $\sim$ 100 Mpc, the Universe is observed to be statistically homogeneous and isotropic. However, on smaller scales ($\sim$ 10–50 Mpc), galaxy surveys reveal a complex network of structures known as the cosmic web, consisting of clusters, filaments, and voids. These structures arise from the gravitational growth of primordial density perturbations in the early Universe [12].

Observationally, large-scale structure is mapped using galaxy redshift surveys, where the positions and redshifts of galaxies are measured to reconstruct their three-dimensional distribution. For nearby galaxies ($z \ll 1$), distances can be approximated using Hubble's law,

$$d \approx \frac{c}{H_0} z \,, \tag{1.4}$$

while at higher redshifts, a full cosmological model is required to convert redshift into distance.

In a Universe composed solely of baryonic matter, the growth of density perturbations is strongly suppressed prior to recombination due to the tight coupling between baryons and photons. Consequently, structure formation would proceed too slowly to account for the observed abundance and distribution of galaxies. In contrast, dark matter, being non-relativistic and weakly interacting, does not couple to radiation and can begin to grow under gravity soon after matter–radiation equality. These early dark matter overdensities form gravitational potential wells into which baryons fall after recombination, leading to the formation of the observed structures.

Numerical simulations incorporating cold dark matter (CDM) successfully reproduce both the large-scale distribution of galaxies and the statistical properties of matter clustering

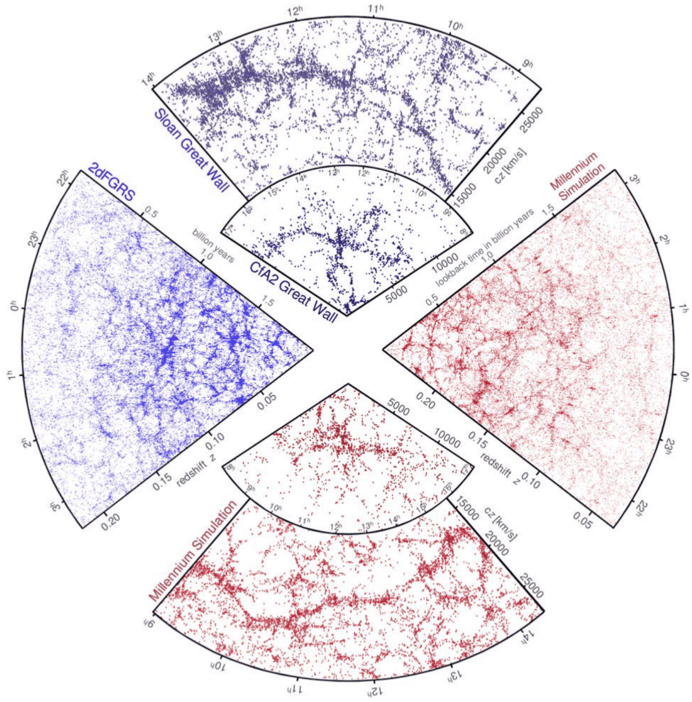

FIGURE 1.5: Large-scale structure of the Universe from galaxy redshift surveys compared with numerical simulations based on cold dark matter models. The agreement demonstrates that cold dark matter successfully reproduces the observed clustering properties of galaxies. Adapted from [13].

(Fig. 1.5). In contrast, models without dark matter, or those with hot (relativistic) dark matter, fail to reproduce the observed structures. In particular, hot dark matter suppresses the formation of small-scale structures due to free-streaming effects [12].

In addition to large-scale structure observations, complementary probes such as cosmic microwave background anisotropies and Big Bang nucleosynthesis provide independent and consistent constraints on the dark matter content of the Universe [6].

Taken together, the observational evidences discussed above establish a compelling and coherent case for the existence of dark matter. The consistency across multiple independent probes, spanning vastly different physical scales and epochs, strongly supports the conclusion that dark matter is a fundamental component of the Universe. Understanding its nature remains one of the central goals of contemporary physics and motivates the experimental efforts discussed in the subsequent sections of this thesis.

1.2 Dark Matter

The compelling observational evidence discussed in the previous sections strongly indicates the presence of a dominant, non-luminous component of matter in the Universe, known as *dark matter* (DM). This component constitutes approximately 85% of the total matter density and plays a central role in the formation and evolution of cosmic structures [6]. Despite its abundance, the fundamental nature of dark matter remains unknown, making it one of the most important open questions in modern physics.

Within the framework of the Standard Model (SM) of particle physics, there is no viable candidate that simultaneously satisfies all astrophysical and cosmological constraints on dark matter. This has motivated extensive theoretical and experimental efforts to explore new physics beyond the Standard Model [14].

1.2.1 General Properties of Dark Matter

Observational and cosmological considerations impose several robust and largely model-independent constraints on the properties of dark matter.

First, dark matter must be *non-luminous* and electrically neutral, implying that it does not emit, absorb, or scatter electromagnetic radiation at an observable level. This is inferred from the absence of electromagnetic signatures associated with the dominant mass component in astrophysical systems.

Second, dark matter must be *non-baryonic*. Measurements of primordial light element abundances and observations of the Cosmic Microwave Background constrain the baryonic matter density to be significantly smaller than the total matter density [6]. Therefore, dark matter cannot be composed of ordinary baryons.

Third, dark matter must be *stable* on cosmological timescales, or at least possess a lifetime much longer than the age of the Universe, ensuring its continued presence today.

Fourth, dark matter must be predominantly *cold* (non-relativistic) at the time of structure formation. Cold dark matter allows for the growth of small-scale structures, in agreement with observations, whereas hot dark matter would suppress such structures due to free-streaming effects [12].

Fifth, dark matter must interact predominantly through gravity, with at most very weak non-gravitational interactions. Observations such as the Bullet Cluster indicate that dark matter is effectively collisionless, placing strong constraints on its self-interaction cross-section [5].

Taken together, these properties strongly suggest that dark matter consists of a new form of matter beyond the Standard Model [14].

A wide range of theoretical models has been proposed to explain the nature of dark matter, spanning many orders of magnitude in mass and interaction strength. These candidates can be broadly classified according to their production mechanisms in the early Universe.

Weakly interacting massive particles (WIMPs) are a well-studied class that achieve the observed relic abundance through thermal freeze-out. In contrast, very weakly interacting particles can be produced via non-thermal mechanisms such as freeze-in. Light bosonic candidates, including axions and axion-like particles (ALPs), are typically produced via coherent oscillations of a light scalar field in the early Universe. Another class, dark photons, arises from hypothetical hidden-sector gauge symmetries and can kinetically mix with ordinary photons, leading to distinctive experimental signatures.

These production scenarios yield characteristic signals that motivate different detection strategies. In this thesis, a few well-motivated candidates are discussed in detail in their respective chapters, including their theoretical framework, expected differential event rates, and potential signatures in direct detection experiments. A brief overview of these candidates is provided below.

1.2.2 Dark Matter Candidates

In this thesis, we focus on three well-motivated classes of dark matter candidates that span a broad range of masses and interaction strengths. Their typical mass ranges and dominant interaction channels, along with the corresponding detection strategies, are illustrated in Fig. 1.6.

Weakly Interacting Massive Particles

Weakly interacting massive particles are among the most extensively studied dark matter candidates. They arise naturally in well-motivated extensions of the Standard Model, such as supersymmetry and extra-dimensional theories [14]. WIMPs interact with Standard Model particles through weak-scale interactions and can naturally reproduce the observed relic abundance via thermal freeze-out [15].

Typical WIMP masses range from a few GeV to several TeV, although sub-GeV WIMPs are also possible. They can scatter elastically off atomic nuclei, producing nuclear recoils with characteristic energy spectra, which makes them prime targets for direct detection experiments.

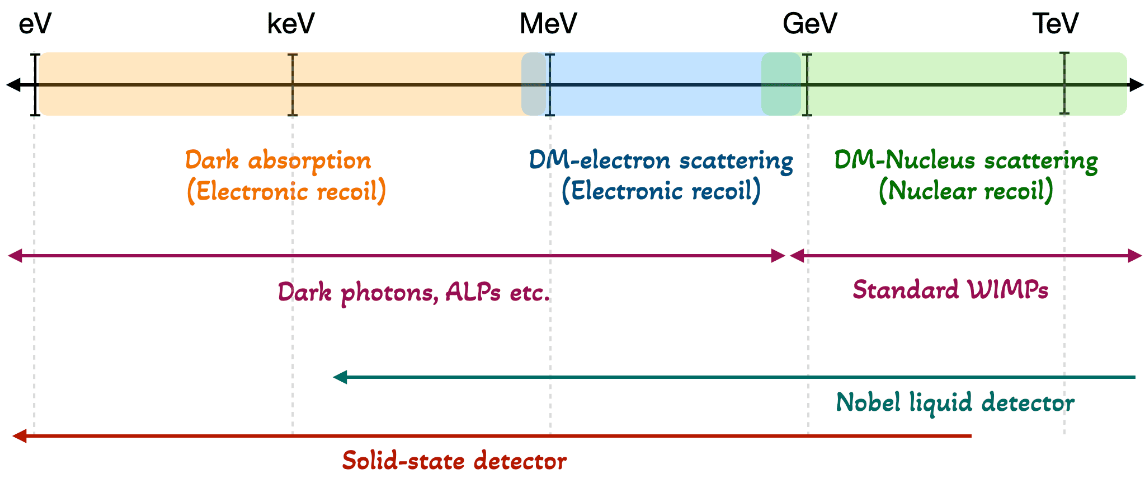

FIGURE 1.6: Representative dark matter candidates considered in this thesis, showing their approximate mass ranges and interaction strengths, together with the corresponding experimental detection strategies. Adapted from [16].

Axions and Axion-Like Particles

Axions were originally proposed to solve the strong CP problem in quantum chromodynamics (QCD) [17–19]. More generally, ALPs arise in theories with spontaneously broken global symmetries and are well-motivated in string-inspired frameworks [20].

Unlike WIMPs, axions and ALPs are typically produced non-thermally in the early Universe through coherent oscillations of a light scalar field, following the spontaneous breaking of the underlying symmetry. Their interactions with Standard Model particles are suppressed by a large energy scale, resulting in extremely weak couplings. These particles can be probed experimentally via their interactions with photons (Primakoff effect) or electrons, making them particularly relevant for low-threshold direct detection experiments [21].

Dark Photons

Dark photons are hypothetical vector bosons associated with an additional $U(1)$ gauge symmetry in a hidden sector [22]. They can kinetically mix with the ordinary photon, providing a portal between the dark sector and Standard Model particles.

Depending on their mass and production mechanism, dark photons can constitute all or part of the dark matter density. They can be detected in direct detection experiments through absorption or scattering, producing monoenergetic electron recoil signatures in detector materials [23]. Light dark photons produced via non-thermal mechanisms, such as freeze-in or misalignment-like processes, are particularly relevant for low-threshold searches.

1.2.3 Dark Matter Detection Strategies

Given the wide range of viable dark matter candidates, multiple complementary detection strategies have been developed to probe their properties. These approaches can be broadly classified into collider searches, indirect detection, and direct detection. A schematic overview of these detection techniques is shown in Fig. 1.7.

For clarity, we denote Standard Model particles by ψ and dark matter particles by χ.

- **Collider Searches** ($\psi\,\psi \rightarrow \chi\,\chi$): In high-energy particle collisions, such as those at the Large Hadron Collider (LHC), dark matter particles may be produced if kinematically accessible. Since dark matter particles are weakly interacting, they escape the detector without depositing energy. Their presence is therefore inferred from an imbalance in the measured momentum, commonly referred to as missing transverse energy.

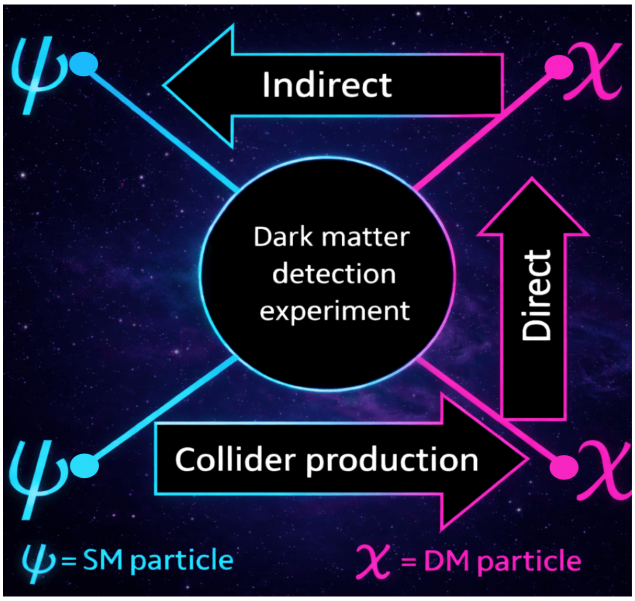

FIGURE 1.7: Schematic representation of the three primary dark matter detection strategies: collider production, indirect detection, and direct detection.

- **Indirect Detection** ($\chi\,\chi \rightarrow \psi\,\psi$): Indirect detection experiments search for Standard Model particles produced via dark matter annihilation or decay in astrophysical environments, such as the Galactic center, dwarf spheroidal galaxies, or galaxy clusters. Observable signatures include gamma rays, neutrinos, and charged cosmic rays, which arise from the decay or hadronization of the primary annihilation or decay products. The expected signal depends on the dark matter density distribution and annihilation or decay rates.

- **Direct Detection** ($\chi\,\psi \rightarrow \chi\,\psi$): Direct detection experiments aim to measure the scattering or absorption of dark matter particles in terrestrial detectors. For WIMP-like candidates, this typically involves elastic scattering off nuclei, producing nuclear recoils with energies in the eV–keV range. In contrast, lighter dark matter candidates, such as axions, axion-like particles, or dark photons, can deposit energy via absorption processes, leading to electron recoil signals.

Among these approaches, direct detection experiments are uniquely sensitive to the local dark matter density and probe dark matter interactions at very low energies. The search for low-mass dark matter, in particular, requires detectors with ultra-low energy thresholds, excellent energy resolution, and strong background discrimination capabilities. In this following section, we focus on the theoretical and experimental framework of direct detection, which forms the central theme of this thesis.

1.3 Direct Detection of Dark Matter

Direct detection experiments aim to observe the interaction of DM particles with ordinary matter in terrestrial detectors. Unlike indirect or collider-based searches, direct detection probes the local dark matter halo of the Milky Way and is therefore sensitive to the present-day properties of dark matter [14, 24]. The basic principle involves measuring the small energy deposited when a dark matter particle scatters off or is absorbed by atoms in the detector medium.

Given the wide range of viable dark matter candidates, the underlying interaction mechanisms and resulting signal characteristics can differ significantly. For example, weakly interacting massive particles predominantly produce nuclear recoils through elastic scattering, whereas lighter candidates such as axions, axion-like particles, and dark photons typically deposit energy via absorption processes, leading to electron recoil signals.

As a result, the theoretical framework governing the expected event rates and signal spectra is inherently model-dependent. Therefore, detailed formulations of interaction rates, cross-sections, and detector responses are presented separately in the respective chapters dedicated to each dark matter candidate.

Over the past decades, significant advances in detector technology have enabled unprecedented sensitivity to rare interaction events, pushing experimental searches into regimes where irreducible backgrounds, such as neutrinos, become increasingly important [25]. In the following, we provide an overview of the key interaction channels and experimental techniques employed in direct detection experiments.

1.3.1 Dark Matter Interactions with Matter

Direct detection experiments probe two primary interaction channels: nuclear recoils and electron recoils.

Nuclear Recoils: In elastic scattering off nuclei, a dark matter particle transfers kinetic energy to the nucleus, producing a nuclear recoil. This channel is most relevant for WIMP-like candidates, with typical recoil energies in the keV range [24]. The recoil spectrum is approximately exponential, with most events occurring at low energies.

Electron Recoils: Light dark matter candidates, such as axions, axion-like particles, and dark photons, can interact with electrons via scattering or absorption processes. These interactions typically produce electron recoils at sub-keV energies, requiring detectors with ultra-low energy thresholds [23, 26].

The distinction between nuclear and electron recoils is crucial for background discrimination, as most radioactive backgrounds predominantly produce electron recoil signals.

1.3.2 Experimental Detection Techniques

Modern direct detection experiments employ a variety of detection technologies to measure the small energy depositions associated with dark matter interactions. The primary observables include ionization, scintillation, and phonons.

Ionization Detectors: Semiconductor detectors, such as germanium and silicon, measure the charge produced by ionization. These detectors provide excellent energy resolution and low energy thresholds, making them particularly suitable for low-mass dark matter searches [16].

Scintillation Detectors: Noble liquid detectors, such as liquid xenon and argon, produce scintillation light when particles interact within the medium. Dual-phase time projection chambers (TPCs) measure both scintillation and ionization signals, enabling powerful background discrimination [16].

Cryogenic Phonon Detectors: Cryogenic detectors operate at millikelvin temperatures and measure phonons generated by particle interactions. Experiments such as SuperCDMS utilize combined phonon and ionization measurements to achieve excellent background rejection and ultra-low energy thresholds [16].

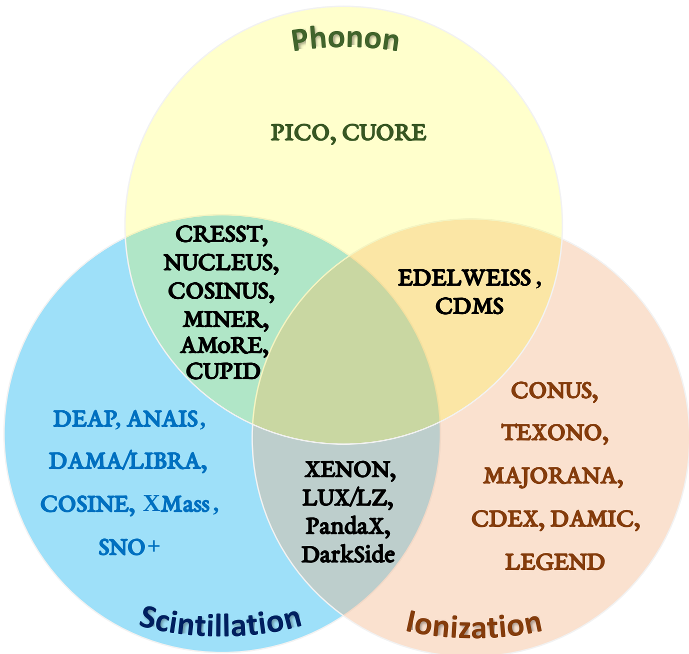

FIGURE 1.8: Primary signal channels in direct detection experiments: phonons (heat), scintillation (light), and ionization (charge). Different detector technologies exploit one or more of these observables to enhance sensitivity and background discrimination. Adapted from [16].

Simultaneous measurement of multiple signal channels (see Fig. 1.8) enables powerful discrimination between nuclear recoil and electron recoil events, which is essential for suppressing background contributions. This discrimination is typically achieved through the use of yield parameters. In detectors that measure both ionization and phonons, such as cryogenic semiconductor experiments, the *ionization yield*, defined as the ratio of ionization energy to total recoil energy, differs significantly between nuclear and electron recoils, allowing efficient event-by-event separation at sufficiently high energies. Similarly, in detectors combining scintillation with either ionization or phonons, the *light yield*, the ratio of scintillation signal to deposited energy, provides a robust handle for distinguishing between interaction types. Nuclear recoils generally produce less ionization or scintillation compared to electron recoils of the same energy due to quenching effects [27, 28]. At very low recoil energies, however, this discrimination becomes less effective due to reduced signal-to-noise ratios, and statistical separation techniques are often required. These multi-channel detection techniques form the basis of background discrimination strategies in modern direct detection experiments.

1.3.3 Backgrounds in Direct Detection

A major challenge in direct detection experiments is the suppression and precise understanding of background events that can mimic dark matter signals [24, 25]. These backgrounds are broadly classified based on their origin into *radiogenic* and *cosmogenic* sources, each contributing through different physical processes.

Radiogenic Backgrounds: Radiogenic backgrounds arise from radioactive decays within detector materials and the surrounding environment. Trace contamination from isotopes such as ^{238}U, ^{232}Th, and ^{40}K leads to the emission of gamma rays and beta particles, producing predominantly electron recoil events [29, 30].

In addition to electromagnetic backgrounds, radiogenic processes can also generate neutrons through spontaneous fission and (α, n) reactions. These neutrons can scatter elastically off nuclei, producing nuclear recoils that are indistinguishable from WIMP-like dark matter interactions on an event-by-event basis [24]. Consequently, fast neutrons constitute one of the most critical backgrounds for direct detection experiments.

Cosmogenic Backgrounds: Cosmogenic backgrounds originate from cosmic-ray interactions. Even in deep underground laboratories, high-energy muons can penetrate the overburden and produce secondary particles through spallation processes [31]. These interactions can generate fast neutrons, which can induce nuclear recoils similar to those expected from dark matter.

At the highest experimental sensitivities, neutrino-induced recoils form an additional and irreducible component of the cosmogenic background. Neutrinos interact with detector nuclei via coherent elastic neutrino–nucleus scattering (CEνNS), producing nuclear recoils that are indistinguishable from dark matter signals on an event-by-event basis [25]. The CEνNS cross-section is coherently enhanced approximately as N^2, making this effect particularly important for heavy target nuclei.

The dominant neutrino sources include solar neutrinos, atmospheric neutrinos, and reactor antineutrinos [25]. Solar neutrinos dominate the background for low-mass dark matter searches, while atmospheric neutrinos become relevant at higher masses. Reactor antineutrinos can significantly enhance the neutrino-induced background for experiments located near nuclear facilities.

The recoil spectrum from neutrino interactions closely resembles that expected from low-mass dark matter, particularly in the sub-10 GeV/c^2 region. This irreducible background defines the so-called *neutrino floor*, where statistical discrimination between signal and background becomes increasingly challenging [25].

Mitigation strategies include operating detectors in deep underground laboratories to suppress cosmic-ray flux, employing passive shielding to reduce gamma and neutron backgrounds, using active veto systems to tag cosmogenic events, and selecting ultra-low radioactivity materials for detector construction [29, 32]. While radiogenic and cosmogenic neutron backgrounds can be significantly reduced, neutrino-induced recoils cannot be shielded and must instead be modeled and statistically distinguished from potential dark matter signals.

1.3.4 Current Status of Direct Detection Experiments

Direct detection experiments have made substantial progress over the past decade, probing an increasingly broad region of dark matter parameter space across a variety of candidate models [14]. In the high-mass regime, particularly for WIMPs, experiments based on liquid noble gas time projection chambers have achieved leading sensitivities. These experiments have constrained the spin-independent dark matter–nucleon scattering cross-section down to $\sim 10^{-47}$ cm^2 for dark matter masses of $O(10)$ GeV/c^2 [29].

The absence of a confirmed signal in this parameter space has motivated a strong shift in focus toward the low-mass region below ~ 10 GeV$/c^2$, where experimental sensitivity is primarily limited by detector energy thresholds and background discrimination. In this regime, cryogenic detectors play a central role due to their excellent energy resolution and ultra-low threshold capabilities. Operating at millikelvin temperatures, these detectors measure athermal phonons with high precision, enabling sensitivity to energy depositions at the eV to sub-keV scale. This makes them particularly well suited for searches for low-mass dark matter candidates [30].

Recent technological developments in cryogenic semiconductor detectors, together with innovations such as skipper charge-coupled devices (CCDs), have significantly extended sensitivity into the sub-GeV dark matter regime [26]. These ultra-low-threshold technologies enable the exploration of interaction channels beyond conventional nuclear recoils, including electron recoils and absorption processes. Such channels are particularly relevant for light dark matter candidates, including axions, ALPs, and dark photons.

A diverse set of experimental approaches, including liquid noble detectors, cryogenic detectors, and other solid-state technologies, collectively probe a wide range of interaction channels and energy scales. Among these, cryogenic detectors remain at the forefront of low-mass dark matter searches, where achieving ultra-low thresholds and precise energy reconstruction is critical.

Despite these advances, no conclusive evidence for dark matter has yet been observed. As experimental sensitivities continue to improve, they are approaching regimes where irreducible backgrounds, particularly those arising from coherent elastic neutrino–nucleus scattering (CEνNS), become increasingly significant [25]. Future progress will therefore require not only increased exposure and further background reduction, but also continued innovation in detector technologies optimized for rare-event detection at ultra-low energies.

The current global experimental landscape for dark matter candidates, including WIMPs, axions/axion-like particles, and dark photons, is summarized in Fig. 1.9.

By simultaneously measuring phonon and ionization signals at millikelvin temperatures, cryogenic semiconductor detectors achieve precise energy reconstruction and powerful discrimination between electron and nuclear recoils, enabling sensitivity to a broad range of dark matter interaction channels. The Super Cryogenic Dark Matter Search (SuperCDMS) experiment represents a leading implementation of this approach. Designed specifically to probe the low-mass dark matter parameter space, SuperCDMS employs advanced cryogenic detector technologies to achieve ultra-low energy thresholds and excellent background rejection. The central focus of this thesis is the search for low-mass dark matter using the SuperCDMS experiment. These efforts are essential for enabling robust and sensitive

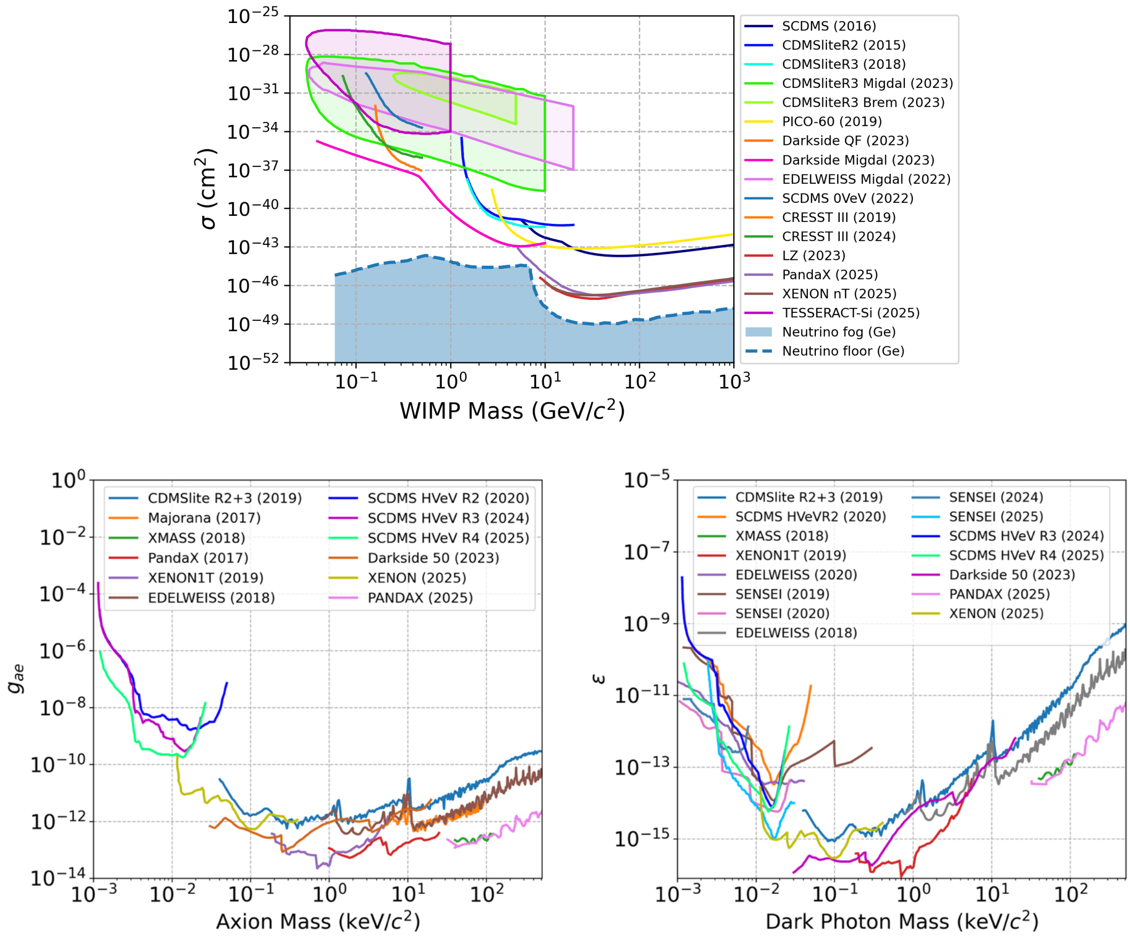

FIGURE 1.9: Exclusion curves (90% CL) from global direct detection experiments. Top: constraints on WIMP–nucleon scattering cross-section, including the neutrino floor. Bottom left: limits on axions/ALPs. Bottom right: limits on dark photons. Results from experiments including SuperCDMS, EDELWEISS, Majorana, SENSEI, TESSERACT, PICO, DarkSide, CRESST, LZ, PandaX, and XENON are shown. Adapted from [16].

searches for low-mass dark matter candidates.

1.4 Scope and Outline of This Thesis

This thesis presents a comprehensive and experimentally grounded framework for the search for low-mass dark matter, combining detailed studies of cryogenic detector physics, precision calibration, background characterization, and statistically rigorous analysis techniques to maximize sensitivity to rare interactions.

A central focus of this work is the characterization of SuperCDMS silicon cryogenic calorimeters and the development of a novel sub-keV energy calibration. Bias-dependent studies of detector response, together with precise sub-keV calibration using Si Compton steps, improve the understanding of detector behavior for low energy depositions and enable enhanced sensitivity to dark matter candidates with masses in the sub-GeV/c^2 range for WIMPs and down to a few eV/c^2 for axion-like particles and dark photons [33, 34].

Statistical analysis is another key component of this work. Profile likelihood ratio (PLR) methods are applied to SuperCDMS Soudan data to constrain couplings of axion-like particles and dark photons, providing improved sensitivity compared to conventional Poisson or Optimum Interval approaches.

Background characterization is an important complementary aspect of this thesis. Independent studies of coherent elastic neutrino–nucleus scattering (CEνNS) quantify the impact of reactor antineutrino fluxes on the neutrino floor, emphasizing site-dependent considerations for future low-threshold experiments. Additionally, fast-neutron energy calibrations using EJ-301 liquid scintillation detectors provide validated tools for modeling and mitigating nuclear-recoil backgrounds, ensuring robust interpretation of potential dark matter signals.

Collectively, these studies enhance the scientific reach of SuperCDMS and other direct-detection experiments, guiding future detector design, experimental site selection, and analysis strategies for probing the particle nature of dark matter.

The thesis is organized as follows: Chapter 2 provides an overview of the SuperCDMS experiment. Chapter 3 presents a comprehensive study of Compton-step-based sub-keV energy calibration and bias-dependent detector response in SuperCDMS silicon detectors.

Chapter 4 reports searches for axion-like particles and dark photons using PLR methods in SuperCDMS. Chapter 5 investigates the impact of reactor antineutrino–induced CEνNS on the neutrino floor for low-mass WIMP searches. Chapter 6 focuses on fast-neutron background characterization and the calibration of EJ-301 liquid scintillation detectors. Finally, Chapter 7 is the concluding chapter summarises the key findings and discusses their future implications for advancing direct dark matter searches.

Bibliography

[1] F. Zwicky. "Die Rotverschiebung von extragalaktischen Nebeln". *Helvetica Physica Acta* 6 (1933), pp. 110–127.

[2] F. Zwicky. "On the Masses of Nebulae and of Clusters of Nebulae". *Astrophysical Journal* 86 (1937), pp. 217–246.

[3] V. C. Rubin and W. K. Ford. "Rotation of the Andromeda Nebula from a Spectroscopic Survey of Emission Regions". *Astrophysical Journal* 159 (1970), pp. 379–403.

[4] V. C. Rubin, W. K. Ford, and N. Thonnard. "Rotational properties of 21 SC galaxies with a large range of luminosities and radii". *Astrophysical Journal* 238 (1980), pp. 471–487.

[5] D. Clowe, M. Bradač, A. H. Gonzalez, M. Markevitch, S. W. Randall, C. Jones, and D. Zaritsky. "A Direct Empirical Proof of the Existence of Dark Matter". *Astrophysical Journal Letters* 648 (2006), pp. L109–L113. arXiv: astro-ph/0608407.

[6] Planck Collaboration, N. Aghanim, Y. Akrami, M. Ashdown, et al. "Planck 2018 results. VI. Cosmological parameters". *Astronomy & Astrophysics* 641 (2020), A6. arXiv: 1807.06209.

[7] Matthew Newby. *Galaxy Rotation Curve*. https://sites.temple.edu/profnewby/2019/05/04/galaxy-rotation-curve/. May 2019.

[8] J. F. Navarro, C. S. Frenk, and S. D. M. White. “The Structure of Cold Dark Matter Halos”. *Astrophysical Journal* 462 (1996), pp. 563–575. arXiv: astro-ph/9508025.

[9] P. Schneider, J. Ehlers, and E. E. Falco. *Gravitational Lenses*. Berlin, Heidelberg: Springer-Verlag, 1992.

[10] M. Bartelmann. *Gravitational Lensing*. Berlin, Heidelberg: Springer, 2010.

[11] Johanna L. Miller. “Gravitational-lensing measurements push Hubble-constant discrepancy past 5σ”. *Physics Today* (2020).

[12] G. R. Blumenthal, S. M. Faber, J. R. Primack, and M. J. Rees. “Formation of galaxies and large-scale structure with cold dark matter”. *Nature* 311 (1984), pp. 517–525.

[13] Volker Springel, Carlos S. Frenk, and Simon D. M. White. “The large-scale structure of the Universe”. *Nature* 440 (2006), pp. 1137–1144.

[14] Gianfranco Bertone, Dan Hooper, and Joseph Silk. “Particle dark matter: Evidence, candidates and constraints”. *Physics Reports* 405 (2005), pp. 279–390.

[15] Edward W. Kolb and Michael S. Turner. *The Early Universe*. Redwood City: Addison-Wesley, 1990.

[16] S. Das, R. Dey, V. K. S. Kashyap, B. Mohanty, D. Mondal, S. Banik, M. Chaudhuri, and V. Iyer. “Rare Event Searches Using Cryogenic Detectors via Direct Detection Methods” (Dec. 2025). arXiv: 2512.02317 [hep-ex].

[17] R. D. Peccei and Helen R. Quinn. “CP Conservation in the Presence of Instantons”. *Phys. Rev. Lett.* 38 (1977), pp. 1440–1443.

[18] Steven Weinberg. “A New Light Boson?” *Phys. Rev. Lett.* 40 (1978), pp. 223–226.

[19] Frank Wilczek. “Problem of Strong P and T Invariance in the Presence of Instantons”. *Phys. Rev. Lett.* 40 (1978), pp. 279–282.

[20] David J. E. Marsh. “Axion Cosmology”. *Physics Reports* 643 (2016), pp. 1–79.

[21] Peter W. Graham, Igor G. Irastorza, Steven K. Lamoreaux, Axel Lindner, and Karl A. van Bibber. “Experimental Searches for the Axion and Axion-Like Particles”. *Annual Review of Nuclear and Particle Science* 65 (2015), pp. 485–514.

[22] Bob Holdom. “Two U(1)’s and Epsilon Charge Shifts”. *Physics Letters B* 166 (1986), pp. 196–198.

[23] Rouven Essig, John A. Jaros, William Wester, et al. “Dark Sectors and New, Light, Weakly-Coupled Particles” (2013). arXiv: 1311.0029 [hep-ph].

[24] J. D. Lewin and P. F. Smith. “Review of mathematics, numerical factors, and corrections for dark matter experiments based on elastic nuclear recoil”. *Astroparticle Physics* 6 (1996), pp. 87–112.

[25] J. Billard, L. Strigari, and E. Figueroa-Feliciano. “Implication of neutrino backgrounds on the reach of next generation dark matter direct detection experiments”. *Phys. Rev. D* 89 (2014), p. 023524.

[26] Rouven Essig, Jeremy Mardon, and Tomer Volansky. “Direct Detection of Sub-GeV Dark Matter”. *Phys. Rev. D* 85 (2012), p. 076007.

[27] Jens Lindhard, Morten Scharff, and Hans E Schiøtt. *Range concepts and heavy ion ranges*. Vol. 33. Munksgaard Copenhagen, 1963.

[28] VI Tretyak. “Semi-empirical calculation of quenching factors for ions in scintillators”. *Astroparticle Physics* 33.1 (2010), pp. 40–53.

[29] E. Aprile et al. “Dark Matter Search Results from a One Ton-Year Exposure of XENON1T”. *Phys. Rev. Lett.* 121 (2018), p. 111302.

[30] R. Agnese et al. “First Dark Matter Constraints from a SuperCDMS Single-Charge Sensitive Detector”. *Phys. Rev. Lett.* 121 (2018), p. 051301.

[31] D.-M. Mei and A. Hime. “Muon-induced background study for underground laboratories”. *Phys. Rev. D* 73 (2006), p. 053004.

[32] R. Agnese et al. “Projected Sensitivity of the SuperCDMS SNOLAB experiment”. *Phys. Rev. D* 95 (2017), p. 082002.

[33] M. F. Albakry et al. “Low-energy calibration of SuperCDMS HVeV cryogenic silicon calorimeters using Compton steps”. *Phys. Rev. D* 112.9 (2025), p. 092014. arXiv: 2508.02402 [physics.ins-det].

[34] M. F. Albakry et al. “Search for low-mass electron-recoil dark matter using a single-charge sensitive SuperCDMS-HVeV Detector” (Sept. 2025). arXiv: 2509.03608 [hep-ex].

CHAPTER 2

Overview of SuperCDMS experiment

Contents

2.1 SuperCDMS Experiment

The Super Cryogenic Dark Matter Search (SuperCDMS) experiment is a direct detection program designed to search for dark matter particle through its interactions with atomic nuclei or electrons in ultra-sensitive cryogenic detectors. Building on the success of earlier CDMS experiments, SuperCDMS employs advanced semiconductor detector technologies operated at millikelvin temperatures to achieve exceptional sensitivity to rare and low-energy interactions.

A defining feature of the SuperCDMS approach is the simultaneous measurement of phonon and ionization signals, which enables precise energy reconstruction and powerful discrimination between signal and background events. Over successive experimental phases, the collaboration has continuously improved detector performance, background rejection, and energy thresholds, allowing it to explore increasingly challenging regions of dark matter parameter space.

In particular, recent theoretical developments and experimental advances have motivated a strong focus on the search for low-mass dark matter candidates. This forms the basis of the dedicated low-mass dark matter program within SuperCDMS.

2.1.1 Low-Mass Dark Matter Program in SuperCDMS

In the context of direct detection of dark matter, particular attention has been devoted to Weakly Interacting Massive Particles (WIMPs). While traditional experiments have focused on WIMP masses above $\sim$ 10 GeV$/c^2$, increasing theoretical and experimental interest has shifted toward the low-mass regime ($\lesssim$ 10 GeV$/c^2$), motivated by models such as asymmetric dark matter, hidden-sector dark matter, and other sub-GeV candidates.

Detecting low-mass dark matter presents significant experimental challenges. The maximum recoil energy transferred in an elastic collision between a dark matter particle of mass m_χ and a target nucleus of mass M is given by

$$E_r^{\max} \approx \frac{2\mu^2 v^2}{M}, \tag{2.1}$$

where $\mu = \frac{m_\chi M}{m_\chi + M}$ is the reduced mass and $v \sim 10^{-3}c$ is the typical dark matter velocity in the Galactic halo. For $m_\chi \ll M$, the recoil energy scales approximately as $E_r \propto m_\chi^2$, leading to recoil energies in the sub-keV or even eV range. This places stringent requirements on detector thresholds and noise performance.

The SuperCDMS experiment is specifically designed to probe this low-mass regime using cryogenic semiconductor detectors operated at millikelvin temperatures [1]. At such low temperatures, thermal noise is strongly suppressed, enabling sensitivity to extremely small energy depositions.

SuperCDMS detectors are based on high-purity germanium (Ge) and silicon (Si) crystals that simultaneously measure phonon and ionization signals produced by particle interactions. This dual-channel readout provides powerful discrimination between electron recoils and nuclear recoils, while maintaining excellent energy resolution at low energies [2, 3].

The phonon signal is measured using superconducting sensors, primarily Transition Edge Sensors, coupled to aluminum phonon-collecting fins. These sensors operate in the narrow transition region between superconducting and normal states, where small temperature changes result in large resistance variations. The TES signals are read out using Superconducting Quantum Interference Devices (SQUIDs), enabling sensitivity to energy depositions at the level of a few electronvolts [4–6].

An important feature of SuperCDMS detectors is the ability to operate in high-voltage (HV) mode, where the drift of charge carriers in an applied electric field produces additional phonons via the Neganov–Trofimov–Luke (NTL) effect. This mechanism amplifies the phonon signal in proportion to the number of electron–hole pairs, enabling ultra-low energy thresholds and extending sensitivity to sub-GeV dark matter candidates [7]. However, this comes at the cost of losing event-by-event discrimination between electron recoils (ER) and nuclear recoils (NR). At high bias voltage, the phonon signal becomes dominated by NTL phonons, which are directly proportional to the ionization produced in the event. As a result, the measured phonon signal effectively tracks the ionization signal, and the two observables (Phonon and ionization) are no longer independent. This removes the ability to construct an ionization yield parameter, thereby collapsing the discrimination space and preventing ER/NR separation on an event-by-event basis.

The SuperCDMS program has evolved through multiple experimental phases. Earlier deployments at the Soudan Underground Laboratory demonstrated the effectiveness of cryogenic detector technology and established leading limits on low-mass dark matter interactions [2]. The next-generation experiment at SNOLAB builds upon these results with improved detector design, larger target mass, and a lower background environment [8, 9].

Together, these developments enable SuperCDMS to explore previously inaccessible regions of parameter space and to serve as a leading platform for investigating dark matter interactions at the lowest accessible energy scales.

2.1.2 Scientific Goals of SuperCDMS

The primary scientific objective of the SuperCDMS program is to search for low mass dark matter candidates with world-leading sensitivity. This region of parameter space remains largely unexplored due to the experimental challenges associated with detecting extremely small energy depositions.

Traditional direct detection experiments, optimized for heavy WIMPs ($\gtrsim 10$ GeV$/c^2$), typically have energy thresholds of order keV. Such thresholds severely limit their sensitivity to lighter dark matter particles, for which the expected recoil energies fall below the detection threshold. SuperCDMS addresses this limitation through the development of phonon-sensitive detectors with sub-keV and even eV-scale thresholds [8, 10].

The scientific goals of SuperCDMS can be broadly categorized as follows:

- **Search for low-mass WIMPs:** SuperCDMS primarily aims to detect nuclear recoils induced by WIMPs with masses below $\sim$ 10 GeV/c^2. By achieving ultra-low energy thresholds, the experiment probes spin-independent interaction cross sections beyond the reach of previous experiments [1, 8].

- **Probe sub-GeV bosonic dark matter candidates:** In addition to nuclear recoils, SuperCDMS is sensitive to electron recoils arising from interactions of light dark matter candidates such as axion-like particles (ALPs), dark photons, and other hidden-sector particles. These interactions can occur via scattering or absorption processes, producing signals at the eV scale [11–13].

- **Search for fractionally charged particles:** SuperCDMS is also sensitive to particles carrying electric charges smaller than that of the electron, i.e., $q = fe$ with $0 < f < 1$. Such particles would produce signals significantly smaller than those expected from minimum ionizing particles. Previous SuperCDMS analyses have placed constraints on the parameter space of fractionally charged particles by setting upper limits on their interaction rates (and hence intensity) as a function of the fractional charge f [14, 15].

- **Approach the neutrino floor:** As detector sensitivities improve, neutrino-induced backgrounds from solar, atmospheric, and diffuse supernova neutrinos become increasingly relevant. SuperCDMS aims to reach parameter space approaching the so-called neutrino floor, where coherent elastic neutrino–nucleus scattering (CEνNS) from solar neutrinos constitutes an irreducible background [1]. In this regime, dark matter searches become increasingly challenging due to the similarity between WIMP-induced nuclear recoils and neutrino-induced recoils. Consequently, novel detection strategies will be required to distinguish signals below the neutrino floor.

- **Advance cryogenic detector technology:** A key objective of SuperCDMS is the continued development of cryogenic detector technologies, including improved phonon sensors, optimized charge readout, and scalable detector architectures. These advancements are essential for future experiments aiming to achieve even lower energy thresholds and larger exposures [1].

Achieving these goals requires ultra-low energy thresholds, excellent energy resolution, and stringent control of backgrounds from radioactive contamination, cosmogenic activation, and environmental radiation. The combination of these capabilities positions SuperCDMS as a leading experiment in the global effort to detect low-mass dark matter.

2.2 Detector Technology

SuperCDMS detectors are based on high-purity Ge and Si crystals operated at cryogenic temperatures ($\sim$ 10–50 mK). At these temperatures, thermal excitations are strongly suppressed, allowing extremely small energy depositions to be measured with high precision. When a particle interacts within the detector, its energy is partitioned into lattice excitations (phonons) and electron–hole (e/h) pair creation. The simultaneous measurement of these two channels enables precise energy reconstruction and powerful discrimination between different types of interactions [6, 7, 16].

The core detector design is the interleaved Z-sensitive Ionization and Phonon (iZIP) configuration. Each iZIP consists of a cylindrical semiconductor crystal instrumented on both faces with interleaved phonon sensors and ionization electrodes. This geometry enables three-dimensional event reconstruction and provides strong rejection of surface backgrounds, which typically exhibit incomplete charge collection.

During operation, a voltage bias is applied across the detector, causing electron–hole pairs generated by particle interactions to drift toward the electrodes. The drift of these charge carriers produces additional phonons through the NTL effect, effectively amplifying the phonon signal. SuperCDMS detectors can therefore be operated in two complementary modes:

- **Standard iZIP mode:** A low bias voltage (±2–4 V) is applied, enabling precise position reconstruction and excellent background discrimination through simultaneous phonon and ionization readout. Such operating mode is called low background mode.
- **High-voltage mode:** A larger bias voltage (typically 70–150 V) is applied to enhance the phonon signal via NTL amplification. This mode sacrifices ER-NR discrimination capability in favor of achieving extremely low energy thresholds, extending sensitivity to sub-keV and eV-scale energy depositions [7]. Such operation is called low-threshold mode.

2.2.1 Ionization Signal

When a particle interacts with the detector, a portion of its deposited energy produces electron–hole (e^-/h^+) pairs through ionization processes in the semiconductor crystal [6, 7]. In cryogenic Ge and Si detectors, the average energy required to create a single electron–hole pair is $\epsilon \approx 3.0$ eV for Ge and 3.8 eV for Si. These values are significantly larger than the corresponding bandgap energies ($E_g \approx 0.74$ eV for Ge and 1.12 eV for Si), reflecting additional energy losses to phonon production during the charge creation process [6]. This additional energy loss arises because Ge and Si are indirect bandgap semiconductors, in which momentum conservation during electron excitation requires the involvement of the crystal lattice. As a result, phonons must be produced to provide the necessary momentum transfer, leading to energy being partitioned between ionization and lattice excitations.

Following their creation, the charge carriers form a localized cloud near the interaction site and drift under the applied electric field toward the detector electrodes. During transport, carriers may be trapped by impurities or crystal defects, reducing charge collection efficiency. To mitigate these effects, periodic LED flashing is used to neutralize space charge and restore the electric field configuration [6].

The motion of charge carriers induces signals on the electrodes. The amplitude of the charge pulse is proportional to total image charge created. The total ionization energy is given by

$$E_Q = N_{e/h}\,\epsilon, \tag{2.2}$$

where $N_{e/h}$ is the number of electron–hole pairs.

The ionization yield is defined as

$$Y(E_r) = \frac{E_Q}{E_r}, \tag{2.3}$$

where E_r is the recoil energy. Electron recoils typically exhibit $Y \approx 1$, while nuclear recoils have suppressed yield ($Y < 1$), as a larger fraction of the recoil energy is transferred to lattice excitations. This behavior is commonly described by Lindhard quenching theory.

The number of charge carriers can therefore be written as

$$N_{e/h} = \frac{Y(E_r)\,E_r}{\epsilon}. \tag{2.4}$$

In HV mode, the drift of these charge carriers under a strong electric field produces additional phonons via the NTL effect [17], thereby amplifying the phonon signal and improving sensitivity to low-energy recoils [7].

2.2.2 Phonon Signal

Phonons are quanta of lattice vibrations generated when energy is deposited in the detector crystal [18]. The total phonon signal in SuperCDMS detectors consists of multiple contributions arising from different physical processes.

Three primary phonon components are identified:

1. **Primary phonons:** generated directly from the initial recoil,
2. **NTL phonons:** produced during charge drift,
3. **Relaxation phonons:** generated during charge recombination near surfaces.

At cryogenic temperatures ($T \sim$ 10–50 mK), the thermal phonon population in a solid is strongly suppressed. The phonon occupation number follows the Bose–Einstein distribution,

$$\langle n(\omega) \rangle = \frac{1}{e^{\hbar\omega/k_B T} - 1}, \tag{2.5}$$

where $\hbar\omega$ is the phonon energy and $k_B T$ is the thermal energy scale. In the low-temperature limit, for modes satisfying $\hbar\omega \gg k_B T$, the occupation number reduces to

$$\langle n(\omega) \rangle \approx e^{-\hbar\omega/k_B T} \ll 1, \tag{2.6}$$

indicating an exponential suppression of thermal phonons.

In the Debye approximation, the total thermal energy of the lattice scales as

$$U(T) \propto T^4, \tag{2.7}$$

for temperatures well below the Debye temperature. As a result, at ~mK temperatures, the lattice contains a negligible population of thermal phonons and is close to its ground vibrational state. When a particle scatters off an electron or nucleus in the crystal, a significant fraction of the deposited energy is converted into lattice excitations, with approximately 70% of the energy ultimately transmitted as phonons through the subsequent thermalization cascade. Such interactions generate non-equilibrium (athermal) phonons, which have energies significantly above the thermal background. These phonons propagate through the crystal and can be collected by sensors before thermalization, enabling highly sensitive phonon detection.

Primary Phonons

Primary phonons are generated promptly at the interaction site and initially possess high frequencies. Their propagation through the crystal is governed by:

- **Anharmonic decay:** high-frequency phonons decay into multiple lower-energy phonons,
- **Elastic isotope scattering:** phonons scatter elastically off isotopic disorder and impurities.

As phonons down-convert in frequency, their mean free path increases, and they eventually propagate ballistically across the detector. The detector phonon sensors located on the top and bottom surfaces, primarily collect the phonons during this ballistic scattering of phonons.

The energy stored in primary phonons is given by [19]

$$E_P = E_r - N_{e/h} E_g, \tag{2.8}$$

where E_g represents the bandgap energy associated with electron–hole pair creation. This expression reflects the partitioning of recoil energy between ionization and lattice excitation at the microscopic level.

Relaxation Phonons

As charge carriers drift and eventually recombine or relax to the Fermi level near detector surfaces, their residual energy is released into the lattice as phonons. These relaxation phonons are typically produced near the detector surfaces and are efficiently collected by the phonon sensors.

The corresponding energy contribution can be expressed as [19],

$$E_R = N_{e/h} E_g + E_{\text{K.E.}}, \tag{2.9}$$

where $E_{\text{K.E.}}$ denotes the residual kinetic energy of the charge carriers prior to recombination.

NTL Phonons

NTL phonons arise from the work done by the electric field on drifting charge carriers. As electrons and holes traverse a potential difference V_b, they gain energy qV_b, which is subsequently transferred to the lattice as phonons.

The total NTL phonon energy is given by [19]

$$E_{\text{Luke}} = qN_{e/h} V_b - E_{\text{K.E.}} \tag{2.10}$$

$E_{\text{K.E.}}$ is returned to the crystal during the relaxation of the carriers.

Total Phonon Energy

The total phonon energy measured is the sum of all contributions:

$$E_{\text{ph}}^{\text{total}} = E_P + E_R + E_{\text{Luke}} \tag{2.11}$$

$$= E_r + qN_{e/h} V_b. \tag{2.12}$$

Using $N_{e/h} = E_Q/\epsilon$, this becomes

$$E_{\text{ph}}^{\text{total}} = E_r \left(1 + \frac{qV_b}{\epsilon} Y(E_r)\right). \tag{2.13}$$

Phonon Detection with Transition Edge Sensors (TES)

Phonons generated in the detector are measured using quasiparticle-trap-assisted electrothermal-feedback Transition Edge Sensors (QETs). Each QET consists of superconducting aluminum (Al) phonon-collecting fins coupled to a tungsten (W) Transition Edge Sensor. The Al fins possess a higher superconducting critical temperature ($T_C \sim 1.2$ K) compared to the tungsten TES, which is operated within its superconducting transition at millikelvin temperatures ($T_C \sim 10$–80 mK). The detector is cooled such that the aluminum fins remain in the superconducting state, while the tungsten TES is biased and maintained within its superconducting-to-normal transition using electrothermal feedback, enabling highly sensitive temperature-dependent resistance measurements.

When a phonon in the detector reaches a bare Ge/Si surface, it is predominantly reflected back into the detector. In contrast, if a phonon encounters a surface instrumented with an aluminum fin, it can be absorbed into the fin. Ballistic phonons may undergo multiple reflections within the detector volume until they eventually enter a phonon-absorbing fin. Incident phonons absorbed in the Al fins lead to the breaking of Cooper pairs and the generation of quasiparticles. The characteristic energy scale required for quasiparticle creation in a superconductor is determined by the superconducting energy gap, given approximately by

$$E_{\text{gap}} \approx 1.76\, k_B T_C, \tag{2.14}$$

within BCS theory [5, 20]. For aluminum, this corresponds to an energy of order $\sim 340\,\mu$eV.

The generated quasiparticles diffuse through the Al fins and are subsequently collected into the tungsten TES, where the superconducting gap is significantly smaller ($\sim 30\,\mu$eV). This facilitates efficient energy absorption in the TES. During this transport process, some energy loss occurs due to acoustic impedance mismatch at material interfaces, quasiparticle recombination, and trapping at the Al–W boundary, which reduce the overall transmission efficiency.

Once the quasiparticles are absorbed in the TES, their energy is transferred to the electrical signal. The deposited energy is rapidly redistributed through electron–electron and electron–phonon interactions, driving the system toward a quasi-equilibrium state between the electronic and lattice subsystems. As the TES is thermally weakly coupled to the heat bath via a thin thermal link, the absorbed energy leads to a transient increase in the TES temperature. In this regime, the initial temperature rise can be approximated by $\Delta T \approx E_{\mathrm{abs}}/C$, where E_{abs} is the absorbed energy and C is the heat capacity of the TES. Due to the extremely small heat capacity at millikelvin temperatures, even small energy depositions produce measurable temperature changes, followed by thermal relaxation back to the bath temperature with a characteristic time constant determined by the thermal conductance.

The TES is voltage-biased within its superconducting transition, where its resistance exhibits a steep dependence on temperature. Consequently, the increase in temperature leads to a significant increase in resistance, which modifies the current flowing through the TES. This current variation is read out using a superconducting quantum interference device (SQUID) circuit, enabling precise measurement of the deposited phonon energy. Furthermore, negative electrothermal feedback stabilizes the TES operation by reducing Joule heating as the resistance increases, thereby improving the linearity, response time, and energy resolution of the detector.

Overall, the combination of quasiparticle-mediated phonon collection in the aluminum fins, efficient energy absorption in the tungsten TES, and sensitive SQUID-based readout allows SuperCDMS detectors to achieve excellent sensitivity to small energy depositions. This capability is essential for rare event searches, particularly in the low-energy regime

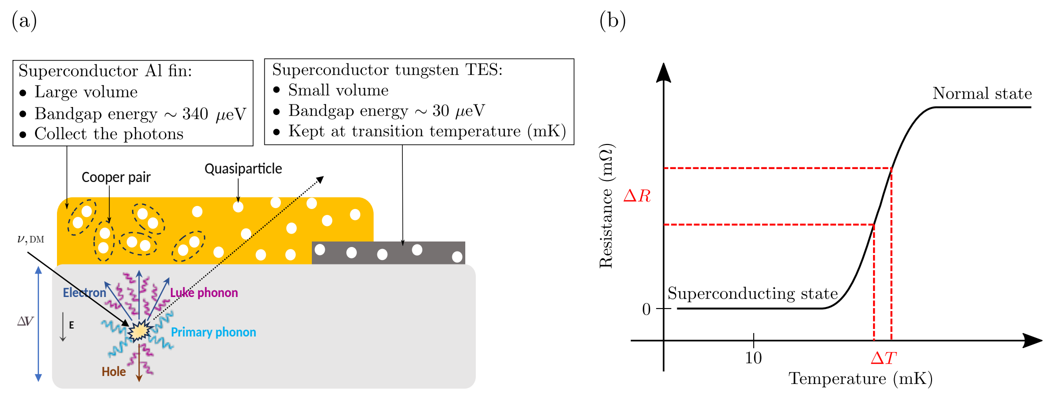

FIGURE 2.1: (a) Schematic illustration of a SuperCDMS phonon sensor (QET), showing aluminum phonon-collecting fins coupled to a tungsten Transition Edge Sensor. Incident phonons deposit energy in the Al fins, producing quasiparticles that diffuse into the TES, resulting in a measurable change in resistance. (b) Typical TES transition curve, illustrating the sharp resistance variation near the superconducting transition temperature T_C, which enables high sensitivity to small energy depositions. Adapted from [21].

relevant for low-mass dark matter interactions.

2.3 Data Acquisition and Data Processing

In this section, the data acquisition and data processing framework of the SuperCDMS experiment is described. These systems are designed to enable the precise measurement of extremely small phonon and ionization signals while maintaining low noise and high stability, which are essential for rare-event searches. The discussion reflects the general methodology employed across the SuperCDMS program, including the Soudan, NEXUS, and SNOLAB experiments. While specific hardware implementations and operational parameters may vary between these experimental phases, the core principles of signal digitization, triggering, and waveform-based reconstruction using optimal filtering techniques remain common.

2.3.1 Data Acquisition

The SuperCDMS data acquisition (DAQ) system is responsible for recording signals from both phonon and ionization channels with high fidelity.

Phonon Readout: Phonon signals are measured using TES sensors coupled to SQUIDs [19, 22]. The TES sensors are voltage-biased within their superconducting transition, where small temperature changes result in large resistance variations. The resulting current changes are amplified by SQUIDs, which provide ultra-low-noise readout of the phonon signals.

The analog signals from the SQUID readout are first amplified and then digitized using high-resolution analog-to-digital converters (ADCs) integrated within the SuperCDMS data acquisition electronics. The resulting digitized waveforms are handled by the Data Concentrator and Readout Controller (DCRC), a custom DAQ module that is part of the SuperCDMS readout system. The DCRC is responsible for data formatting, buffering, synchronization, and transmission to the central acquisition software. Depending on the operational mode, the readout can operate in either continuous or triggered acquisition configurations.

Ionization Readout: For iZIP detectors, ionization signals are measured using charge-sensitive amplifiers. The induced charge on the electrodes is converted into a voltage signal and digitized. The ionization readout chain is designed to achieve low electronic noise, enabling the detection of small charge signals corresponding to low-energy events.

Triggering and Event Building: Event triggering in SuperCDMS is primarily based on phonon signals due to their superior sensitivity at low energies. The trigger system operates on analog sums of phonon and charge channels, which are compared against configurable threshold levels.

Multiple trigger thresholds are defined for each detector, including phonon low and high thresholds (Plo, Phi), charge thresholds (Qlo, Qhi), and an ultra-low phonon threshold (Pwhisper). In standard operation, the trigger condition is defined by a threshold crossing of the phonon low level (Plo), which provides optimal efficiency for low-energy event detection.

When the trigger condition is satisfied in a detector, a *detector trigger* is issued. Among all detectors, the first to trigger defines the *global trigger*. Waveforms from all relevant channels are then recorded and time-aligned with respect to this global trigger, ensuring consistent event reconstruction across the detector array.

Waveforms are recorded over a fixed time window that includes both pre-trigger and post-trigger regions, allowing accurate baseline estimation and pulse reconstruction. Depending on the data-taking configuration, either the full detector array or a subset of detectors may be read out following a trigger.

In addition to physics triggers, the DAQ system periodically generates *random triggers*, which record waveforms independent of energy depositions inside detector. These events provide an unbiased measurement of the baseline noise and are essential for characterizing the noise power spectral density used in offline signal reconstruction. The overall trigger rate also serves as an important diagnostic of detector performance and background conditions.

Regular calibration runs are performed using known energy sources (e.g., gamma-ray sources or LED pulsing for charge neutralization) to monitor detector response, gain stability, and noise performance. These calibrations are essential for maintaining consistent detector performance over long data-taking periods.

2.3.2 Data Processing

The recorded waveform data are processed offline to extract physical observables such as energy, timing, and interaction position. This reconstruction chain involves baseline correction, noise characterization, pulse fitting, and event-level selection. Although developed and validated in the context of SuperCDMS Soudan, the same framework forms the basis of the analysis strategy for current and future SuperCDMS experiments, including SNOLAB, with extensions to more advanced filtering techniques.

Preprocessing: Each digitized waveform is first corrected for baseline offsets using the pre-trigger region. The baseline subtraction ensures a stable zero-level reference for all channels. Noise properties are then characterized using randomly triggered events, which provide unbiased samples of detector noise. These events are used to compute the noise power spectral density (PSD), a key input for all optimal filtering procedures.

Optimal Filtering Framework: Pulse reconstruction in SuperCDMS is based on the optimal filter (OF) formalism, which provides a minimum-variance estimator for pulse amplitude under the assumption of stationary Gaussian noise and a known signal template [23].

For a measured waveform $S(t)$, the signal model is expressed as

$$S(t) = a\,A(t - t_0) + n(t), \tag{2.15}$$

where $A(t)$ is the template pulse, a is the amplitude, t_0 is the time offset, and $n(t)$ is noise.

Transforming into the frequency domain, the amplitude estimator is obtained by minimizing

$$\chi^2(a) = \sum_f \frac{|\tilde{S}(f) - a\,\tilde{A}(f)|^2}{J(f)}, \tag{2.16}$$

where $\tilde{S}(f)$ and $\tilde{A}(f)$ are Fourier transforms of the signal and template, and $J(f)$ is the noise PSD.

The analytic solution for the optimal amplitude is

$$\hat{a} = \frac{\sum_f \frac{\tilde{A}^*(f)\,\tilde{S}(f)}{J(f)}}{\sum_f \frac{|\tilde{A}(f)|^2}{J(f)}}. \tag{2.17}$$

Time delay is incorporated through phase rotation:

$$\tilde{A}(f, t_0) = \tilde{A}(f)\, e^{-2\pi i f t_0}, \tag{2.18}$$

and the joint minimization over (a, t_0) yields the best-fit pulse parameters.

This formulation can also be interpreted as applying a frequency-domain filter

$$\tilde{\phi}(f) = \frac{\tilde{A}^*(f)}{J(f)}, \tag{2.19}$$

which optimally weights frequency components by their signal-to-noise ratio.

Pulse templates are constructed by averaging good events of a given energy with high signal-to-noise ratios. Separate templates are defined for different detector channels to account for spatial and electronic variations in pulse shapes.

To improve reconstruction performance beyond the basic OF model, several extensions are employed [23]. A brief comparison of each is presented below.

(1) Standard 1D Optimal Filter: The basic OF assumes stationary noise and a fixed template shape. It is primarily used for energy estimation and instrumental background rejection.

(2) Non-Stationary Optimal Filter (NSOF): In kg-scale large detectors, pulse shapes may vary with position of particle intercations, introducing correlated deviations from the template. These effects are treated as an additional noise source by replacing the scalar PSD with a covariance matrix:

$$\chi^2 = (\tilde{S} - a\tilde{A})^\dagger V^{-1}(\tilde{S} - a\tilde{A}), \tag{2.20}$$

where V encodes correlations between frequency modes derived from pulse residuals. This improves energy resolution by down-weighting position-dependent distortions.

(3) Two-Template Optimal Filter (2T-Fit): To explicitly capture pulse shape variations, the signal is modeled as a superposition of fast and slow components:

$$S(t) = a_1 A_1(t - t_0) + a_2 A_2(t - t_0) + n(t), \tag{2.21}$$

leading to the minimization

$$\chi^2 = \sum_f \frac{|\tilde{S}(f) - a_1\tilde{A}_1(f) - a_2\tilde{A}_2(f)|^2}{J(f)}. \tag{2.22}$$

This method provides enhanced sensitivity to event position through relative pulse contributions.

(4) NxM Filter (SuperCDMS SNOLAB): SuperCDMS SNOLAB employs a generalized matrix-based pulse reconstruction framework known as the $N \times M$ filter [24]. This approach extends the conventional optimal filtering formalism to simultaneously analyze multiple readout channels while explicitly accounting for both correlated noise and position-dependent pulse shape variations.

Each detector is instrumented with Transition Edge Sensors (TESs) patterned on the top and bottom faces of a Ge or Si crystal. The TESs are grouped into six phonon readout channels per face, resulting in multiple partially correlated signal streams. In addition to electronic and thermal correlations between channels, the large detector geometry introduces strong position dependence in phonon propagation, leading to significant variations in pulse shapes depending on the interaction location within the substrate.

To address these effects, the detector response is modeled as a linear combination of multiple templates across all channels:

$$\mathbf{S}(f) = \sum_{j=1}^{M} \mathbf{A}_j(f)\, a_j + \mathbf{n}(f), \tag{2.23}$$

where $\mathbf{S}(f)$ is the vector of Fourier-transformed waveforms across N readout channels, $\mathbf{A}_j(f)$ represents the j^{th} pulse template across all channels, a_j are the corresponding amplitudes, and $\mathbf{n}(f)$ denotes the noise contribution.

Correlations between channels are incorporated through a full noise covariance matrix V, leading to the generalized estimator

$$\hat{\mathbf{a}} = \left(\mathbf{A}^{\dagger} V^{-1} \mathbf{A}\right)^{-1} \mathbf{A}^{\dagger} V^{-1} \mathbf{S}. \tag{2.24}$$

This formulation simultaneously accounts for inter-channel noise correlations and non-uniform pulse shapes arising from position-dependent phonon transport. The pulse templates are typically derived using data-driven techniques such as principal component analysis (PCA), which captures dominant modes of pulse variation across the detector volume.

The outputs of the $N \times M$ filter provide a compact representation of the event topology and are further processed using multivariate methods, such as gradient boosted decision trees (GBDTs), to extract reconstructed energy and position information.

This framework significantly improves reconstruction performance by mitigating correlated noise and reducing systematic effects from position-dependent signal variations. In simulated mono-energetic events, energy resolution improvements exceeding a factor of three have been demonstrated, with reconstructed low-energy peaks reaching resolutions below 50 eV in CDMSlite-like configurations, compared to approximately 100 eV using conventional methods.

Overall, the $N \times M$ filter forms the core reconstruction strategy for SuperCDMS SNOLAB, enabling simultaneous optimization of energy resolution, position sensitivity, and multi-channel consistency.

The Summary of different Optimal Filter Usage is shown in 2.1.

TABLE 2.1: Primary applications of optimal filtering algorithms in SuperCDMS data reconstruction.

Method	**Primary Use**
1D Optimal Filter (OF)	Energy estimation and instrumental background discrimination
Non-Stationary OF (NSOF)	Improved energy resolution with position-dependent effects
Two-Template OF (2T-Fit)	Event position and pulse-shape characterization
nxM Filter (SNOLAB)	Multi-channel global reconstruction framework

The optimal filter amplitude is proportional to deposited energy and is converted using calibration constants derived from known radioactive sources. After reconstruction, events are subjected to quality cuts based on pulse shape, timing consistency, and inter-channel agreement to reject noise, poorly reconstructed events and pile-up events.

The SuperCDMS reconstruction pipeline is designed to extract maximal information from low-energy detector signals using statistically optimal estimators. The combination of frequency-domain filtering, template-based reconstruction, and multi-channel extensions enables precise measurement of energy depositions down to the eV scale, which is essential for low-mass dark matter searches.

2.4 SuperCDMS Soudan

The SuperCDMS Soudan experiment was the successor to the CDMS II experiment [25] and represented an advanced phase of the Cryogenic Dark Matter Search (CDMS) program.

It was operated from approximately 2012 to 2015 at the Soudan Underground Laboratory in Minnesota, USA, at a depth of approximately 713 m underground corresponding to 2100 m water equivalent (m.w.e.). The experiment was designed to probe WIMPs, with particular emphasis on improving sensitivity to low-mass dark matter through reduced energy thresholds and enhanced background discrimination.

Building upon the CDMS II experiment, SuperCDMS Soudan introduced advanced cryogenic Ge detectors featuring improved phonon and ionization readout based on transition-edge sensors. These developments enabled more precise energy reconstruction and significantly enhanced rejection of electron-recoil backgrounds. A key advancement in the Soudan phase was the implementation of high-voltage detector operation in a low ionization threshold mode, known as CDMSlite. In this mode, the NTL effect is exploited to amplify the phonon signal, thereby extending sensitivity to very low-energy interactions. The achieved energy thresholds were 56 eV$_{ee}$ and 70 eV$_{ee}$ for CDMSlite Run 2 and Run 3 for two different detectors, respectively [11]. The primary differences between these two runs are the use of different detectors and operating high-voltage settings.

A central component of this thesis focuses on constraining ALPs and dark photons using SuperCDMS Soudan CDMSlite data through an advanced likelihood framework that combines the CDMSliteRun 2 and CDMSliteRun 3 datasets, as described in Chapter 4.

2.4.1 Soudan underground laboratory

The Soudan Underground Laboratory (SUL), located in northern Minnesota, USA, is situated in a former iron mine that has been repurposed for underground scientific research. Over the past few decades, it has hosted several experiments in particle and astroparticle physics, including neutrino and dark matter searches, and provides a well-established infrastructure for low-background experiments.

The experiment was operated deep underground at the Soudan Underground Laboratory to suppress backgrounds induced by cosmic rays, particularly high-energy muons. At a depth of ~2100 m.w.e. (meters water equivalent), the cosmic muon flux is reduced by approximately five orders of magnitude relative to the surface.

This reduction is crucial because muons interacting in the surrounding rock and shielding materials can produce secondary particles, especially neutrons via spallation processes. These neutrons can generate nuclear recoil events in the detectors that are indistinguishable from potential dark matter interactions on an event-by-event basis. The dependence of muon flux on depth and the strong suppression achieved at Soudan are shown in Fig. 2.2.

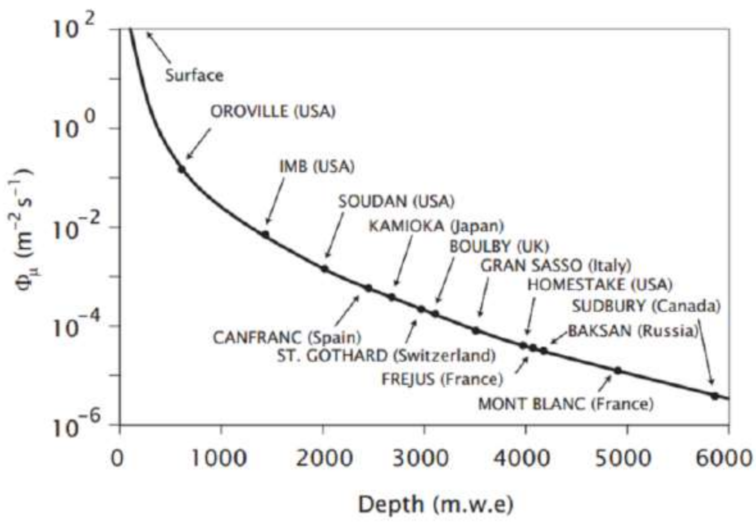

FIGURE 2.2: Dependence of cosmogenic muon flux on depth. The Soudan Underground Laboratory achieves a reduction of approximately $\sim 5 \times 10^4$ relative to surface levels. The plot also shows that deeper underground sites, such as SNOLAB in Sudbury, Canada, provide even greater muon flux suppression due to increased overburden. SuperCDMS SNOLAB, the next generation SuperCDMS experiment will be operated at this deeper site to further reduce cosmogenic backgrounds. Adapted from [16].

2.4.2 Shielding configuration and Background Mitigation

In addition to the natural shielding provided by the iron-rich rock of the former iron mine, the experimental setup was surrounded by multiple layers of passive and active shielding to reduce both radiogenic and cosmogenic backgrounds originating from the surrounding laboratory environment.

The shielding configuration includes:

- **Inner copper shielding:** High-purity copper components within the cryostat provide an average of ~2 cm equivalent shielding, attenuating gamma and beta radiation originating from nearby materials and internal components.

- **Lead shielding:** a total thickness of ~22–23 cm used to suppress external gamma-ray backgrounds, consisting of an outer layer of low activity lead (~18 cm) and an inner ~4.5 cm layer of low-radioactivity ancient lead to minimise background from ^{210}Pb contamination,

- **Polyethylene shielding:** hydrogen-rich material used for neutron mitigation, including an outer ~40 cm layer to moderate fast neutrons and an additional ~10 cm inner layer to absorb neutrons produced within the shielding materials themselves,

- **Active muon veto system:** an array of plastic scintillator panels (Bicron BC-408) instrumented with photomultiplier tubes, arranged in an overlapping geometry to provide nearly full 4π coverage and eliminate direct line-of-sight paths to the detectors.

This multilayer configuration mitigates backgrounds through complementary physical processes: neutron moderation and absorption in hydrogen-rich media, gamma attenuation in high-Z materials, and active rejection of cosmogenic events via the muon veto. Although the ~2090 m.w.e. overburden at Soudan reduces the cosmic muon flux by approximately 5×10^4, the remaining muons can still produce secondary neutrons via spallation in the surrounding rock and shielding materials. The active veto system therefore plays a critical role in identifying and rejecting such events through coincidence tagging.

Within the passive shielding, the outer polyethylene layer moderates incident neutrons to lower energies, after which they can be more effectively absorbed. The lead shielding primarily attenuates gamma radiation; however, interactions within the lead can also generate secondary neutrons and bremsstrahlung radiation. The inclusion of ancient lead in the innermost region reduces internal gamma backgrounds associated with radioactive impurities. The inner polyethylene layer is therefore essential to absorb neutrons generated within the lead and outer shielding layers.

Additional shielding elements were implemented to address environmental and instrumental effects. A thin **mu-metal shield** (approximately 0.4 mm thick, composed primarily of Ni-Fe alloy) surrounds the cryostat to suppress ambient magnetic fields that could degrade the performance of superconducting sensors and SQUID-based readout electronics. The enclosed volume was also maintained using **radon-reduced air** ("old air"), in which ^{222}Rn and its short-lived progeny were allowed to decay prior to circulation, thereby minimizing backgrounds from radon plate-out on detector and shielding surfaces.

The shielding system was housed within a controlled cleanroom environment (RF-shielded room), which further reduced contamination from dust-borne radioisotopes and protected the experiment from electromagnetic interference. Penetrations through the shielding for the cryogenic (C-stem) and electronic (E-stem) connections were minimized to preserve shielding integrity.

The overall shielding layout is shown in Fig. 2.3.

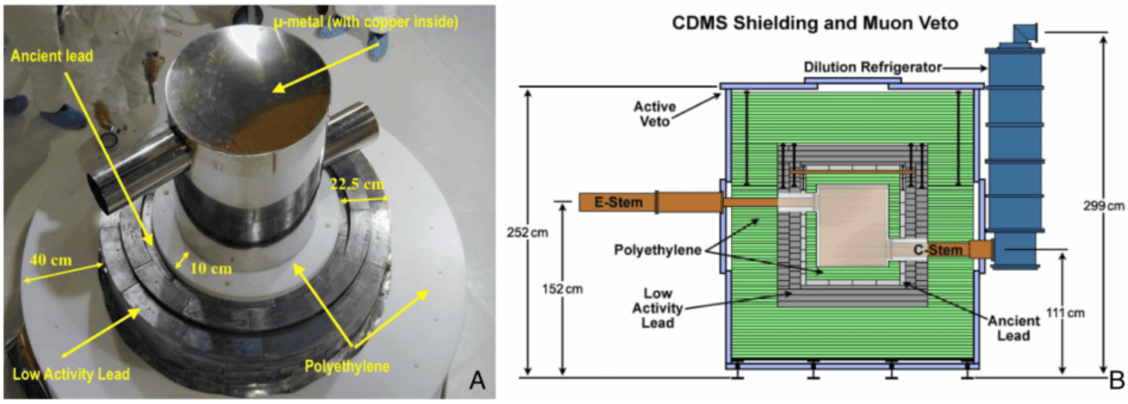

FIGURE 2.3: Shielding configuration of the SuperCDMS Soudan experiment showing the layered arrangement of the active muon veto, polyethylene neutron moderators, lead gamma shielding (including low-radioactivity ancient lead), and the inner cryostat surrounding the detector payload. Adapted from [16].

The SuperCDMS Soudan shielding was roughly 99% hermetic, with the only gaps being along the stems that connected the cryostat to the electronics and dilution refrigerator.

2.4.3 Detector Design: iZIP Technology

The primary detectors used in SuperCDMS Soudan are iZIP detectors. Each detector consists of a cylindrical high-purity Ge crystal with a diameter of 76 mm, a thickness of 25 mm, and a mass of approximately 600 g.

Both faces of each detector are instrumented with interleaved ionization electrodes and phonon sensors. The phonon sensors are based on superconducting transition-edge sensors coupled to aluminum fins that collect athermal phonons generated in the crystal.

The interleaved electrode geometry provides several important capabilities:

- Simultaneous measurement of ionization and phonon signals for event-by-event discrimination,
- Fiducialization of the detector volume by rejecting events near surfaces,

- Strong rejection of surface electron-recoil events that can mimic nuclear recoils due to incomplete charge collection.

The ionization yield (ratio of ionization energy to recoil energy) is a key observable used to distinguish between electron recoils and nuclear recoils.

2.4.4 Detector Configuration

The SuperCDMS Soudan detector array consisted of 15 iZIP detectors arranged in five vertical towers within a cryostat (Fig. 2.4). Two detectors were operated in CDMSlite (high-voltage) mode, while the remaining detectors were operated in standard iZIP mode. Each tower comprised a stack of detectors with controlled spacing to minimize cross-talk and enable independent readout. Detector properties are summarized in Table 2.2.

TABLE 2.2: Summary of detector configurations in the SuperCDMS Soudan experiment, including standard iZIP detectors and CDMSlite high-voltage operation mode [11].

	iZIP	**CDMSlite (HV)**
Mass per detector [kg]	~0.6	~0.6
Phonon channels per detector	8	4 (one sided readout)
Baseline phonon energy resolution [eV]	~70-100	~10
Charge energy resolution [eV]	~450	–
Bias voltage [V]	~4	~70 (CDMSLiteR2) and 75 (CDMSliteR3)

Each detector is segmented into multiple channels, 4 phonon channels and 2 charge channels per side, enabling reconstruction of the interaction position based on the relative timing and amplitude of signals. This spatial information, combined with ionization measurements, allows precise definition of a fiducial volume, which is essential for suppressing surface-related backgrounds.

An electric field is applied across each detector to drift electron–hole pairs produced by particle interactions toward the electrodes. In addition, in HV operation mode, stronger

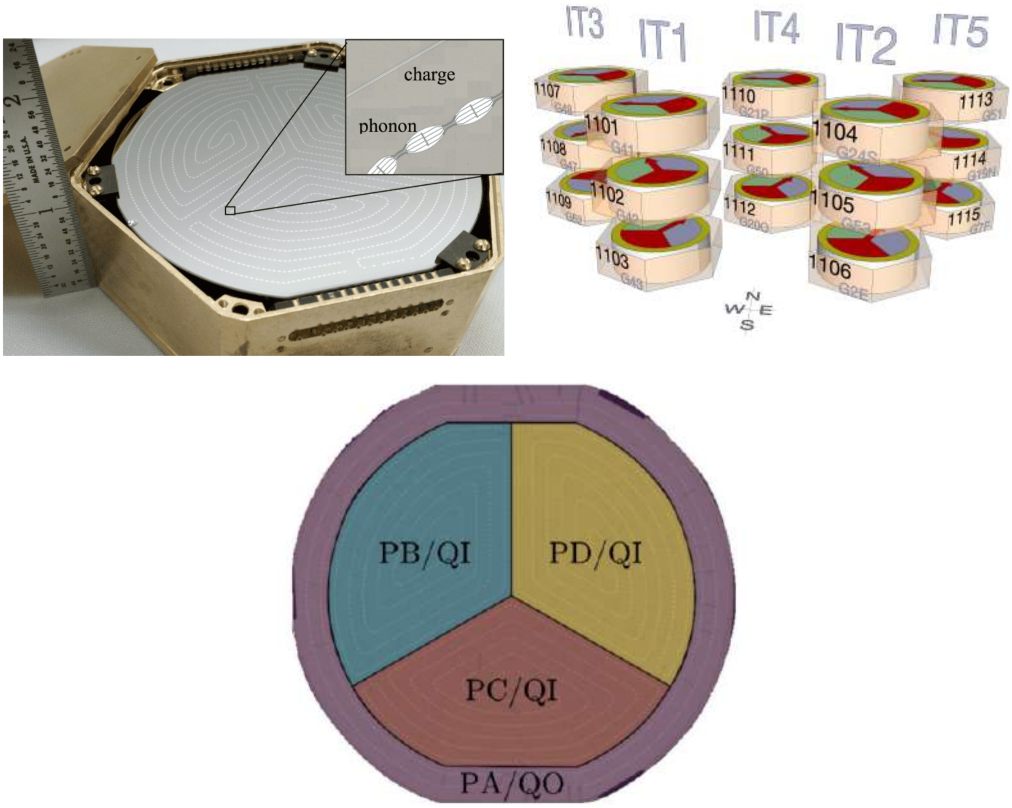

FIGURE 2.4: Detector configuration of the SuperCDMS Soudan experiment. (upper left) Schematic view of an iZIP detector showing charge and phonon sensors. (upper right) Tower configuration consisting of 15 Ge detectors. (lower) Illustration of ionization and phonon sensor channels in an iZIP detector. Adapted from Ref. [16, 19]

.

electric fields are used to amplify the phonon signal through the NTL effect, where drifting charge carriers generate additional phonons. This amplification effectively lowers the detectable energy threshold. The T5Z2 (Tower 5, ZIP 2) and T2Z1 (Tower 2, ZIP 1) detectors were operated in CDMSlite mode with bias voltages of 70 V (CDMSliteR2) and 75 V (CDMSliteR3), respectively.

2.4.5 Physics Reach

The SuperCDMS Soudan experiment produced world-leading and competitive results in searches for low-mass dark matter and fractionally charged particles, enabled by its low energy thresholds, ionization–phonon discrimination capability, and operation in a deep underground environment [2, 11, 15, 26].

No statistically significant dark matter signal was observed during the run period. Consequently, the experiment placed stringent constraints on WIMP–nucleon cross sections, particularly in the low-mass regime. The technological advancements and operational experience gained from SuperCDMS Soudan played a crucial role in informing the design of the subsequent SuperCDMS SNOLAB experiment, which aims to further enhance sensitivity through increased detector mass, lower energy thresholds, and improved background suppression.

2.5 SuperCDMS SNOLAB

SuperCDMS SNOLAB is the next stage of the SuperCDMS program, aiming to significantly enhance sensitivity to low-mass dark matter beyond what was achieved in the Soudan experiment [8]. The experiment is currently in its commissioning phase, with science data taking anticipated to begin by August, 2026.

The SNOLAB experiment incorporates a newly designed cryogenic system, upgraded shielding configuration, next-generation detectors, and improved readout electronics. While the overall experimental concept builds upon the design principles established in SuperCDMS Soudan, a key advancement is the implementation of detectors specifically optimized for high-voltage operation. In contrast to Soudan, where HV operation (CDMSlite mode) was realized using detectors and electronics originally developed for iZIP operation, SuperCDMS SNOLAB employs dedicated HV detectors with electronics tailored to support this mode from the outset.

2.5.1 Deep Underground Site and Background Reduction

The experiment is located at SNOLAB in Ontario, Canada, at a depth of approximately 6000 m.w.e.. This large overburden reduces the cosmic-ray muon flux by roughly two orders of magnitude compared to the Soudan site. The significantly lower cosmogenic background at SNOLAB enables improved control of nuclear-recoil backgrounds and allows for longer exposure times. This deeper underground environment is therefore essential for achieving the background levels required for next-generation low-mass dark matter searches.

2.5.2 Experimental Design and Detector Array

SuperCDMS SNOLAB employs an array of cryogenic semiconductor detectors composed of both Ge and Si, arranged in a modular tower configuration. The full detector payload consists of 24 detectors deployed in four towers, with each tower containing six detectors. The baseline configuration includes 18 Ge detectors and 6 Si detectors [27].

All detectors are fabricated as cylindrical crystals with a diameter of 100 mm and a thickness of 33.3 mm. The corresponding masses are approximately 1.39 kg for Ge and 0.61 kg for Si [27]. Both detector types share identical geometrical dimensions and fabrication techniques, but differ in sensor layout and operating mode.

Two complementary detector designs are implemented: iZIP and high-voltage detectors.

- **iZIP detectors:** These detectors are optimized for background discrimination through simultaneous measurement of ionization and phonon signals. Each detector face is instrumented with interleaved ionization electrodes and segmented phonon sensors. The phonon system consists of six channels per side, arranged as a central region surrounded by segmented outer channels, while the ionization system is divided into inner and outer electrodes. A low bias voltage (typically ±3 V for Ge and ±4 V for Si) is applied across the ionization electrodes.

- **HV detectors:** Unlike SuperCDMS Soudan HV detectors, SNOLAB HV detectors are instrumented only with phonon sensors and do not directly measure ionization. Each face contains 6 phonon channels that provide position sensitivity and rejection of edge-related events. HV detectors are operated at bias voltages around $\sim$ 100 V.

In iZIP detectors, segmentation enables reconstruction of event position and identification of surface interactions through asymmetric charge collection. In HV detectors, phonon-only readout is optimized to retain position sensitivity, which is essential for rejecting surface backgrounds that may exhibit reduced NTL amplification.

The expected detector performance and planned exposures for the SuperCDMS SNOLAB experiment are summarized in Table 2.3 [27]. The quoted phonon energy resolutions correspond to the combined response of all phonon channels, while ionization resolutions correspond to a single inner-electrode channel.

TABLE 2.3: Updated summary of detector configuration and expected performance for SuperCDMS SNOLAB. The exposures assume five years of operation with approximately 80% live time [28].

	iZIP (Ge)	**iZIP (Si)**	**HV (Ge)**	**HV (Si)**
Number of detectors	10	2	8	4
Total exposure [kg·yr]	56	4.8	44	9.6
Phonon resolution [eV]	50	25	10	5
Ionization resolution [eV_{ee}]	100	110	–	–
Bias voltage [V]	6	8	100	100

The detector technologies and corresponding channel layouts are illustrated in Fig. 2.5.

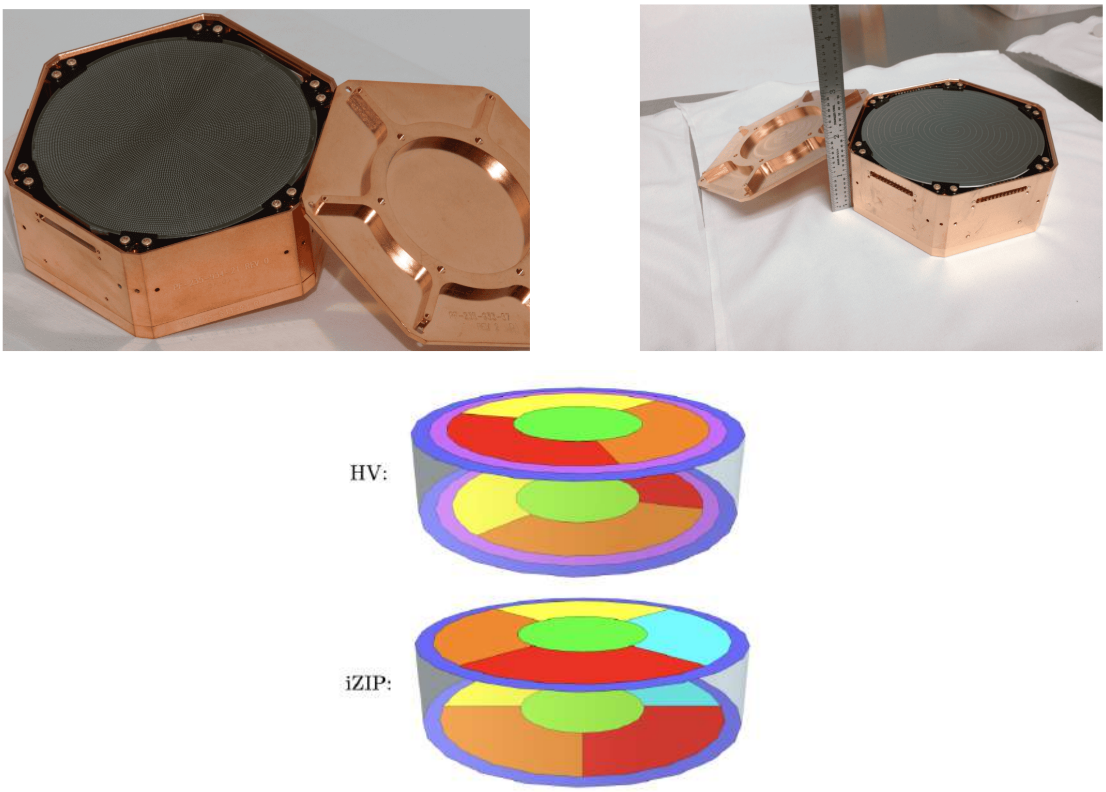

FIGURE 2.5: Detector technologies used in SuperCDMS SNOLAB, including high-voltage detectors and iZIP detectors. The iZIP detectors provide both phonon and ionization readout channels, while HV detectors operate in phonon-only mode with enhanced charge drift fields for low-threshold operation. Adapted from [8].

2.5.3 Cryogenic System and SNOBOX

The SuperCDMS SNOLAB detectors are operated at millikelvin temperatures using a dilution refrigerator, with a base temperature of approximately 15 mK and typical operating temperatures around 30 mK. The cryogenic system incorporates intermediate thermal stages at $\sim$ 50 K and 4 K, established using cryocoolers, which provide the necessary precooling for the dilution unit [27]. These low temperatures are essential to suppress thermal phonon populations and enable sensitivity to eV-scale energy depositions.

The cold experimental volume is housed within the SNOBOX, a cryogenic enclosure consisting of multiple nested cylindrical copper vessels. In the baseline design, the SNOBOX comprises six concentric copper cans, each thermally anchored to a different stage of the cryogenic system. This configuration provides a graded thermal structure that ensures efficient heat sinking while maintaining thermal isolation between stages [27]. The outermost vessel, together with associated structural components, defines the vacuum boundary of the cryostat.

Detector towers are mounted to the lowest-temperature stage of the SNOBOX and are thermally connected to multiple intermediate stages. Each tower hosts six detectors and includes cryogenic readout components such as SQUID amplifiers for phonon signals and low-noise electronics for ionization readout. The tower structure also provides thermal anchoring for readout wiring and supports additional components, including bias resistors, thermometry, and calibration systems such as LEDs.

Electrical and cryogenic connections between the cold volume and external systems are provided through dedicated feedthrough structures. An electronics stem (E-stem) routes signal cables between the detectors and room-temperature electronics, while a cryogenic stem (C-stem) connects the SNOBOX to external cooling infrastructure [27].

Shielding and Radon Mitigation

To suppress environmental backgrounds, SuperCDMS SNOLAB employs a multilayer shielding system designed to mitigate neutron and gamma-ray backgrounds originating from the surrounding cavern and detector materials [8, 27].

The shielding system is organized in a nested geometry surrounding the cold detector region (SNOBOX), with each layer targeting specific background sources:

- **SNOBOX (cryogenic copper enclosure):** The innermost structure consists of multiple nested copper cans (6 cans of width 0.9525 cm each) that house the detector towers. This cryogenic assembly provides a few centimeters of intrinsic copper shielding and is thermally anchored to the dilution refrigerator via the C-stem. It defines the ultra-low temperature environment for detector operation ($T < 30$ mK).

- **Inner polyethylene shielding (∼40 cm):** Surrounding the SNOBOX, a thick layer of high-density polyethylene (HDPE) moderates fast neutrons via elastic scattering on hydrogen nuclei, reducing their energies prior to capture.

- **Lead shielding (∼23 cm):** A layer of low-radioactivity lead surrounds the inner polyethylene, providing strong attenuation of external gamma radiation through Compton scattering and photoelectric absorption. This layer offers nearly full 4π coverage around the detector region.

- **Outer polyethylene and water shielding:** Additional neutron moderation is provided by outer HDPE layers and large water tanks (approximately 60 cm thick). The water shielding acts as an effective neutron moderator and contributes significantly to attenuation of cosmogenic and cavern-originated neutron flux.

- **Radon mitigation system:** The shielding volume is enclosed and continuously purged with low-radon air or nitrogen boil-off to suppress radon ingress. This reduces backgrounds arising from ^{222}Rn decay and its progeny, which can otherwise contribute surface and bulk radioactive contamination.

- **Magnetic shielding:** A mu-metal layer is installed near the cryogenic region to reduce ambient magnetic fields that could interfere with superconducting sensors and SQUID-based readout electronics.

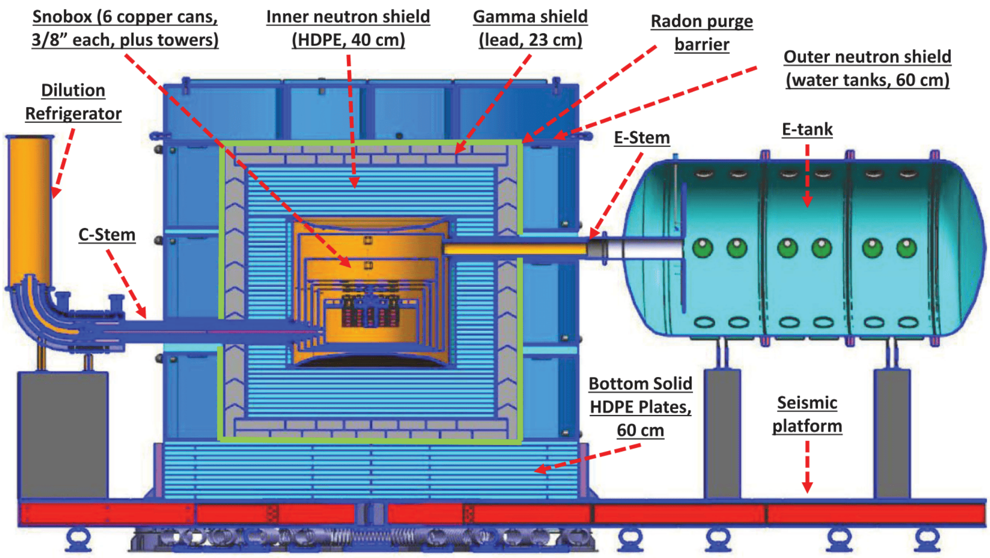

FIGURE 2.6: Shielding and cryogenic design of the SuperCDMS SNOLAB experiment. The central SNOBOX houses the detector towers and is thermally linked to the dilution refrigerator via the C-stem. Surrounding layers include polyethylene, lead, radon exclusion system, and outer water shielding for background suppression. Adapted from [8].

The shielding structure is mechanically supported and seismically isolated using a dedicated platform that stabilizes the dilution refrigerator, shielding assemblies, and room-temperature electronics. The experiment is coupled to the cryostat via two main interfaces: the C-stem (thermal connection to the SNOBOX) and the E-stem (electronics feedthrough).

This layered design reflects the different interaction mechanisms of background radiation. Gamma rays are efficiently suppressed using high-Z materials such as lead, while neutrons are moderated in hydrogen-rich materials before capture. Radon-induced backgrounds are mitigated through environmental control and continuous purging of the shielding enclosure.

The overall shielding and cryogenic layout of the SuperCDMS SNOLAB experiment is shown in Fig. 2.6.

2.5.4 Detector Advancements over Soudan

Apart from the two orders of magnitude reduction in cosmic-muon-induced background at SNOLAB compared to the Soudan laboratory, several key improvements define the SuperCDMS SNOLAB upgrade. A major advancement lies in the optimized sensor layout and readout channel architecture, which significantly enhances event reconstruction and background discrimination. The increased phonon channel granularity enables more precise localization of energy depositions within the detector volume, thereby improving fiducialization and strengthening the rejection of surface and edge-related events. In addition, the Ge detector mass has been increased from 0.6 kg at Soudan to 1.4 kg at SNOLAB, resulting in a higher target mass per detector module and improved exposure efficiency.

The detector design is also inherently scalable and modular. The tower-based architecture, together with a cryogenic system engineered to accommodate additional payload, allows straightforward expansion in both detector mass and readout channels without requiring major modifications to the existing infrastructure [27].

Furthermore, high-voltage detector operation is substantially expanded at SNOLAB. A total of 12 HV detectors will be deployed in the initial SNOLAB configuration, compared to only 2 HV detectors operated at Soudan. This reflects the increased emphasis on low-threshold operation and enhanced sensitivity to sub-GeV dark matter, enabled by phonon-amplified signal readout.

2.5.5 Physics Reach and Sensitivity

The physics reach of SuperCDMS SNOLAB is determined by the interplay between detector threshold, background environment, and exposure. The combination of ultra-low thresholds achieved in HV detectors and strong background discrimination in iZIP detectors enables sensitivity across a wide range of dark matter masses and interaction channels [27].

In the low-mass regime, the experiment is particularly sensitive to dark matter interactions producing small ionization signals, including electron recoils from absorption processes and low-energy nuclear recoils. At higher masses, iZIP detectors provide near background-free operation in the fiducial volume for nuclear recoils above the ionization detection threshold, allowing competitive constraints on WIMP–nucleon scattering.

The projected sensitivity, shown in Fig. 2.7, demonstrates that SuperCDMS SNOLAB will significantly extend current limits in the sub-10 GeV/c^2 mass range. The experiment is expected to probe regions of parameter space approaching the neutrino-induced background limit, where coherent elastic neutrino–nucleus scattering constitutes an irreducible background.

Operating in this regime will require precise understanding of detector response, background modeling, and statistical interpretation of rare events. The combination of complementary detector technologies within a low-background environment positions SuperCDMS SNOLAB to explore this frontier with unprecedented sensitivity.

At sufficiently low cross sections, the experiment approaches the so-called neutrino floor, where coherent neutrino–nucleus scattering becomes an irreducible background. Achieving sensitivity to this regime represents one of the ultimate goals of SuperCDMS SNOLAB experiment.

Overall, SuperCDMS SNOLAB represents a substantial advancement over previous

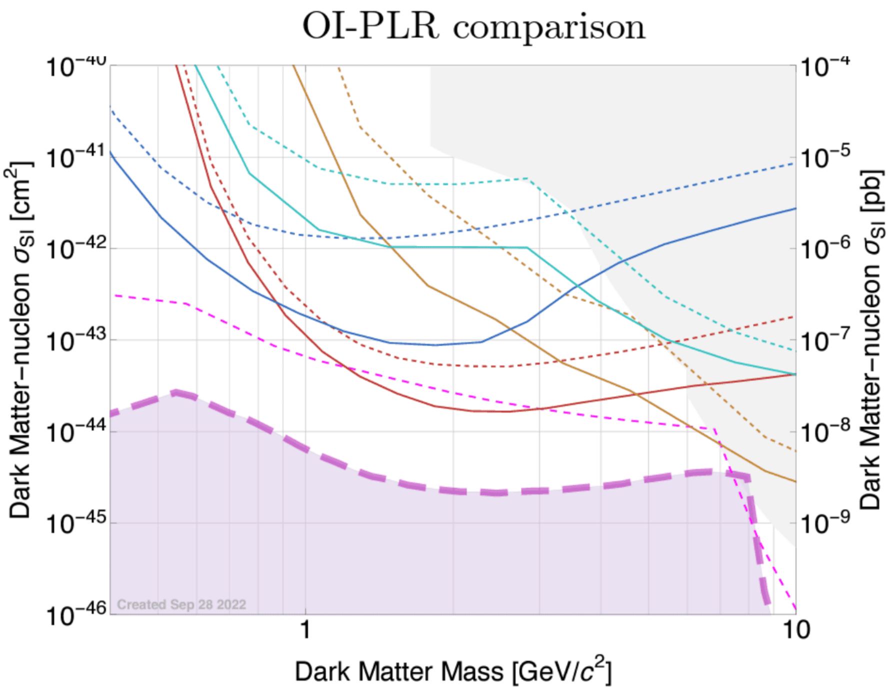

FIGURE 2.7: Projected sensitivity of SuperCDMS SNOLAB in the spin-independent WIMP-nucleon cross section versus dark matter mass parameter space. Adapted from [27].

phases, combining improved detector technology, deeper underground operation, and enhanced shielding to push the sensitivity frontier in the search for dark matter.

2.6 SuperCDMS test facility at NEXUS

During the commissioning phase of SuperCDMS SNOLAB, the collaboration also extensively studied state-of-the-art prototype gram-scale detectors known as High Voltage electron-Volt (HVeV) detectors at the NEXUS (Northwestern Experimental Underground Site) facility at Fermilab. These gram-scale detectors achieve excellent eV-scale energy resolution, making them highly suitable for probing very low-mass dark matter, beyond the reach of kilogram-scale SuperCDMS HV detectors. A central part of this thesis focuses on understanding the detector response of HVeV detectors and their capability to perform sub-keV calibrations at the NEXUS facility using HVeV Run4 (HVeVR4) datasets.

2.6.1 NEXUS Underground Facility

NEXUS at Fermilab is a dedicated SuperCDMS test facility designed for the development, characterization, and calibration of next-generation cryogenic detectors. The laboratory (Fig. 2.8) is located approximately 107 m underground, corresponding to an overburden of $\sim$ 225 m.w.e., which provides a good suppression of cosmic-ray-induced backgrounds.

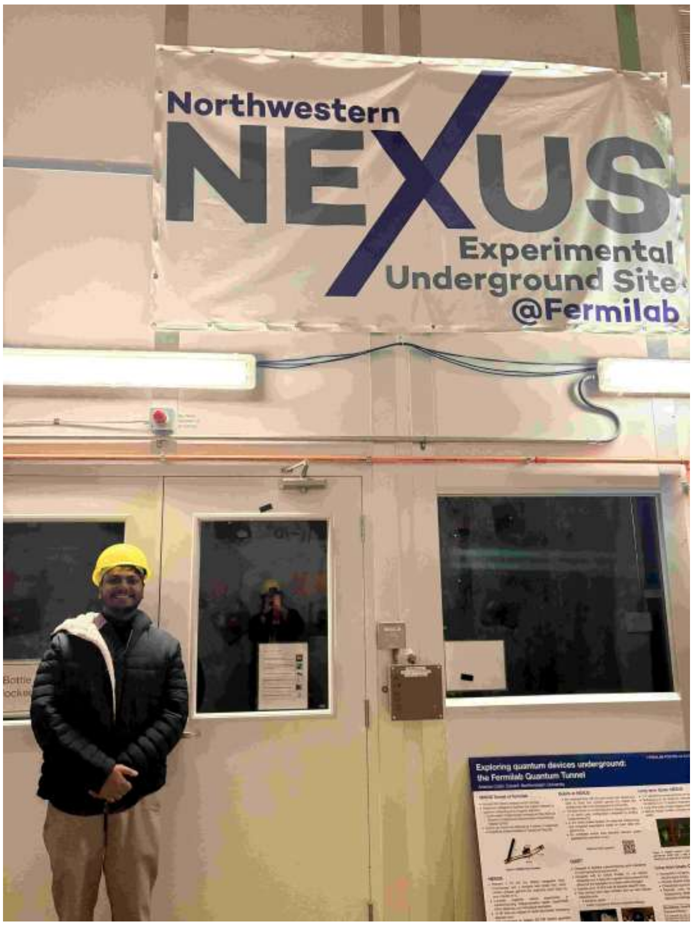

FIGURE 2.8: Photograph of the cleanroom at the NEXUS underground facility located in the MINOS tunnel at Fermilab. The facility is situated approximately 107 m underground, corresponding to an overburden of ~225 m.w.e.

The facility is optimized for the operation of gram-scale cryogenic detectors, particularly

High Voltage electron-Volt detectors, which are designed to achieve sensitivity to energy depositions at the eV scale. The underground location, combined with localized shielding, enables low-background operation suitable for precision detector studies.

2.6.2 Cryogenic Infrastructure and Shielding

The detectors are operated in a CryoConcept dilution refrigerator capable of reaching a base temperature of approximately 10 mK. During stable operation, the detectors are maintained at a temperature of approximately 11 mK, ensuring suppression of thermal phonon populations and enabling sensitivity to athermal phonon signals.

The refrigerator is surrounded by lead shielding on the sides and bottom, with partial coverage on the top. This shielding configuration reduces ambient gamma-ray backgrounds while accommodating necessary cryogenic infrastructure and mechanical components.

2.6.3 Detector Configuration and Mounting

The NEXUS facility operates a set of SuperCDMS HVeV detectors fabricated from high-purity Si crystals. Each detector has dimensions of $10 \times 10 \times 4$ mm^3 and a mass of approximately 0.93 g.

Four detectors are typically deployed in the experimental configuration: one NFE detector, one NFH detector, and two NFC detectors. Here, “NF” denotes NEXUS–Fermilab, while the suffixes E, H, and C refer to different QET sensor readout patterns. These detectors originate from different fabrication batches and test campaigns, enabling systematic comparisons of detector performance.

The detectors are mounted inside a copper housing thermally coupled to the mixing chamber of the dilution refrigerator. The housing consists of two stacked copper boxes,

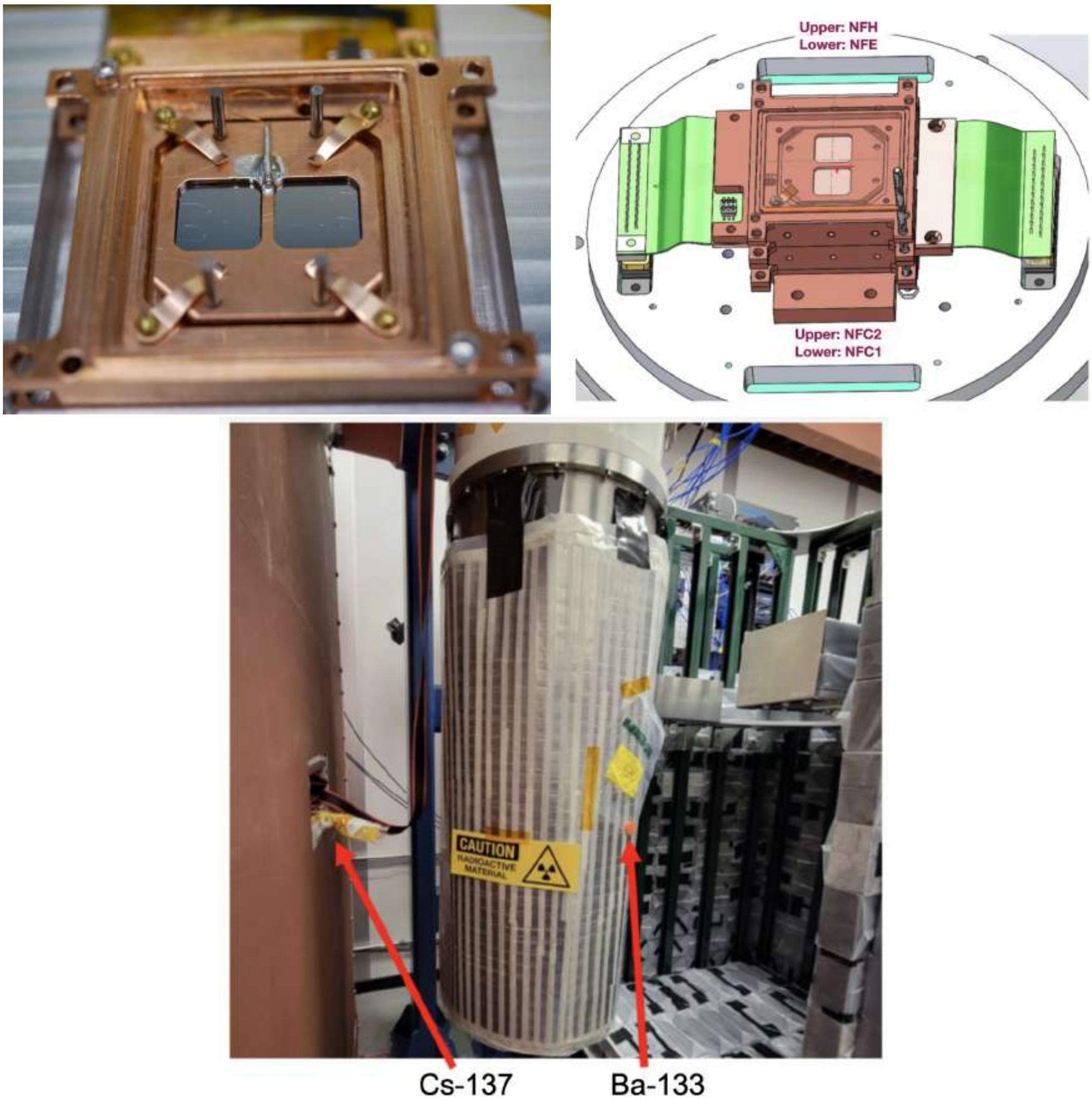

FIGURE 2.9: **Top left**: Photograph of HVeV detectors mounted in the NEXUS detector tower. **Top right**: Schematic representation of the detector tower configuration. **Bottom**: Overview of the dilution refrigerator and shielding arrangement at the NEXUS facility.

each accommodating two detectors. The lower box contains the NFE and NFC1 detectors, while the upper box houses the NFH and NFC2 detectors, as shown in Fig. 2.9.

A key feature of this configuration is that the instrumented faces of detectors in the upper and lower assemblies are oriented toward each other through an opening in the housing.

This geometry enables studies of coincident energy depositions across detectors.

The detector housing design minimizes the use of printed circuit board (PCB) materials, motivated by prior observations that such materials can contribute to excess low-energy background events.

2.6.4 Phonon Readout

Each HVeV detector is instrumented on one face with QETs. The QETs are arranged into two concentric square channels of equal surface area, referred to as the inner and outer channels. This segmentation provides position sensitivity by comparing signal amplitudes between channels. Within each channel, the QETs are connected in parallel, forming a collective readout structure, as shown in Fig. 2.10.

The total QET surface coverage varies among detector types:

- NFE: $\sim 8.5\ \mathrm{mm}^2$
- NFH: $\sim 21.6\ \mathrm{mm}^2$
- NFC: $\sim 31.8\ \mathrm{mm}^2$

The QET-instrumented face of each detector is electrically grounded to the refrigerator chassis. The opposite face is patterned with an aluminum grid covering approximately 5% of the surface area, which can be biased relative to ground to enable high-voltage operation. The QET signals are read out using SQUID-based amplifiers, with output signals measured in units of current.

The combination of low operating temperature, efficient phonon collection, and phonon amplification via the NTL effect allows HVeV detectors to achieve excellent energy resolution and sensitivity to low-energy interactions, making them well suited for studies of low-mass dark matter and precision detector calibration.

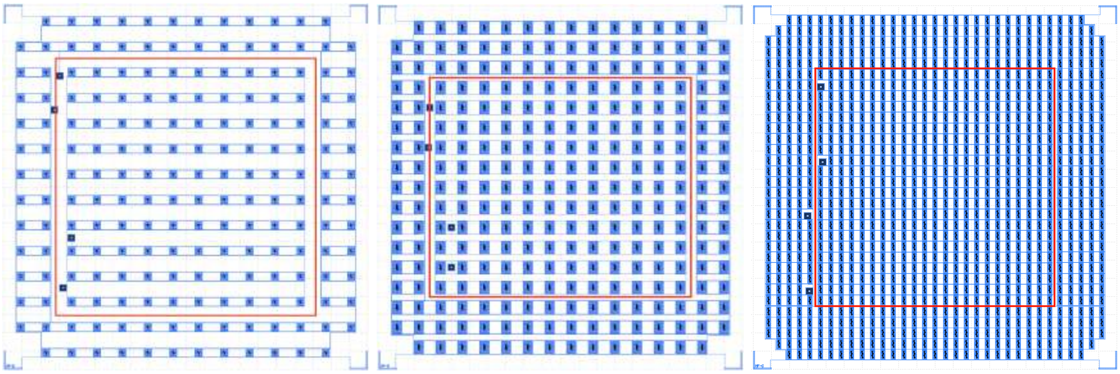

FIGURE 2.10: QET patterns for the NFE (left), NFH (middle), and NFC (right) detectors. Aluminum fins are shown in blue, while the TES elements are shown in black. The increasing QET coverage reflects the evolution of detector design toward improved phonon collection efficiency.

2.6.5 Relevance of the NEXUS Study in SuperCDMS

SuperCDMS SNOLAB aims to detect low-mass dark matter using ultra-low energy threshold cryogenic Ge and Si detectors. While Ge detectors were extensively characterized at Soudan, Si cryogenic detectors were not deployed in that phase of the experiment. Therefore, a dedicated characterization study of Si detector response became essential for their deployment at SNOLAB. At the NEXUS facility, SuperCDMS Si prototype gram-scale detectors with ultra-low energy thresholds were operated to understand their detector response and to evaluate their performance for low-mass dark matter searches. In particular, this thesis work focuses on the detailed characterization of cryogenic Si detector response at low-energy depositions and the study of voltage-bias-dependent signal formation.

A precise sub-keV energy calibration using the Compton step from a ^{137}Cs source at 0 V bias was investigated using HVeVR4 data sets and compared with high-voltage detector response studies using optical photons from an LED-based calibration system. Notably, for the first time, a Compton-step-based calibration technique in Si cryogenic detectors was demonstrated at this facility. This is a crucial development for understanding and calibrating kg-scale HV Si detectors planned for operation at SNOLAB. Overall, this study provides a robust framework for detector response modeling and calibration, enabling reliable low-mass dark matter searches using Si-based cryogenic detectors.

Bibliography

[1] M. F. Albakry et al. "A Strategy for Low-Mass Dark Matter Searches with Cryogenic Detectors in the SuperCDMS SNOLAB Facility". In: *Snowmass 2021*. Mar. 2022. arXiv: 2203.08463 [physics.ins-det].

[2] R. Agnese et al. "Results from the Super Cryogenic Dark Matter Search Experiment at Soudan". *Phys. Rev. Lett.* 120 (2018), p. 061802.

[3] R. Agnese et al. "Low-mass dark matter search with CDMSlite". *Phys. Rev. D* 97.2 (2018), p. 022002. arXiv: 1707.01632 [astro-ph.CO].

[4] J. Rothe et al. "TES-Based Light Detectors for the CRESST Direct Dark Matter Search". *J. Low Temp. Phys.* 193.5-6 (2018), pp. 1160–1166.

[5] M. Tinkham. *Introduction to Superconductivity*. 1996.

[6] Mark David Pepin. "Low-mass dark matter search results and radiogenic backgrounds for the cryogenic dark matter search". PhD thesis. University of Minnesota, 2016.

[7] R. Agnese et al. "First Direct Limits on Sub-GeV Dark Matter from a SuperCDMS Experiment". *Phys. Rev. Lett.* 121 (2018), p. 051301.

[8] R. Agnese et al. "Projected Sensitivity of the SuperCDMS SNOLAB experiment". *Phys. Rev. D* 95 (2017), p. 082002.

[9] *SNOLAB: Deep Underground Science Facility*. https://www.snolab.ca. 2020.

[10] R Ren, Corey Bathurst, YY Chang, R Chen, CW Fink, Z Hong, NA Kurinsky, N Mast, N Mishra, Valentina Novati, et al. *Phys. Rev. D* 104.3 (2021), p. 032010.

[11] T Aralis, T Aramaki, Isaac J Arnquist, Elham Azadbakht, W Baker, Samir Banik, D Barker, Corey Bathurst, DA Bauer, LVS Bezerra, et al. "Constraints on dark photons and axionlike particles from the SuperCDMS Soudan experiment". *Phys. Rev. D* 101.5 (2020), p. 052008.

[12] R Agnese, T Aralis, T Aramaki, IJ Arnquist, E Azadbakht, W Baker, S Banik, D Barker, DA Bauer, T Binder, et al. "First dark matter constraints from a SuperCDMS single-charge sensitive detector". *Phys. Rev. Lett.* 121.5 (2018), p. 051301.

[13] DW Amaral, T Aralis, T Aramaki, IJ Arnquist, E Azadbakht, S Banik, D Barker, C Bathurst, DA Bauer, LVS Bezerra, et al. "Constraints on low-mass, relic dark matter candidates from a surface-operated SuperCDMS single-charge sensitive detector". *Phys. Rev. D* 102.9 (2020), p. 091101.

[14] R. Agnese et al. "First Direct Limits on Lightly Ionizing Particles with Electric Charge Less than $e/6$". *Phys. Rev. Lett.* 114 (11 2015), p. 111302.

[15] I. Alkhatib et al. "Constraints on Lightly Ionizing Particles from CDMSlite". *Phys. Rev. Lett.* 127.8 (2021), p. 081802. arXiv: 2011.09183 [hep-ex].

[16] Brett Durcan Cornell. "A Dark Matter Search Using the Final SuperCDMS Soudan Dataset and the Development of a Large-Format, Highly-Multiplexed, Athermal-Phonon-Mediated Particle Detector". PhD thesis. CALIFORNIA INSTITUTE OF TECHNOLOGY, 2018.

[17] Maurice P Chapellier, Gabriel Chardin, Lino Miramonti, and Xavier Francois Navick. "Physical interpretation of the Neganov–Luke and related effects". *Physica B: Condensed Matter* 284 (2000), pp. 2135–2136.

[18] J. M. Ziman. *Electrons and Phonons*. 1960.

[19] Mark David Pepin. "Low-mass dark matter search results and radiogenic backgrounds for the cryogenic dark matter search". PhD thesis. University of Minnesota, 2016.

[20] K. D. Irwin and G. C. Hilton. "Transition-edge sensors for photon detection". *Topics in Applied Physics* 99 (2005), pp. 63–150.

[21] S. Das, R. Dey, V. K. S. Kashyap, B. Mohanty, D. Mondal, S. Banik, M. Chaudhuri, and V. Iyer. "Rare Event Searches Using Cryogenic Detectors via Direct Detection Methods" (Dec. 2025). arXiv: 2512.02317 [hep-ex].

[22] John Clarke and Alex I. Braginski. "The SQUID Handbook". *Reviews of Modern Physics* 70 (1999), pp. 889–904.

[23] William Alexander Page. "Searching for Low-Mass Dark Matter with SuperCDMS Soudan Detectors". PhD thesis. British Columbia U., 2019.

[24] M. F. Albakry et al. "Multi-channel, multi-template event reconstruction for SuperCDMS data using machine learning". *Nucl. Instrum. Meth. A* 1087 (2026), p. 171437. arXiv: 2508.20090 [physics.ins-det].

[25] Z. Ahmed et al. "Results from the Final Exposure of the CDMS II Experiment". *Science* 327 (2010), pp. 1619–1621.

[26] R. Agnese et al. "Search for Low-Mass WIMPs with SuperCDMS". *Phys. Rev. Lett.* 112 (2014), p. 241302.

[27] M. F. Albakry et al. "A Strategy for Low-Mass Dark Matter Searches with Cryogenic Detectors in the SuperCDMS SNOLAB Facility". *arXiv preprint arXiv:2203.08463* (2022).

[28] R. Agnese et al. "Projected Sensitivity of the SuperCDMS SNOLAB experiment". *Phys. Rev. D* 95.8 (2017), p. 082002. arXiv: 1610.00006 [physics.ins-det].

CHAPTER 3

Low-Energy Calibration of SuperCDMS Si HVeV Detectors Using Compton Steps

Contents

3.1 Motivation

The search for low-mass dark matter (DM) candidates with masses $\lesssim$ 10 GeV/c^2 demands detectors with ultra-low energy thresholds and excellent energy resolution. The Super-CDMS SNOLAB experiment will deploy two detector technologies, High Voltage (HV) and interleaved Z-sensitive Ionization and Phonon (iZIP), constructed from germanium (Ge) and silicon (Si) crystals operated at cryogenic temperatures [1]. For sub-10 GeV/c^2 dark matter, the expected nuclear recoil spectrum falls steeply toward very low energies, with recoil energies in the range of O(0.1–10 keV). Consequently, a precise understanding of the detector response in the sub-keV to keV regime is essential.

Si detectors are particularly well suited for probing low-mass dark matter due to their lighter nuclear mass compared to Ge. For lower mass dark matter, scattering off lighter nuclei results in larger recoil energies, thereby improving sensitivity compared to Ge detectors. Fully exploiting this kinematic advantage requires an accurate and robust calibration of the Si detector response in the sub-keV energy regime.

In cryogenic calorimeters, energy calibration refers to establishing a unique mapping between the measured detector response, such as phonon signal amplitude (in units of current), and the true energy deposited in the crystal. This response function must be accurately characterized down to the lowest measurable energies. Any miscalibration or unaccounted non-linearity in the sub-keV region can distort the reconstructed recoil spectrum and directly impact the inferred dark matter limits. Therefore, achieving precise calibration in the sub-keV to keV energy range is crucial for maximizing experimental sensitivity.

Low-energy calibration, however, presents significant challenges. In Ge detectors, neutron calibration using a ^{252}Cf source produces cosmogenic activation of ^{71}Ge, which decays via electron capture with a half-life of 11.43 days [2]. This decay results in well-defined K-, L-, and M-shell peaks at 10.37 keV, 1.3 keV, and 160 eV, respectively [2]. These monoenergetic internal lines provide natural calibration anchors extending into the sub-keV regime. Si, in contrast, does not produce analogous activation lines suitable for low-energy calibration, creating a critical gap precisely in the energy region most relevant for low-mass dark matter searches.

An alternative calibration strategy exploits atomic effects in Compton scattering. The scattering cross section of gamma rays with atomic electrons changes abruptly at the binding energy of each atomic shell. This produces step-like features in the measured energy spectrum, known as *Compton steps* [3]. In Si, these steps occur at the K-shell binding energy (1.8 keV) and the L-shell binding energies (approximately 0.15 keV for L1 shell and 0.1 keV for L2 shell) [4]. The step positions are fixed by atomic binding energies, while their relative heights are determined by the number of electrons in each shell. These intrinsic and material-dependent spectral features therefore provide potential calibration markers in the sub-keV regime [5].

Figure 3.1 outlines the calibration strategies for Ge and Si detectors in different SuperCDMS technologies across low (few eV) and intermediate (up to 10 keV) energy ranges.

Although SuperCDMS SNOLAB will ultimately operate kilogram-scale Si HV detectors, this study focuses on gram-scale Si HVeV (High Voltage eV-resolution) detectors as a testbed. These detectors achieve energy resolutions of O(eV) and are capable of resolving single electron-hole pair excitations in the crystal. Their excellent resolution and well-understood response make them ideal for precisely measuring and validating Compton step features.

A detailed understanding of Compton steps in Si HVeV detectors is therefore a crucial step toward establishing a reliable low-energy calibration strategy for the larger SNOLAB

Energies		Low (few eV)	Intermediate (up to 10 keV)	
Procedure		Optical photons	Compton steps	Intrinsic Activation lines
Ge	HV	✗	!	✓
Si	HV	✗	!	✗
Si	HVeV	✓	?	✗

FIGURE 3.1: Calibration strategies for Ge and Si detectors in different SuperCDMS technologies across low (few eV) and intermediate (up to 10 keV) energy ranges. Green check marks denote established calibration methods, red crosses indicate methods that are not applicable, blue exclamation marks represent techniques with limited applicability, and yellow question marks indicate the approach discussed in this chapter.

Si HV detectors. This work directly supports the broader goal of enhancing the sensitivity of SuperCDMS to low-mass dark matter candidates.

3.2 Experimental Setup

The measurements presented in this work were performed at the Northwestern Experimental Underground Site (NEXUS) facility at Fermilab. NEXUS is a dedicated SuperCDMS test facility optimized for the operation and characterization of gram-scale cryogenic detectors, in particular High Voltage electron-Volt (HVeV) devices.

A detailed description of the NEXUS facility, including its underground location, cryogenic infrastructure, and detector configuration, is provided in the SuperCDMS overview chapter (see Sec. 2.6). In this section, only the experimental elements directly relevant to the present analysis are summarized.

Two dedicated calibration datasets were collected during the NEXUS Run 13 (R13) and Run 14 (R14) campaigns, which together constitute the HVeVR4 dataset.

The Compton step calibration was performed using gamma rays with energies of $O(100\text{ keV})$, a regime in which Compton scattering dominates in Si. In Run 13, a ^{137}Cs source emitting 662 keV photons served as the primary calibration source. The source was positioned outside the dilution refrigerator at a radial distance of 65 cm from the detectors and approximately aligned with their vertical center (Fig. 2.9).

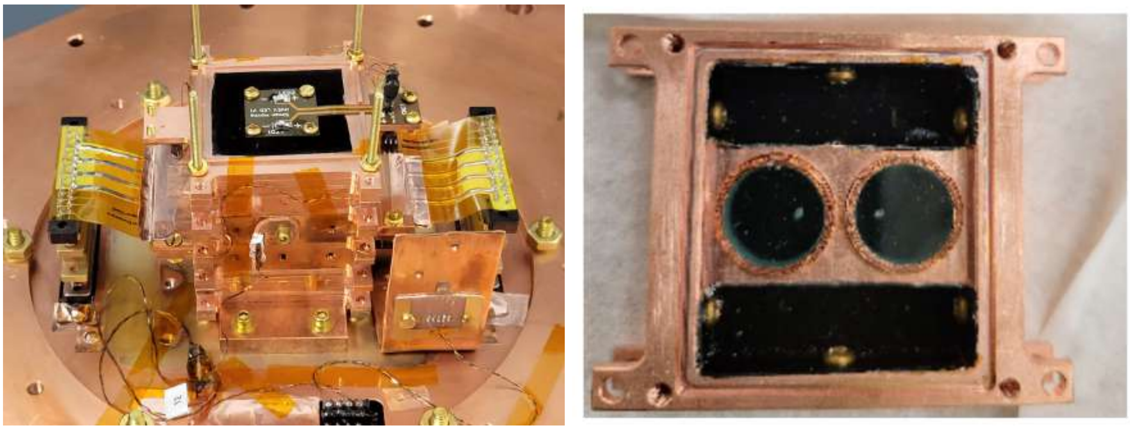

FIGURE 3.2: **Left:** Detector tower configuration during Run 14 (HV LED calibration), showing the additional LED modules installed above and below the Run 13 configuration. **Right:** LED pinholes covered with an infrared filter (SCHOTT KG3) to suppress thermal radiation from the warm, activated LEDs.

A ^{133}Ba source was also mounted on the outer body of the cryogenic refrigerator. However, its contribution to the measured spectrum is expected to be negligible. The activity of the ^{133}Ba source (20,002 Bq as of March 2022) was significantly lower than that of the ^{137}Cs source (3,139,488 Bq as of March 2022). In addition, the dominant gamma-ray energies from ^{133}Ba (365 keV, 81 keV, and 303 keV) are substantially lower than the 662 keV photons from ^{137}Cs. As a result, ^{133}Ba photons experience stronger attenuation in the surrounding materials and are less likely to reach the detector volume.

The higher energy of the ^{137}Cs photons provides greater penetration through the copper detector housing and surrounding structures, leading to a dominant contribution in the recorded spectrum. This expectation was validated using dedicated GEANT4 simulations. Consequently, only contributions from the ^{137}Cs source are considered in the subsequent analysis.

In Run 14, an LED-based calibration was performed under high-voltage detector operation to study detector nonlinearity at keV-scale energies and to compare detector response between 0 V and HV bias configurations. To accommodate the calibration system, two additional copper stages were integrated into the detector assembly—one above and one below the detector housing—to host LED modules (see Fig. 3.2).

Each detector was illuminated by a dedicated LED emitting optical photons with an energy of approximately 2 eV. The light was directed through a pinhole aligned with the center of the aluminum grid (back side) of each detector. To suppress thermal radiation from the LEDs, the pinholes were covered with infrared filters (SCHOTT KG3).

The LEDs were driven using a sinusoidal signal with a half-period of approximately 1.7 μs and a burst repetition frequency of 10 Hz. The mean photon energy, measured using a Thorlabs CCS100 spectrometer, was approximately 2 eV. The photon flux was varied across subdatasets by adjusting the LED drive current, enabling controlled studies of detector response over a range of signal amplitudes.

3.3 Simulation Framework

Electrons in crystalline solids occupy discrete atomic shells (K, L, . . .) in accordance with the Pauli exclusion principle. Compton scattering is an inelastic photon–electron interaction in which an incident photon transfers part of its energy to a bound or free electron, producing a lower-energy scattered photon and a recoiling electron [6, 7]. At low energies in the Compton spectrum, a notable feature called a *Compton step* appears in the differential cross section when the energy transferred to the electron is below the binding energy of a subset of electrons [4]. In such cases, these electrons do not participate in the scattering process, as they lack available final states. This leads to a drop in the scattering cross section at the corresponding atomic binding energies. The positions of these steps are therefore determined by the electronic structure of the material, making them an intrinsic property of the target atoms rather than a feature of the incident photon energy.

We investigated Si Compton steps through a detailed comparison between measured spectra and Monte Carlo simulations. Two complementary approaches were employed. A full detector simulation using Geant4 [8] was used to model energy depositions from external gamma rays across the keV scale and above, while *ab initio* atomic calculations using FEFF [9] were used to obtain a more accurate description of Compton scattering in the sub-keV regime [5].

3.3.1 Geant4 Simulations

A comprehensive detector simulation was performed using Geant4 (v10.07.p04) [8] to model energy depositions at the keV scale and above. The full experimental setup was implemented, including the Si HVeV detectors, copper housing, dilution refrigerator components, and surrounding lead shielding. The simulated NEXUS facility geometry is shown in Fig. 3.3.

The simulation models interactions of 661.7 keV gamma rays with the detector setup, with the source placed at the same position as in the experiment. In the low-energy region relevant for Compton step studies ($\mathcal{O}$(keV) and below), several distinct features appear, as shown in Fig. 3.4 (top left):

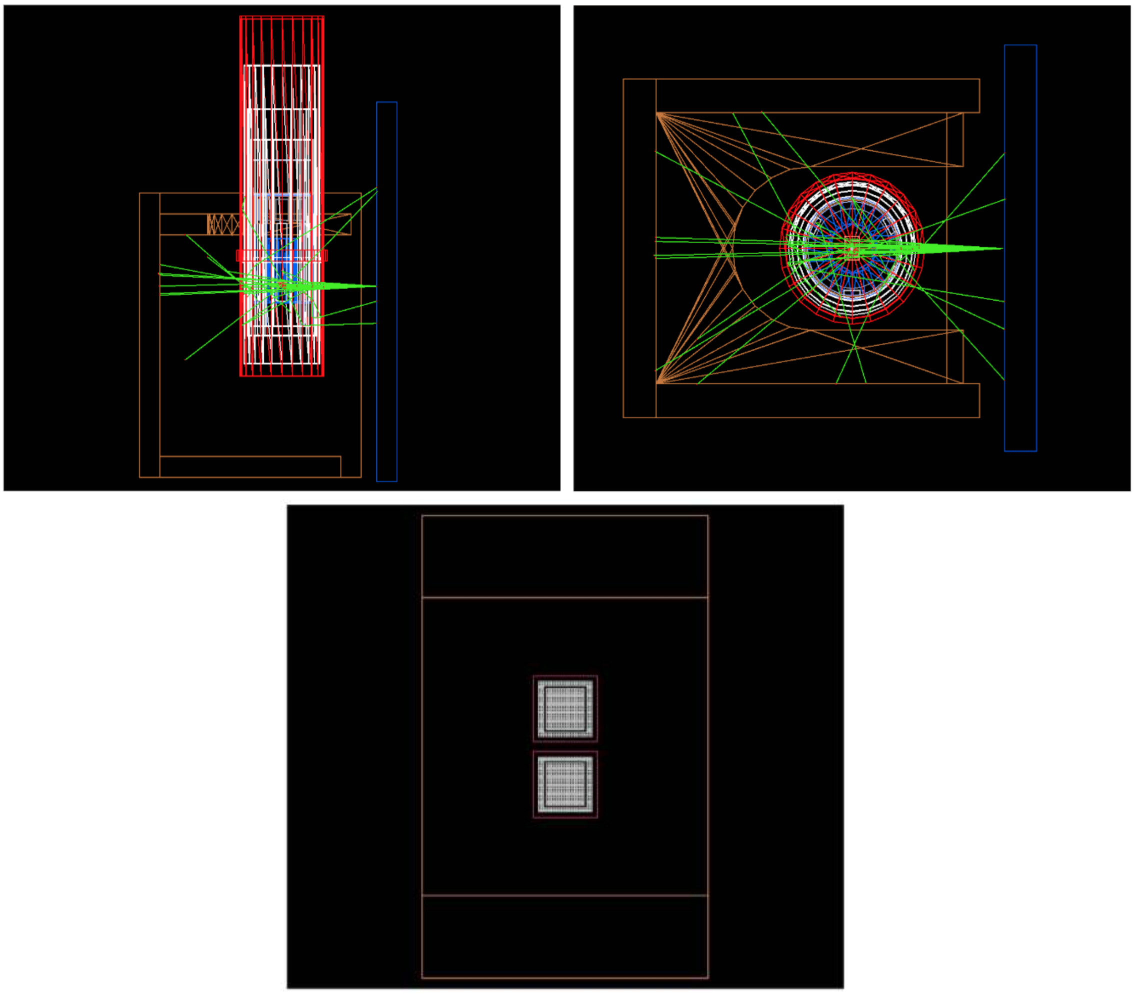

FIGURE 3.3: Overview of the NEXUS facility geometry implemented in the GEANT4 simulation. **Top Left:** Side view showing the lead shield (brown) and lead wall (blue). The dilution refrigerator is at the center, with its layers depicted; the outermost layer is shown in red. The ^{137}Cs source is embedded in the lead wall, and green lines indicate representative gamma-ray trajectories. **Top Right:** Top view highlighting the spatial arrangement of the detector and surrounding components. **Bottom:** Top view showing the two HVeV detectors inside the copper housing.

- Copper fluorescence X-ray peaks near 8 keV originating from the detector housing.

- A Si K-shell Compton step at 1.8 keV.

Compton scattering was modeled using the Monash physics library in GEANT4, which implements the Relativistic Impulse Approximation (RIA) to describe bound-electron scattering at keV energies. The simulation indicates that, between approximately 50 eV and 2 keV, energy depositions from the ^{137}Cs source are dominated by Compton interactions in Si. However, previous precision studies have shown that the RIA loses accuracy below roughly 500 eV, motivating complementary atomic-level calculations for the sub-keV regime (see Sec. 3.3.2).

Figure 3.4 (top right) shows a comparison of spectra across multiple detectors based on the Kolmogorov–Smirnov (KS) test, with the respective p-values reported. Small p-values indicate a low probability that the spectra originate from the same underlying distribution; a threshold of 0.05 is commonly used to indicate inconsistency. The KS tests show that the spectra across detectors are consistent within the selected energy windows, confirming that the underlying physical processes are well-reproduced.

The bottom panel of Fig. 3.4 focuses on the Compton step region. A resolution of 2% motivated from previous HVeV studies [10] is applied to the simulation. A clear K-shell Compton step is observed near 1.8 keV, and two L-shell Compton steps appear near 150 eV and 100 eV. The L-shell steps occur below 500 eV and are studied in detail using FEFF-based atomic calculations (Sec. 3.3.2).

3.3.2 FEFF Simulations

To achieve a more accurate description of Compton scattering at low energy transfers, differential cross sections were computed using the FEFF (v10) package [9]. Unlike the standard GEANT4 implementation, FEFF explicitly accounts for the electronic structure of crystalline Si when calculating excitation probabilities.

The differential cross section in the 50–500 eV range was evaluated using

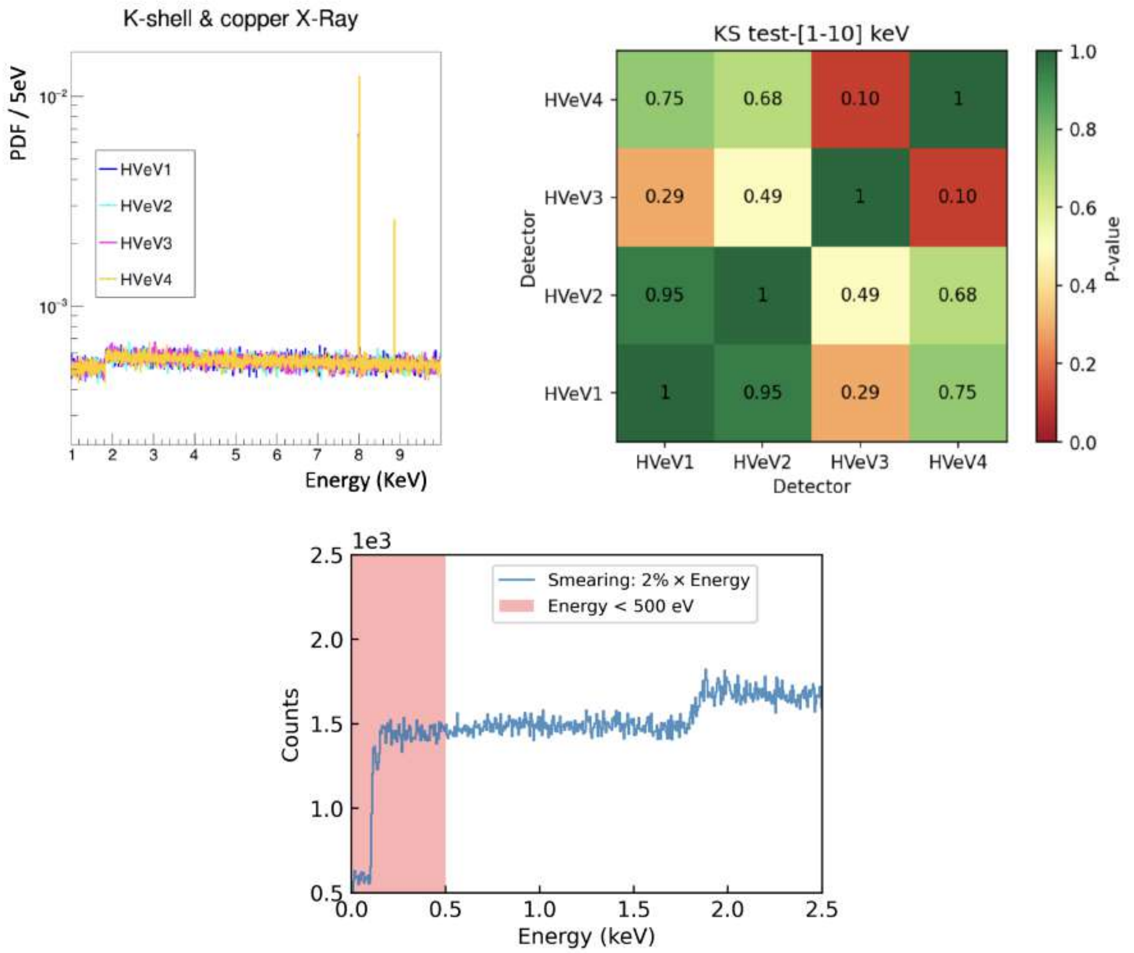

FIGURE 3.4: Geant4 simulation results for 661.7 keV gamma rays from ^{137}Cs. **Top Left**: Simulated detector response in the 1–10 keV region, highlighting the K-shell Compton step and Cu X-ray peak (Credit: Stefan Zatshler). **Top Right**: KS test results showing consistency of the Compton spectrum across detectors, indicating similar underlying physics (Credit: Ata Sattari). **Bottom**: Close-up of the K-shell Compton step with 2% energy smearing [5]. The shaded region below 500 eV corresponds to the L-shell Compton steps, which are analyzed in detail using FEFF simulation.

$$\frac{d\sigma}{dw} = r_0^2 \int d\Omega \left(\frac{1+\cos^2\theta}{2}\right)\left(1-\frac{w}{w_i}\right)\sum_{nl} S_{nl}(q,w), \tag{3.1}$$

where r_0 is the classical electron radius, θ is the scattering angle, w and q represent the transferred energy and momentum, w_i is the incident photon energy (661.7 keV), and

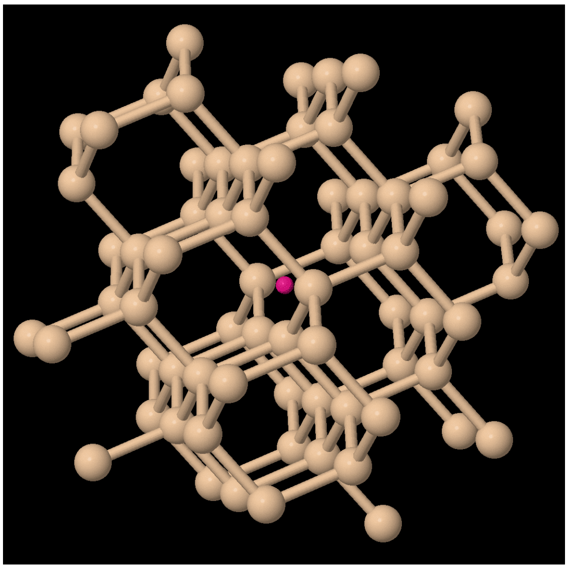

FIGURE 3.5: Si cluster used in FEFF simulations. The central atom (pink) is treated as the absorber. The cluster includes multiple surrounding layers to capture local electronic structure effects. Calculations were performed with both 35 and 71 atoms; identical cross sections were obtained. The 71-atom cluster results are used in this work. (Credit: Ata Sattari)

$S_{nl}(q, w)$ is the dynamic structure factor (DSF) for electrons in shell (n, l) [11]. The DSF describes the probability of electronic excitations as a function of energy and momentum transfer.

FEFF calculations were performed for a Si cluster containing 71 atoms, as illustrated in Fig. 3.5. To verify convergence, the calculations were repeated with a 35-atom cluster, yielding consistent DSFs.

Separate DSFs were generated for:

- The three L-subshells,
- Valence electrons.

The Compton profile, describing the electron momentum density along the momentum transfer direction, was calculated for valence electrons and rescaled to ensure the correct

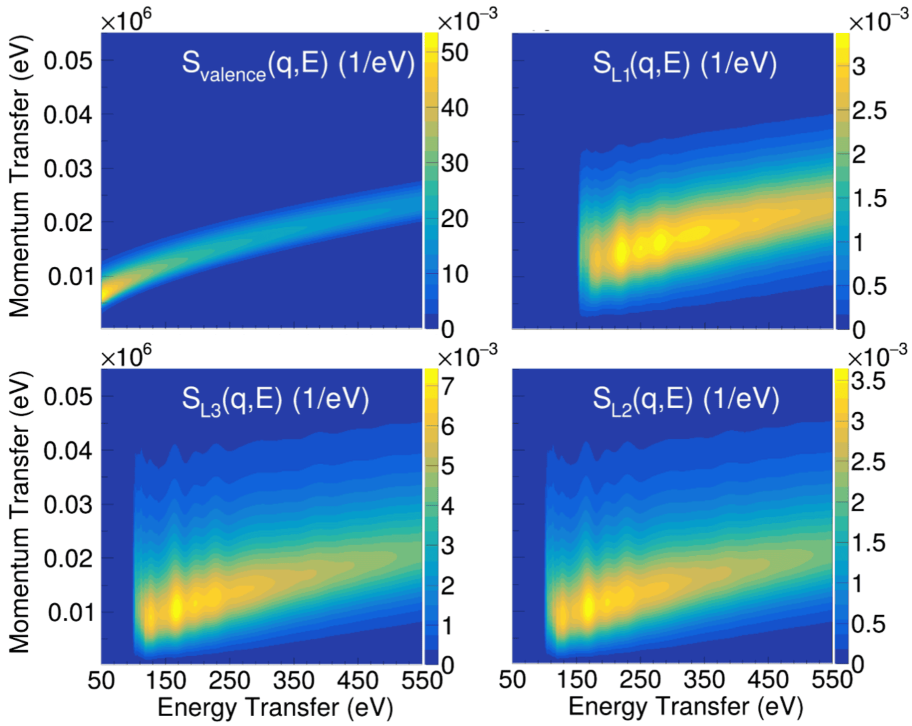

FIGURE 3.6: Dynamic structure factors computed using FEFF for electrons in different shells. The x and y axes represent energy and momentum transfer, respectively, and the color scale indicates the DSF magnitude. Adapted from Ref. [5].

electron count per Si unit cell. These profiles were then converted to the corresponding DSFs. Figure 3.6 shows the resulting DSFs for the valence and L-shell electrons.

The integration in Eq. 3.1 was carried out by expressing the angular dependence in terms of momentum transfer using energy–momentum conservation. Since the differential cross section shape varies only weakly with the incident photon energy in this regime, the incident energy was fixed at 661.7 keV.

FEFF allows calculations both including and excluding the effect of the vacated core-hole on the scattered electron. Both configurations were considered to estimate systematic uncertainties associated with atomic modeling. The calculations excluding the core-hole were adopted as the primary prediction, while the alternative was used to quantify un-

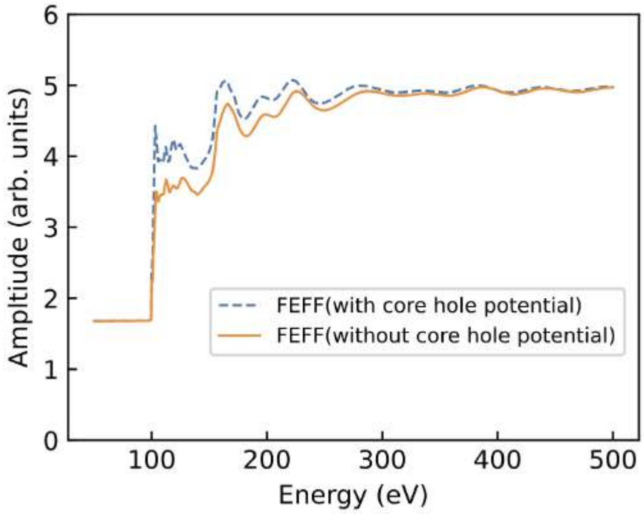

FIGURE 3.7: FEFF-based simulation of the Si L-shell Compton step. Results are shown for calculations with and without inclusion of the core-hole potential. No core hole potential spectrum is used for calibration purpose while with core hole potential spectrum is used to study the systematic uncertainty arising due to the core-hole effect. Adapted from Ref. [5].

certainties in the Compton step based calibration. The resulting signal PDF from FEFF simulation is shown in Fig. 3.7.

Combined with GEANT4 simulations, the FEFF calculations provide a consistent description of energy depositions from the keV scale down to $\mathcal{O}(100\text{ eV})$, enabling precise modeling of Compton step features for low-energy detector calibration.

3.4 Experimental Dataset

3.4.1 Data sets Overview

The Compton scattering analysis presented in this work is based on several calibration and background data sets collected under different detector bias configurations. All primary calibration measurements were performed in a closed shield configuration in order to suppress environmental backgrounds.

Four main categories of data were acquired [5]:

1. **^{137}Cs Calibration at 0 V Bias:** Approximately two days of calibration data were collected using an external ^{137}Cs gamma source with an activity of approximately 3 MBq during the measurement campaign. No electric field was applied across the detector substrate (0 V bias). These data serve as the primary reference for studying Compton steps under electric field-free conditions.

2. **Background Data at 0 V Bias:** Four days of background data were recorded without any radioactive source, also at 0 V bias. These runs are used to characterize intrinsic detector backgrounds near 100 eV energy range i.e. low energy excess (LEE) background and validate spectral features observed in calibration data.

3. **Background Data at 100 V Bias:** Six days of background data were collected with a 100 V bias applied across the detector substrate. These data allow investigation of detector response and noise behavior in the presence of an applied electric field. The $\sim$100 eV calibration point, corresponding to the first electron–hole (e^-h^+) pair peak observed in the background spectrum, provides an approximate energy reference for selecting the L-step region of interest in the 50–300 eV energy range.

4. **LED Calibration Data at 150 V Bias:** Multiple LED sub-datasets were collected with a 150 V detector bias. In these runs, optical photons were periodically shone towards the detectors. The LEDs emitted photons with a mean energy of approximately 2 eV, independently characterized using a Thorlabs CCS100 spectrometer. The light intensity varied across sub-datasets. High-intensity datasets were used to establish the keV-scale calibration, while low-intensity datasets were used to quantify cross-talk between detector readout cables and LED power lines. Combination of

high and low intensity data were used to study surface energy deposition effects from optical photons, known as surface trapping effect [12]. The duration of the high-intensity LED calibration dataset was approximately 2 hours.

Data sets collected at 0 V and 100 V bias were obtained using the Compton calibration configuration in R13, whereas the LED data were taken using a updated optical calibration setup in R14 as discussed in 3.2. During Compton data taking in closed shield configuration in R13, the Mixing Chamber (MC) temperature of the fridge were confirmed to be stable at 11 mK as shown in Fig. 3.8.

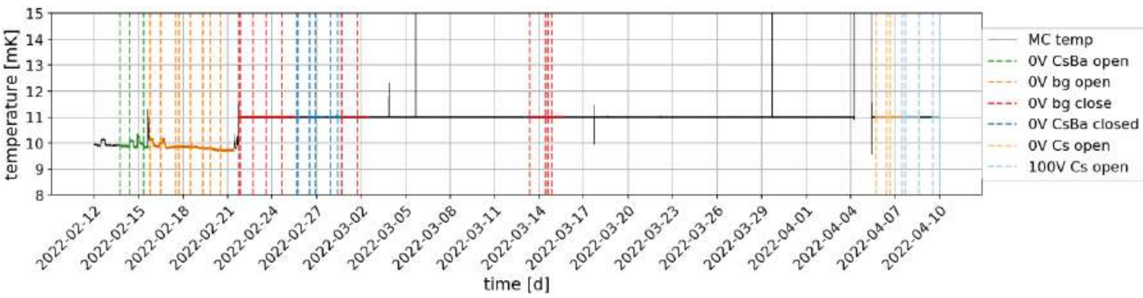

FIGURE 3.8: Mixing chamber temperature for R13 data sets collected for the calibration study. The final data sets for our study include '0 V bg close' (red) and '0 V CsBa close' (blue). Credit: Ata Sattari

3.4.2 ^{137}Cs and ^{133}Ba activities

Combined ^{137}Cs and ^{133}Ba calibration data were collected at 0 V bias. However, due to the significantly lower activity of the ^{133}Ba source compared to ^{137}Cs, spectral features associated with the 356 keV gamma ray line of ^{133}Ba were not clearly visible in the measured spectrum. Consequently, the 0 V calibration spectrum is effectively treated as a ^{137}Cs spectrum for Compton-step studies.

Table 3.1 summarizes the radioactive source properties used in the calibration measurements.

TABLE 3.1: Radioactive source properties used in calibration measurements.

Source	FNAL ID	Activity (Aug 2020) [Bq]	Activity (Mar 2022) [Bq]	Prominent γ Peaks [keV]
^{133}Ba	1330.13	22200	20002	81.00 (33%), 302.85 (18%), 356.01 (62%)
^{137}Cs	1372.32	3265000	3139488	661.66 (85%)

3.4.3 LED HV Data and Detector Working Points

For LED calibration runs, a HV bias was applied across the crystal. The effective current gain of the detector, determined from the position of the first electron–hole peak in the energy estimator (expressed in current units), was influenced by additional wiring required to allocate the LED system into the detector payload.

To enable a direct comparison between HV and 0 V calibrations, the current gain must be matched between datasets. During the R14 LED campaign, a scan of the detector operating point along the resistance–temperature (R–T) transition curve was performed to find the closest match of the detector response with that of the R13 series. In addition to that a linear correction to exactly match the current gain was performed. Three working points (WP1, WP2, and WP3) were selected for this study. These correspond to different bias currents applied to the QETs, thereby placing the TES at different positions along the superconducting transition. A higher bias current corresponds to a higher position of operating point along the transition curve and it results in a reduced effective current gain.

WP3 lies between WP1 and WP2 in the transition curve, providing an intermediate gain configuration. WP3 LED HV data is used for primary energy calibration whereas WP2 and WP1 data sets are used for uncertainty estimate arising from linear gain correction during the WP alignment of LED data between R13 and R14. The analysis includes LED data at both 100 V and 150 V bias to study relative gain differences between the two voltages.

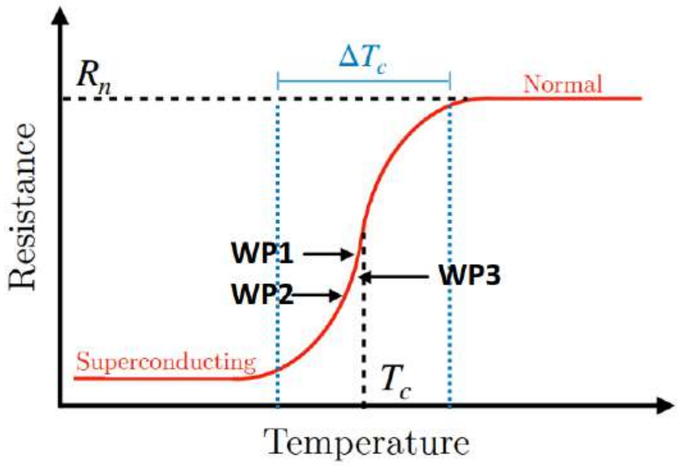

FIGURE 3.9: Schematic representation of the three working points (WP1, WP2, and WP3) selected along the TES resistance–temperature (R–T) transition curve during LED data collection. The working points are defined by different applied QET bias currents. Increasing the QET bias current shifts the operating point upward in the transition curve and reduces the effective current gain of the detector response.

The NFH, NFC1, and NFC2 detectors were included in the HV studies. The NFE detector, which has the smallest Transition Edge Sensor (TES) volume, exhibits a stronger nonlinear response at higher deposited energies. Therefore, NFE was analyzed only at low energies near the Compton L-steps, and no LED calibration data were collected for this detector due to its degraded high-energy resolution in keV scale.

3.5 Event Reconstruction

The detector data were continuously recorded and written to disk in segments of 0.5 s duration, referred to as *traces*, with a sampling frequency of 156.25 kHz. For each HVeV detector, the readouts from the inner and outer phonon channels were summed. The summed traces were then passed through an offline triggering and reconstruction pipeline.

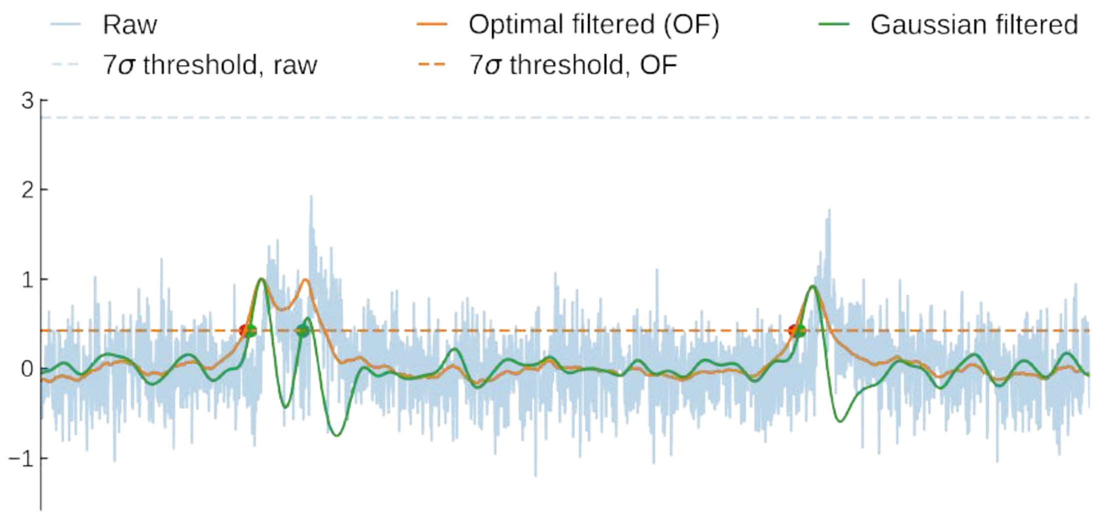

FIGURE 3.10: Illustration of data filtering using a derivative-of-Gaussian kernel. The trigger threshold is greater than 7σ, where σ denotes the standard deviation of the baseline noise amplitude from Optimal Filter method.

3.5.1 Triggering and Event Window Selection

A threshold trigger was applied to the summed traces after filtering them with a kernel given by the first derivative of a Gaussian function. The Gaussian width used in the filter was 38.4 μs, optimized to enhance sensitivity to pulse-like features while suppressing low-frequency noise. The resulting Gaussian-filtered (GF) trace provides improved sensitivity for triggering of closely spaced pulses compared to the optimal filtered (OF) trace [13] as illustrated in Fig. 3.10.

For each identified pulse, the trigger time was defined as the location of the maximum of the Gaussian-derivative filtered trace. Around this trigger point, a fixed analysis window of 13.1 ms was selected, consisting of 1024 pre-trigger and 1024 post-trigger samples. Each sample corresponds to 6.4 μs. This window sufficiently captures the pulse rise and falls for keV scale events while preserving sufficient baseline information for noise estimation.

The LED system operated at a constant flashing frequency of 10 Hz. The periodicity of the LED pulses, together with the timestamps of threshold-triggered events, allowed identification of all LED-induced events. A dedicated logic ensured that LED events were recorded with full efficiency, independent of the nominal trigger threshold. Such custom triggering ensures background event rejection at the time when no LED events are expected.

3.5.2 Optimal Filtering and Event Reconstruction

After defining the trigger time and corresponding analysis window, each pulse is processed using the OF algorithm implemented in the frequency domain [13]. The OF constructs a linear amplitude estimator using a predefined pulse template and the measured noise power spectral density (PSD), maximizing the signal-to-noise ratio. A free time-shift parameter can be included to account for small temporal misalignments between the pulse and the template.

The pulse template was generated by averaging ~100 eV phonon events from the 100 V dataset. Pulse shapes were verified to be consistent between the 0 V and HV data sets, as shown in Fig. 3.11. The noise PSD was derived from randomly triggered traces in the 100 V dataset after rejecting events containing pulse-like structures. Noise-only traces were selected using cuts on their mean, standard deviation, slope, and skewness.

Two amplitude estimators are obtained from the OF procedure:

- A_{OF}: amplitude extracted with a free time-shift parameter,
- A_{OF0}: amplitude extracted with the time-shift fixed at zero.

The A_{OF0} estimator is particularly useful for very low-energy events near threshold, where random noise fluctuations can bias the time alignment procedure. For each event, the reconstruction also provides a χ^2/NDF value, which quantifies the goodness-of-fit

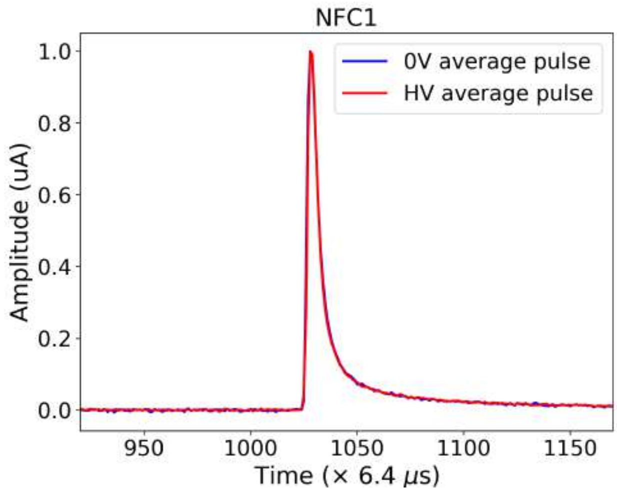

FIGURE 3.11: Comparison of normalized pulse templates obtained from 0 V and HV datasets, demonstrating consistent pulse shapes.

between the measured pulse and the template. The calibrated A_{OF} amplitude is used as the primary low-energy estimator.

Figure 3.12 shows representative raw traces from the NFC1 HVeV detector near the K-shell Compton step (~1.8 keV). At these energies ($\mathcal{O}$(keV) and below), the predefined pulse window fully captures the pulse rise and decay, ensuring unbiased amplitude reconstruction.

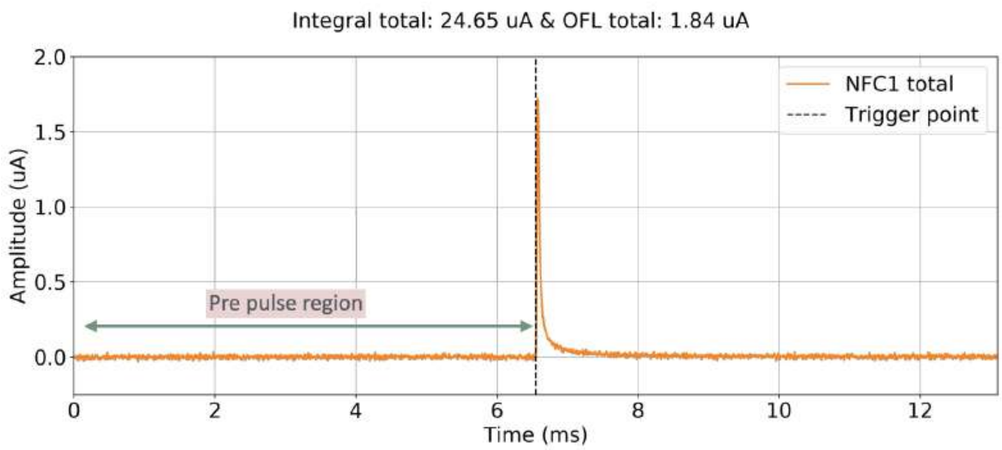

FIGURE 3.12: Representative raw traces from NFC1 HVeV detector near K shell Compton steps (~1.8 keV) inside its analysis window of 13.1 ms.

A list of Reduced Quantities (RQ) obtained from processed data set used in this analysis are shown in Tab. 3.2.

TABLE 3.2: Reconstructed quantities (RQs) used in the Compton calibration analysis. The asterisk (*) denotes the detector and channel designation (inner, outer, or total). For instance, `OFL_NFC1_total` corresponds to the OFL amplitude for the NFC1 detector using the combined (inner + outer) channel response.

RQ Name	**Definition**
`trig_ch`	Detector responsible for issuing the trigger.
`trig_loc`	Sample index of the trigger within the trace (0–78125), corresponding to a 0–0.5 s window of raw data.
`filename_idx`	Identifier of the associated MIDAS file.
`trig_traceidx`	Position of the 0.5 s trace within the MIDAS file.
`timestamp_corr`	Trigger timestamp with correction applied to account for the 2^{32} rollover of the MIDAS clock.
`OF0_*`	Optimal filter pulse amplitude evaluated with the time shift fixed to zero.
`OFL_*`	Optimal filter pulse amplitude allowing a free time-shift parameter limited to 6 samples.
`OFL_chi2_*`	Frequency-domain χ^2 value used to assess fit quality.
`MeanBase_*`	Average value of the pre-trigger baseline region.
`Integral_*`	Time-domain pulse integral over a 13.1 ms window after baseline subtraction and low-pass filtering (cutoff 20 kHz).
`FallTime1_*`	Decay time of the filtered pulse from 50% to 30% of its maximum.
`FallTime2_*`	Decay time from 90% to 50% of peak amplitude.
`FallTime3_*`	Decay time from 100% to 90% of peak amplitude.

3.6 Energy Calibration at 0 V Bias Using Si Compton Steps

The 0 V ^{137}Cs datasets were used to study the Si Compton step features in the measured Compton spectrum. The primary focus of this analysis is the low-energy region below 2 keV, where the L- and K-shell Compton steps should provide well-defined calibration features.

Processed datasets may contain poorly reconstructed events, including pileup events (such as multiple energy depositions within a single analysis window or energy deposition of an event on the long tail of a very high energetic event) and instrumental glitches unrelated to particle interactions in the detector. These events must be removed to obtain a clean spectrum suitable for calibration.

3.6.1 Data Filtering

Several selection cuts were developed to eliminate poorly reconstructed events and instrumental artifacts. These cuts are grouped into two categories:

1. **Live-Time Cuts:** Remove periods of unstable detector operation from the total live-time.

2. **Data Quality Cuts:** Applied on an event-by-event basis using pulse-shape and reconstruction quality parameters.

The complete list of applied cuts is shown in Tab. 3.3. The individual cuts used in the analysis are described below.

Trigger dead time cut

Continuous data acquisition occurs in 0.5-second chunks (78125 samples) called traces. The reconstruction algorithm uses a 2048-sample window around triggers to extract RQs. To ensure sufficient sample points, the algorithm doesn't trigger within the first and last 1024 (6.5 ms) samples of each trace, creating a dead time region. Energy deposition from events in this region remains untriggered. The selection prevented processing artifacts at the edges of the traces. The trigger dead time cut removes the first and last 13 ms intervals

TABLE 3.3: Overview of the data-quality selections applied in the 0 V analysis. The **Type** column indicates whether a cut is livetime-based or event-based (applied event by event). The **Domain** column specifies whether a selection is defined during processing (Processing), evaluated per data-taking segment (Series-based), or determined using the full combined dataset (All data).

<table>
<tr><th>Selection</th><th>Type</th><th>Domain</th><th>L-step</th><th>K-step</th></tr>
<tr><td>Trigger dead time</td><td>Livetime</td><td>Processing</td><td colspan="2">✓</td></tr>
<tr><td>High-trigger rate</td><td>Livetime</td><td>Series-based</td><td colspan="2">✓</td></tr>
<tr><td>Coincidence</td><td>Event-based</td><td>All data</td><td>✓</td><td>✗</td></tr>
<tr><td>ΔT</td><td>Event-based</td><td>Processing</td><td colspan="2">✓</td></tr>
<tr><td>Mean baseline</td><td>Event-based</td><td>Series-based</td><td colspan="2">✓</td></tr>
<tr><td>OF-χ^2</td><td>Event-based</td><td>All data</td><td>✓</td><td>✗</td></tr>
<tr><td>Pulse-width</td><td>Event-based</td><td>All data</td><td>✗</td><td>✓</td></tr>
</table>

from each 0.5-second trace. It is a live-time cut. Overall it removes 5% of the total live time.

High trigger rate cut

The second live-time cut is applied to remove periods during which a sudden increase in the event rate is observed. From dark matter, we expect uniform event rate over time, so such intervals with elevated trigger rates at arbitrary time are not expected from them. Therefore they must be excluded from the analysis. These high-rate intervals are likely caused by external radio-frequency (RF) noise generated by other experiments operating within the same dilution refrigerator. They typically appear as a train of square-shaped pulses, as shown in Fig. 3.13.

These events are removed by examining the distribution of the trigger rate and applying a threshold cut. We reject any time interval for which the trigger rate exceeds 5σ above the mean value expected from a Poisson distribution of the event rate (Fig. 3.14). In addition, one extra time bin (10 s for ^{137}Cs data and 100 s for background data) is removed on both

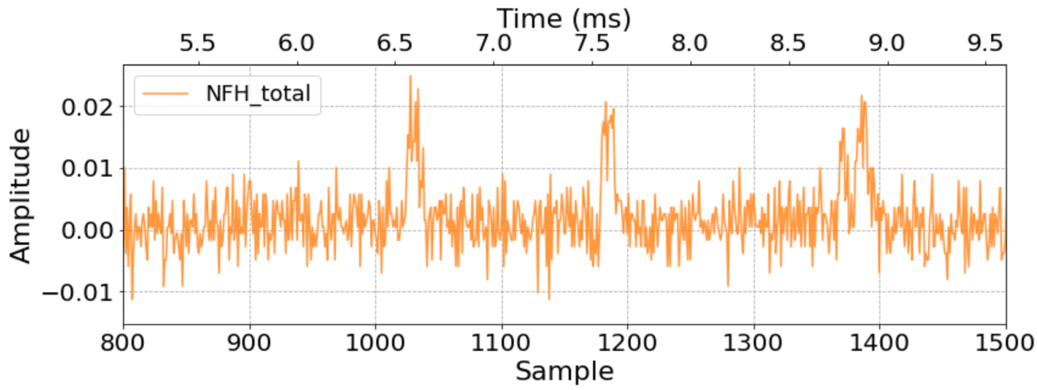

FIGURE 3.13: Example trace of high trigger-rate events in the NFH detector. Such events typically appear in bursts within short time intervals, significantly increasing the trigger rate.

sides of each rejected interval to ensure complete suppression of the high-rate bursts.

This cut removes 6% and 18% of the total run time from the ^{137}Cs and background datasets respectively.

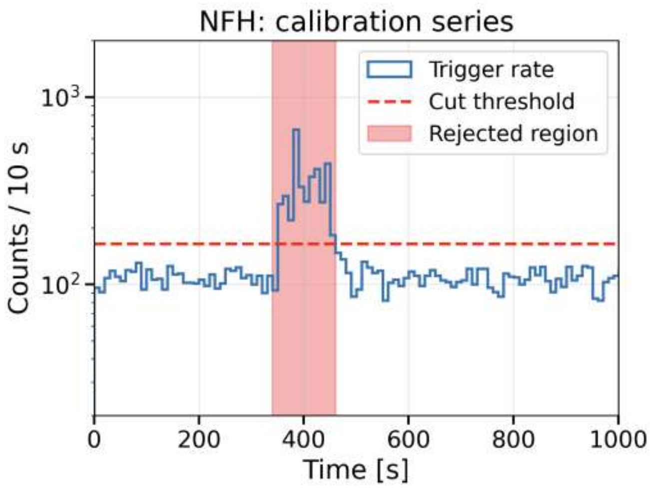

FIGURE 3.14: Example of a removed time interval using the high trigger-rate cut in NFH detector. The highlighted interval, likely caused by external noise from other experiments operating in the same refrigerator, is removed for all detectors.

Fridge temperature

Variations in the MC temperature can modify the current gain of the readout system and potentially introduce systematic effects in the reconstructed quantities. For this reason, we examined the stability of the MC temperature to determine whether a temperature-dependent cut was required. As shown in Sec. 3.4 (Fig. 3.8), the temperature remained stable throughout the data sets used in this analysis. Therefore, no temperature-based selection criterion was applied.

DT and Coincidence Cuts

Events occurring very close in time can distort the reconstruction of pulse properties and therefore must be removed. Two complementary selections are applied to remove such events: the ΔT (or DT) cut and the coincidence cut.

The ΔT cut eliminates events that occur too close to a preceding trigger within the same detector. Such closely spaced events, commonly referred to as pileup, lead to overlapping pulses that cannot be reliably reconstructed. We impose a minimum time separation of 1024 + 15 samples between successive triggers in the same detector, corresponding to a duration slightly longer than half of the reconstruction window. This requirement effectively suppresses pileup events and ensures stable pulse reconstruction.

The coincidence cut removes events that occur nearly simultaneously across multiple detectors. These are typically non-physical triggers caused by electronic glitches or cross-talk. In addition, we often observed that high-energy depositions in the NFC1 detector simultaneously induced low energy triggers in the outer channel of the NFE detector. The most plausible explanation is cross-talk arising from adjacent readout cables of the NFC1 and NFE detectors. To remove such coincidence effects, events occurring within 96 μs (15 samples) across different detectors are rejected. Figure 3.15 shows an example raw traces

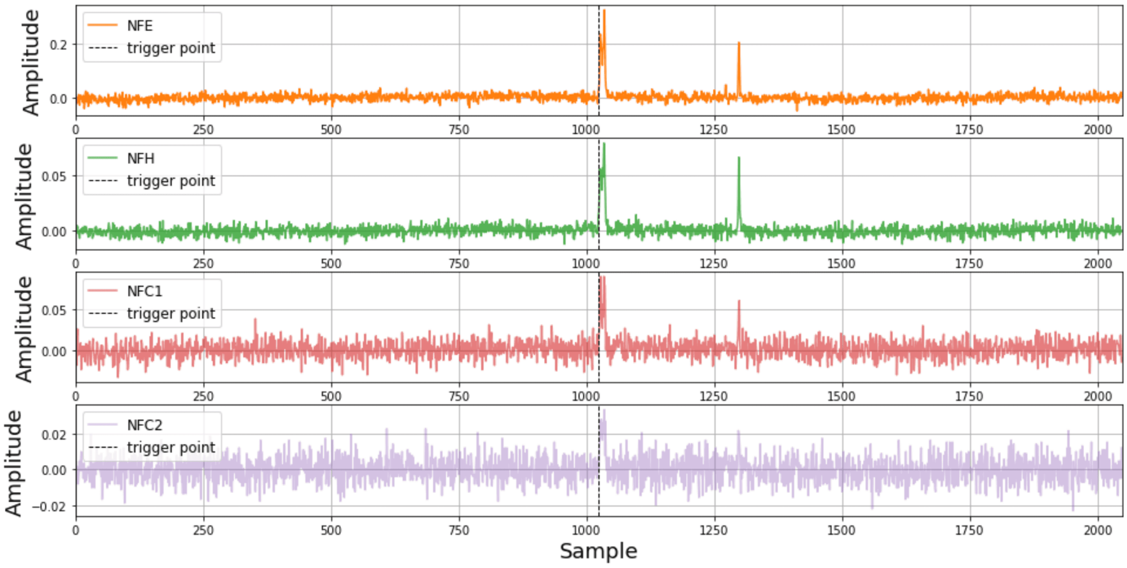

FIGURE 3.15: Example raw traces showing pileup events in a single detector and cross-talk-induced coincidence events across detectors. These events are removed by the ΔT and coincidence selections.

containing both pileup events and cross-talk events.

These coincident noise events were found to populate the L-step energy region. Therefore, the coincidence selection is applied within the L-step window, while excluding the keV signal region to avoid removing genuine energy depositions that may coincide with spike-like triggers.

Mean Baseline (MB) Cut

During calibration runs with 662 keV Cs source, the detector frequently records very high energetic events with large-amplitude values. Such signals decay slowly back to the baseline. Because of these long tails, subsequent triggers can occur while the detector response has not yet fully stabilized. In such cases, the new pulse is superimposed on a residual offset from the previous event. This effect alters the apparent baseline level and can bias the reconstructed pulse amplitude. To minimize this source of systematic distortion, a

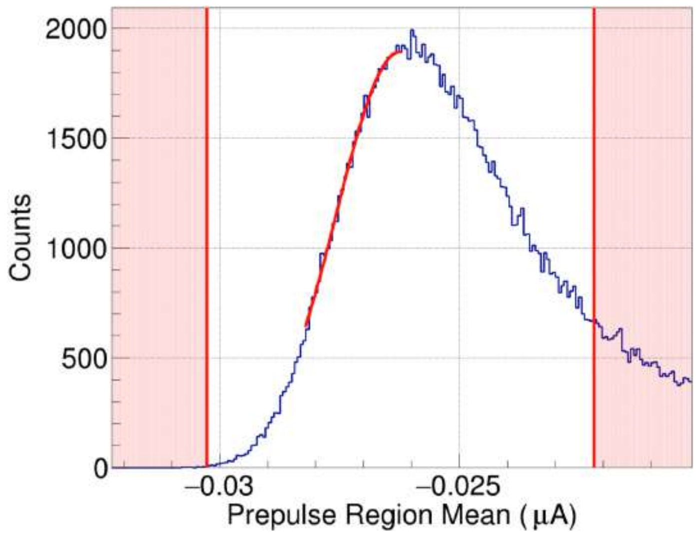

FIGURE 3.16: Distribution of the mean base (ν_{base}) for calibration events. A Gaussian fit to the left side estimates the baseline mean and standard deviation. Events more than three standard deviations above the mean (shaded region) are rejected by the Mean Baseline cut. Adapted from Ref. [5].

MB cut was introduced.

The MB selection is based on the average value of the signal in the pre-trigger portion of each waveform, denoted by ν_{base}. When the detector is operating under stable conditions and pulses are well separated in time, the pre-trigger averages fluctuate around a constant baseline and are expected to follow a Gaussian distribution determined by the electronic noise. However, the presence of a high energetic pulse tail can shift these averages away from their nominal value, producing an asymmetric distribution with an extended tail (Fig. 3.16).

To identify uncontaminated events, a Gaussian function was fitted to the left (unaffected) side of the ν_{base} distribution. The mean and standard deviation obtained from this fit define the acceptable baseline region. Events with ν_{base} values more than three standard deviations above the fitted mean were rejected, as they are likely influenced by residual pulse tails.

Although this requirement significantly reduces baseline distortions, a small asymmetry remains in the distribution, indicating that a limited number of affected events may still survive. The potential impact on the energy calibration was evaluated using data collected at 100 V bias with the radioactive source installed. Events corresponding to the first e^-h^+ peak at 100 eV were selected after applying the MB cut, and the reconstructed pulse amplitudes were examined as a function of ν_{base}. Any residual dependence (approximately a few eV) was found to be negligible compared to other calibration uncertainties.

χ^2 Cut

The reduced χ^2 value (χ^2/NDF) obtained from the OF fit quantifies how well a recorded pulse matches the expected single-phonon template. Events that follow the standard pulse shape yield χ^2/NDF values clustered around a characteristic mean, while pulses with distorted or non-standard shapes result in larger values. Therefore, χ^2/NDF provides a powerful discriminator against non-ideal events.

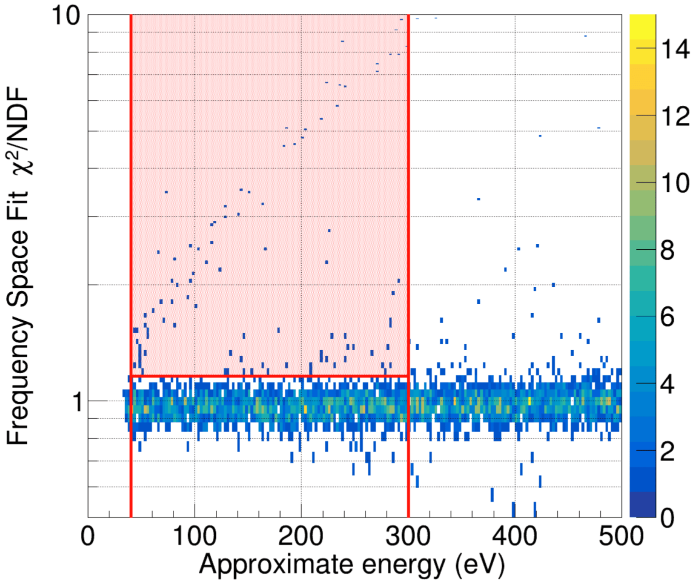

FIGURE 3.17: Reduced χ^2 (χ^2/NDF) as a function of reconstructed energy for the ^{137}Cs dataset. The main cluster corresponds to pulses consistent with the single-phonon template. A flat 3σ threshold (horizontal line) is applied within the selected L-step analysis window [5].

A small subset of events exhibited systematically elevated pulse tails. These pulses are understood to originate from direct energy depositions in the QET aluminum fins rather than in the Si absorber [14]. Because their temporal shape differs from that of bulk phonon events, they are not well described by the nominal pulse template and consequently produce higher χ^2/NDF values.

When χ^2/NDF is plotted as a function of reconstructed energy, these events appear as a diagonal band above the main population, particularly within the L-step search region (Fig. 3.17). The effect is most pronounced at low energies, around $O(100\text{ eV})$, which is the region relevant for L-step calibration.

To suppress these non-standard events, the χ^2/NDF distribution was examined within the selected L-step energy window (40–300 eV). The distribution of the main event population was modeled using a Gaussian function to determine its mean and standard deviation. Events with χ^2/NDF values exceeding three standard deviations above the fitted mean were rejected. This corresponds to a flat 3σ threshold in the selected energy range.

In Fig. 3.17, vertical lines indicate the energy interval used to project events onto the χ^2/NDF axis. The central horizontal line represents the mean of the Gaussian model, while the upper horizontal line marks the 3σ rejection threshold. Events in the shaded region above this boundary were excluded from the low-energy analysis.

Pulse-Width Cut

At higher energies (keV scale), the detector response deviates from the pulse shape observed at low energies, which was used to construct the Optimal Filter template. As a result, the χ^2/NDF distribution rapidly shifts and broadens with increasing energy. In this regime, the reduced χ^2 is no longer a reliable discriminator between well-behaved pulses and distorted events. For this reason, a pulse-width selection was introduced for the high-energy analysis.

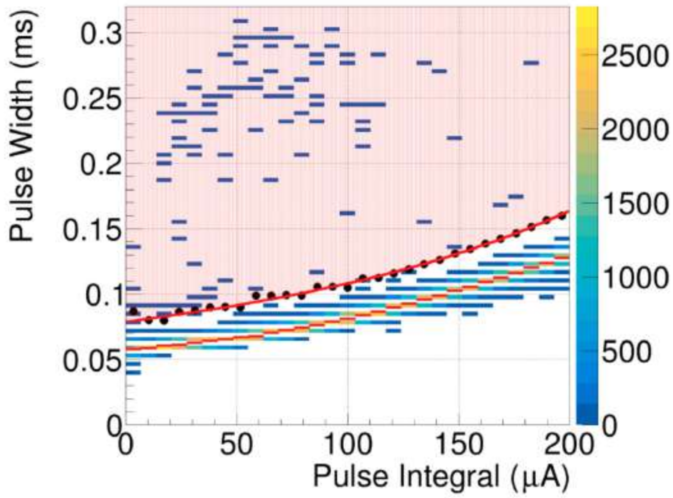

FIGURE 3.18: Pulse width as a function of pulse integral for high-energy events. The solid red line corresponds to a 7σ threshold above the nominal distribution. Events above this threshold are rejected by the pulse-width cut. Credit: Ata Sattari

Although the pulse amplitude remains the primary estimator of deposited energy, non-standard events, particularly those with elevated or prolonged tails, can be identified through their pulse shape characteristics. The pulse width was defined as the time difference between the rising and falling edges measured at 30% of the maximum pulse height. Under normal conditions, the pulse-width distribution follows a well-defined trend as a function of pulse integral. However, events with anomalously extended tails exhibit significantly larger widths.

To reject such events, the pulse-width distribution was examined as a function of the pulse integral (Fig. 3.18). The mean behavior was determined, and an upper threshold corresponding to 7σ above the nominal distribution was applied. The relatively loose 7σ criterion was chosen to minimize the impact on signal efficiency while still suppressing clearly non-standard pulses. All events with pulse-width values above this threshold were rejected. This selection effectively removes high-energy events with elevated tails.

3.6.2 Filtered Spectrum

After applying all livetime and data-quality selections, the final reconstructed spectra are presented in Figs. 3.19 and 3.20. The Optimal Filter Limited (OFL) energy estimator is used for the Compton step analysis because of its superior resolution compared to the pulse-integral estimator in the low-energy regime (a few keV and below).

The L-step features are not visually distinguishable due to the presence of excess low-energy background. To define the L-step region of interest, a preliminary energy calibration is performed using the position of the first e^-h^+ peak from the 100 V background dataset, corresponding to approximately 100 eV energy depositions. The calibrated low-energy spectra for both the ^{137}Cs calibration data and the low-background dataset are shown in Fig. 3.19. After applying all selections, the overall passage fraction is approximately 50% and remains similar across detectors.

The NFE detector is not included in the high-energy presentation, as it is optimised for low-energy interactions due to its lowest QET coverage and exhibits significant pulse saturation in the keV range. For high energies, the K step feature can be clearly identified, therefore we did not use any approximate calibration. The filtered high-energy calibration spectrum is shown in Fig. 3.20.

The Coincidence cut is not applied in high energy region because such events arose from instrumental glitches and primarily affected the low-energy events. In addition, the χ^2 selection is replaced with the pulse-width cut, which more effectively identifies distorted or saturated pulses at high energies.

The livetime selections reject entire time intervals rather than individual triggers and therefore do not introduce energy-dependent signal efficiency in the spectra. The ΔT and Baseline cuts primarily remove overlapping pulses and residual tails from preceding events.

Monte Carlo studies with randomly injected pseudo-pulses confirm that rejecting overlapping events does not introduce significant energy-dependent bias in the signal acceptance. In the low-energy region, the Coincidence selection suppresses non-physical triggers without significantly reducing genuine signal candidates. Since ~100 keV gamma rays in Si have mean free paths of several centimeters, true low-energy Compton scatters are unlikely to produce simultaneous interactions across multiple detectors. The χ^2 selection (low energy) and pulse-width selection (high energy) further remove events with elevated tails that deviate from the expected signal template. Overall, these selections improve the spectral quality while maintaining approximately energy-independent signal efficiency within the respective analysis windows.

3.6.3 Trigger Efficiency Estimation

A precise modeling of the trigger efficiency is crucial for the low-energy calibration, particularly for the extraction of the L-shell Compton step. The L-step is located near ~ 100 eV, and the fitting window extends down to approximately 50 eV (see Section 3.6.4). Since this region overlaps with the detector trigger threshold, the finite trigger turn-on must be explicitly incorporated into the L-step fit.

The trigger efficiency is modeled as a function of the OFL energy estimator, A_{OF}, using a sigmoid parameterization:

$$\epsilon(A_{\mathrm{OF}} \mid k_1, k_2) = \frac{1}{1 + \exp\left(-\frac{A_{\mathrm{OF}} - k_1}{k_2}\right)}, \tag{3.2}$$

where k_1 and k_2 are free parameters. The parameter k_1 corresponds approximately to the 50% trigger efficiency point, while k_2 characterizes the width of the efficiency turn-on region.

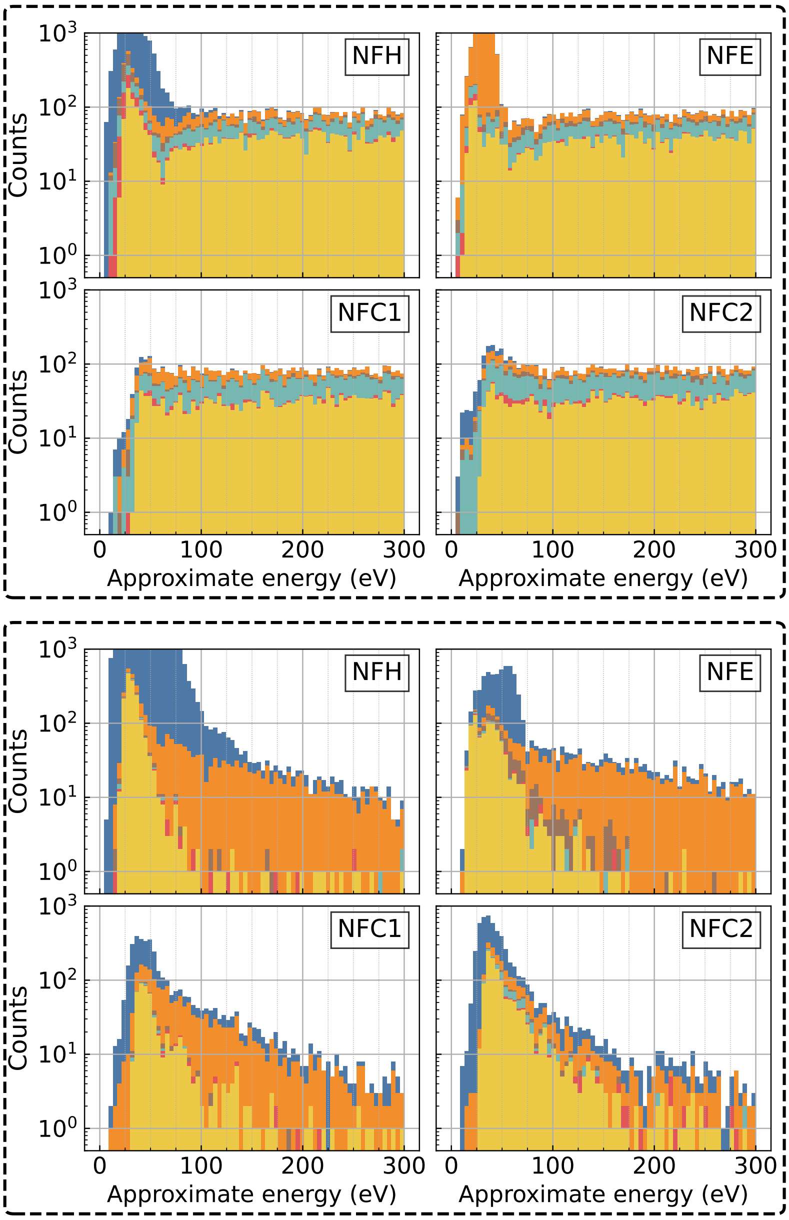

FIGURE 3.19: Low-energy spectra at 0 V after applying all livetime and data-quality selections. An approximate energy calibration using ~ 100 eV calibration point from 100 V bias data in performed for L-step region of interest selection. Top: ^{137}Cs calibration dataset. Bottom: low-background dataset [5].

The parameters of this model are determined using a Monte Carlo–based pulse injection study. Pulse templates are constructed by averaging well-reconstructed events within 100 eV

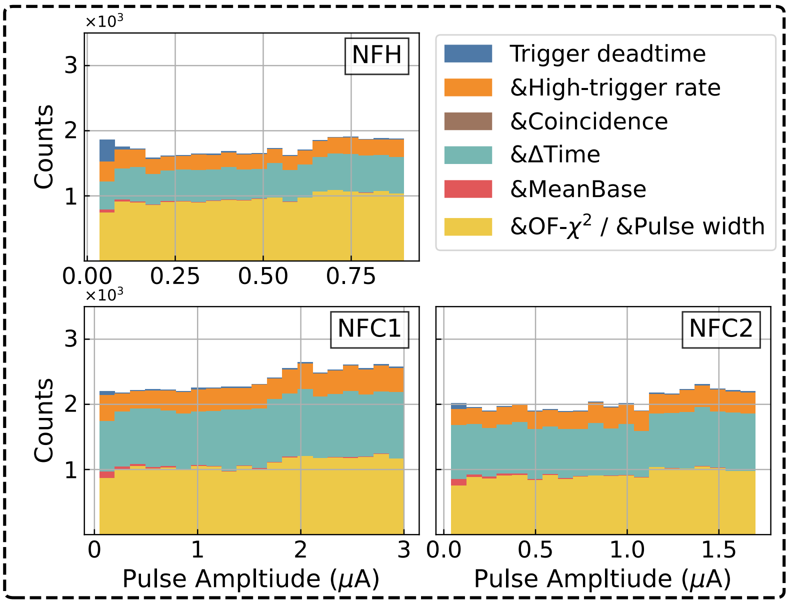

FIGURE 3.20: K-step region of the ^{137}Cs spectrum at 0 V after applying all selection criteria. The OFL estimator is shown in units of current (μA) [5]. Distinct K-step features are visible in all HVeV detectors. The NFE detector is excluded from this analysis due to prominent pulse saturation in the keV range.

energy intervals from a ^{137}Cs 0 V calibration series. A χ^2 selection is applied to retain only pulses consistent with the nominal pulse shape.

To model detector noise, pulse-free traces from randomly triggered events in the same dataset are selected. A cut on the pulse amplitude (defined as maximum minus minimum) removes traces potentially contaminated by pileup or residual activity.

Synthetic events are generated by injecting scaled pulse templates into the selected noise traces over an energy range extending up to 500 eV. For each 2 eV energy bin, 100 pseudo-events are produced. These simulated traces are processed using the same Gaussian Derivative Filter (GDF) trigger algorithm employed in the standard data reconstruction chain. The trigger efficiency at each energy is calculated as the fraction of pseudo-events satisfying the trigger condition.

Figure 3.21 illustrates the template construction and pulse injection procedure. The

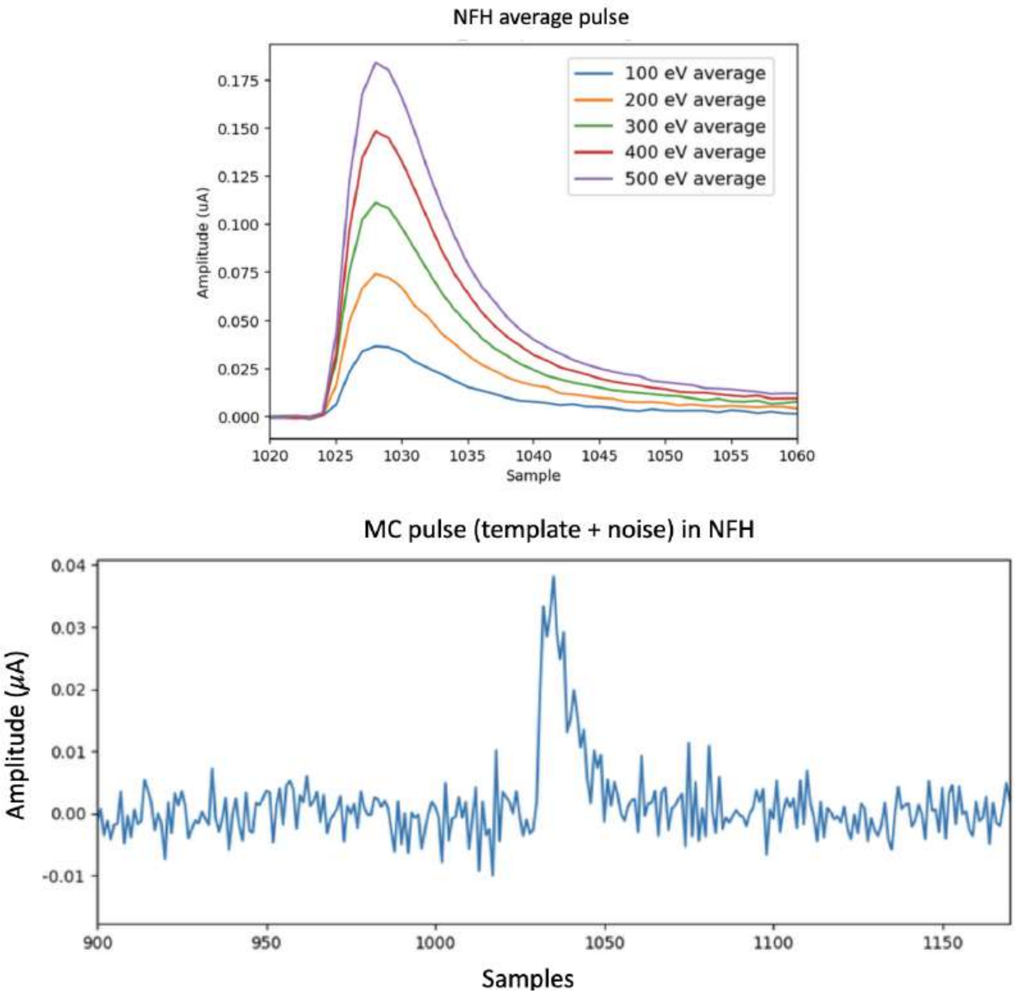

FIGURE 3.21: Top: Energy-dependent pulse templates constructed by averaging calibration pulses up to 500 eV. Bottom: Example of a 100 eV pseudo-event generated by scaling the pulse template and adding it to a randomly triggered noise trace.

top panel shows the energy-dependent pulse templates obtained from averaged calibration events, while the bottom panel displays an example of a 100 eV injected pseudo-event formed by adding a scaled template to a noise trace from the same dataset.

The resulting efficiency curves as a function of A_{OF} are shown in Fig. 3.22. The data points represent the fraction of injected pseudo-events that satisfy the trigger requirement, and the solid curves show the best-fit sigmoid model described by Eq. (3.2). The black dashed line in each panel indicates the OFL value corresponding to 50% trigger efficiency.

Using the energy calibration derived from the L_1 Compton step at 100 eV (Section 3.6.4), the energy equivalents of the 50% trigger efficiency are determined to be approximately 50 eV, 37 eV, 54 eV, and 50 eV for NFE, NFH, NFC1, and NFC2, respectively.

These parameter constraints are incorporated into the L-step fitting procedure to properly account for the finite trigger turn-on behavior in the low-energy analysis region.

3.6.4 L-step Calibration at 0 V

The low-energy calibration of HVeV detectors relies on the measurement of pulse amplitudes (A_{OF}) corresponding to the Si Compton steps. In the L-step region, we assume a linear mapping between the pulse amplitude and deposited energy up to approximately 300 eV, expressed as

$$E_{\mathrm{OF}} = C \cdot A_{\mathrm{OF}}, \tag{3.3}$$

where C is the calibration parameter. This parameter is extracted by fitting the FEFF-simulated Compton spectrum (no-core-hole) to calibration data obtained with a Cs-137 source at 0 V bias. A data-driven background model representing the LEE is included in the fit, constrained by background measurements collected at 0 V without the source. Since the FEFF simulation is expressed in units of energy (keV), while the measured pulses are recorded in current (μA), the calibration factor C is necessary to convert the simulation

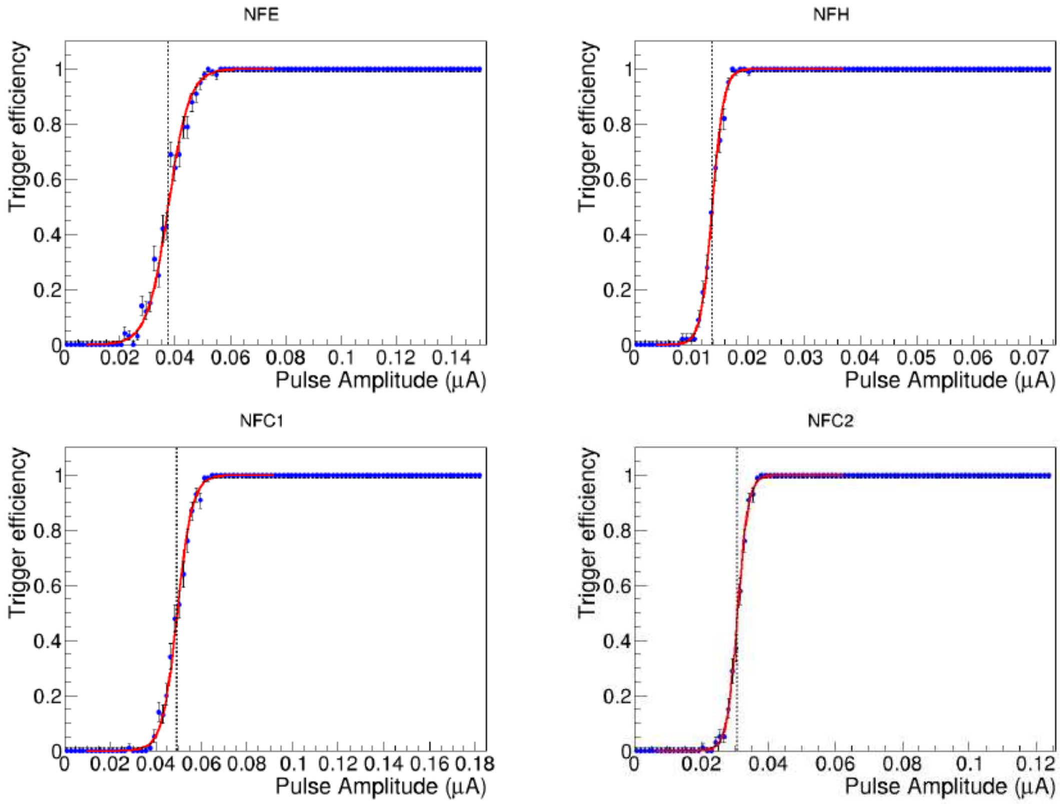

FIGURE 3.22: Trigger efficiency as a function of the OFL energy estimator for detectors NFE, NFH, NFC1, and NFC2. The data points show the fraction of triggered pseudo-events at each energy bin, while the solid lines represent the best-fit sigmoid model. The dashed vertical line indicates the 50% trigger efficiency point.

into the OFL domain, allowing a consistent comparison and fit between the simulated and measured spectra.

Probability Density Function and Trigger Efficiency

The measured spectrum for each detector is modeled as a combination of the Compton PDF from the FEFF simulation and the LEE background. The LEE spectrum is described by a single-parameter power law, x^{-d}, where d is a free parameter. Each component is convolved with a Gaussian of constant width σ to account for detector resolution and is multiplied by the pre-determined trigger efficiency function $\epsilon(A_{\mathrm{OF}} \mid k_1, k_2)$:

$$\mathrm{PDF}_l^{\mathrm{eff}}(A_{\mathrm{OF}}) = \frac{\mathrm{PDF}_l(A_{\mathrm{OF}}) \times \epsilon(A_{\mathrm{OF}} \mid k_1, k_2)}{\int \mathrm{PDF}_l(A_{\mathrm{OF}}) \times \epsilon(A_{\mathrm{OF}} \mid k_1, k_2) dA_{\mathrm{OF}}}, \tag{3.4}$$

where l indicates either the source or background dataset.

The combined PDF for each dataset is

$$\begin{aligned} \mathrm{PDF}_l(A_{\mathrm{OF}} \mid C, \sigma, d, N_l^{\mathrm{Comp}}, N_l^{\mathrm{LEE}}) = & \frac{N_l^{\mathrm{Comp}}}{N_l} \mathrm{PDF}^{\mathrm{Comp}}(C \cdot A_{\mathrm{OF}} \mid \sigma) \\ & + \frac{N_l^{\mathrm{LEE}}}{N_l} \mathrm{PDF}^{\mathrm{LEE}}(A_{\mathrm{OF}} \mid d), \end{aligned} \tag{3.5}$$

with $N_l = N_l^{\mathrm{Comp}} + N_l^{\mathrm{LEE}}$ and N_l^{Comp}, N_l^{LEE} the number of events associated with the Compton and LEE components, respectively.

Likelihood Function

The calibration parameters for each detector are extracted using an unbinned profile likelihood fit, which simultaneously accounts for the Compton signal and the low-energy background contributions.

$$\begin{aligned} \mathcal{L} = & \mathcal{N}_2(\vec{\mu}, \mathbf{\Sigma}; k_1, k_2) \\ & \times \prod_{l \in \{\mathrm{bg}, \mathrm{calib}\}} \mathrm{Pois}(n_l \mid N_l(\vec{\theta}_l)) \\ & \times \prod_{i=1}^{n_l} \mathrm{PDF}_l^{\epsilon}(x_l^i \mid \vec{\theta}_l, N_l^{\mathrm{Comp}}, N_l^{\mathrm{LEE}}), \end{aligned} \tag{3.6}$$

where $\vec{\theta}_l = (C, \sigma, d, k_1, k_2)$ controls the shape of the PDFs. x_l^i are measured pulse amplitudes (A_{OF}) for event ‘i’, n_l is the number of observed events, and $\mathcal{N}_2$ is a two-dimensional Gaussian constraint on the trigger-efficiency parameters k_1 and k_2. The calibration parameter C linearly stretches the simulation to align with measured amplitudes. Figure 3.23 shows the resulting fits for all detectors.

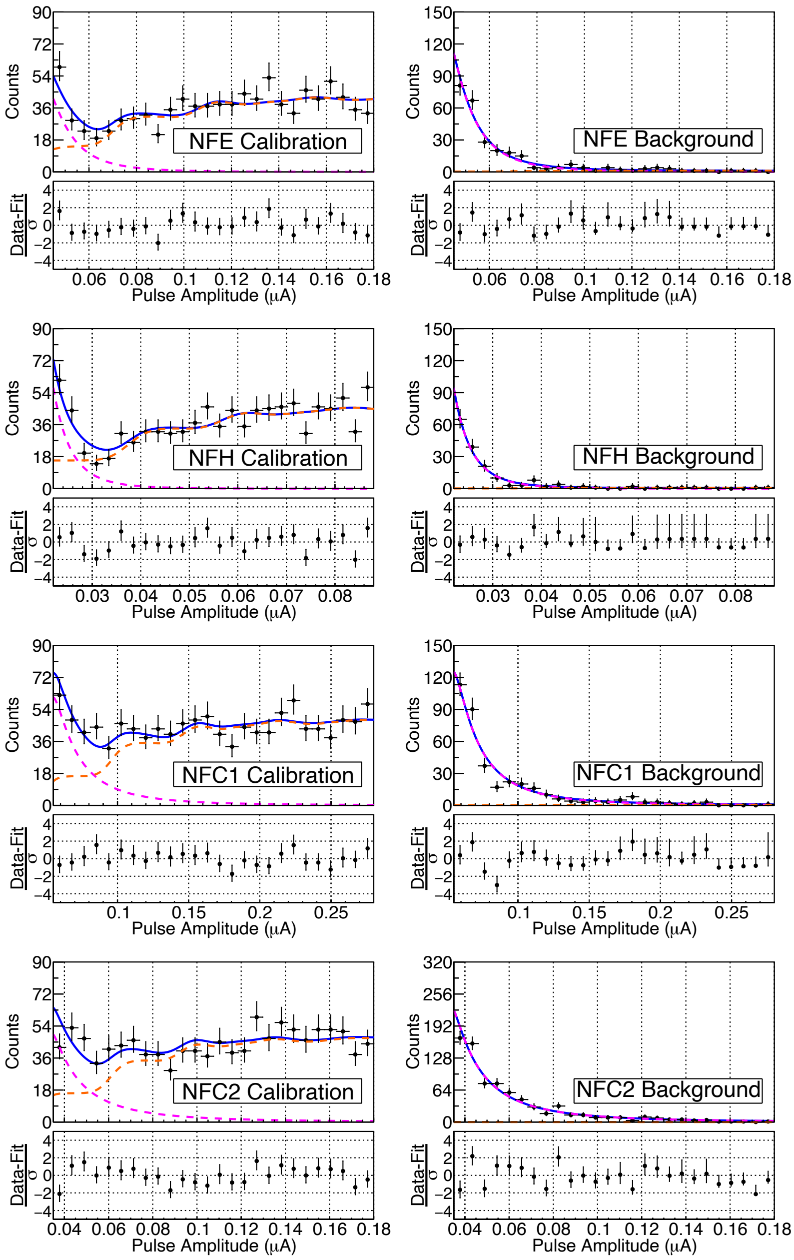

FIGURE 3.23: Simultaneous fits of calibration (left) and background (right) data for the Compton L-steps. Solid blue lines indicate the total best fit; dashed lines represent contributions from Compton (orange) and LEE (magenta) components. Parameters controlling PDF shapes are shared across datasets, while event counts are independent [5].

Uncertainty Evaluation

The calibration factor C is subject to several sources of uncertainty:

- **Statistical uncertainty:** filtered dataset statistics.
- **Systematic uncertainty I:** correlations between C and nuisance parameters in the likelihood.
- **Systematic uncertainty II:** variations in FEFF simulation assumptions, including core-hole effects.
- **Systematic uncertainty III:** modeling of the LEE background spectrum.

Statistical uncertainties dominate. Systematic uncertainties from FEFF simulations were evaluated by comparing no-core-hole and core-hole fits. LEE background uncertainties were negligible. The total uncertainty was obtained by summing the profiled-likelihood and FEFF contributions in quadrature (Table 3.4).

TABLE 3.4: Calibration factors converting A_{OF} to energy for 0 V datasets. Uncertainties from profile likelihood (PL) and FEFF simulations are listed separately; the total uncertainty is their quadrature sum. Calibration is valid up to 300 eV.

Detector	C (keV/μA)	PL (Stat & Sys) (keV/μA)	FEFF (Sys) (keV/μA)
NFE	1.5 ± 0.1	0.08	0.06
NFH	2.7 ± 0.2	0.20	0.06
NFC1	1.06 ± 0.04	0.04	0.01
NFC2	1.65 ± 0.08	0.08	0.01

3.6.5 K-step and Extended Calibration at 0V

The K-step features in the Compton spectrum are clearly visible in the filtered OFL spectrum (Fig. 3.25). We extract the K-step positions from both experimental data and Geant4 simulations using a modified error function:

$$f(a,b,\mu,\sigma) = \frac{a}{2}\left[1 + \mathrm{erf}\left(\frac{x-\mu}{\sqrt{2}\sigma}\right)\right] + b, \tag{3.7}$$

where a is the step height, b is the baseline, μ is the step center, and σ characterizes the step width, accounting for the detector resolution. The probability density function (PDF) is normalized within a window around the K-step. In experimental data, the fit center provides the pulse amplitude corresponding to the K-step, whereas in simulations it provides the corresponding energy. Detector resolution was taken as 2% based on NFC1 measurements [10] and varied between 1–3% in simulations; the uncertainty from this smearing was negligible. The K-step fits for HVeV detectors are shown in Fig. 3.25. The NFE detector is excluded due to nonlinear response at higher energies, attributed to limited QET coverage.

The Geant4-simulated Compton spectrum in the keV region is shown in Fig. 3.24 (left). In addition to the K-shell Compton step, a Cu K-α X-ray photopeak is visible, originating from the Cu detector housing. Simulations indicate that the Cu K-β peak is not expected to be observable due to the detector resolution and the available statistics, with the intensity ratio $K_\alpha : K_\beta = 100 : 17$. In experimental data, the OFL energy estimator does not clearly capture the Cu X-ray peak due to strong pulse saturation near 8 keV. However, the Pulse Integral energy estimator, which measures the pulse area rather than the height, resolves the Cu X-ray peak more reliably, albeit with slightly worse energy resolution than OFL. The Integral spectrum for the NFC1 detector is shown in Fig. 3.24 (right), with the K-step region in OFL shown in the inset. Since our focus is on the Compton steps, and the K-step feature is visible in both estimators, we adopt the OFL estimator due to its superior energy resolution.

By combining the L- and K-step measurements, the calibration function is extended up to 1.8 keV. The L-step provides the pulse amplitude for the L1-step at 150 eV, while the

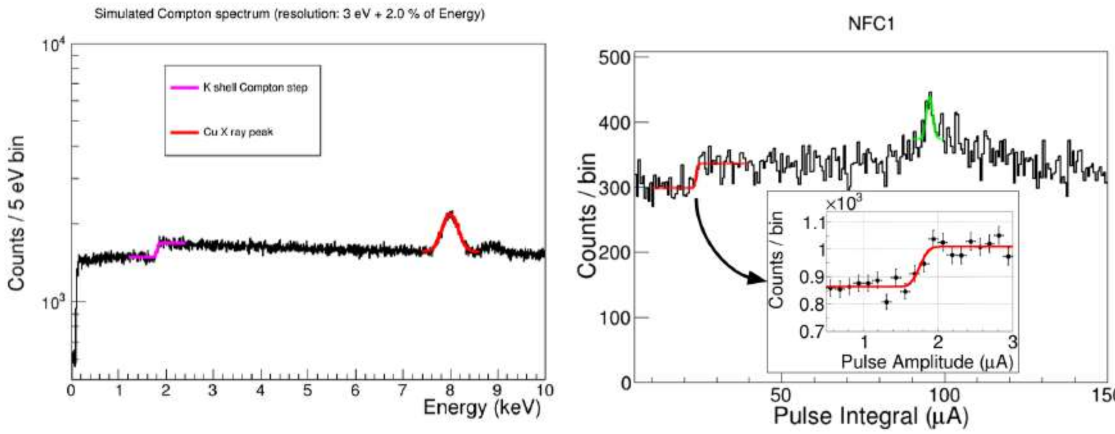

FIGURE 3.24: Geant4-simulated Compton spectrum. **Left**: and NFC1 Integral spectrum. **Right**: The inset highlights the K-step region. Cu X-ray peaks are also indicated.

K-step serves as a higher-energy reference.

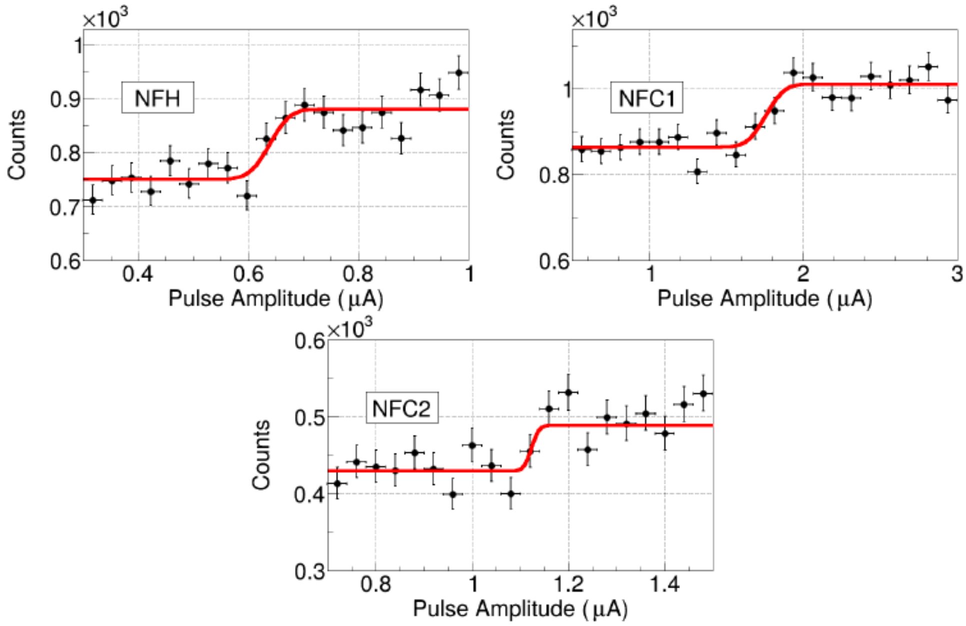

FIGURE 3.25: Pulse amplitude spectra around the K-shell Compton steps for NFH, NFC1, and NFC2. Red curves indicate the fits. NFE is excluded due to nonlinear response at higher energies caused by limited QET coverage [5] .

In the keV region, the detector response begins to show nonlinearity. As discussed in Sec. 3.7, LED measurements confirm this, motivating a quadratic calibration function:

$$E_{\mathrm{OF}} = \alpha A_{\mathrm{OF}} + \beta A_{\mathrm{OF}}^2, \tag{3.8}$$

where A_{OF} is the OFL pulse amplitude. The measured coefficients for each detector are listed in Table 3.5. The quadratic term at 0 V is statistically consistent with zero, confirming that the linear calibration used for the L-step analysis is valid. The 0 V calibration curves are shown in Fig 3.26. While a single representative L-step point is used to calibrate up to 1.8 keV, the approximate positions of both L-step Compton features is shown.

TABLE 3.5: 0 V calibration coefficients relating A_{OF} to energy.

Detector	α **(keV/**μ**A)**	β **(keV/(**μ**A)**^{2}**)**
NFH	2.7 ± 0.2	0.2 ± 0.4
NFC1	1.06 ± 0.05	-0.01 ± 0.03
NFC2	1.66 ± 0.09	-0.03 ± 0.08

3.7 Energy Calibration at HV Bias Using LED Spectrum

A precise energy calibration in the keV region is achieved by analyzing the detector response to optical photons from LED sources. LED data were collected for the NFH, NFC1, and NFC2 detectors (the NFE detector was excluded, as it was not studied for the keV energy scale) under a high bias voltage. HV calibration using LED data serves two main purposes:

- The detector response becomes increasingly non-linear in the keV energy range. To accurately characterize this non-linearity, several calibration points across the keV region are required.
- A previous study [10] indicates that the detector response for the same total measured phonon energy differs between 0 V and HV conditions. For example, the pulse amplitude corresponding to ≈150 eV of measured energy is expected to differ between

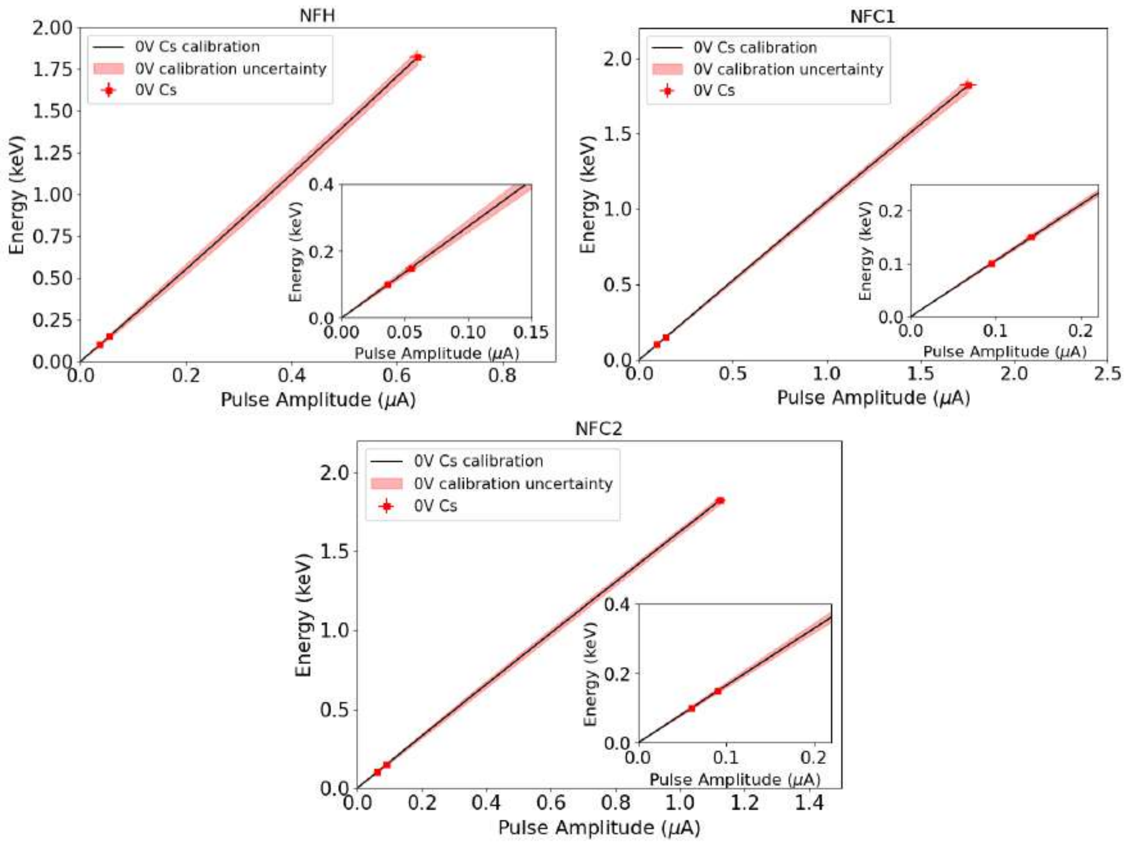

FIGURE 3.26: 0V energy calibration curve for HVeV detectors using OFL energy estimator. The calibration curve is obtained using L1 step and K step calibration points, while both L1 and L2 calibration points are shown, as they both feature in the simulated spectrum. Inset plot shows the low energy region of the calibration function.

HV mode (e.g., arising from the first e^-h^+ peak in the 150 V LED data) and L1-shell Compton step events in the 0 V data. While the Compton step calibration at 0 V reflects bulk event interactions, HV LED events also generate phonons in the bulk as the e^-h^+ pairs drift across the crystal, even though these pairs are initially created near the surface by 2 eV photons. Comparing these calibrations provides a direct assessment of how the detector response varies between 0 V and HV operating conditions.

We focus on LED calibration using a 150 V bias to achieve precise energy calibration up to a few keV. Each LED photon carries approximately 2 eV of energy and, when absorbed, generates a single e^-h^+ pair, as illustrated in Fig. 3.27. Since the absorption length of 2 eV photons is on the order of microns, much smaller than the detector thickness, these pairs are initially created near the detector surface. As the e^-h^+ pairs drift across the crystal under the 150 V bias, they produce Neganov–Trofimov–Luke (NTL) phonons. The total phonon energy for a single e^-h^+ pair traversing the crystal is therefore 152 eV (2 eV from the primary photon plus 150 eV from the NTL phonons).

Increasing the LED intensity allows multiple photons to be absorbed simultaneously, so that N e^-h^+ pairs ideally produce $152 \times N$ eV of total phonon energy. In some cases, e^-h^+ pairs may recombine before fully drifting, contributing no NTL phonons; we refer to such events as the *surface trapping effect*. The impact of this effect on LED calibration is discussed in detail in Sec. 3.7.3.

The burst frequency of the LED source is 10 Hz. The number of generated e^-h^+ pairs that undergo NTL amplification in each burst follows a Poisson distribution with mean λ. Higher λ values correspond to higher-intensity LED data. For the calibration series, we use LEDs with λ typically between 10 and 15.

HVeV detectors are sensitive to single-charge excitations, resulting in a response that exhibits distinct peaks corresponding to integer numbers of e^-h^+ pairs. By identifying the ordinal number of each peak and the associated energy, we can establish an accurate energy calibration for the OFL estimator.

3.7.1 Detector Response to LED Photons

The exceptional energy resolution of HVeV detectors, on the order of a few eV, allows individual e^-h^+ pair peaks to be clearly resolved in the measured energy spectrum. In LED series with low mean photon number ($\lambda \approx 1$), there is a finite probability that no e^-h^+

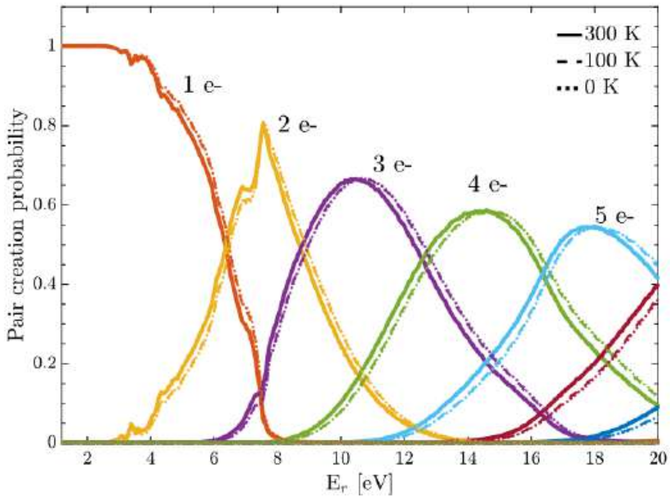

FIGURE 3.27: Probability of e^-h^+ pair creation as a function of electron recoil energy at 0 K, 100 K, and 300 K [15]. It can be seen that the e^-h^+ pair creation probability from 2 eV photon is 1.

pairs are generated. In such cases, no Luke phonons are produced, and consequently, no energy is deposited in the TES. Nevertheless, as discussed in Sec. 3.5, the LED triggering algorithm ensures that events are recorded according to the LED burst frequency, even when the detector signal does not exceed the trigger threshold. Forced recording of events with zero e^-h^+ pair generation produces a population of events near zero amplitude in the energy spectrum. This feature, referred to as the *zeroth peak*, provides a natural reference for determining the order of subsequent e^-h^+ peaks.

In LED series with high mean photon number, the zeroth peak is often suppressed, making it difficult to assign the ordinal number of the first visible peak. To address this, multiple LED series with varying λ values were combined, enabling the observation of all e^-h^+ pair peaks and determination of their positions. Across all HVeV detectors, individual e^-h^+ peaks remain well resolved. Figure 3.28 presents an example of the combined LED spectrum for the NFC1 detector, where low-intensity LEDs populate lower-order e^-h^+ peaks and high-intensity LEDs populate higher-order peaks. The OFL estimator exhibits sharp peaks due to its optimized energy resolution, facilitating clear identification of each e^-h^+ peak.

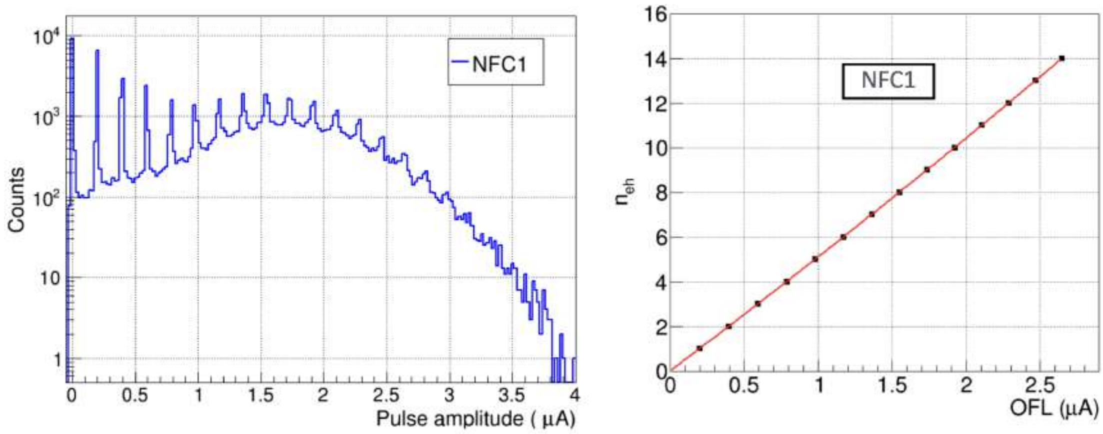

FIGURE 3.28: **Left**: Combined LED spectrum for the NFC1 detector at varying LED intensities. Low-intensity LEDs populate lower-order e^-h^+ peaks, while high-intensity LEDs contribute to higher-order peaks. **Right**: Relation between e^-h^+ peak order and OFL for HVeV detectors. This relation enables identification of peak numbers in high-intensity LED series where the zeroth peak is suppressed.

It should be note that the combined LED series is not used for absolute energy calibration. The surface trapping effect depends on LED intensity (i.e., the λ of each series) and induces an overall energy offset in the spectrum (Sec. 3.7.3). As a result, different LED series are affected to varying degrees, which broadens the e^-h^+ peaks in the combined spectrum and could bias their position estimation. The energy shift due to surface trapping is approximately 1 eV per unit λ (Sec. 3.7.3). However, this shift, typically up to $\sim$ 10 eV, is small compared to the spacing between peaks (e.g., 150 eV at 150 V bias) and therefore has a no effect on the determination of peak order.

3.7.2 LED Data Filtering

An energy-dependent χ^2 selection is applied to reject pulses inconsistent with the single-phonon pulse template used in the OFL reconstruction. In LED calibration data, this cut primarily removes burst and pile-up events. Figure 3.29 shows the reduced χ^2 (χ^2/n.d.f.) as a function of reconstructed energy. Populations at elevated χ^2 values are dominated by correlated pile-up events occurring in the tail of preceding pulses. These distort the pulse shape and bias the reconstructed energy, making their removal essential for reliable calibration.

To construct a robust energy-dependent χ^2 cut, LED series with different mean photon numbers (λ) were combined for each detector to provide sufficient statistics across the full spectral range. An approximate first-order calibration was obtained from the position of the first e^-h^+ peak. Using this calibration, events were selected in narrow windows around each resolved e^-h^+ peak, and their χ^2/n.d.f. distributions were studied.

For each peak, the χ^2/n.d.f. distribution was modeled with a Gaussian plus constant to describe the core population and residual background. The acceptance region was defined as the mean $\pm 2\sigma$ of the Gaussian component, providing a balance between signal efficiency and pile-up rejection. The resulting acceptance boundaries, evaluated at multiple e^-h^+ peak energies, were parameterized with a smooth polynomial function of energy to define the final energy-dependent χ^2 selection. Events with χ^2/n.d.f. above this threshold are rejected.

Figure 3.30 shows the LED spectrum before and after applying the energy-dependent χ^2 cut for the NFC1 detector. The corresponding passage fractions are 72% for NFH, 24% for NFC1, and 56% for NFC2.

3.7.3 Study of Cross Talk Amplitude and Surface Trapping Effect

The zeroth peak in the energy spectrum corresponds to the photons that do not undergo Luke amplification. We observed an offset for the zeroth peak in LED spectrum. This offset depends on the λ of the series. Two effects contribute to the zeroth peak offset: (a)

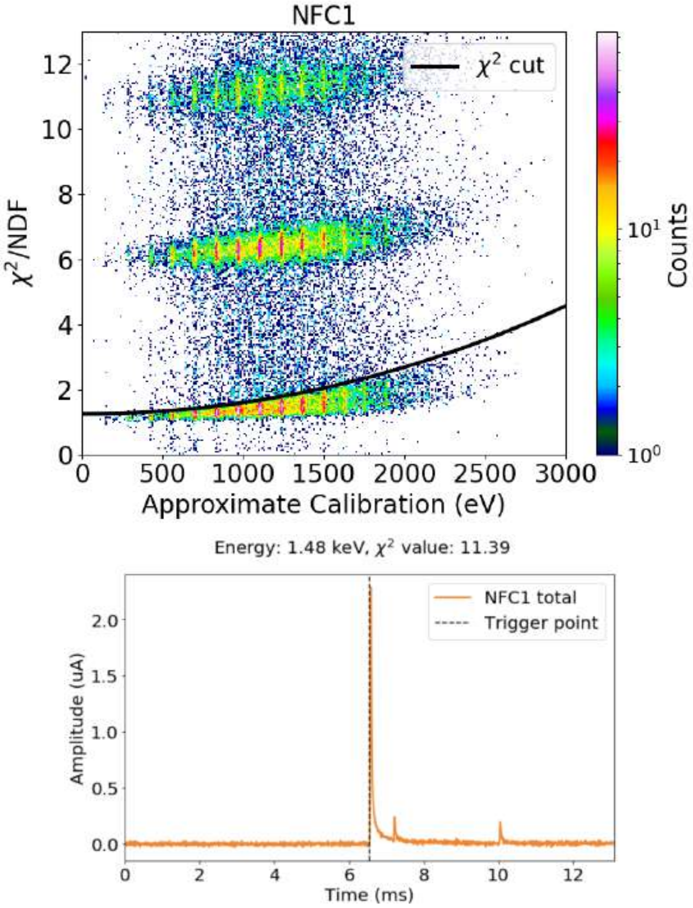

FIGURE 3.29: (top) Reduced χ^2 from the frequency-domain OFL fit as a function of reconstructed energy for the high-voltage LED calibration series in the NFC1 detector. High-χ^2/n.d.f. populations are dominated by pile-up events. (bottom) Example of events rejected by the χ^2 selection.

the Cross Talk Amplitude (CTA) and (b) the Surface Trapping Effect.

Parameterizing the LED Intensity

The LED intensity is measured by the λ value of the series, which is obtained from the experimental LED spectrum. We used high-intensity LED data to study the detector response in the keV range. To determine the lambda values for the calibration series, a Gaussian function is fit to the quantized e^-h^+ pair peaks in the OFL spectrum. The

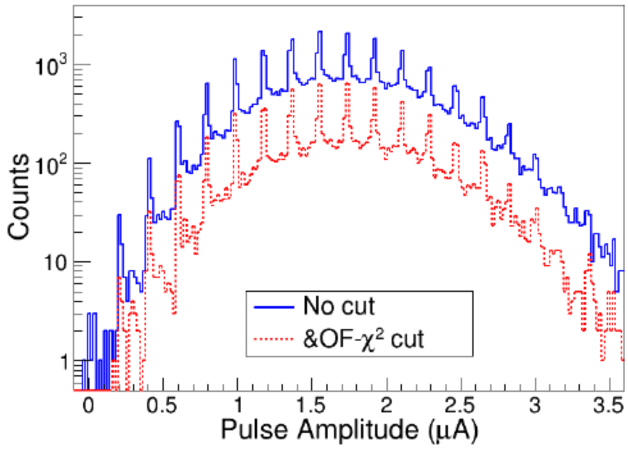

FIGURE 3.30: OFL spectrum before and after the energy-dependent χ^2 selection for the LED calibration series in the NFC1 detector. Adapted from Ref. [5].

amplitudes of each of the e$^-$h$^+$ pair peaks are then obtained from the Gaussian fit. A Poisson function is then fit (Fig. 3.31) to the data points to extract the Poissonian mean λ, which measures the LED intensity. It was found that the calibration series has $\lambda \sim O(10)$.

Quantifying CTA and Surface Trapping Coefficient

LED photons with energies of approximately 2 eV are absorbed within a few microns of the Si surface due to their short absorption length. As a result, a fraction of the generated charge carriers may fail to drift across the full applied electric field due to recombination. These incomplete events do not undergo full NTL amplification, depositing only the photon energy, and therefore introduce a systematic shift in the LED spectrum.

Experimentally, a shift in the zeroth e^-h^+ peak is observed as the LED intensity (characterized by λ) is varied, as shown in Fig. 3.32. The dependence of the average zeroth-peak position on λ is well described by a linear relation,

$$\bar{A}_{\text{offset}} = m\lambda + n, \tag{3.9}$$

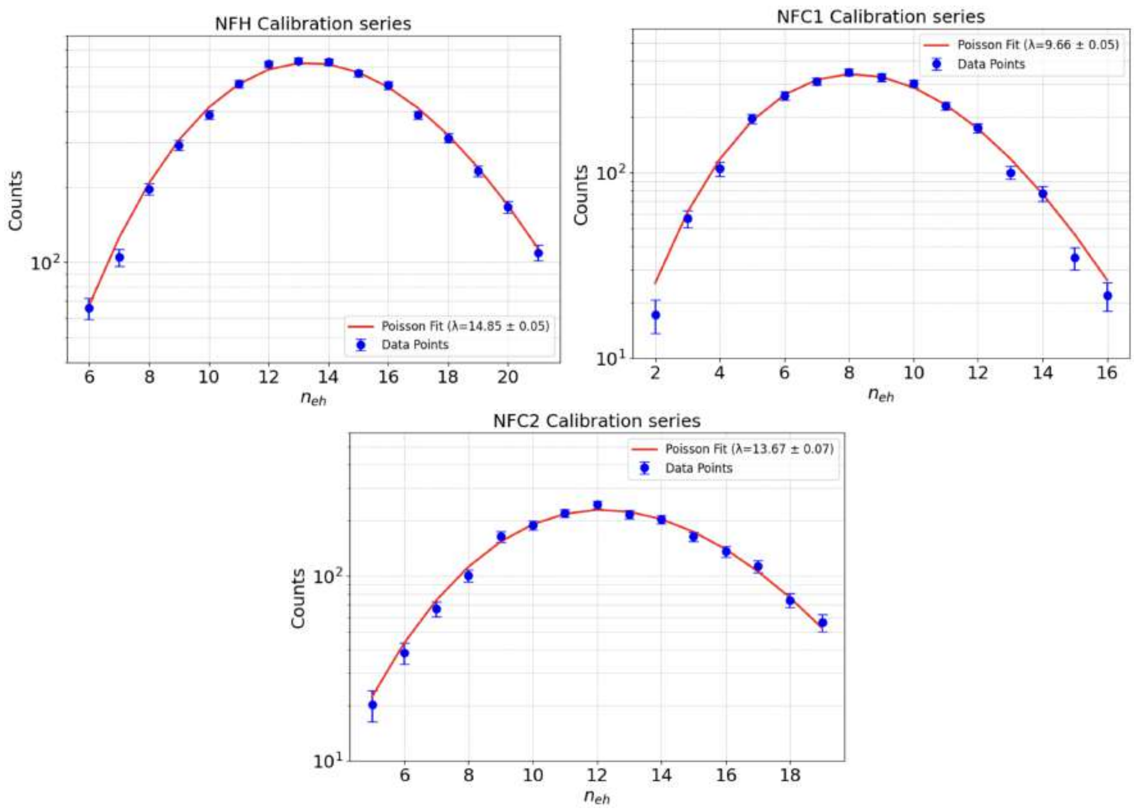

FIGURE 3.31: Determination of λ values for high lambda LED series at 150V bias voltage. The fit parameters shows the λ values for corresponding LED calibration series.

where the slope m quantifies the intensity-dependent shift and the intercept n represents an intensity-independent contribution. The intercept arises from electrical cross-talk between the LED drive lines and the detector readout and defines the *cross-talk amplitude*. The CTA produces a constant offset in current units and is determined from the y-intercept of the linear fit. All pulse amplitudes are corrected for this effect before further analysis.

The slope m is defined as the *surface trapping coefficient*. It measures the spectral shift per unit λ attributable to incomplete charge transport. Physically, this effect can be understood as a fraction of the generated e^-h^+ pairs recombining due to their initial random trajectories and thus failing to traverse the full electric field, as supported by G4CMP simulations [16].

Statistically, the number of absorbed LED photons follows a Poisson distribution with mean λ_{true}. Each absorbed photon has an independent probability f_{trap} of being surface-trapped and therefore failing to produce a drifting e$^-h^+$ pair. Under this process, the number of trapped photons also follows a Poisson distribution [16] with mean

$$\lambda_{\text{trapped}} = f_{\text{trap}}\, \lambda_{\text{true}}. \tag{3.10}$$

The remaining photons generate e$^-h^+$ pairs that drift across the applied field and undergo full NTL amplification. The mean number of such amplified events is therefore referred to as λ of the LED series.

Therefore,

$$\lambda_{\text{true}} = \lambda + \lambda_{\text{trapped}}.$$

As can be seen in Eq. 3.10, the mean number of trapped photons does not depend on the observed peak order n_{eh}. Furthermore, the variance associated with the trapped component is small compared to the intrinsic energy resolution of the detector [16]. Consequently, the dominant observable effect is an approximately uniform shift of the entire LED spectrum by the mean offset energy $\bar{E}_{\text{offset}}$.

Impact of Surface Trapping on LED Calibration

At high LED intensities ($\lambda \sim O(10)$), the zeroth e^-h^+ peak is often not clearly visible in the spectrum. In this regime, its position can be inferred by extrapolating the linear dependence of the peak offset on λ, as described in Eq. 3.9. To validate that this linear scaling remains applicable at large λ, higher-order e^-h^+ peaks that are visible in both low- and high-λ data sets were examined.

The offset of the second and third e^-h^+ peak as a function of λ is shown for NFC1 in Fig. 3.33 (top left and right). A clear linear dependence is observed, consistent with the

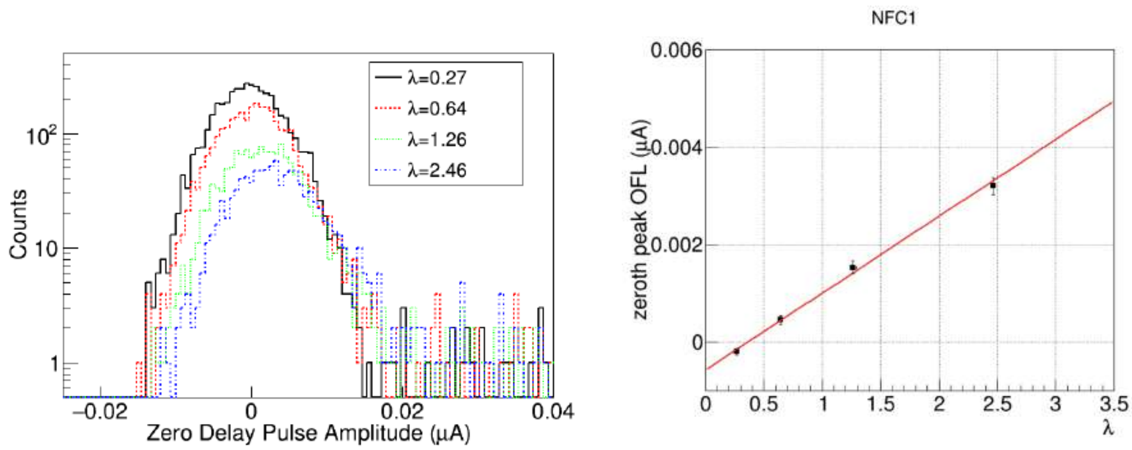

FIGURE 3.32: **Left**: Zeroth peak of the LED spectrum in the OFL estimator for different λ values in NFC1 detector. **Right**: Linear dependence of the zeroth-peak offset on λ in NFC1.

surface-trapping model. Similar behavior is found for other HVeVs. The slopes extracted from linear fits to the peak displacement define the quantity $A_{\text{offset}}/\lambda$, expressed in pulse-amplitude units. These slopes are shown in Fig. 3.33 (top right) for several e^-h^+ peaks. The agreement of $A_{\text{offset}}/\lambda$ across different peak orders within a given detector demonstrates that the spectral shift can be explained well by the surface trapping hypothesis.

To express the surface-trapping effect in physical energy units, the equivalent energy shift of the zeroth peak, $\bar{E}_{\text{offset}}$, is calculated as

$$\bar{E}_{\text{offset}} = \frac{152 \text{ eV}}{(A^1_{\text{OF}} - A^0_{\text{OF0}})} \times m\lambda, \tag{3.11}$$

where 152 eV corresponds to the total phonon energy from a single absorbed photon including the additional NTL amplification, i.e., the energy separation between successive e^-h^+ peaks. The quantities A^1_{OF} and A^0_{OF0} represent the mean cross-talk-corrected optimal-filter amplitudes of the first and zeroth e^-h^+ peaks, respectively. The term $m\lambda$ denotes the extrapolated zeroth-peak shift (in pulse-amplitude units) due to surface trapping, obtained from Eq. 3.9. The prefactor in Eq. 3.11 provides a linear conversion from amplitude to energy. The resulting energy-equivalent offsets for several LED data sets are summarized in Table 3.6.

TABLE 3.6: Energy offset in the LED spectrum arising from surface trapping. The measured ratio $\bar{E}_{\text{offset}}/\lambda$ is approximately 1 eV, implying an expected total shift of ~10–15 eV for high-intensity calibration series.

Detector	λ	$\bar{E}_{\text{offset}}$ **(eV)**
NFH	14.85 ± 0.05	16 ± 2
NFC1	9.66 ± 0.05	10.6 ± 0.7
NFC2	13.67 ± 0.07	13 ± 4

The bottom panel of Fig. 3.33 shows the corresponding quantity $E_{\text{offset}}/\lambda$, obtained by converting $A_{\text{offset}}/\lambda$ into calibrated energy units. The measured shift is approximately 1.1 eV per unit λ, with consistent values across detectors. For calibration data with $\lambda \sim O(10)$, this implies a total energy shift of order $O(10\text{ eV})$.

3.7.4 Working Point Alignment and Corrections

During LED Run 14 (R14), the addition of the LED box to the payload (absent in NEXUS R13) introduced a change in the parasitic resistance of the detector readout circuit of approximately $O(100\ \mu\Omega)$. This modification altered the current scale of the detector response, defined by the position of the first e^-h^+ peak in units of current (μA). Consequently, an identical working point (WP) on the superconducting transition curve (R–T curve) in R13 and R14 does not correspond to the same current scale.

To enable a direct comparison between the R14 high-voltage LED calibration and the R13 ^{137}Cs 0 V calibration data, the current scales must be matched. Since the detector current scale depends on the chosen WP along the R–T transition, a dedicated WP scan was performed in the R14 LED data by varying the QET bias. This procedure allowed identification of WPs that produce current scales comparable to those observed in R13.

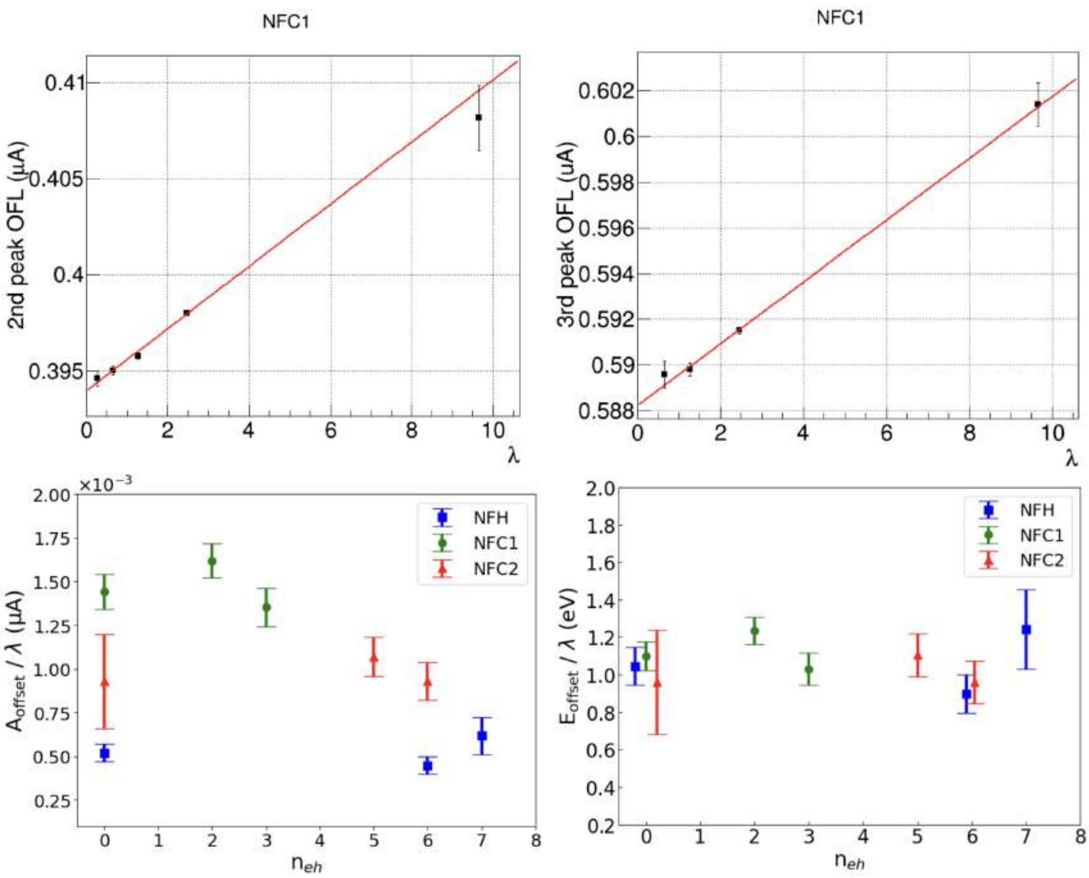

FIGURE 3.33: **Top left and Top right**: Offset of the second and third e^-h^+ peak as a function of λ for NFC1, demonstrating the linear scaling predicted by Eq. 3.9. **Bottom left**: Extracted slope $A_{\text{offset}}/\lambda$ for multiple e^-h^+ peaks, expressed in pulse-amplitude units. **Bottom right** Corresponding slope converted to calibrated energy units, $E_{\text{offset}}/\lambda$, using Eq. 3.11. Adapted from Ref. [5].

After selecting a comparable WP, a linear working point correction was applied to align the current scales between runs. The validity of the linear approximation was evaluated by estimating the associated systematic uncertainties, which were found to be at the level of a few percent.

Three working points were used in this study: WP1 (lowest current scale), WP3 (intermediate current scale), and WP2 (highest current scale). As illustrated in Fig. 3.34, WP3 lies between WP1 and WP2 in terms of current scale. The high-λ LED series at

WP3 was used for the primary energy calibration, while the corresponding high-λ series at WP1 and WP2 were used to evaluate systematic uncertainties associated with the linear WP correction.

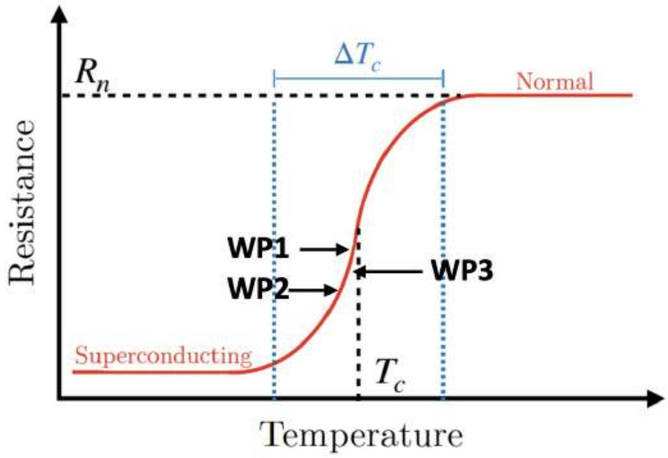

FIGURE 3.34: Illustration of different working points (WPs) along the superconducting R–T transition curve. Points lower on the transition correspond to a higher current scale (i.e., a larger first e^-h^+ peak position in current units). WP2 corresponds to the highest current scale, WP3 to an intermediate current scale, and WP1 to the lowest current scale.

Current Scale Determination for R13 and R14 data

The detector current scale (gain) is defined by the position of the first e^-h^+ peak in the LED spectrum at a given WP and bias voltage. Any change in the detector WP directly affects the measured current gain.

For LED and low-background data, the current scale is defined as

$$\text{Current Scale}_{\text{R14 LED}} = A^1_{\text{OFL}} - A^0_{\text{OF0}}, \tag{3.12}$$

$$\text{Current Scale}_{\text{R13}} = A^1_{\text{OFL}}. \tag{3.13}$$

Here, the superscripts 1 and 0 denote the first and zeroth e^-h^+ peaks, respectively. For R14 LED data, the zeroth peak is clearly visible and is subtracted to correct for the surface-trapping offset. In contrast, for R13 Cs data, no surface-trapping effect is observed, and the position of the first peak alone defines the scale.

Linear Working Point Correction

To apply the LED calibration to the R13 Cs spectrum, the R14 LED current scale must be matched to the R13 current scale. Since the R13 Cs data were acquired at 0 V and do not show a resolved $e^- h^+$ peak pair, we use 100 V low-background data as a proxy for the R13 current scale. The R14 calibration series was taken at 150 V to maximize energy coverage.

Because R13 and R14 were taken at different bias voltages, their gains differ due to the Luke phonon amplification. Therefore, the relative HV gain must first be determined.

The WP correction factor is defined as

$$\text{WP correction factor} = \frac{\text{Current Scale}_{\text{R13 (100V)}} \times \text{Relative HV Gain}}{\text{Current Scale}_{\text{R14 (150V)}}}. \tag{3.14}$$

The relative HV gain was measured using R14 LED data taken at 100 V and 150 V. An energy-independent χ^2 cut was applied to remove pulses with burst-like tails. The positions of distinct $e^- h^+$ peaks were then extracted for both voltages.

The ratio of corresponding peak positions was plotted as a function of n_{eh} and fitted with a constant to obtain the relative HV gain. An example for the NFC1 detector is shown in Fig. 3.35.

The extracted values are:

- NFC1: 1.479 ± 0.001
- NFC2: 1.478 ± 0.001
- NFH: 1.49 ± 0.003

The theoretical expectation of Luke gain ratio is

$$\frac{1 + 150/3.8}{1 + 100/3.8} \approx 1.4816,$$

.

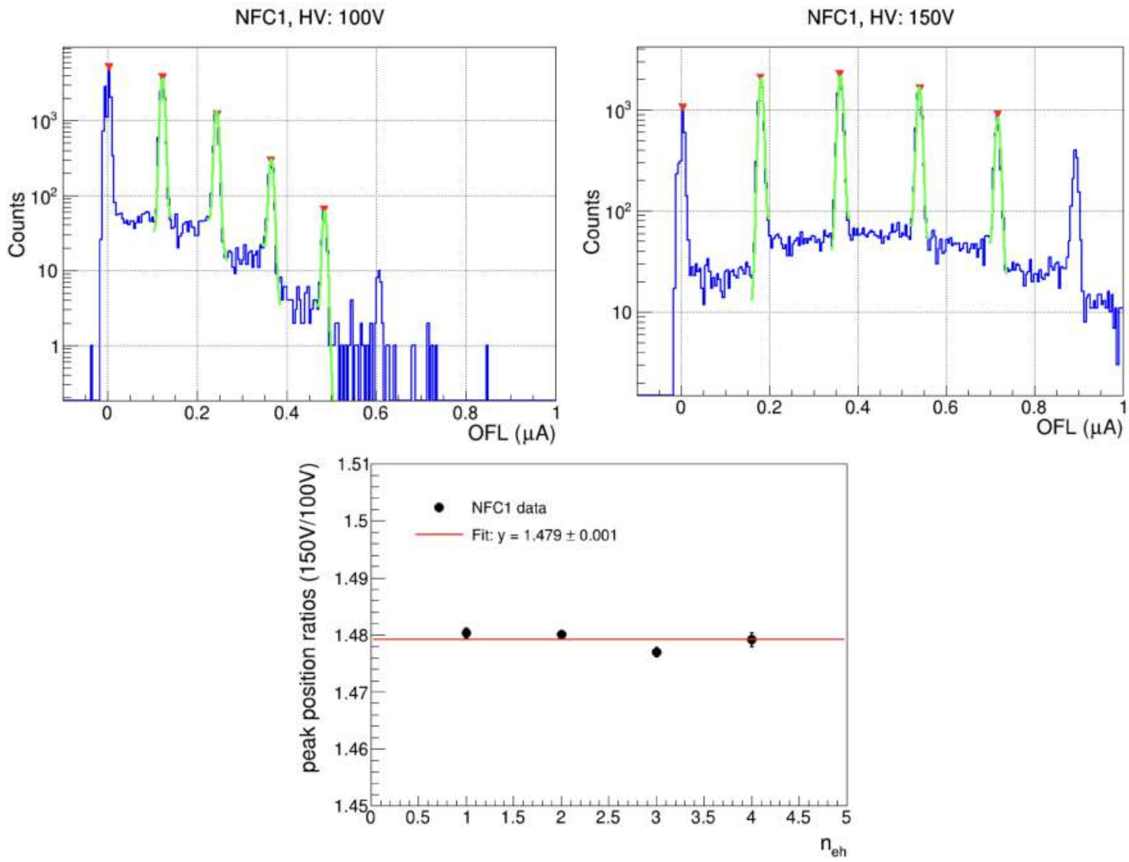

FIGURE 3.35: Relative HV gain determination for the NFC1 detector. **Top left**: LED spectrum at 100 V after χ^2 cut. **Top right**: LED spectrum at 150 V after χ^2 cut. **Bottom**: Peak ratio as a function of n_{eh} used to extract the relative HV gain.

The final WP correction factors are shown in Tab. 3.7. These factors are applied to the R14 calibration LED data sets (WP3) to align it with the R13 Cs data.

TABLE 3.7: Summary of WP correction parameters for each detector.

Detector	R14 LED 150 V (μA)	R13 100 V Low-BG (μA)	Relative HV Gain	WP Correction Factor
NFH	0.0757 ± 0.0001	0.0527 ± 0.0001	1.490 ± 0.003	1.026 ± 0.003
NFC1	0.199 ± 0.001	0.1385 ± 0.0001	1.479 ± 0.001	1.028 ± 0.001
NFC2	0.1472 ± 0.0001	0.09262 ± 0.00006	1.478 ± 0.001	0.930 ± 0.001

Effect of Non-Linearities in the Linear Working Point Correction

The linear WP correction assumes that small shifts along the superconducting transition curve produce proportional changes in the detector current scale. However, the detector response may exhibit mild non-linearities, particularly in the keV region. We therefore evaluate the validity of the linear approximation.

To study this effect, LED data were analyzed at three working points: WP1 (lowest current scale), WP3 (intermediate), and WP2 (highest current scale). The LED high-λ calibration series corresponds to WP3. As shown in Fig. 3.36 (left), WP3 lies between WP1 and WP2 in terms of current scale.

We first applied a forced calibration to the WP1 and WP2 data sets using the calibration function derived from the WP3 LED spectrum. This allowed conversion of the current scales into an equivalent energy scale. Differences in the reconstructed energies of individual e^-h^+ peaks among the three WPs provide a direct estimate of the variation in current scale.

Next, linear WP correction factors were derived from the ratios of the e^-h^+ peak positions (in current units) between different WPs and applied to the respective data sets. The residual differences in reconstructed energies after applying the correction quantify the non-linear component of the response.

As shown in Fig. 3.36 (right), the residual deviations are at the level of $\sim O(1\%)$ across the calibration range. This demonstrates that a linear WP correction is sufficient to match the current scales in the keV region, with only small residual non-linear effects.

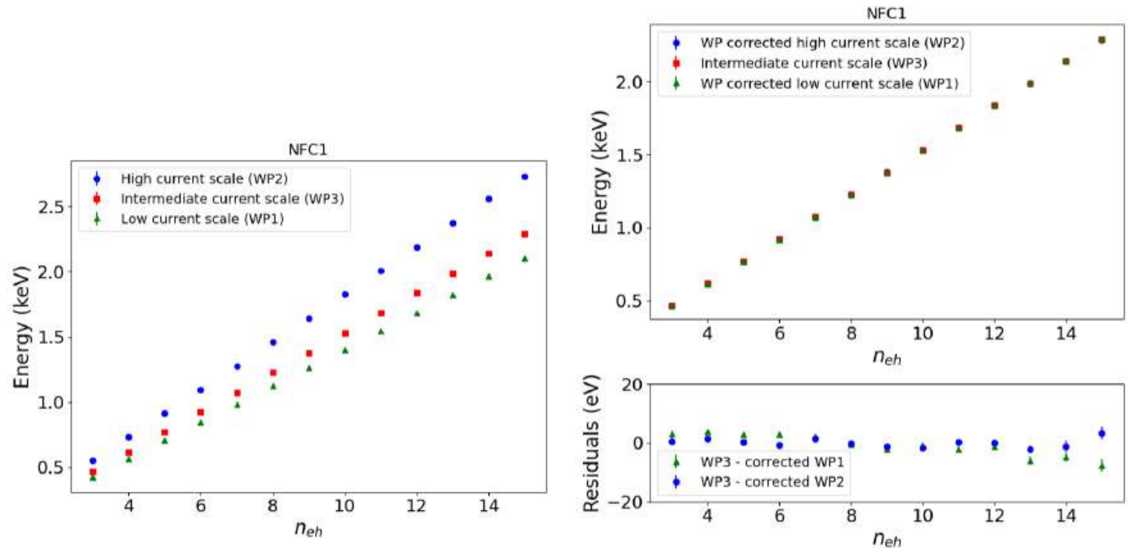

FIGURE 3.36: Energy differences among different working points before (left) and after (right) applying the linear WP correction. The residual deviations after correction are at the $\sim 1\%$ level.

3.7.5 HV Energy Calibration Using LED

Having established that the linear WP correction is adequate, the correction factors are applied to the LED data to align the current scale with the R13 Cs 0 V data. The energy calibration is then performed using the WP-corrected OFL pulse amplitude.

The calibration curve is parameterized as a quadratic function:

$$E_{\mathrm{cal}}(A^c_{\mathrm{OFL}}) = p_0 A^c_{\mathrm{OFL}} + p_1 \left(A^c_{\mathrm{OFL}}\right)^2, \tag{3.15}$$

where A^c_{OFL} denotes the WP-corrected OFL pulse amplitude used for the LED calibration series.

The expected energy of the n^{th} e^-h^+ peak is

$$E_n = n\left(E_\gamma + eV_{\mathrm{bias}}\right) + E_{\mathrm{offset}}, \tag{3.16}$$

where E_γ is the LED photon energy, eV_{bias} is the Luke phonon contribution per carrier pair, and E_{offset} accounts for surface trapping effects.

The associated X and Y statistical uncertainties on the LED calibration data points are defined as $\Delta E_n = \Delta E_{\text{offset}}$, and $\Delta A^c_{\text{OFL}} = \sqrt{\sigma^2_{\text{WP}} + \sigma^2_{\text{CTA}}}$.

The resulting LED energy calibration curves are shown in Fig. 3.37. The residuals are at the level of $\sim 1\%$, which is taken as the systematic uncertainty associated with the calibration function.

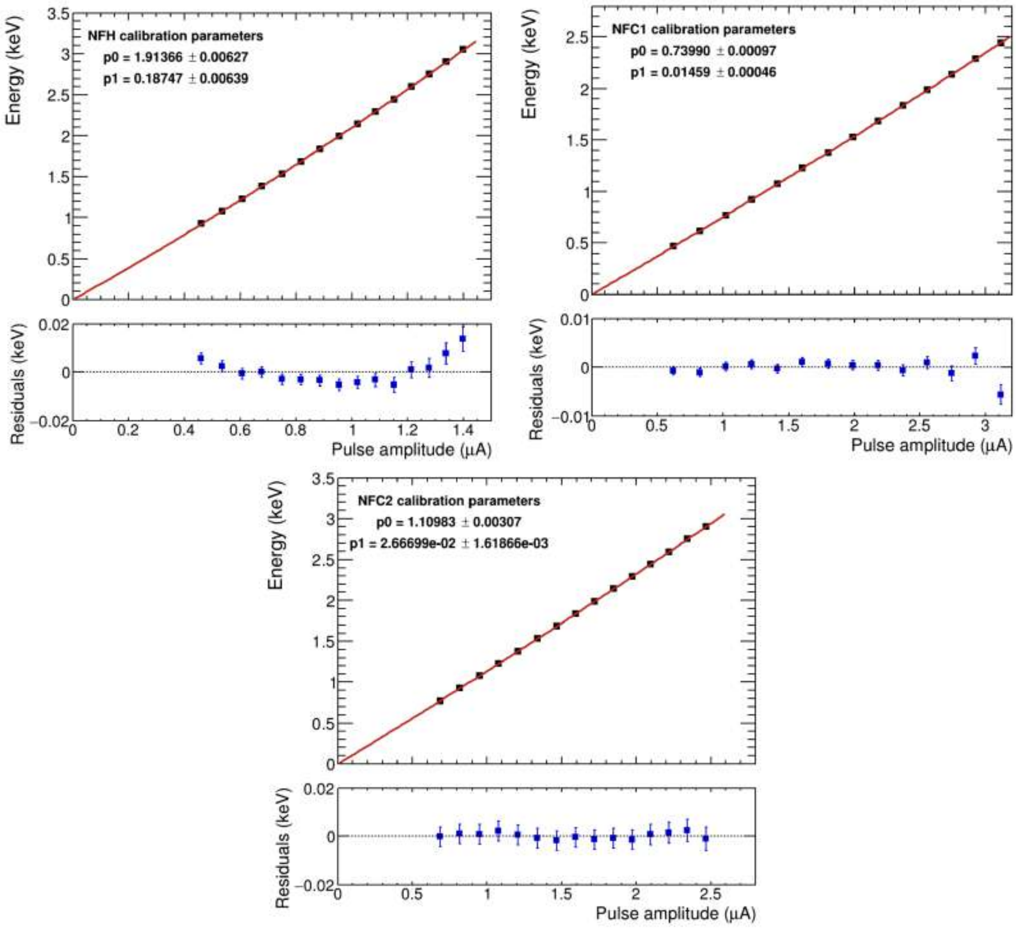

FIGURE 3.37: Energy calibration using the WP-corrected OFL amplitude for different HVeV detectors.

Statistical Uncertainty from the Energy Calibration Fit

The statistical uncertainty on the calibrated energy originates from the uncertainties on the fit parameters p_0 and p_1. These are propagated using the covariance matrix returned by the fit.

For a given corrected amplitude A^c_{OFL}, the variance on the calibrated energy is obtained via standard error propagation:

$$\text{Var}[E_{\text{cal}}] = \begin{bmatrix} A^c_{\text{OFL}} & \left(A^c_{\text{OFL}}\right)^2 \end{bmatrix} \mathbf{C} \begin{bmatrix} A^c_{\text{OFL}} \\ \left(A^c_{\text{OFL}}\right)^2 \end{bmatrix}, \tag{3.17}$$

where $\mathbf{C}$ is the covariance matrix of the fit parameters:

$$\mathbf{C} = \begin{bmatrix} \text{Var}(p_0) & \text{Cov}(p_0, p_1) \\ \text{Cov}(p_1, p_0) & \text{Var}(p_1) \end{bmatrix}. \tag{3.18}$$

Explicitly, the statistical uncertainty on the calibrated energy is

$$\sigma_{\text{stat}}(E_{\text{cal}}) = \sqrt{\sigma^2_{p_0} \left(A^c_{\text{OFL}}\right)^2 + \sigma^2_{p_1} \left(A^c_{\text{OFL}}\right)^4 + 2 \left(A^c_{\text{OFL}}\right)^3 \text{Cov}(p_0, p_1)}. \tag{3.19}$$

Systematic Uncertainty from Linear WP Correction

The systematic uncertainty from the linear WP correction is the dominant contribution to the LED calibration uncertainty. Residual deviations after applying the linear WP correction (Fig. 3.36) are propagated as systematic uncertainty. For each prominent e^-h^+ peak, the deviation relative to the WP3 calibrated scale is evaluated, and the maximum deviation across the calibration range is taken as a conservative estimate. This contribution is $O(10\,\text{eV})$.

Systematic Uncertainty from the Energy Calibration Function

An additional systematic uncertainty arises from the choice of the quadratic parameterization used to describe the relationship between the calibrated energy and the WP- and CTA-corrected OFL amplitude, A^c_{OFL}.

The measured e^-h^+ peak energies exhibit small deviations from the quadratic calibration curve. These residuals quantify how well a second-order polynomial describes the data and effectively capture any potential higher-order (non-quadratic) contributions that are not explicitly modeled in the fit. To conservatively account for this effect, the maximum absolute residual observed in Fig. 3.37 is assigned as the systematic uncertainty associated with the calibration function. This contribution is found to be approximately 10 eV.

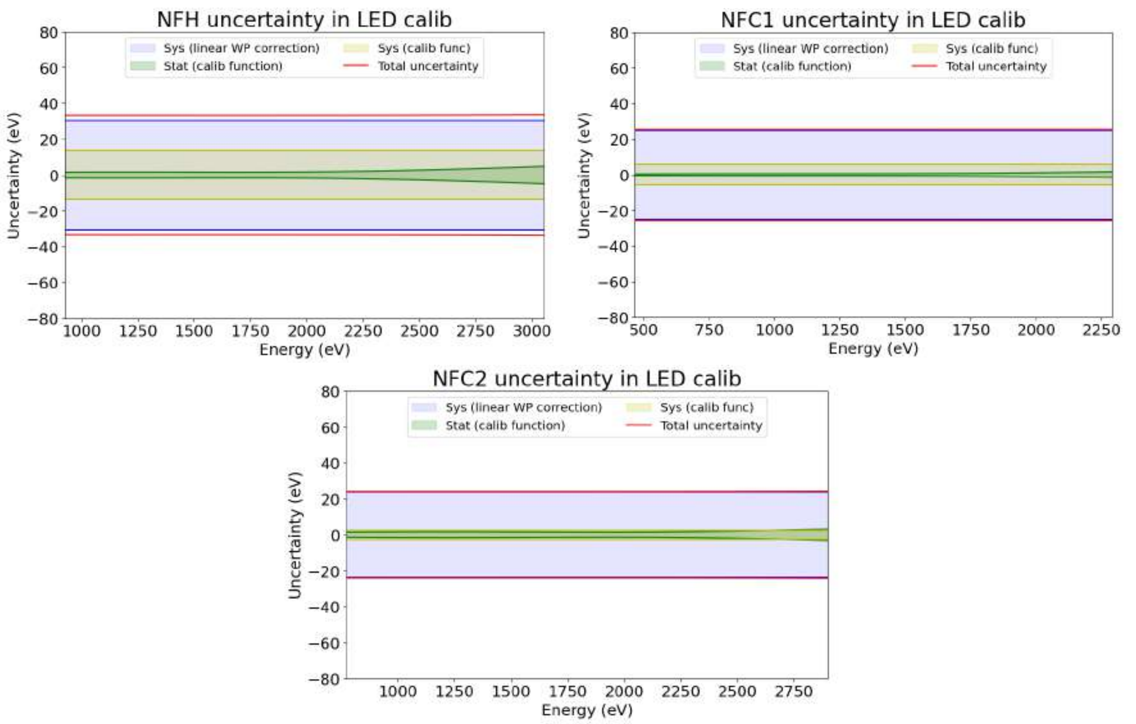

FIGURE 3.38: Total uncertainty arising from LED energy calibration as a function of energy. The dominant contribution originates from the linear WP correction.

TABLE 3.8: Energy calibration factors for HV LED calibration of the A_{OF} estimator.

Detector	p_0 (keV/μA)	p_1 (keV/(μA)^2)
NF-H	1.90 ± 0.04	0.20 ± 0.04
NF-C1	0.74 ± 0.01	0.014 ± 0.006
NF-C2	1.11 ± 0.02	0.027 ± 0.008

Total Uncertainty

The total uncertainty is computed as the quadrature sum of all statistical and systematic contributions. The dominant component arises from the linear WP correction. The overall uncertainty is approximately $O(10\,\mathrm{eV})$ across the calibration range, as shown in Fig. 3.38.

The calibration parameters for the HV LED calibration functions, including total uncertainties, are listed in Table 3.8.

3.8 0V–HV Calibration Comparison

Figure 3.39 displays the combined calibration points derived from the WP-corrected LED spectrum at HV bias and from the ^{133}Cs Compton spectrum at 0 V bias. A clear calibration difference in detector response is observed between the 0 V calibration points and the HV LED calibration points.

3.8.1 0V → HV Calibration Scaling Parameter

The calibration difference is quantified by introducing a single multiplicative scale parameter relating the HV calibration function to the 0 V calibration points.

Let $f_{\mathrm{calib}}^{\mathrm{HV}}(A)$ denote the quadratic HV calibration function obtained from the LED data. The 0 V calibration function is modeled as

$$f_{\mathrm{calib}}^{0V}(A) = \frac{1}{C_0} f_{\mathrm{calib}}^{\mathrm{HV}}(A), \tag{3.20}$$

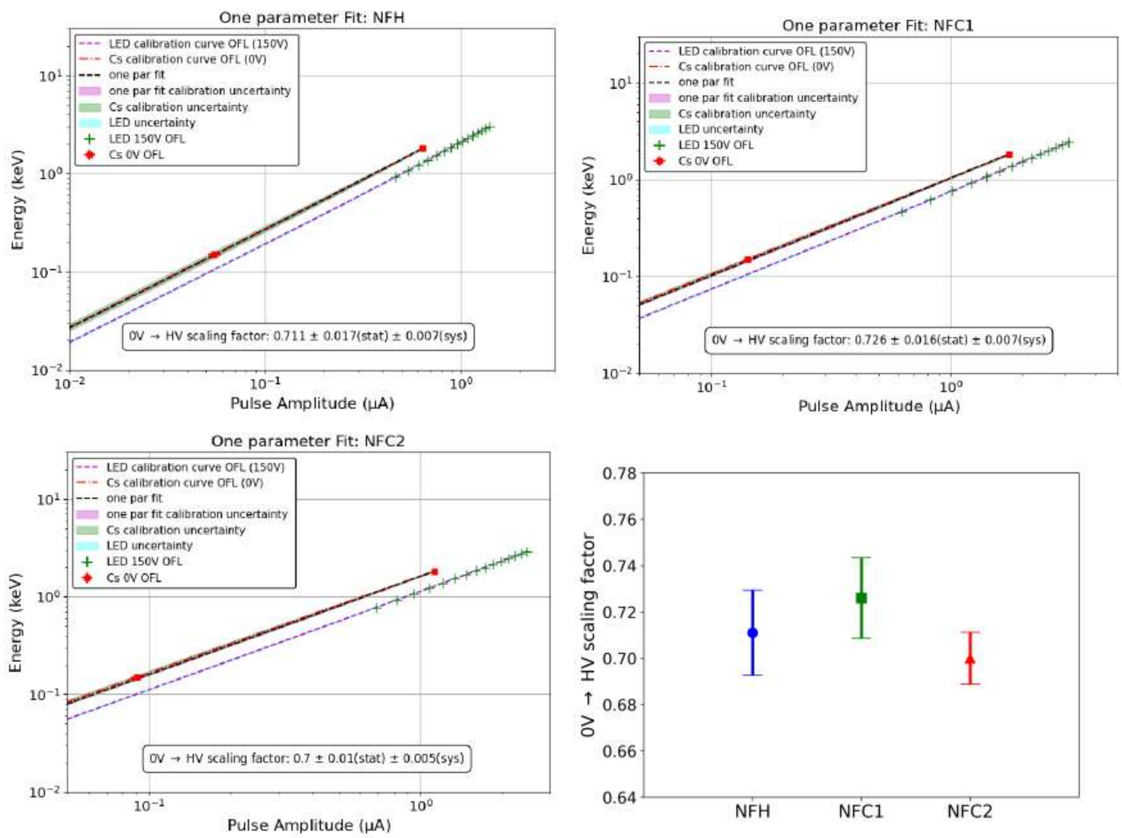

FIGURE 3.39: Scaling between 0 V and HV calibration determined from a one-parameter fit for the three HVeV detectors. The bottom-right panel compares the extracted scaling parameters, which are consistent across detectors within uncertainties.

The Cs 0 V calibration data points are fitted using this one-parameter model, keeping the shape of the HV quadratic calibration fixed and allowing only an overall normalization change. The best-fit value of C_0 serves as the nominal measure of the detector response difference between 0 V and HV operation. The $1/C_0$ value scales HV calibration to return 0 V calibration.

The dashed black curves shown in the first three panels of Fig. 3.39 correspond to the result of this one-parameter fit. The consistency of scaled HV calibration curve with the 0 V calibration curve indicates that the calibration difference can be well described by a single, energy-independent scaling factor up to the keV scale. Table 3.9 summarizes the relative percentage differences between the 0 V and HV calibrations, taking the 0 V calibration as the reference.

TABLE 3.9: Relative percentage difference between the 0 V and HV calibrations for different HVeV detectors, using the 0 V calibration as the reference [5].

Detector	Calibration difference (%)	Stat. (%)	Sys. (%)
NF-H	29 ± 2	1.7	0.7
NF-C1	27 ± 2	1.6	0.7
NF-C2	30 ± 1	1.0	0.5

From this procedure, we observe an approximately 30% difference in the calibrated energies at HV relative to the 0 V energy scale.

The bottom-right panel of Fig. 3.39 compares the extracted scaling parameters for all three HVeV detectors. The scaling factors are consistent within uncertainties, suggesting that the detector response difference is common across the devices.

The HV LED calibration carries both statistical and systematic uncertainties, which propagate into the scaling parameter.

To determine the systematic uncertainty associated with the HV calibration, the LED calibration curve is randomly sampled within its total uncertainty while accounting for correlations between calibration parameters. For each sampled calibration curve, the one-parameter scaling fit to the 0 V data is repeated, yielding a corresponding value of the scaling, C_0.

This procedure produces a distribution of scaling parameters. The spread of this distribution is taken as the systematic uncertainty on C_0. This systematic contribution is combined in quadrature with the statistical uncertainty from the nominal one-parameter fit.

An additional HV calibration point is obtained from the first e^-h^+ pair peak observed in background data at 100 V bias. This peak corresponds to an energy of approximately

101.1 eV, composed of 100 eV Luke phonon energy plus the band-gap recombination energy.

As shown in Fig. 3.40, this independent calibration point lies on the HV LED calibration curve, providing additional validation of the HV energy scale and supporting the robustness of the extracted calibration difference.

3.8.2 Possible Physical Origin of the Detector Response Difference

Although the exact origin of the 0 V–HV calibration difference is not yet fully understood, several mechanisms may contribute [10]:

- At 0 V bias, the TES primarily senses prompt (primary) phonons generated directly by the recoil interaction and by e^-h^+ pair recombination. In contrast, at HV bias, a substantial fraction of the measured signal arises from NTL phonons generated during charge drift. Differences in phonon production, propagation, and collection efficiency between primary and Luke phonons may lead to a bias-dependent TES response.

- In Si, the average ionization energy is approximately 3.8 eV, while the band gap is about 1.1 eV. The excess energy (~2.7 eV, or about 70%) is promptly converted into phonons, which are sensed by the TES. Upon recombination, an e^-h^+ pair ideally releases energy equal to the band gap (~1.2 eV, or about 30%). However, full or partial recombination energy may not always be converted into detectable phonons, implying that the full band-gap energy may not be recovered in the phonon signal. This effect is expected to dominate at 0 V bias, where the signal is primarily composed of primary phonons. At HV bias, although recombination still occurs, the total signal is dominated by the much larger NTL phonon contribution, making this effect comparatively small. Consequently, the energy response at 0 V may differ from that at HV bias.

A similar calibration difference between 0 V and HV operation has been reported previously for NFC1 [10] in $\mathcal{O}$(keV) region. In that study, the 0 V calibration was based on surface X-ray interactions, whereas the present analysis uses bulk Compton interactions. The persistence of a comparable detector response difference in both cases suggests that the effect may be intrinsic to the detector response rather than solely related to interaction topology. A detailed investigation of the underlying mechanism is left for future work.

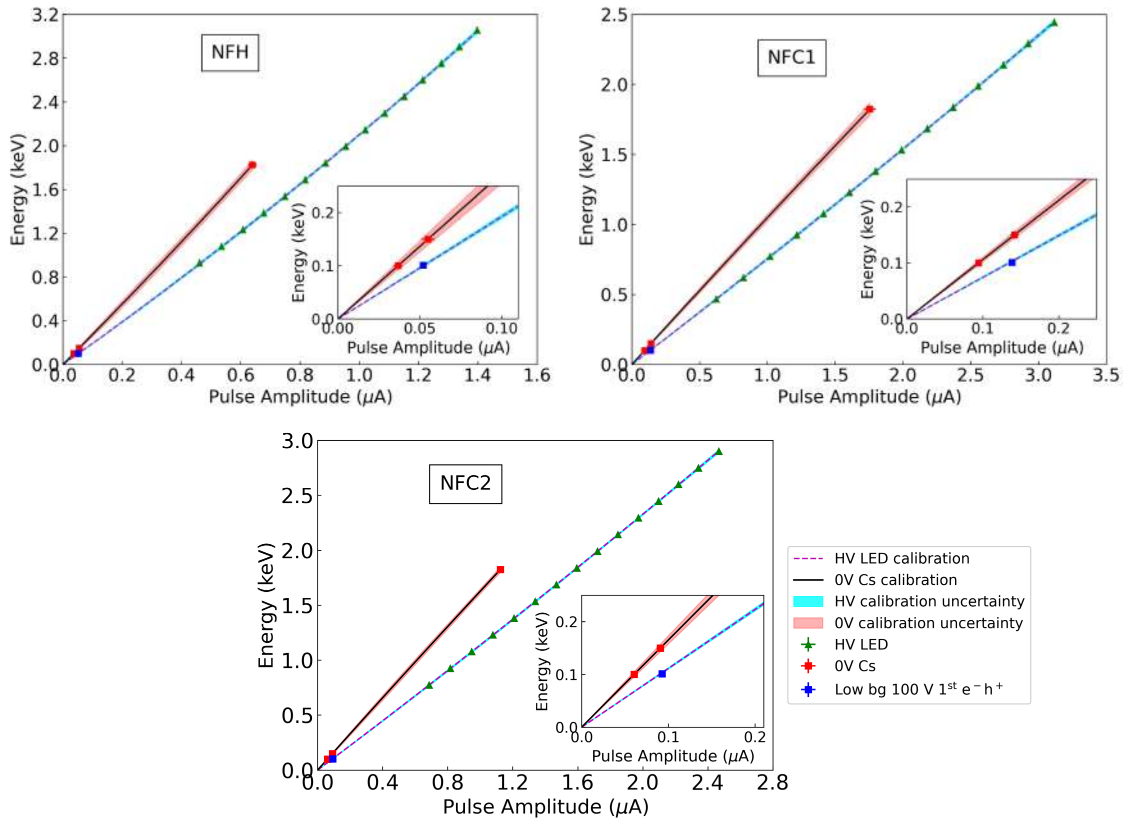

FIGURE 3.40: Energy calibration curves at 0 V and HV (150 V) bias for NFH, NFC1, and NFC2. A bias-dependent detector response difference is observed. Insets show the low-energy region of the calibration curves. Adapted from Ref. [5].

3.9 Conclusion and Outlook

We investigated the L-shell (0.1 keV and 0.15 keV) and K-shell (1.8 keV) Compton steps in Si HVeV detectors using ^{137}Cs data collected at 0 V detector bias. Using these features, we calibrated the energy scale of the detector at 0 V bias across the crystal. This study represents the first measurement of Si L-shell Compton steps in cryogenic phonon-sensitive calorimeters. The primary experimental challenges included excess low-energy background, which limited the statistical precision of the L-shell measurements, and non-linear detector response effects that become relevant in the keV region for the K-shell step.

A detailed study of the detector nonlinearity was performed up to the keV scale using HV LED calibration with bursts of ~2 eV optical photons. This calibration enabled precise characterization of the quadratic energy response in the keV regime and allowed a detailed investigation of surface trapping effects.

A clear calibration difference between 0 V and HV operation was observed and found to be consistent across the HVeV detectors. The HV calibration factor is approximately 30% smaller than the corresponding 0 V calibration factor, indicating a bias-dependent detector response for the same nominal phonon energy. Although the exact physical origin of this response difference is not yet fully understood, it is likely related to differences in TES sensitivity to primary phonons (dominant at 0 V) versus NTL phonons (dominant at HV bias), and/or incomplete conversion of e^-h^+ recombination energy into detectable phonons.

Future measurements with higher statistics Compton calibration datasets, together with improved modeling of core-hole effects in FEFF calculations, will help refine the low-energy response and validate the interpretation of the Compton step structure. In addition, dedicated experimental studies of phonon production and collection under different bias conditions will be essential to fully understand the observed calibration difference.

The Compton-step-based calibration framework developed in this study for cryogenic Si calorimeters is an important step toward enabling next-generation dark matter searches. In particular, the SuperCDMS experiment at SNOLAB will rely on a precise understanding of detector response at sub-keV energies to fully exploit the low energy threshold and excellent resolution of kg-scale HV detectors in the search for low-mass dark matter candidates.

Bibliography

[1] R Agnese, AJ Anderson, T Aramaki, I Arnquist, W Baker, D Barker, R Basu Thakur, DA Bauer, A Borgland, MA Bowles, et al. *Phys. Rev. D* 95.8 (2017), p. 082002.

[2] T Aralis, T Aramaki, Isaac J Arnquist, Elham Azadbakht, W Baker, Samir Banik, D Barker, Corey Bathurst, DA Bauer, LVS Bezerra, et al. “Constraints on dark photons and axionlike particles from the SuperCDMS Soudan experiment”. *Phys. Rev. D* 101.5 (2020), p. 052008.

[3] F Gasser and C Tavard. *Phys. Rev. A* 27.1 (1983), p. 117.

[4] K. Ramanathan et al. “Measurement of Low Energy Ionization Signals from Compton Scattering in a Charge-Coupled Device Dark Matter Detector”. *Phys. Rev. D* 96.4 (2017), p. 042002. arXiv: 1706.06053 [physics.ins-det].

[5] M. F. Albakry et al. “Low-energy calibration of SuperCDMS HVeV cryogenic silicon calorimeters using Compton steps”. *Phys. Rev. D* 112.9 (2025), p. 092014. arXiv: 2508.02402 [physics.ins-det].

[6] Arthur H. Compton. “A Quantum Theory of the Scattering of X-rays by Light Elements”. *Phys. Rev.* 21 (1923), pp. 483–502.

[7] Chen-Kai Qiao, Jian-Wei Wei, and Lin Chen. “An Overview of the Compton Scattering Calculation”. *Crystals* 11.5 (2021), p. 525.

[8] Sea Agostinelli, John Allison, K al Amako, John Apostolakis, H Araujo, Pedro Arce, Makoto Asai, D Axen, Swagato Banerjee, GJNI Barrand, et al. *Nucl. Instrum. Methods Phys. Res. A* 506.3 (2003), pp. 250–303.

[9] John J Rehr, Joshua J Kas, Fernando D Vila, Micah P Prange, and Kevin Jorissen. “Parameter-free calculations of X-ray spectra with FEFF9”. *Phys. Chem. Chem. Phys.* 12.21 (2010), pp. 5503–5513.

[10] R Ren, Corey Bathurst, YY Chang, R Chen, CW Fink, Z Hong, NA Kurinsky, N Mast, N Mishra, Valentina Novati, et al. *Phys. Rev. D* 104.3 (2021), p. 032010.

[11] E Klevak, FD Vila, JJ Kas, JJ Rehr, and GT Seidler. “Finite-temperature calculations of the Compton profile of Be, Li, and Si”. *Phys. Rev. B* 94.21 (2016), p. 214201.

[12] DW Amaral, T Aralis, T Aramaki, IJ Arnquist, E Azadbakht, S Banik, D Barker, C Bathurst, DA Bauer, LVS Bezerra, et al. “Constraints on low-mass, relic dark matter candidates from a surface-operated SuperCDMS single-charge sensitive detector”. *Phys. Rev. D* 102.9 (2020), p. 091101.

[13] E. Gatti and P. F. Manfredi. “Processing the Signals From Solid State Detectors in Elementary Particle Physics”. *Riv. Nuovo Cim.* 9N1 (1986), pp. 1–146.

[14] Ziqing Hong, Runze Ren, Noah Kurinsky, Enectali Figueroa-Feliciano, Lise Wills, Suhas Ganjam, Rupak Mahapatra, Nader Mirabolfathi, Brian Nebolsky, H. Douglas Pinckney, et al. “Single electron–hole pair sensitive silicon detector with surface event discrimination”. *Nucl. Instrum. Methods Phys. Res. A: Accelerators, Spectrometers, Detectors and Associated Equipment* 963 (2020), p. 163757.

[15] Karthik Ramanathan and Noah Kurinsky. “Ionization yield in silicon for eV-scale electron-recoil processes”. *Phys. Rev. D* 102.6 (2020), p. 063026.

[16] M. J. Wilson et al. “Improved modeling of detector response effects in phonon-based crystal detectors used for dark matter searches”. *Phys. Rev. D* 109.11 (2024), p. 112018. arXiv: 2403.01259 [physics.ins-det].

CHAPTER 4

Search for Axion-Like Particles and Dark Photons in SuperCDMS Soudan

Contents

4.1 Motivation

The absence of confirmed experimental evidence for Weakly Interacting Massive Particles (WIMPs) [1, 2] to date has motivated the exploration of alternative dark matter candidates, particularly in the low-mass regime. This largely unexplored region of parameter space, extending down to the keV/c^2 scale and below, provides an opportunity to probe new classes of dark matter. Among the well-motivated candidates in this mass range are axions and Axion-Like Particles (ALPs) [3, 4], as well as dark photons [5]. These particles could have been produced in the early Universe and may constitute a significant fraction of the present-day dark matter density.

Several direct-detection experiments have searched for these candidates in addition to WIMPs [6, 7]. Within the SuperCDMS program, such searches have been performed using ultra-pure germanium cryogenic detectors operated in CDMSlite (CDMSearch Low Ionization Threshold Experiment) or HV mode as well as in low-bias voltage mode at the Soudan Underground Laboratory [8]. In addition, High Voltage electron-volt (HVeV) detectors have been deployed at various test facilities [9, 10]. These studies have placed constraints on the couplings of ALPs and dark photons to Standard Model particles.

HVeV detectors are particularly sensitive to very low-mass dark matter due to their excellent energy resolution and extremely low energy thresholds, enabling sensitivity to masses of $\mathcal{O}(10\,\mathrm{eV}/c^2)$ and below. However, their gram-scale target mass limits the achievable exposure and therefore reduces sensitivity at higher masses. In contrast, the kilogram-scale CDMSlite detectors operated at SuperCDMS Soudan provide significantly larger exposures, making them well suited to probe dark matter masses in the range $\mathcal{O}(100\,\mathrm{eV}/c^2)$ to $\mathcal{O}(10\,\mathrm{keV}/c^2)$, despite their relatively higher energy thresholds.

Previous SuperCDMS analyses searching for ALPs and dark photons adopted conservative approaches in which upper limits on the axio-electric coupling (g_{ae}) and the dark photon kinetic mixing parameter (ϵ) were derived without explicitly modeling background contributions [8]. The resulting exclusion limits on g_{ae} and ϵ are shown in Fig. 4.1.

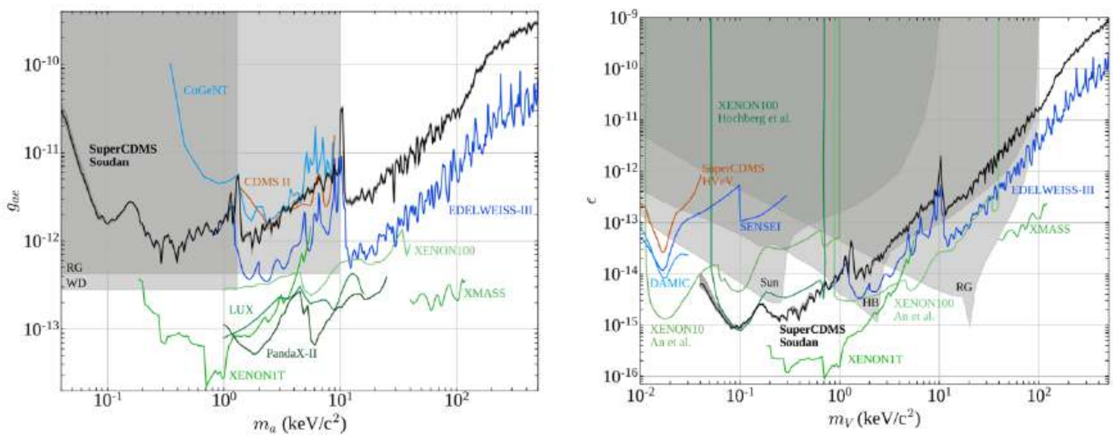

FIGURE 4.1: Exclusion limits on ALPs (left) and dark photons (right) from the SuperCDMS Soudan experiment (in black solid lines). Limits from other direct detection experiments and astrophysical constraints are also shown. Adapted from Ref. [8].

PLR

The limits obtained by the SuperCDMS Soudan experiment were derived using the Poisson upper-limit method, which first sets bounds on the signal rate without incorporating an explicit background model and then converts the upper limit on the event rate into an upper limit on the coupling strengths. In this work, we aim to improve upon these constraints by performing a likelihood-based analysis using the Profile Likelihood Ratio (PLR) method that incorporates detailed background knowledge. Unlike the Poisson upper-limit approach, the likelihood framework naturally accounts for systematic uncertainties in the measurements. Consequently, constraints derived using the likelihood method lead to improved sensitivity for dark matter and enable potential signal discovery.

In this analysis, we study approximately 110 kg · days of *CDMSlite* data collected during Runs 2 and 3 of the SuperCDMS Soudan experiment. Unlike previous studies that combined CDMSlite and iZIP (interleaved Z-sensitive ionization and phonon) detectors, our analysis focuses exclusively on the CDMSlite operating mode of iZIP detectors. This approach enables a dedicated search for ALPs and dark photons in the mass range up to $25\,\mathrm{keV}/c^2$, with the goal of setting more stringent constraints on the axio-electric coupling g_{ae} and the dark photon kinetic mixing parameter ϵ.

4.2 SuperCDMS Soudan Experimental Setup and Data Sets

4.2.1 Experimental Setup

The datasets used in this analysis were collected during the SuperCDMS Soudan operation, an upgraded phase of the earlier CDMS-II experiment [11, 12]. A detailed description of the detector configuration, tower layout, and shielding is provided in Sec. 2.4. A brief overview of the detector operation is given below.

SuperCDMS Soudan detectors were operated in two primary modes:

a) **Low-bias (iZIP) mode:** A bias voltage of 4 V is applied across the crystal. The simultaneous measurement of phonon and ionization signals enables efficient discrimination between nuclear recoil (NR) and electron recoil (ER) events, resulting in strong background suppression. Detectors in this mode are therefore optimized for low-background operation.

b) **High-bias (CDMSlite) mode:** In this mode, a high bias voltage (70 V in Run 2 and 75 V in Run 3) is applied to enhance Neganov–Trofimov–Luke (NTL) phonon amplification. This significantly lowers the effective energy threshold to $\mathcal{O}(10\text{ eV})$, improving sensitivity to low-mass dark matter. However, the dominance of NTL phonons removes the ability to discriminate between ER and NR events.

Two detectors were operated in CDMSlite mode: T5Z2 (Run 2) and T2Z1 (Run 3). This analysis uses data exclusively from these detectors to constrain the g_{ae} and ϵ. Data from the standard iZIP mode are not included due to their higher energy thresholds ($\mathcal{O}$(keV)), which limit sensitivity to low-mass dark matter. At higher masses, stronger constraints are provided by tonne-scale liquid xenon experiments such as *XENONnT* [13], *LZ* [14], and *PandaX* [15].

4.2.2 Data Sets

Two primary categories of data were collected during the SuperCDMS Soudan experiment:

- Calibration data
- Low-background data

Calibration Data

Calibration data were collected using radioactive sources to characterize the detector response to both electron-recoil and nuclear-recoil interactions. The primary calibration sources used were ^{133}Ba and ^{252}Cf.

- **^{133}Ba Source:** ^{133}Ba decays to ^{133}Cs via electron capture and emits several gamma rays, with prominent lines at 81 keV, 302.8 keV, 356 keV, and 383.8 keV. These well-defined peaks are used to calibrate the electron-recoil energy scale in the standard iZIP operating mode.

- **^{252}Cf Source:** ^{252}Cf undergoes spontaneous fission and emits neutrons with an average energy of approximately 2.1 MeV, accompanied by gamma rays. These neutrons interact with the germanium detectors and produce nuclear recoils, enabling calibration of the NR response. Neutron capture on ^{70}Ge can also produce metastable ^{71}Ge, whose electron-capture decay generates characteristic low-energy X-ray peaks that are useful for energy calibration in CDMSlite mode.

In CDMSlite mode, the large bias voltage produces significant NTL amplification, causing the transition-edge sensor (TES) phonon sensors to saturate at energies of order $O(100\ \mathrm{keV_{ee}})$. As a result, high-energy gamma-ray and neutron interactions cannot be used for calibration. Instead, the energy scale is determined using the low-energy X-ray peaks from the decay of neutron-activated ^{71}Ge observed in the low-background data set (see Sec. 4.2.2).

Low-Background Data

During low-background data taking, all external calibration sources were removed. Events recorded during these runs therefore arise primarily from ambient backgrounds or potential dark matter interactions.

Following neutron calibration with ^{252}Cf, activated ^{71}Ge nuclei remain in the detectors. These nuclei decay via electron capture to ^{71}Ga, producing vacancies in the inner atomic shells (K, L, or M). The subsequent atomic relaxation leads to the emission of characteristic X-rays corresponding to the binding energies of these shells. The resulting peaks are clearly visible in the low-background data and serve as precise low-energy calibration references for the CDMSlite detectors. They also allow detailed studies of the detector energy resolution as a function of deposited energy.

The energies and branching ratios of the ^{71}Ge electron-capture peaks are summarized in Table 4.1.

Shell	Energy (keV)	Branching Ratio
K	10.37	87.6%
L	1.30	10.5%
M	0.16	1.78%

TABLE 4.1: Electron-capture X-ray energies and branching ratios from the decay of ^{71}Ge.

4.3 Axions/Axion-Like-particles and Dark Photons

4.3.1 Axions/Axion-Like Particles

Axions are hypothetical elementary particles originally proposed to solve the strong Charge–Parity (CP) problem in quantum chromodynamics (QCD) [16–19]. CP symmetry implies that the laws of physics remain invariant under the combined transformation of charge conjugation (C), which exchanges particles with their antiparticles, and parity (P), which corresponds to spatial inversion.

While CP violation is well established in weak interactions, no evidence for CP violation has been observed in the strong interaction. However, the QCD Lagrangian permits a CP-violating term proportional to the parameter θ, which would generate observable effects such as a neutron electric dipole moment. Experimental measurements place extremely stringent limits on the neutron electric dipole moment, implying that the effective value of θ must be extremely small. This apparent fine-tuning is known as the *strong CP problem*.

The Peccei–Quinn mechanism introduces a new global $U(1)_{\mathrm{PQ}}$ symmetry that is spontaneously broken at a high energy scale [17]. This mechanism dynamically relaxes the effective θ parameter to zero, thereby removing the CP-violating term from the QCD Lagrangian. The pseudo-Nambu–Goldstone boson associated with this symmetry breaking is known as the axion [18, 19]. As a result, the axion provides a natural explanation for the absence of CP violation in the strong interaction.

The QCD axion mass is related to the Peccei–Quinn symmetry breaking scale f_a through

$$m_a \simeq 5.7\,\mu\text{eV}\left(\frac{10^{12}\,\text{GeV}}{f_a}\right), \tag{4.1}$$

which follows from the relation $m_a \propto f_\pi m_\pi / f_a$ derived from chiral symmetry breaking in QCD [20, 21]. Astrophysical and cosmological constraints typically require $f_a \sim 10^9$–10^{12} GeV, corresponding to axion masses in the approximate range $m_a \sim 10^{-6}$–10^{-3} eV (i.e., μeV to meV) [20–22]. Astrophysical observations also constrain the allowed axion parameter space. In particular, the duration of the neutrino burst observed from Supernova 1987A limits excessive energy loss from the supernova core due to axion emission, implying that the canonical QCD axion mass is typically below $\sim 10^{-2}\text{eV}/c^2$ [22].

In addition to the QCD axion, many extensions of the Standard Model predict similar particles referred to as ALPs [3, 4]. These particles are also pseudo-Goldstone bosons associated with spontaneously broken global symmetries but do not necessarily obey the strict mass–coupling relation characteristic of the QCD axion. Consequently, ALPs can span a much wider range of masses and interaction strengths. This broader parameter space allows experiments such as SuperCDMS to probe ALPs through their possible interactions with detector materials.

ALPs can interact with Standard Model fermions through derivative couplings to the axial current. The relevant interaction term in the Lagrangian is

$$\mathcal{L} \supset \frac{g_{ae}}{2m_e}(\partial_\mu a)\,\bar{e}\gamma^\mu\gamma^5 e, \tag{4.2}$$

where a denotes the ALP field, g_{ae} is the dimensionless axion–electron coupling constant, and m_e is the electron mass. In direct detection experiments, this interaction allows ALPs to be absorbed by bound electrons, producing observable electronic recoil signals.

4.3.2 Dark Photons

Dark photons are hypothetical vector bosons that arise in extensions of the Standard Model containing an additional $U(1)$ gauge symmetry in the dark sector [5]. In these models, the dark photon can interact with Standard Model particles through kinetic mixing with the ordinary photon.

The corresponding interaction term in the Lagrangian is

$$\mathcal{L} \supset -\frac{\epsilon}{2} F_{\mu\nu} V^{\mu\nu}, \tag{4.3}$$

where $F_{\mu\nu}$ and $V_{\mu\nu}$ are the field strength tensors of the Standard Model photon and the dark photon, respectively, and ϵ is the kinetic mixing parameter.

This mixing induces an effective coupling between the dark photon and the electromagnetic current, allowing dark photons to interact with charged particles. As a result, dark photons can be absorbed by electrons in detector materials in a process analogous to the photoelectric effect.

If the dark photon mass satisfies $m_V > 2m_e$, the decay channel $V \to e^+e^-$ becomes kinematically allowed. However, the decay rate depends on the kinetic mixing parameter ϵ, which determines the effective coupling of the dark photon to the electromagnetic current. For sufficiently small values of ϵ, the decay rate can be highly suppressed, allowing dark photons with $m_V > 2m_e$ to remain cosmologically long-lived and therefore viable dark matter candidates [5, 23].

Similar to ALPs, dark photons can be absorbed by electrons in detector materials through their effective coupling to the electromagnetic current, producing electronic recoil signals that can be measured in direct detection experiments.

4.4 Data Processing

In CDMSlite detectors, event reconstruction relies primarily on the phonon readout channels. For each triggered event, the phonon pulse trace is analyzed using an Optimal Filter (OF) algorithm to extract the signal amplitude and timing information.

The Optimal Filter operates in the frequency domain by fitting a template pulse to the measured trace while accounting for the detector noise power spectral density (PSD). This approach maximizes the signal-to-noise ratio and provides statistically optimal estimates of the pulse parameters. Details on the data processing using Optimal Filter method is discussed in 2.3.2. The Optimal Filter returns the best-fit values of the pulse amplitude, the time offset, and the reduced chi-square, which quantifies the quality of the fit. The calibrated pulse amplitude serves as the primary energy estimator for each event and forms the basis of energy spectrum.

4.5 PLR-Based Analysis Flow

The primary goal of this analysis is to obtain a stronger constraint on the coupling parameters of ALPs and dark photons through the dark absorption process using the PLR method. This work reanalyzes the same data from the previously published SuperCDMS dark absorption study [8], which employed a Poisson-based approach to set upper limits on the signal rate without explicitly incorporating background models in the statistical interpretation. In contrast, the present study includes detailed background modeling within the likelihood framework. The overall workflow of the PLR-based reanalysis is illustrated in Fig. 4.2.

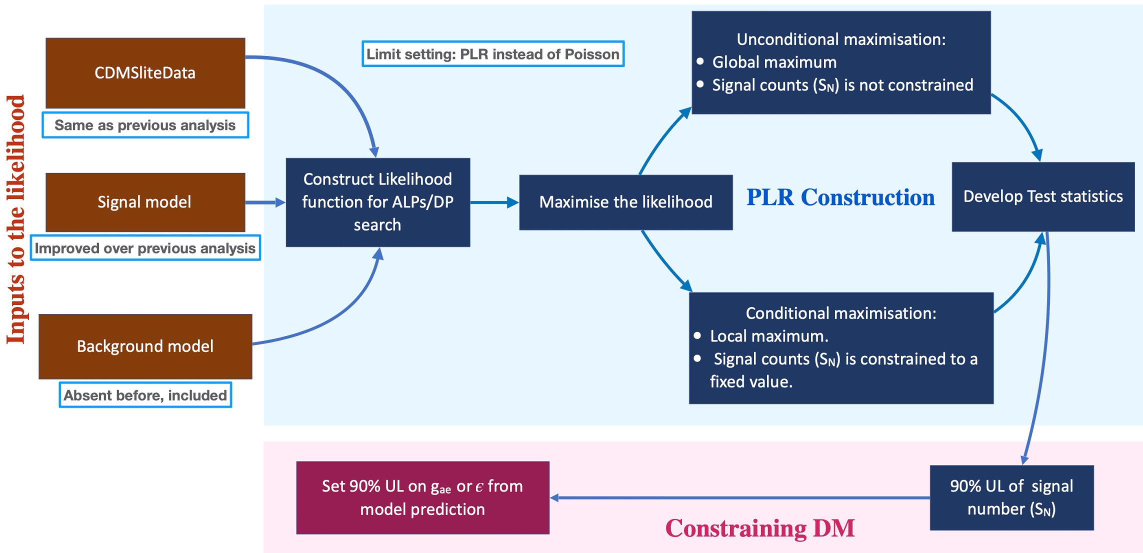

FIGURE 4.2: Flowchart illustrating the Profile likelihood ratio based analysis framework for constraining ALPs and Dark photons. The text in blue boxes describes the improvements over previous analysis.

The PLR method offers several advantages over the previously used Poisson-based approach. First, by incorporating background models directly into the likelihood fit, it enables stronger and more robust constraints on the signal rate. Second, systematic uncertainties in both signal and background models can be incorporated as nuisance parameters and propagated naturally into the final sensitivity. Finally, the PLR framework allows the statistical significance of a potential signal excess to be quantified, enabling both exclusion limits and discovery tests. In this work, however, we restrict the analysis to setting exclusion limits. This is due to the presence of an unmodeled background arising from low-frequency noise (LFN) at energies around 100 eV and below, which limits the reliability of a discovery interpretation in this region. The LFN originated from mechanical vibrations of the cryocooler used to maintain the detector and electronics at cryogenic temperatures. These vibrations produced pulses with variable shapes that could mimic signal events, making them particularly challenging to reject using standard selection cuts in this low-energy regime.

The event selection criteria, signal efficiencies, and detector energy resolution models used in this work follow those developed in previous CDMSlite dark absorption analysis and analyses of WIMP search via inelastic Migdal and Bremsstrahlung channels [8, 24]. Signal models for ALPs and dark photons are constructed, and the corresponding event rates are calculated while accounting for the *in-medium effect*, which was not included in the earlier SuperCDMS dark absorption analysis. This effect modifies the absorption rate in the detector material and introduces a correction of approximately 5–10% in the low-energy region ($\sim$ 100 eV and below). Background models are adopted from the CDMSlite Migdal/Bremsstrahlung WIMP analysis [24].

Using the signal and background models, the profile likelihood function, and consequently the PLR test statistic, are constructed for the dark absorption analysis. An unbinned likelihood function is employed in the analysis. The PLR method is then used to derive 90% confidence level (CL) upper limits on the event rate across a range of axion-like particle and dark photon masses. These limits are subsequently translated into constraints on the g_{ae} for ALPs and the ϵ for dark photons.

ALPs and Dark photons can also interact via dark Compton scattering [25] process. However, preliminary studies within the SuperCDMS collaboration showed that this process contributes negligibly within the CDMSlite region of interest (below 25 keV$_{\mathrm{ee}}$). The most stringent constraints from the dark Compton channel are expected at higher recoil energies, accessible to iZIP detectors (above $O(100)$ keV). This behavior is analogous to standard electromagnetic interactions, where the photoelectric effect dominates at low photon energies, while Compton scattering becomes significant at higher energies. A similar hierarchy is expected between dark absorption and dark Compton scattering. Consequently, the dark Compton scattering channel is not included in the present analysis.

Table 4.2 summarizes the key differences between the SuperCDMS published dark absorption analysis [8] using Soudan data and the methodology adopted in this study.

TABLE 4.2: Key differences between the published CDMSlite dark absorption analysis [8] and this study.

Aspect	**CDMSlite Dark Absorption (2020) [8]**	**This Study**
Data	CDMSlite R2, R3, iZIP	CDMSlite R2, R3
Efficiency Model	Efficiency derived from measurements and treated as a fixed input. Upper and lower efficiency bounds were propagated to obtain corresponding variations in the final limits.	Measured efficiency included as a constrained morphing parameter in the likelihood fit, with constraints derived from measurements. Systematic effects are naturally propagated into the final upper limits.
Resolution Model	Conservative uncertainty treatment without accounting for parameter correlations; bands defined by ± uncertainties on best-fit values.	Resolution modeled directly within the likelihood fit with constraints from measurements, including correlations among parameters.
Signal Rate Modeling	No in-medium effects included	In-medium effects included
Background Model	Not included	Background PDFs are included in likelihood fit. Best fit determines the background Normalisation constant.
Limit-Setting Method	Poisson upper-limit method	Profile Likelihood Ratio method

4.6 Data Selection and Signal Efficiency

To suppress instrumental noise and poorly reconstructed events, several event selection criteria are applied to the data. The selection cuts and signal efficiency models used in this analysis follow those developed in previous CDMSlite dark absorption and WIMP search studies [24, 26, 27].

After applying these selection criteria, the total exposure of the CDMSlite Run 2 (R2) dataset is 70.1 kg-days, while the Run 3 (R3) dataset corresponds to an exposure of 36.92 kg-days.

Both R2 and R3 datasets are further divided into sub-runs: R2a/R2b and R3a/R3b. In Run 2, this division corresponds to a maintenance period of the cryocooler system. In the R2 analysis, the two sub-runs were combined and treated as a single dataset. In contrast, the R3 datasets were analyzed separately because of a change in the detector noise environment during the run. Consequently, the R3a and R3b datasets are modeled with independent energy resolution and efficiency functions in the likelihood analysis.

The filtered energy spectra obtained after applying the quality and livetime cuts are shown in Fig. 4.3. Prominent activation lines from post-^{252}Cf calibration are clearly visible in the spectra, corresponding to the K-shell, L-shell, and M-shell electron-capture peaks of ^{71}Ge.

The signal efficiency corresponding to the applied event selection cuts for the CDMSlite R2 and R3 datasets is shown in Fig. 4.4. These efficiency curves are incorporated into the likelihood analysis when modeling the expected signal spectra.

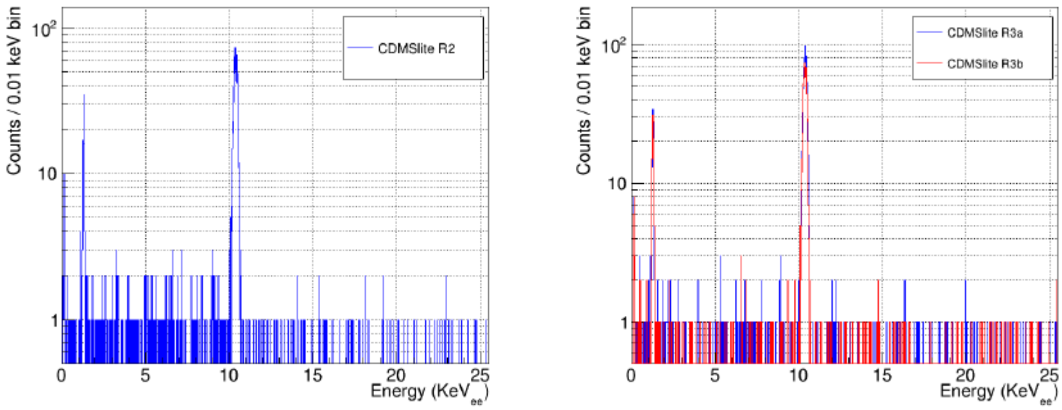

FIGURE 4.3: Energy spectra from CDMSlite Run 2 and Run 3 after applying quality and livetime cuts. Run 3 is divided into two sub-runs due to changes in the detector noise environment. Prominent electron-capture peaks from ^{71}Ge are visible at approximately 10.37 keV, 1.3 keV, and 0.16 keV. The spectra are reproduced from the data reported in Refs. [24, 26, 27].

4.7 Energy Resolution Determination of the CDMSlite Detector

The energy resolution of the CDMSlite detector is determined using the characteristic electron-capture peaks of germanium: the **K-shell** (10.37 keV$_{ee}$), **L-shell** (1.30 keV$_{ee}$), and **M-shell** (0.16 keV$_{ee}$) lines. Each peak in the filtered energy spectrum is fitted with a Gaussian function, and the corresponding resolution at that energy is obtained from the standard deviation (σ) of the fit.

The *baseline resolution* is measured independently using the pulse amplitude estimator obtained from a zero-delay optimal filter applied to randomly triggered traces. This baseline measurement accounts for electronic and environmental noise contributions.

The resolution model adopted here follows the methodology used in previous CDMSlite dark absorption and WIMP search analyses [24, 26, 27].

The total energy resolution, σ_T, is parameterized as

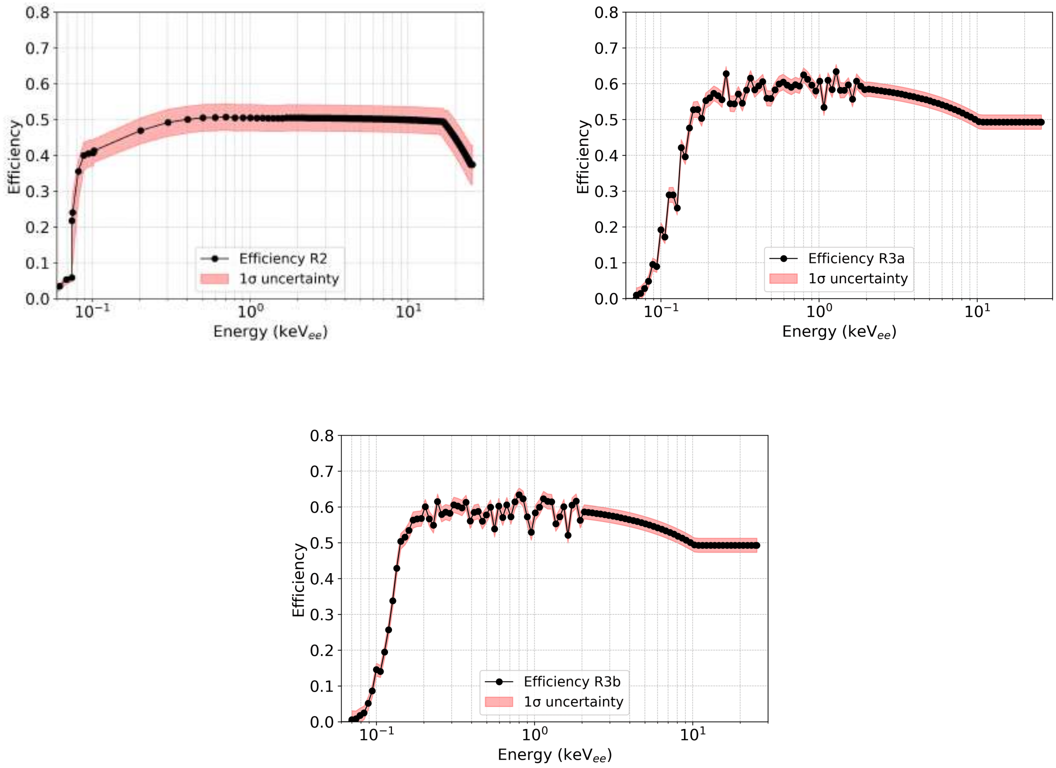

FIGURE 4.4: Signal efficiency for event selection cuts in CDMSlite Run 2 and Run 3 datasets. Separate efficiency models are used for the R3a and R3b sub-runs. The figures are reproduced from the data reported in Refs. [24, 26, 27].

$$\sigma_T = \sqrt{\sigma_E^2 + \sigma_F^2(E_{ee}) + \sigma_{PD}^2(E_{ee})} \tag{4.4}$$

$$= \sqrt{\sigma_E^2 + F\epsilon E_{ee} + (AE_{ee})^2}, \tag{4.5}$$

where

- σ_T is the total energy resolution,
- σ_E represents the baseline resolution arising from electronic and environmental noise,

- $\sigma_F(E_{ee})$ accounts for Fano fluctuations in the ionization process,
- $\sigma_{PD}(E_{ee})$ describes position-dependent variations in the pulse shape, parameterized by the coefficient A,
- F is the Fano factor,
- ϵ is the average energy required to create an electron–hole pair in germanium,
- E_{ee} is the electron-equivalent recoil energy.

The best-fit parameters for the energy resolution model are summarized in Table 4.3.

CDMSlite Run	$\boldsymbol{\sigma_E}$ (eV)	$\boldsymbol{\epsilon F}$ (eV)	$\boldsymbol{A}$ **($\times 10^{-3}$)**
R2	9.26 ± 0.11	0.64 ± 0.11	5.68 ± 0.94
R3a	9.87 ± 0.04	0.87 ± 0.12	4.94 ± 1.27
R3b	12.7 ± 0.04	0.80 ± 0.12	5.49 ± 1.15

TABLE 4.3: Best-fit parameters of the energy resolution model for CDMSlite Run 2 and Run 3 datasets [8].

Using this resolution model for the CDMSlite detector (R2 and R3 datasets), signal models for ALPs and dark photons are constructed as Gaussian peaks centered at the energy corresponding to the particle mass. The width of each signal peak is determined by the detector resolution evaluated at the corresponding energy.

4.8 Dark Absorption Signal Modeling

The detection mechanism considered in this analysis is based on *dark absorption*, which is analogous to the *photoelectric effect*. In this process, a dark-sector particle is absorbed by an atom in the detector material, transferring its energy to an electron and producing an electronic recoil.

For dark matter masses above the semiconductor band gap (approximately 0.7 eV in germanium at cryogenic temperatures), the absorbed energy excites an electron from the valence band to the conduction band. For masses below the band gap, absorption may still occur through multiphonon excitations in the lattice, enabling sensitivity to dark matter particles in the $O(0.01\,\text{eV})$ to $O(1\,\text{eV})$ mass range [28]. However, since the energy resolution and threshold of our detectors are $O(10\,\text{eV})$, they are not sensitive to the latter process.

In this work, we focus on non-relativistic Galactic ALPs and dark photons with masses above the band gap of the detector material. In this regime, the absorption of a bosonic dark matter particle deposits an energy approximately equal to its rest-mass energy, $E \simeq m_\chi c^2$, since the kinetic energy of halo dark matter particles is negligible compared to their mass. Consequently, the expected signal appears as a monoenergetic electronic recoil with energy corresponding approximately to the particle mass.

To constrain the g_{ae} for ALPs and ϵ for dark photons, we first determine the upper limit on the absorption event rate. The absorption cross-sections depend on the photoelectric cross-section of the target material, which in this experiment is germanium (Ge).

Assuming the dark matter particles are non-relativistic and constitute the entire local dark matter density, the dark matter flux can be written as

$$\phi = \frac{\rho_\chi v_\chi}{m_\chi}, \tag{4.6}$$

where ρ_χ is the local dark matter density, m_χ is the dark matter mass, and v_χ is the dark matter velocity. Throughout this analysis we assume $\rho_\chi = 0.3\ \text{GeV}/c^2\text{cm}^{-3}$.

4.8.1 Dark Absorption of ALPs

Axion-like particles can be absorbed in detector through the axio-electric effect. The interaction strength is characterized by the axio-electric coupling constant g_{ae}.

The absorption cross-section for ALPs in a material can be expressed in terms of the photoelectric cross-section σ_{pe} [8]:

$$\sigma_a(E_a) = \sigma_{pe}(E_a)\frac{g_{ae}^2}{\beta_a}\frac{3E_a^2}{16\pi\alpha m_e^2 c^4}\left(1 - \frac{\beta_a^{2/3}}{3}\right), \tag{4.7}$$

where σ_a is the ALP absorption cross-section, $\sigma_{pe}(E_a)$ is the photoelectric cross-section of the target material evaluated at energy E_a, and g_{ae} is the axio-electric coupling constant describing the interaction strength between the ALP and the electron. Here E_a is the ALP energy, $\beta_a = v_a/c$ is the dimensionless ALP velocity with v_a the ALP velocity and c the speed of light, and α is the fine-structure constant that characterizes the strength of the electromagnetic interaction. Under the assumption of non-relativistic ALPs, $\beta_a = v_a/c$ «1. Therefore the first term in the Eq. 4.7 dominates.

For non-relativistic ALPs that constitute galactic dark matter, the absorption event rate per unit detector mass can be written as

$$R_a = \phi\sigma_a = \rho_\chi \frac{3g_{ae}^2 c}{16\pi\alpha}\frac{m_a}{m_e^2}\sigma_{pe}(m_a c^2), \tag{4.8}$$

where R_a is the absorption event rate, ϕ is the incident ALP flux, ρ_χ is the local dark matter mass density, m_a is the ALP mass, and m_e is the electron mass. In this expression the ALP energy is approximately equal to its rest-mass energy, $E_a \approx m_a c^2$, since galactic dark matter particles are non-relativistic.

At low energies, the absorption rate is modified by in-medium effects arising from interactions of the particle with the electronic structure of the material. Including these effects, the event rate can be written as [28]

$$R_a = \frac{\rho_\chi}{\rho m_a} \frac{3m_a^2}{4m_e^2} \frac{g_{ae}^2}{e^2} \sigma_1(m_a c^2), \tag{4.9}$$

where ρ is the mass density of the detector material, e is the elementary electric charge, and σ_1 is the real part of the complex optical conductivity of the medium evaluated at energy $m_a c^2$.

The optical conductivity is related to the photoelectric cross-section through

$$\sigma_1 = \rho\, c\, \hbar\, n\, \sigma_{pe}, \tag{4.10}$$

where $\hbar$ is the reduced Planck constant and n is the refractive index of the medium.

The event rate therefore depends on two unknown parameters: the ALP mass (m_a) and the axio-electric coupling (g_{ae}). By determining an upper limit on the event rate for a given ALPs mass, the experiment constrains the allowed region in the m_a–g_{ae} parameter space.

4.8.2 Dark Absorption of Dark Photons

Dark photons interact with Standard Model particles through kinetic mixing with the ordinary photon. This interaction allows dark photons to be absorbed by electrons in a process analogous to photoelectric absorption.

The absorption cross-section is given by

$$\sigma_V(E_V) = \frac{\epsilon^2}{\beta_V} \sigma_{pe}(E_V), \tag{4.11}$$

where ϵ is the kinetic mixing parameter and $\beta_V = v_V/c$ is the dark photon velocity factor.

The corresponding absorption event rate can be written as

$$R_V = \frac{\rho_\chi}{m_V}\epsilon^2\sigma_{pe}(m_V c^2)c. \tag{4.12}$$

Similar to the ALP case, the observable event rate depends on two parameters: the dark photon mass (m_V) and the kinetic mixing parameter (ϵ). Experimental limits on the event rate therefore translate into exclusion regions in the m_V–ϵ parameter space.

In a material medium, the effective kinetic mixing is modified by the electromagnetic polarization tensor Π, which describes the response of the medium to an electromagnetic field. The polarization tensor can be approximated as

$$\Pi(\omega) \approx -i\hat{\sigma}\omega, \tag{4.13}$$

where $\hat{\sigma}$ is the complex conductivity of the material.

Including these in-medium effects, the absorption rate becomes

$$R_V = \frac{1}{\rho}\frac{\rho_\chi}{m_V}\epsilon_{\text{eff}}^2\sigma_1(m_V c^2)c, \tag{4.14}$$

where ϵ_{eff} is the effective kinetic mixing parameter in the medium. It is given by

$$\epsilon_{\text{eff}}^2 = \epsilon^2\frac{m_V^4}{[m_V^2 - \mathrm{Re}\,\Pi(m_V)]^2 + [\mathrm{Im}\,\Pi(m_V)]^2}. \tag{4.15}$$

It is important to note that under the non-relativistic assumption for ALPs and dark photons, the absorption cross sections are inversely proportional to the dark matter particle velocity. At the same time, the dark matter flux is proportional to the particle velocity. Consequently, when calculating the event rate (flux $\times$ cross section), the velocity dependence cancels out, making the rate approximately independent of the dark matter velocity. This is in contrast to traditional WIMP searches, where the interaction rate depends on the Maxwell–Boltzmann velocity distribution of WIMPs in the Galactic halo.

4.8.3 Optical Properties of the Detector Material: Germanium

The in-medium absorption rate depends on the optical properties of the detector material, which are described by the complex conductivity. The real part of the complex conductivity can be determined from the photoelectric cross-section and the refractive index of the material.

The photoelectric cross-section of germanium is constructed from several datasets covering different energy ranges: below 20 eV [29], between 20 eV and 20 keV [30], and above 20 keV [31]. The refractive index data are taken from [29]. The resulting photoelectric cross-section and refractive index used in this analysis are shown in Fig. 4.5.

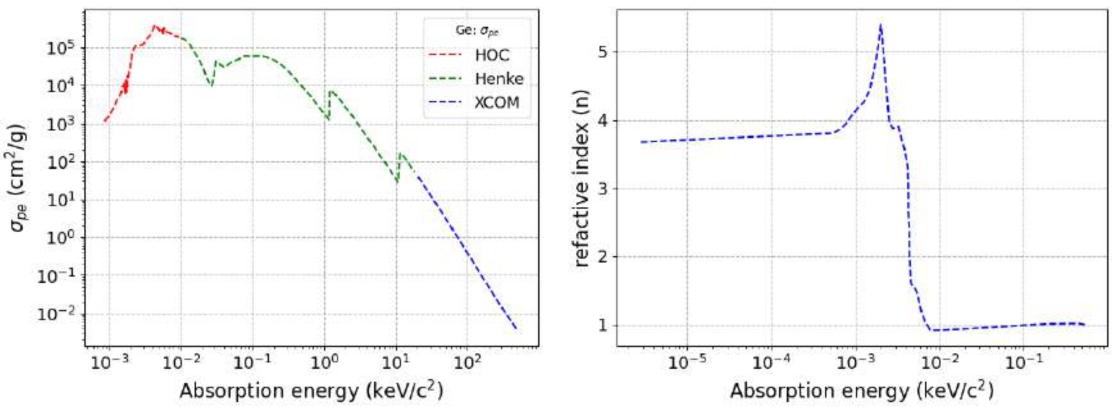

FIGURE 4.5: (Left) Photoelectric cross-section of germanium as a function of energy. The photoelectric cross-section of germanium is constructed from several datasets covering different energy ranges: below 20 eV [29], between 20 eV and 20 keV [30], and above 20 keV [31]. (Right) Refractive index of germanium used in the calculation of optical properties. The refractive index data are taken from [29].

Using these datasets, the real component of the complex conductivity is derived. The imaginary component of the complex conductivity is taken from [28, 29]. The resulting conductivity components are shown in Fig. 4.6.

The dark absorption signal model framework developed in this analysis follows the theoretical calculation by Hochberg *et al.* [28], which incorporates in-medium effects

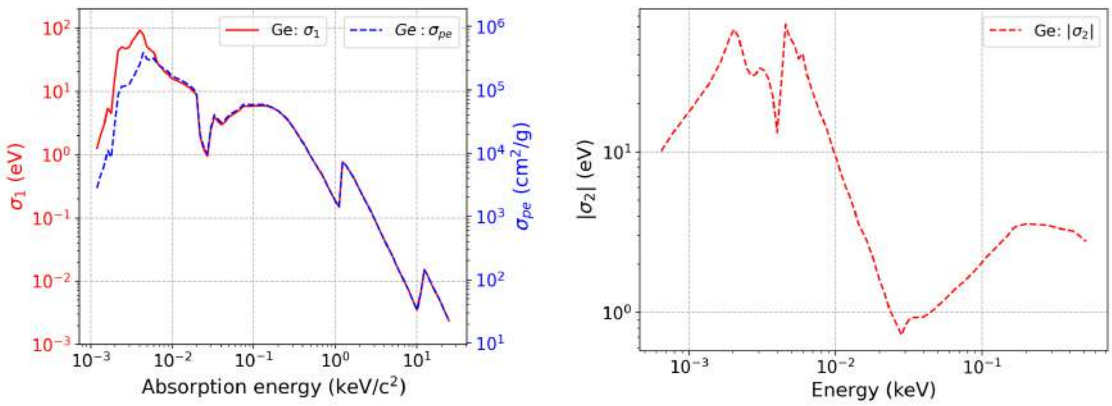

FIGURE 4.6: Real (left) and imaginary (right) parts of the complex conductivity of germanium as functions of absorption energy. The imaginary component of the complex conductivity is taken from [28, 29].

arising from interactions between the dark-sector particle and the electronic structure of the material. These effects become particularly important at low energies, where the electromagnetic response of the medium modifies the absorption rate.

In this work, in-medium corrections are included for absorption energies below approximately 500 eV. At higher energies, the lack of experimental data for the imaginary component of the complex conductivity limits the applicability of the model. Therefore, for $E \geq 500$ eV the in-medium correction factor is assumed to be unity (i.e., no suppression), consistent with the approach adopted in the previous SuperCDMS Soudan analysis [8].

The resulting dark absorption signal models for ALPs and dark photons in germanium are shown in Fig. 4.7. The updated modeling predicts deviations of approximately 5–10% near 100 eV and below compared to models that neglect in-medium effects. Although this difference is modest for the current CDMSlite sensitivity, it may become increasingly important for future low-threshold experiments such as SuperCDMS SNOLAB. Accordingly, the event rate predictions used in this analysis include the full in-medium corrections.

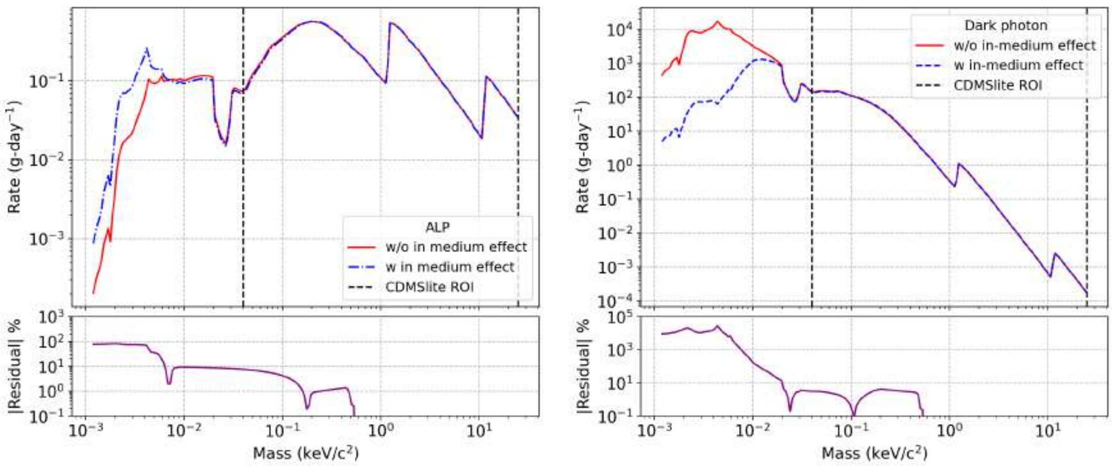

FIGURE 4.7: Predicted dark absorption event rates in germanium for ALPs (left) and dark photons (right) as functions of particle mass up to 25 keV. The predictions are shown for $g_{ae} = 5 \times 10^{-11}$ and $\epsilon = 5 \times 10^{-13}$. Models including in-medium effects are compared with those that neglect these corrections. The residual plots indicate deviations of up to 10% when in-medium effects are included, particularly near the threshold within the analysis energy range. For SuperCDMS SNOLAB, where the expected threshold is lower than in Soudan operation, the inclusion of in-medium effects can have a significant impact.

4.9 Background Modeling

A major advantage of the PLR approach is that it allows detailed background models to be incorporated directly into the statistical analysis. By explicitly modeling all the well-understood and relevant background contributions, the likelihood fit can distinguish potential signal features from known backgrounds, leading to more robust and stringent constraints on the parameters of interest.

The energy region of interest (ROI) for the dark absorption search extends up to 25 $\mathrm{keV_{ee}}$, which corresponds to the full range where absorption signals from ALPs and dark photons are expected to appear in CDMSlite detectors. All significant background components within this ROI are included in the PLR likelihood framework.

Table 4.4 summarizes the background sources considered in this analysis, their physical origins, and whether their contributions are treated as free or constrained parameters in the likelihood fit.

TABLE 4.4: Background sources included in the PLR likelihood analysis. The final column indicates whether the normalization of each component is treated as a free or constrained parameter in the fit.

Background Source	**Description**	**Likelihood Treatment**
Compton	Compton scattering of environmental gamma rays in the detector material.	Free
^{3}H (Tritium)	Beta decay of tritium produced through cosmogenic activation.	Free
^{71}Ge	Electron-capture peaks from neutron activation of germanium.	Free
^{68}Ga	Electron-capture peaks from cosmogenic activation.	Free
^{65}Zn	Electron-capture peaks from cosmogenic activation.	Free
^{55}Fe	Electron-capture peaks from cosmogenic activation.	Free
^{210}Pb–GZ	Surface contamination from ^{210}Pb on the Ge detector surface.	Constrained
^{210}Pb–SH	^{210}Pb contamination on the copper side housing surrounding the detector.	Constrained
^{210}Pb–TL	^{210}Pb contamination on the copper top lid above the detector (R3 only).	Constrained
Neutrons	Cosmogenic and radiogenic neutron interactions.	Not included ($\ll$ 1 event)
Low-rate isotopes	Rare cosmogenic isotopes (e.g. ^{60}Co, ^{54}Mn, ^{49}V).	Not included ($\ll$ 1 event in ROI)

4.9.1 Bulk Backgrounds

Two previous SuperCDMS analyses employed the PLR method with explicit background modeling. The first analysis searched for elastic WIMP–nucleus scattering and used a low-energy ROI up to 2 keV$_{ee}$ [27]. The second study searched for WIMPs via inelastic processes, such as Migdal and Bremsstrahlung signals, and used an extended ROI up to 25 $\mathrm{keV_{ee}}$ [24].

Since the present ALP and dark photon search uses the same ROI as the latter study, we adopt a similar background modeling strategy. Figure 4.8 shows the probability density functions (PDFs) of the bulk background components used in the likelihood analysis.

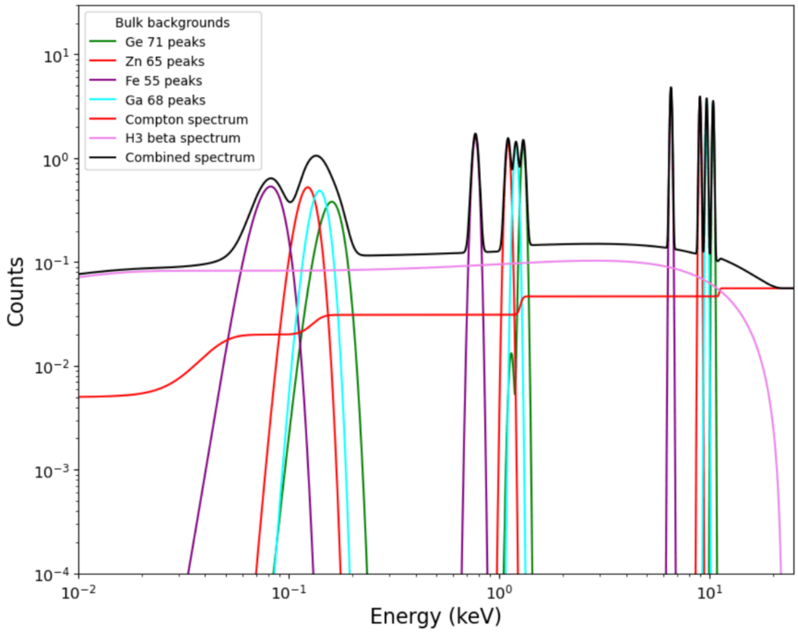

FIGURE 4.8: Probability density functions of the bulk background components included in the likelihood analysis. These components include Compton scattering, cosmogenic activation lines, and tritium beta decay. Each individual spectrum is normalized.

^{71}Ge Neutron Activation Lines

The electron-capture (EC) decay of ^{71}Ge produces some of the most prominent features in the CDMSlite energy spectrum. Following neutron activation during ^{252}Cf calibration runs, ^{71}Ge is produced in the detector and subsequently decays via electron capture to ^{71}Ga.

Electron capture from the K, L, and M shells results in the emission of characteristic X-rays, which deposit their full energy in the detector. These signals appear as Gaussian peaks whose widths are determined by the detector energy resolution.

The ^{71}Ge background model is therefore described as a sum of three Gaussian functions:

$$f_{^{71}\mathrm{Ge}}(E) = \sum_i \frac{A_i}{\sigma_i\sqrt{2\pi}} \exp\left[-\frac{(E-\mu_i)^2}{2\sigma_i^2}\right]. \tag{4.16}$$

The peak positions, resolutions, and relative intensities are summarized in Table 4.5.

Shell	μ_i [keV$_{\mathrm{ee}}$]	σ_i [eV$_{\mathrm{ee}}$]	A_i/A_K
M	0.16	13.9 ± 0.2	0.0203
L	1.30	36.3 ± 0.2	0.1202
K	10.37	108 ± 0.2	1

TABLE 4.5: ^{71}Ge electron capture peak parameters used in the background model.

Cosmogenic Activation Lines

During detector fabrication and transport above ground, cosmic-ray interactions activate long-lived isotopes in the germanium crystal. These isotopes decay through electron capture, producing characteristic peaks in the energy spectrum.

The dominant cosmogenic isotopes contributing to the background are ^{68}Ga, ^{65}Zn, and ^{55}Fe. Their spectral shapes are modeled as Gaussian peaks:

$$f_{\mathrm{cosmo}}(E) = \sum_i \frac{A_i}{\sigma_i\sqrt{2\pi}} \exp\left[-\frac{(E-\mu_i)^2}{2\sigma_i^2}\right]. \tag{4.17}$$

The energies and relative intensities of the corresponding peaks are listed in Table 4.6.

Isotope	K [keV$_{\mathrm{ee}}$]	A_K	L [keV$_{\mathrm{ee}}$]	A_L/A_K	M [keV$_{\mathrm{ee}}$]	A_M/A_K
^{65}Zn	8.98	1	1.097	0.1105	0.123	0.0181
^{68}Ga	9.66	1	1.20	0.1107	0.140	0.0183
^{55}Fe	6.54	1	0.77	0.1016	0.82	0.0079

TABLE 4.6: Cosmogenic electron-capture peak energies and relative intensities.

Tritium Background

Tritium (^{3}H) is produced in germanium through cosmogenic activation and decays via beta emission:

$$^3\mathrm{H} \rightarrow ^3\mathrm{He} + e^- + \bar{\nu}_e.$$

The differential beta decay spectrum is given by [21]

$$N(T_e) = C\sqrt{T_e^2 + 2T_e m_e}(Q - T_e)^2(T_e + m_e c^2)F(Z, T_e), \tag{4.18}$$

where T_e is the kinetic energy of the emitted electron, Q is the decay endpoint energy, m_e is the electron mass, and $F(Z, T_e)$ is the Fermi function that accounts for Coulomb interactions between the outgoing electron and the daughter nucleus.

The normalizations of the bulk backgrounds are treated as a free parameter in the likelihood fit.

4.9.2 Surface Backgrounds

Surface backgrounds originate primarily from radon progeny deposited on detector surfaces and surrounding materials. These radioactive contaminants, particularly isotopes in the ^{210}Pb decay chain, produce low-energy events that can mimic signal-like features.

Due to the complexity of their interaction mechanisms, these backgrounds cannot be described with simple analytical models. Instead, they are constructed using detailed Geant4 simulations of the detector geometry. In these simulations, lead isotopes from the radon decay chain are deposited on various detector surfaces, and the resulting particle interactions are recorded to generate expected energy spectra.

To obtain absolute rates, the simulated spectra are normalized using alpha event rates measured during calibration runs. Since the Geant4 outputs are produced as binned histograms while the PLR analysis requires unbinned PDFs, the simulated spectra are smoothed using kernel density estimation (KDE). This procedure produces continuous probability density functions suitable for likelihood fitting.

For the CDMSlite R3 dataset, the detector T2Z1 (top detector of Tower 2 in Fig. 2.4) is used. In this configuration three primary surface background components are relevant:

- Ge ZiP (GZ): contamination on the germanium detector surface,
- Side Housing (SH): contamination on the copper sidewalls surrounding the detector,
- Top Lid (TL): contamination on the copper lid above the detector.

In contrast, the CDMSlite R2 dataset uses detector T5Z2, which is located in the middle of its tower as shown in the Fig. 2.4. As a result, the top lid contribution is negligible and only the GZ and SH components are included.

Figure 4.9 and Figure 4.10 show the KDE-smoothed surface background models for the R2 and R3 datasets, respectively.

Surface backgrounds are particularly sensitive to the radial fiducial volume cut. Events occurring near the detector sidewalls experience a reduced electric field, leading to a smaller NTL gain and distortions in the reconstructed energy spectrum.

To account for these effects, a morphing procedure is implemented within the likelihood framework. This method introduces nuisance parameters that allow the spectral shapes of surface background components to vary within predefined uncertainty bands, thereby capturing systematic uncertainties arising from electric-field variations and detector geometry.

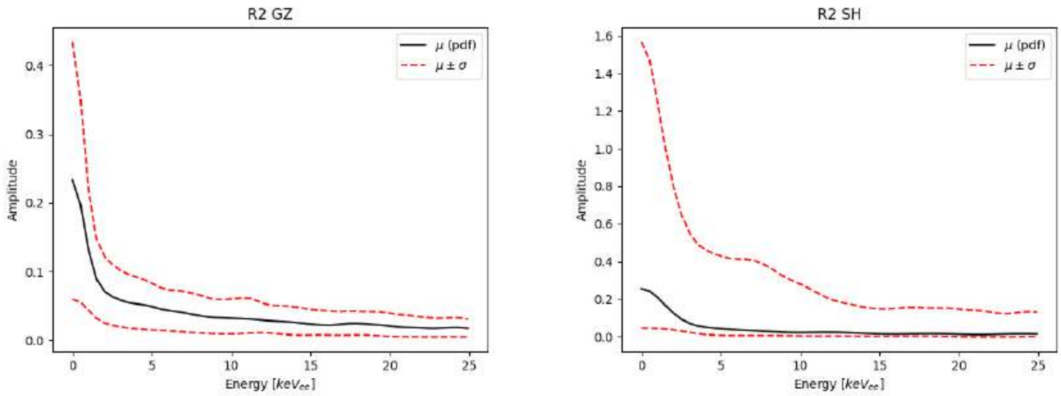

FIGURE 4.9: Smoothed surface background models for CDMSlite Run 2 obtained using KDE: Ge ZIP (left) and side housing (right). The red dashed lines show the 1σ upper and lower uncertainty bands. Adapted from Ref. [32].

Three template spectra for each surface background component are considered: a median spectrum $\rho_{\mathrm{med}}(E)$, and upper and lower variations, $\rho_{\mathrm{upper}}(E)$ and $\rho_{\mathrm{lower}}(E)$, which define the allowed range of spectral shape variations. The PDFs shown in Fig. 3 are normalized to unit area and can be scaled by the expected number of events to obtain the event density spectra $\rho(E)$.

A morphing parameter m is introduced to interpolate linearly between these templates:

$$\rho(E,m) = \begin{cases} \rho_{\mathrm{med}}(E) + m\left[\rho_{\mathrm{upper}}(E) - \rho_{\mathrm{med}}(E)\right], & m > 0, \\ \rho_{\mathrm{med}}(E) + m\left[\rho_{\mathrm{med}}(E) - \rho_{\mathrm{lower}}(E)\right], & m < 0. \end{cases} \tag{4.19}$$

The morphing parameters are allowed to float freely in the likelihood fit, with one parameter assigned to each surface background component. This approach enables the fit to adjust the spectral shape within the predefined uncertainty envelope.

In the final likelihood analysis, the normalization of each surface background component is treated as a constrained parameter.

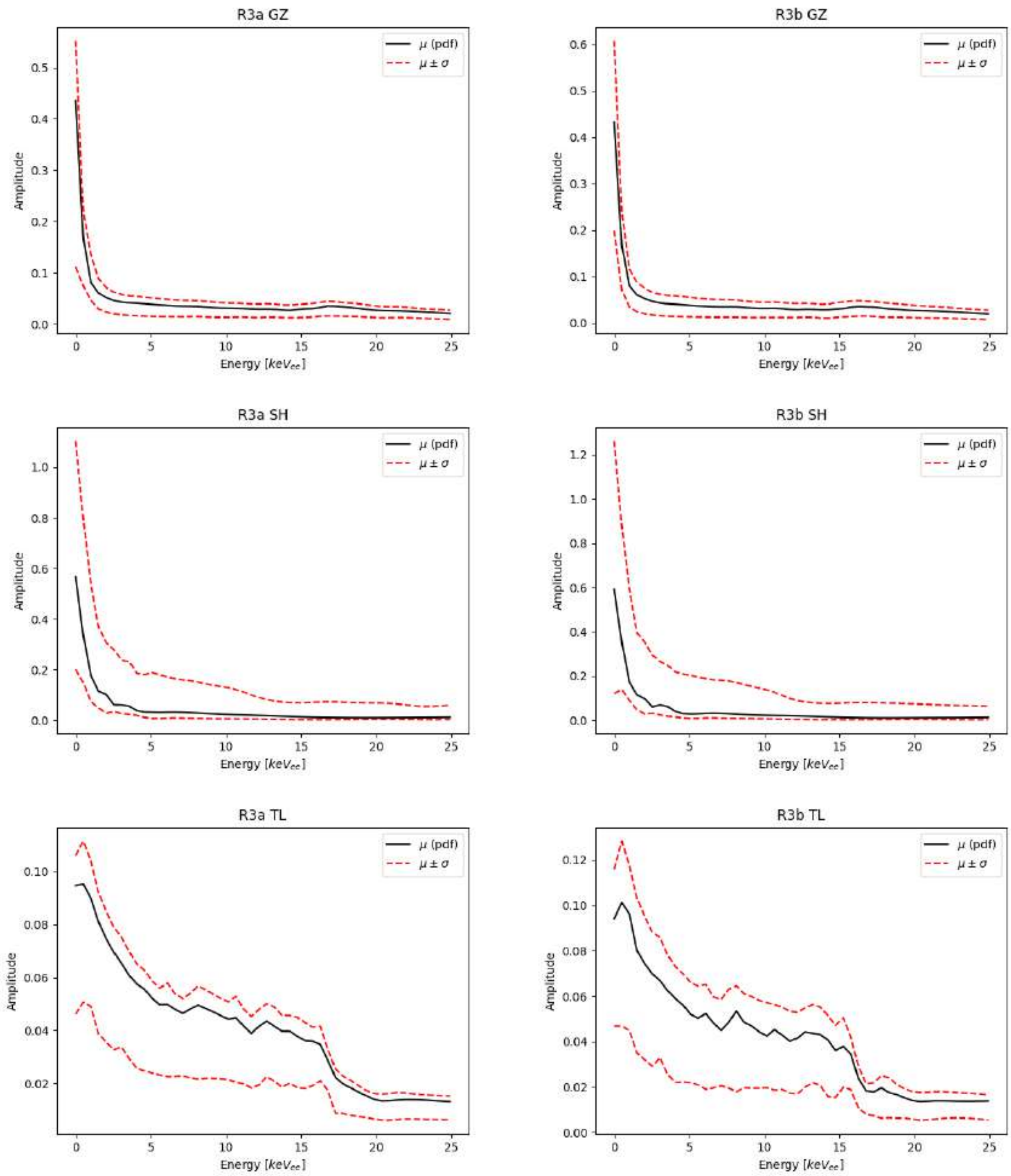

FIGURE 4.10: Smoothed surface background models for CDMSlite R3 using KDE: Ge ZiP (top), Side Housing (middle), and Top Lid (bottom). The red dashed lines show the 1σ upper and lower uncertainty bands. Adapted from Ref. [32].

4.10 Likelihood Construction

A key methodological advancement in this analysis is the use of the PLR technique with a comprehensive treatment of nuisance parameters. Unlike traditional approaches, such as Poisson upper limits or the Optimum Interval method, which lack explicit background modeling incorporation, our analysis employs a statistically rigorous PLR framework. This incorporates detailed signal and background models, alongside pseudo-data to estimate expected sensitivity bands. Data from CDMSlite Runs 2 and 3, totaling approximately 110 kg-days of exposure, are combined in a unified statistical framework. Systematic uncertainties, including those from energy resolution and detection efficiency, are embedded directly into the likelihood, ensuring full propagation into the final sensitivity. This unified approach enables consistent statistical interpretation and improves reproducibility.

We adopt an unbinned PLR method to derive upper limits on the axio-electric coupling and kinetic mixing parameter. The likelihood function is built using signal and background PDFs, and fits are performed to extract the best-fit signal strength.

We search for dark absorption signals (ALPs and dark photons) over the mass range 40 eV$/c^2$ to 25 keV$/c^2$. Notably, the lower bound of this range extends below the detector's trigger threshold (56 eV$_{ee}$ for CDMSliteR2 and 70 $_{ee}$ for CDMSliteR3), where signal efficiency drops to zero. This extension is feasible because the expected signal shape is Gaussian: even when the true energy lies below the threshold, a small fraction of events may be detected due to the Gaussian tail extending above the threshold. The lower bound is set approximately 3σ below the CDMSlite R2 threshold (56 eV$_{\mathrm{ee}}$). However, due to rapidly decreasing efficiency in this region, the resulting exclusion limits quickly weaken below the threshold.

At low energies (below ~100 eV), the CDMSlite R2 dataset exhibits a dominant low-frequency (LFN) noise background originating from vibrations of the cryocooler used to keep the electronics cold. Despite the application of analysis cuts to mitigate this effect, these noise events, with highly variable pulse shapes, pose challenges for accurate modeling. Consequently, the background model in this energy region is less reliable. Due to this unmodeled LFN background, our analysis focuses on setting robust upper limits rather than pursuing a potential discovery of ALPs or dark photons.

An alternative strategy would be to use only the CDMSlite R3 data, where low-frequency noise is better controlled, permitting a discovery-oriented search. However, this would reduce the total exposure (R2 has twice exposure of R3) and thereby degrade sensitivity.

The likelihood functions are constructed separately for each sub-run—R2, R3a, and R3b—and then combined in a joint fit. The parameter of interest is the number of signal events (S_N) from dark absorption, in the global fit. Thus, S_N represents the total signal across R2, R3a, and R3b, rather than separate components.

The variables and definitions used in the likelihood framework are summarized in Table 4.7. We follow the notation convention from the inelastic WIMP search analysis.

4.10.1 Likelihood function

The likelihood function used in the dark matter absorption search consists of three main components:

Poisson Term

This term constrains the total number of predicted events in the model to match the observed number of events in the dataset. It accounts for Poisson fluctuations in the overall event rate and is applied separately for the R2 and R3 data sets.

TABLE 4.7: Variables used in the likelihood function

Variable	Definition	Type
N	Number of events in the data	Constant
n	Iterator over N data events	Iterator
E_i	Energy of event i	Constant
S_N or ν_χ	Number of signal events	Free
f_χ	Signal PDF	Function
b	Iterator over bulk backgrounds	Iterator
ν_b	Number of events in bulk background b	Free
f_b	PDF of background b	Function
sb	Iterator over surface backgrounds (SH, GZ, TL)	Iterator
ν_{sb}	Number of events in surface background sb	Free
ρ_{sb}	Event density of surface background sb	Function
i, j	Iterators over nuisance parameters	Iterator
$x_{k_{i/j}}$	Value of parameter k	Constrained
$\mu_{k_{i/j}}$	Expected value of parameter k	Constant
V	Covariance matrix for systematics	Constant
d	Dimension of Gaussian constraint	Constant
s	Surface background morphing parameter	Constrained
S	Covariance matrix for surface morphing	Constant
r	Resolution nuisance parameter	Constrained
R	Covariance matrix for resolution uncertainty	Constant
Ξ	Efficiency morphing parameter	Constrained
σ_Ξ	Uncertainty in Ξ	Constant

$$\mathcal{L}_{\text{Poisson}} = \frac{\left(\nu_\chi + \sum_b \nu_b\right)^N}{N!} \exp\left[-\left(\nu_\chi + \sum_b \nu_b\right)\right] \tag{4.20}$$

Signal and Background Model Terms

These terms form the core of the likelihood function. They incorporate the PDFs for both the signal and background components, describing the expected distribution of events and assessing the likelihood of each observed event arising from a specific model. The PDFs are tailored for each dataset, R2, R3a, and R3b, due to differences in detector resolution and detection efficiency.

$$\mathcal{L}_{\chi,\mathrm{b}} = \prod_{n=1}^{N} \left[\nu_\chi f_\chi(E_n) + \sum_b \nu_b f_b(E_n) + \sum_{sb} \rho_{sb}(E_n) \right] \tag{4.21}$$

Constraint Term

This component imposes external constraints on the nuisance parameters. These constraints are derived from auxiliary measurements and help stabilize the fit while accounting for systematic uncertainties. We assume that these uncertainties follow Gaussian distributions and incorporate a multivariate Gaussian constraint in the analysis.

$$\mathcal{L}_{\mathrm{constrain}} = \frac{1}{(2\pi)^{d/2}|V|^{1/2}} \exp\left(-\frac{1}{2}(x_i - \mu_{x_i})^T V_{ij}^{-1} (x_j - \mu_{x_j}) \right) \tag{4.22}$$

Here, V is the covariance matrix of dimension $d \times d$.

These constraints fall into three categories:

- Surface background morphing
- Resolution parameters,
- Efficiency parameters.

The total constrained log-likelihood term for CDMSlite R2 and R3 data is the sum of individual log-likelihood components:

$$\begin{aligned} \ln \mathcal{L}_{\mathrm{constrain}} = \; & \ln(\mathcal{L}_{\mathrm{surf}}^{\mathrm{R2}}) + \ln(\mathcal{L}_{\mathrm{surf}}^{\mathrm{R3}}) + \ln(\mathcal{L}_{\mathrm{res}}^{\mathrm{R2}}) + \ln(\mathcal{L}_{\mathrm{res}}^{\mathrm{R3a}}) + \ln(\mathcal{L}_{\mathrm{res}}^{\mathrm{R3b}}) + \\ & \ln(\mathcal{L}_{\mathrm{eff}}^{\mathrm{R2}}) + \ln(\mathcal{L}_{\mathrm{eff}}^{\mathrm{R3a}}) + \ln(\mathcal{L}_{\mathrm{eff}}^{\mathrm{R3b}}) \end{aligned} \tag{4.23}$$

Which expands to:

$$
\begin{aligned}
\ln \mathcal{L}_{\text{Constrain}} = & -\frac{1}{2}\sum_{i,j=1}^{2}(s_i^{\text{R2}} - \mu_{s_i}^{\text{R2}})^T S_{\text{R2}}^{-1}(s_j^{\text{R2}} - \mu_{s_j}^{\text{R2}}) \\
& -\frac{1}{2}\sum_{i,j=1}^{3}(s_i^{\text{R3}} - \mu_{s_i}^{\text{R3}})^T S_{\text{R3}}^{-1}(s_j^{\text{R3}} - \mu_{s_j}^{\text{R3}}) \\
& -\frac{1}{2}\sum_{i,j=1}^{3}(r_i^{\text{R2}} - \mu_{r_i}^{\text{R2}})^T R_{\text{R2}}^{-1}(r_j^{\text{R2}} - \mu_{r_j}^{\text{R2}}) \\
& -\frac{1}{2}\sum_{i,j=1}^{3}(r_i^{\text{R3a}} - \mu_{r_i}^{\text{R3a}})^T R_{\text{R3a}}^{-1}(r_j^{\text{R3a}} - \mu_{r_j}^{\text{R3a}}) \\
& -\frac{1}{2}\sum_{i,j=1}^{3}(r_i^{\text{R3b}} - \mu_{r_i}^{\text{R3b}})^T R_{\text{R3b}}^{-1}(r_j^{\text{R3b}} - \mu_{r_j}^{\text{R3b}}) \\
& -\frac{(\Xi^{\text{R2}} - \mu_{\Xi}^{\text{R2}})^2}{2(\sigma_{\Xi}^{\text{R2}})^2} - \frac{(\Xi^{\text{R3a}} - \mu_{\Xi}^{\text{R3a}})^2}{2(\sigma_{\Xi}^{\text{R3a}})^2} - \frac{(\Xi^{\text{R3b}} - \mu_{\Xi}^{\text{R3b}})^2}{2(\sigma_{\Xi}^{\text{R3b}})^2}
\end{aligned}
\tag{4.24}
$$

4.10.2 Total Likelihood

The full likelihood is the product of the three terms described above. In practice, we work with the log-likelihood:

$$
\begin{aligned}
\ln \mathcal{L}_{\text{total}} =\; & \ln \mathcal{L}_{\text{Poisson}} + \ln \mathcal{L}_{\chi,\text{b}} + \ln \mathcal{L}_{\text{constrain}} \\
=\; & -\left(\nu_{\chi}^{R2} + \sum_{b} \nu_{b}^{R2} + \sum_{sb} \nu_{sb}^{R2}\right) - \left(\nu_{\chi}^{R3} + \sum_{b} \nu_{b}^{R3} + \sum_{sb} \nu_{sb}^{R3}\right) \\
& + \sum_{n=1}^{N^{R2}} \ln\left(\nu_{\chi}^{R2} f_{\chi}^{R2}(E_n) + \sum_{b} \nu_{b}^{R2} f_{b}^{R2}(E_n) + \sum_{sb} \rho_{sb}^{R2}(E_n)\right) \\
& + \sum_{n=1}^{N^{R3a}} \ln\left(\nu_{\chi}^{R3} f_{\chi}^{R3a}(E_n) + \sum_{b} \nu_{b}^{R3} f_{b}^{R3a}(E_n) + \sum_{sb} \rho_{sb}^{R3a}(E_n)\right) \\
& + \sum_{n=1}^{N^{R3b}} \ln\left(\nu_{\chi}^{R3} f_{\chi}^{R3b}(E_n) + \sum_{b} \nu_{b}^{R3} f_{b}^{R3b}(E_n) + \sum_{sb} \rho_{sb}^{R3b}(E_n)\right) \\
& - \frac{1}{2} \sum_{i,j=1}^{2} (s_i^{\text{R2}} - \mu_{s_i}^{\text{R2}})^T S_{\text{R2}}^{-1} (s_j^{\text{R2}} - \mu_{s_j}^{\text{R2}}) \\
& - \frac{1}{2} \sum_{i,j=1}^{3} (s_i^{\text{R3}} - \mu_{s_i}^{\text{R3}})^T S_{\text{R3}}^{-1} (s_j^{\text{R3}} - \mu_{s_j}^{\text{R3}}) \\
& - \frac{1}{2} \sum_{i,j=1}^{3} (r_i^{\text{R2}} - \mu_{r_i}^{\text{R2}})^T R_{\text{R2}}^{-1} (r_j^{\text{R2}} - \mu_{r_j}^{\text{R2}}) \\
& - \frac{1}{2} \sum_{i,j=1}^{3} (r_i^{\text{R3a}} - \mu_{r_i}^{\text{R3a}})^T R_{\text{R3a}}^{-1} (r_j^{\text{R3a}} - \mu_{r_j}^{\text{R3a}}) \\
& - \frac{1}{2} \sum_{i,j=1}^{3} (r_i^{\text{R3b}} - \mu_{r_i}^{\text{R3b}})^T R_{\text{R3b}}^{-1} (r_j^{\text{R3b}} - \mu_{r_j}^{\text{R3b}}) \\
& - \frac{(\Xi^{\text{R2}} - \mu_{\Xi}^{\text{R2}})^2}{2(\sigma_{\Xi}^{\text{R2}})^2} - \frac{(\Xi^{\text{R3a}} - \mu_{\Xi}^{\text{R3a}})^2}{2(\sigma_{\Xi}^{\text{R3a}})^2} - \frac{(\Xi^{\text{R3b}} - \mu_{\Xi}^{\text{R3b}})^2}{2(\sigma_{\Xi}^{\text{R3b}})^2}
\end{aligned}
\tag{4.25}
$$

Each of these terms contributes distinctly to the final fit: - $\mathcal{L}_{\text{Poisson}}$ constrains the total observed events, - $\mathcal{L}_{\chi,\text{b}}$ determines the shape agreement between data and model, and - $\mathcal{L}_{\text{constrain}}$ regulates the influence of nuisance parameters.

4.10.3 Parameter Priors and Constraints

In order to find the best-fit parameters, we maximize the likelihood (or, equivalently, minimize the negative log-likelihood). This optimization is performed using `iminuit`, a Python interface to the widely used `MINUIT` algorithm.

To avoid local minima that do not reflect physical reality, the parameters are bounded with physically motivated limits. For instance:

- Background event counts are constrained to be non-negative and not greater than the number of observed events in each sub-run.
- Surface background morphing parameters are allowed to vary within $\pm 5\sigma$.
- Resolution parameters are permitted within $\pm 10\times$ their nominal estimates.

The priors and constraints used for each parameter in the likelihood analysis are summarized in Table 4.8.

The Gaussian priors are based on independent measurements or calibrations. For instance, surface backgrounds are constrained using α-event rate measurement from iZIP detectors:

- **R2:** SH2: 24.0 ± 2.0; GZ2: 21.6 ± 3.4
- **R3:** TL3: 158.4 ± 16.6; SH3: 22.3 ± 1.4; GZ3: 23.5 ± 5.9

The efficiency and resolution models are similarly constrained by data-driven estimations. These constraints help stabilize the fit and incorporate systematic uncertainties.

We developed the likelihood model for the dark absorption process within the `pylim` software framework primarily made for WIMP search developed by the SuperCDMS Collaboration.

TABLE 4.8: Priors and ranges of parameters used in the likelihood.

Variable	Definition	Type	Values / Ranges
$S_N \equiv \nu_\chi$	Number of signal events	Free	—
ν_b	Bulk background events	Free	$[0, N_{\text{obs}}]$
ν_{sb}	Surface background events	Gaussian constrained	R2: SH2: 24.0 ± 2.0, GZ2: 21.6 ± 3.4 R3: TL3: 158.4 ± 16.6, SH3: 22.3 ± 1.4, GZ3: 23.5 ± 5.9
μ_s	Nominal surface morphing	Constant	0 (all detectors)
s	Surface morphing parameter	Gaussian constrained	[-5σ, +5σ]
S	Covariance matrix (surface morphing)	Constant	$R2 : \begin{bmatrix} 1.21 & 0.97 \\ 0.97 & 0.94 \end{bmatrix}$ $R3 : \begin{bmatrix} 1.09 & 0.87 & 0.93 \\ 0.87 & 1.14 & 0.90 \\ 0.93 & 0.90 & 1.20 \end{bmatrix}$
μ_r	Nominal resolution parameters (σ_E, ϵF, A)	Constant	$R2 :\ \sigma_E = 9.26 \times 10^{-3},\ \epsilon F = 0.64 \times 10^{-3},\ A = 5.68 \times 10^{-3}$ $R3a :\ \sigma_E = 9.87 \times 10^{-3},\ \epsilon F = 0.87 \times 10^{-3},\ A = 4.94 \times 10^{-3}$ $R3b :\ \sigma_E = 12.7 \times 10^{-3},\ \epsilon F = 0.80 \times 10^{-3},\ A = 5.49 \times 10^{-3}$
r	Resolution nuisance parameter	Gaussian constrained	$[0.0001, 0.1]$
R	Covariance matrix (resolution)	Constant	$R2 : \begin{bmatrix} 1.21\times10^{-8} & -2.29\times10^{-10} & 1.73\times10^{-9} \\ -2.29\times10^{-10} & 1.21\times10^{-8} & -1.02\times10^{-7} \\ 1.73\times10^{-9} & -1.02\times10^{-7} & 8.84\times10^{-7} \end{bmatrix}$ $R3a : \begin{bmatrix} 1.60\times10^{-9} & -3.43\times10^{-11} & 3.07\times10^{-10} \\ -3.43\times10^{-11} & 1.47\times10^{-8} & -1.47\times10^{-7} \\ 3.07\times10^{-10} & -1.47\times10^{-7} & 1.63\times10^{-6} \end{bmatrix}$ $R3b : \begin{bmatrix} 1.60\times10^{-9} & -4.23\times10^{-11} & 3.39\times10^{-10} \\ -4.23\times10^{-11} & 1.47\times10^{-8} & -1.32\times10^{-7} \\ 3.39\times10^{-10} & -1.32\times10^{-7} & 1.32\times10^{-6} \end{bmatrix}$
μ_Ξ	Nominal efficiency morphing parameter	Constant	0 (all subruns)
σ_Ξ	Efficiency morphing uncertainty	Constant	1
Ξ	Efficiency morphing parameter	Gaussian constrained	[-5σ, +5σ]

4.11 Upper Limit Estimation Using Profile Likelihood Ratio methods

Upper limits on the axio-electric coupling and kinetic mixing parameters are derived using the PLR approach. This method incorporates both signal and background components into the likelihood function, as illustrated in the flowchart in Fig. 4.2.

Procedure Summary

1. **Likelihood Construction:** The likelihood function is constructed using both signal and background PDFs:

    - The signal PDF is a mono-energetic response modeled as a Gaussian peak, with its width determined by the detector energy resolution. Since both ALPs and dark photons result in monoenergetic energy depositions, a common signal model is used for both.
    - The background PDF is obtained either by fitting experimental data using parameterized forms of known background components or by simulation.

    Throughout the analysis, it is assumed that either ALPs or dark photons constitute the entirety of dark matter in the Universe.

2. **Experimental Data Input:** The input to the likelihood function is the filtered experimental energy spectrum from CDMSlite Run 2 and Run 3.

3. **Parameters of Interest and Nuisance Parameters:** The parameter of interest is the signal count N_s. All other parameters, including those that describe the background shape, resolution, and detection efficiency, are treated as nuisance parameters and profiled during the fit.

4. **Likelihood Maximization:** The likelihood is maximized in two different ways:

   - *Unconditional fit:* All parameters (including N_s) are allowed to vary freely to maximize the likelihood globally. Examples for CDMSlite Run 2 and Run 3 likelihood fits at a test mass of 10 keV/c^2 are shown in Fig. 4.11 and Fig. 4.12.

   - *Conditional fit:* The signal yield N_s is fixed at a set of values, and the likelihood is maximized only over the nuisance parameters. This produces the conditional likelihood curve as a function of N_s.

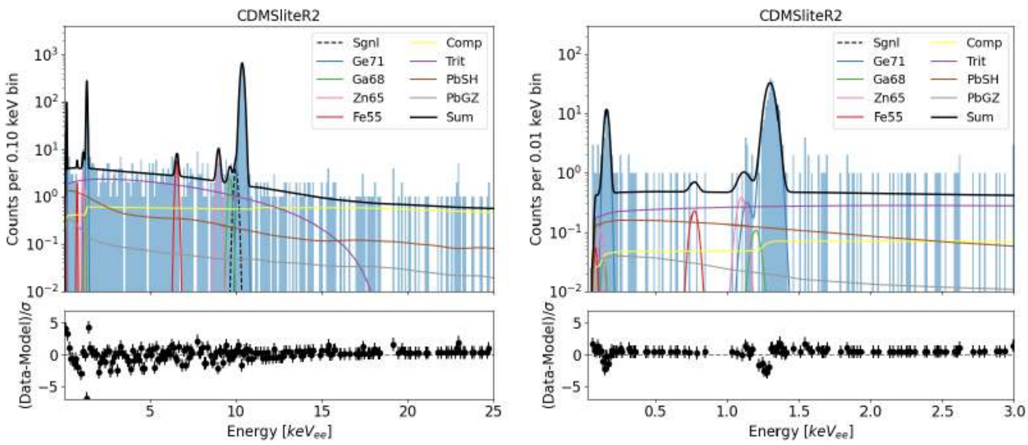

FIGURE 4.11: Unconditional likelihood fit for CDMSlite Run 2 for an axion mass of 10 keV/c^2. The black dashed line shows the best-fit signal model, while the colored solid lines correspond to the best-fit background models. Left: full analysis energy range; right: zoomed-in view.

5. **Profile Likelihood Ratio:** The profile likelihood ratio λ is defined as the ratio of the maximum likelihood under a fixed signal count N_s (conditional) to the global maximum likelihood (unconditional):

$$\lambda(N_s) = \frac{\mathcal{L}(N_s, \hat{\hat{\theta}})}{\mathcal{L}(\hat{N}_s, \hat{\theta})} \tag{4.26}$$

where:

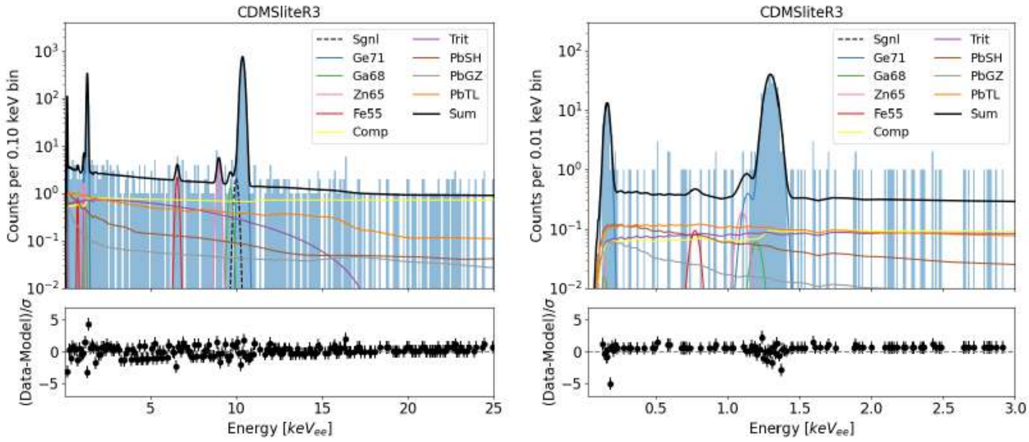

FIGURE 4.12: Unconditional likelihood fit for CDMSlite Run3 for an axion mass of 10 keV/c^2. The black dashed line shows the best-fit signal model, while the colored solid lines correspond to the best-fit background models. Left: full analysis energy range; right: zoomed-in view.

- N_s: Signal event count (parameter of interest).
- $\{\theta\}$: Set of nuisance parameters (e.g., background shape, resolution, efficiency).
- $\hat{N}_s$: Best-fit value of N_s from the "unconditional" fit (maximizes $\mathcal{L}(N_s, \theta)$ over both N_s and θ).
- $\hat{\theta}$: Best-fit nuisance parameters from the "unconditional" fit.
- $\hat{\hat{\theta}}$: Best-fit nuisance parameters from the "conditional" fit, with N_s held fixed.

Since the denominator represents the global maximum, $\lambda(N_s) \leq 1$. The PLR is thus a function of N_s only.

6. **Test Statistic (One-Sided Upper Limit):**

To determine an upper limit on the signal yield N_s, we use the profile likelihood ratio test statistic defined as

$$q(N_s) = \begin{cases} -2\ln\lambda(N_s), & \hat{N}_s \leq N_s \\ 0, & \hat{N}_s > N_s, \end{cases} \tag{4.27}$$

where $\lambda(N_s)$ is the profile likelihood ratio and $\hat{N}_s$ denotes the best–fit estimator of the signal yield obtained from maximizing the likelihood.

This one-sided definition is appropriate for constructing upper limits. If the fitted signal strength satisfies $\hat{N}_s > N_s$, the data represent an upward fluctuation relative to the tested value N_s and therefore do not indicate incompatibility with that hypothesis. Such outcomes are not included in the rejection region of the test, and the test statistic is set to zero in this case. Consequently, larger values of $q(N_s)$ correspond to increasing disagreement between the hypothesized signal yield N_s and the observed data.

7. **Asymptotic Distribution and 90% Upper Limit:**

In the asymptotic regime, the distribution of the test statistic follows the results derived in Ref. [33]. Because the signal yield is physically constrained to be non-negative ($N_s \geq 0$), the estimator $\hat{N}_s$ can lie on the physical boundary when the true signal is zero. Consequently, under the background-only hypothesis the asymptotic distribution of the test statistic becomes a mixture of a χ^2 distribution with one degree of freedom and a delta function at zero,

$$f(q) = \frac{1}{2}\delta(q) + \frac{1}{2}\chi_1^2(q).$$

This behavior arises because, in approximately half of the experimental realizations, the unconstrained estimator of the signal yield would be negative and is therefore projected onto the physical boundary at $N_s = 0$. The remaining realizations follow a χ^2 distribution with one degree of freedom.

The corresponding cumulative distribution function (CDF) for $q > 0$ is

$$F(q) = 0.5 + 0.5\,F_{\chi_1^2}(q).$$

The 90% confidence level upper limit corresponds to the value of q for which the CDF reaches 0.9,

$$F(q) = 0.9.$$

Solving this relation gives

$$q = 1.64.$$

Therefore, the 90% confidence level upper limit on the signal yield is obtained by determining the value of N_s for which

$$q(N_s) = 1.64.$$

Figure 4.13 shows the test statistic as a function of N_s for a test axion mass of 0.692 keV/c^2, together with the cumulative distribution function of the test statistic. The p-value of 0.1 corresponds to $q = 1.64$.

8. **Event Rate Limits at Various ALP/Dark Photon Masses:** The upper limit on the event rate is determined using the test statistic derived from the PLR method, evaluated for various ALP and dark photon masses. For each mass hypothesis, a

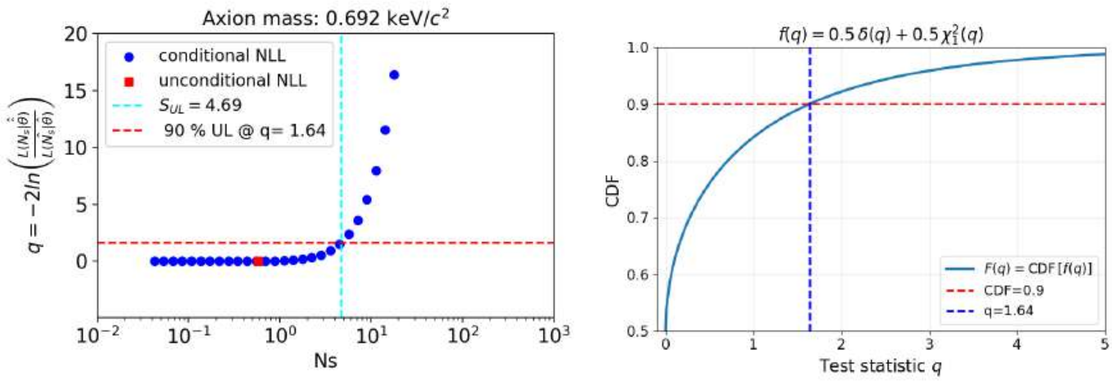

FIGURE 4.13: (Left) Estimation of the 90% upper limit on the event rate for ALPs with a mass of 0.155 keV/c^2. The horizontal line at $q = 1.64$ corresponds to the 90% confidence level threshold for the signal strength N_s. (Right) Distribution of the test statistic q for the one-sided upper-limit test. The asymptotic mixture distribution $0.5\delta(q) + 0.5\chi_1^2$ is shown. The cumulative distribution function reaches 0.9 at $q = 1.64$, defining the 90% confidence level threshold.

90% confidence level upper limit is calculated. The results from CDMSlite R2 , CDMSlite R3, and their combination CDMSlite R2+R3 are shown in Fig. 4.14.

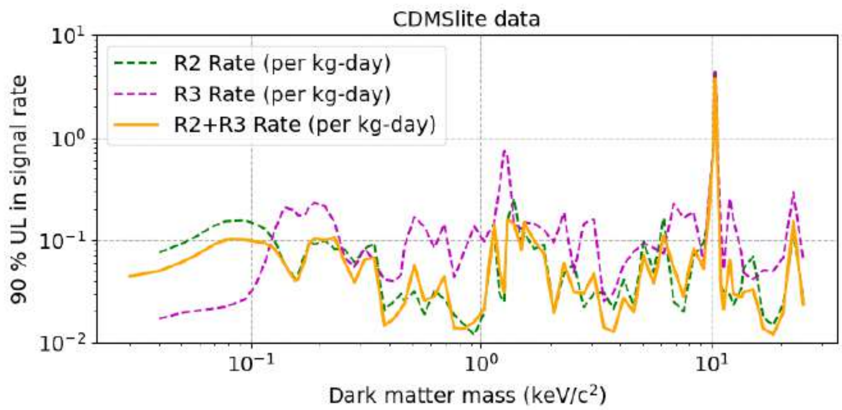

FIGURE 4.14: 90% upper limits on the event rate for the dark absorption process using CDMSlite R2 and R3 data. Since both axion-like particle and dark photon absorption processes produce Gaussian-shaped signals with widths determined by the detector resolution, the experimental upper limits on the event rate are identical for both cases. The event rate shown here corresponds to the dark photon scenario.

9. **90% Upper Limit Estimation on the Coupling Parameter:**

The experimental upper limit on the event rate can be translated into an upper limit on the coupling constants using theoretical predictions for the signal rate. Once the 90% confidence level upper limit on the event rate is obtained from the data, the corresponding constraint on the coupling strength is derived using the model-dependent relations given in Eqs. 4.9 and 4.12. These relations connect the predicted event rate to the underlying coupling parameters of the respective models.

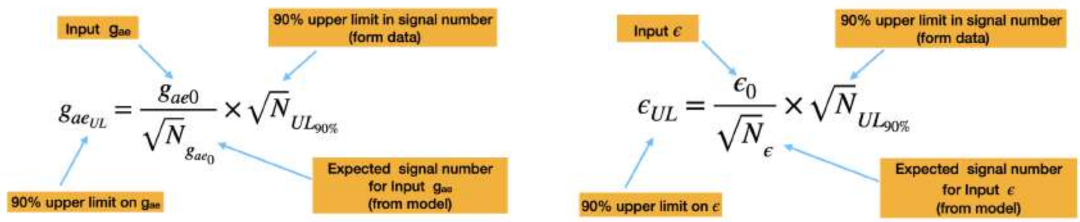

FIGURE 4.15: Procedure for estimating the upper limits on the coupling strengths using theoretical signal-rate predictions (left: ALPs, right: dark photons).

For a given coupling strength, the theoretical model predicts the expected number of signal events. By comparing this prediction with the experimentally observed upper limit, we derive the 90% upper limit on the coupling parameters.

10. **Final Exclusion Curves:** After obtaining the upper limits on the coupling strength across all mass points, we construct the exclusion curves for the axio-electric coupling and the kinetic mixing parameter. Figure 4.16 presents the exclusion limits derived using the PLR method and compares them to previously published results based on the Poisson upper limit approach.

    A factor of approximately two improvement is observed in the PLR limits compared to Poisson-based limits, and up to a factor of five near the L- and M-shell peaks in germanium. For the K-shell, the earlier Poisson limit was derived using a combined exposure of 440 kg-days from CDMSlite and iZIP data. In contrast, the PLR limit from just 110 kg-days is competitive with that result. Below ∼120 eV/c^2, low-frequency noise (LFN) dominates and remains unmodeled, resulting in the PLR limit converging with the Poisson limit in that region.

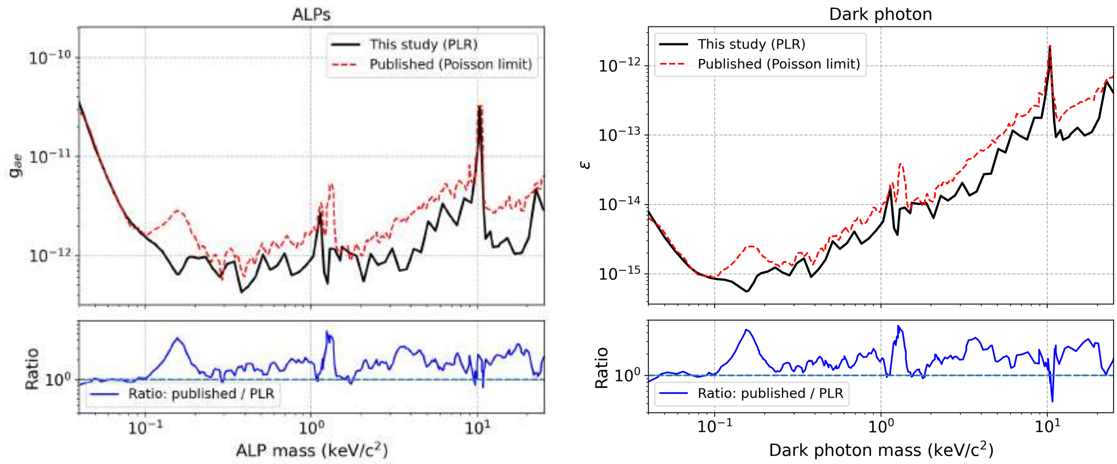

FIGURE 4.16: 90% upper limits on the axio-electric coupling for ALPs and the kinetic mixing parameter for dark photons obtained using the PLR method with CDMSlite R2+R3 data. The results are compared with previously published dark absorption limits from SuperCDMS Soudan based on the Poisson upper limit method.

4.12 Pseudo Limit / Expected Sensitivity Calculations

To estimate the expected sensitivity of our experiment to ALPs and dark photons, pseudo-datasets based on a background-only hypothesis are used. These pseudo-datasets are created by first fitting the filtered CDMSlite data using only background components—excluding any signal contribution. The best-fit parameters from these fits are then used to generate multiple pseudo-datasets via random sampling, simulating what the data would look like under the background-only assumption.

Since these pseudo-datasets do not include any signal component, they serve as a reliable baseline for evaluating the experiment's sensitivity in the absence of a true dark absorption signal. To ensure consistency with previous SuperCDMS analyses, we adopt pseudo-datasets originally generated for the WIMP search via inelastic scattering processes [24]. These are equally applicable for both WIMP and dark absorption searches, as they are derived solely from the same background model fit. Thirty such pseudo-datasets for CDMSlite Run 2 and Run 3 are shown in Fig. 4.17.

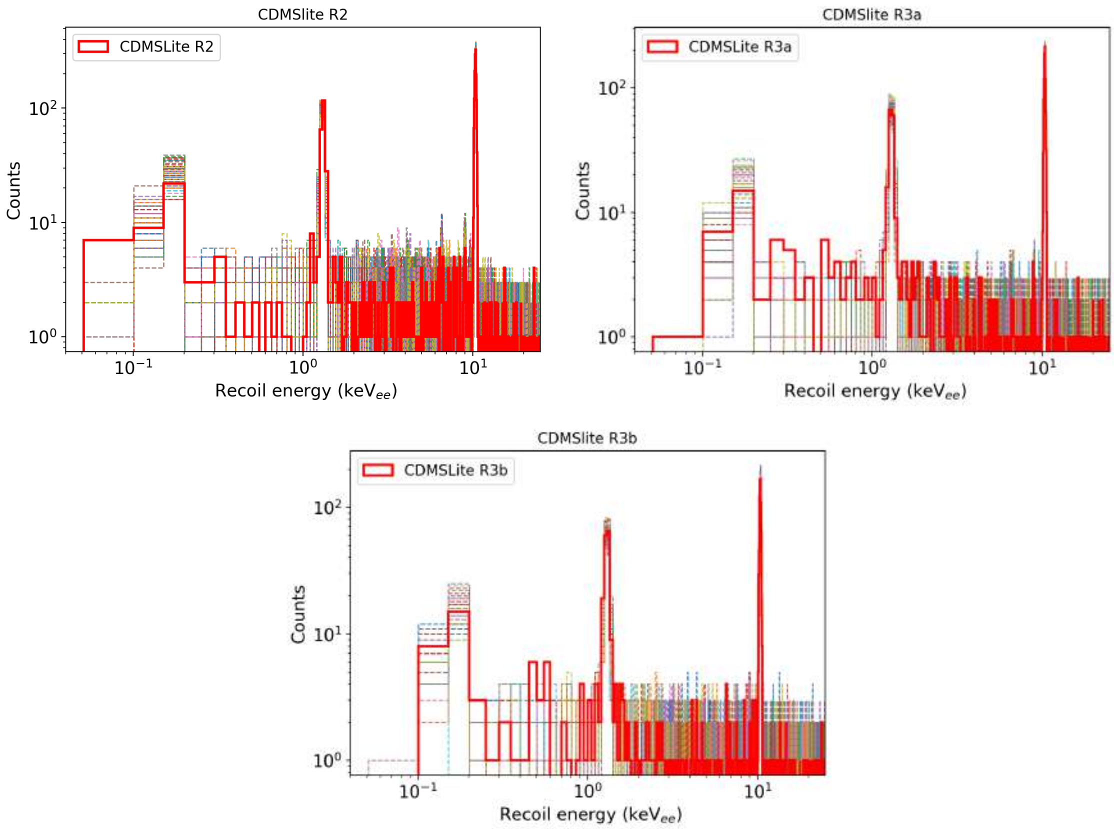

FIGURE 4.17: Pseudo-datasets generated by randomly sampling the best-fit parameters from a background-only fit to the CDMSlite data. The red solid line histogram corresponds to the experimental data whereas the dashed colour lines are pseudo data. **Left:** CDMSlite Run 2 shows an excess at low energies due to unmodeled low-frequency noise (LFN). **Middle and Right:** CDMSlite Run 3a and 3b. These pseudo-datasets are the same as those used in the SuperCDMS inelastic dark matter search analysis, ensuring consistency across studies.

Each pseudo-dataset is analyzed to derive a 90% upper limit on the coupling parameter across a range of ALP and dark photon masses. We used 100 pseudo-datasets, and obtained a distribution of upper limits at each mass point. The spread in these distributions reflects the statistical uncertainties associated with the analysis. For each mass, the 1σ uncertainty band is extracted, providing a quantitative estimate of the expected sensitivity range under the background-only hypothesis. The resulting upper limits and sensitivity bands from

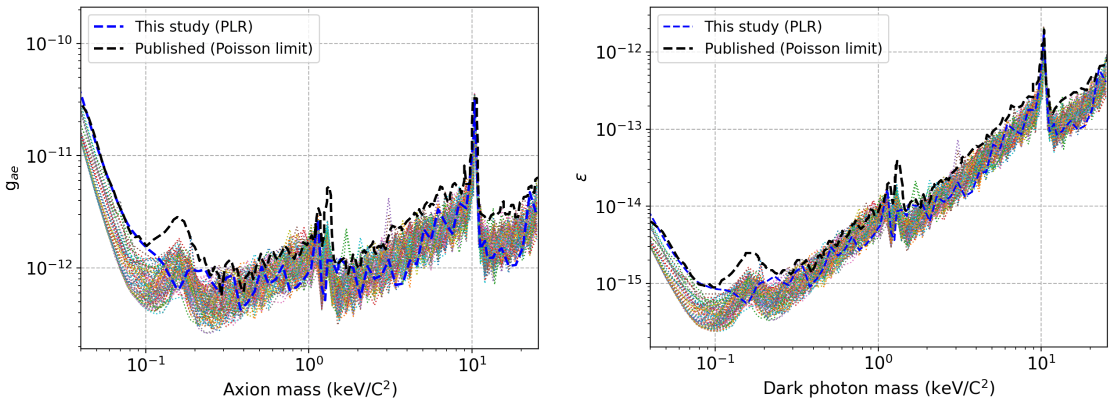

FIGURE 4.18: 90% upper limits on the axio-electric coupling for ALPs (left) and the kinetic mixing parameter for dark photons (right), derived using the PLR method. The blue dashed line shows the PLR limit from CDMSlite, and the black dashed line shows the Poisson-based limit from SuperCDMS Soudan. Coloured dotted curves represent limits from individual pseudo-datasets.

the pseudo-datasets are shown in Fig. 4.18. The blue dashed line represents the exclusion limit from the PLR method applied to the data, while the black dashed line shows the Poisson-based limit from SuperCDMS Soudan, which does not assume any background modeling.

Below approximately 120 eV/c^2, the experimental limit deteriorates due to unmodeled LFN, leading to convergence between the PLR and Poisson limits. Above this threshold, the experimental PLR limit lies within the 2σ sensitivity band in 91% of the pseudo-datasets, consistent with the expected 95%, demonstrating the robustness of the expected sensitivity estimation in regions unaffected by LFN.

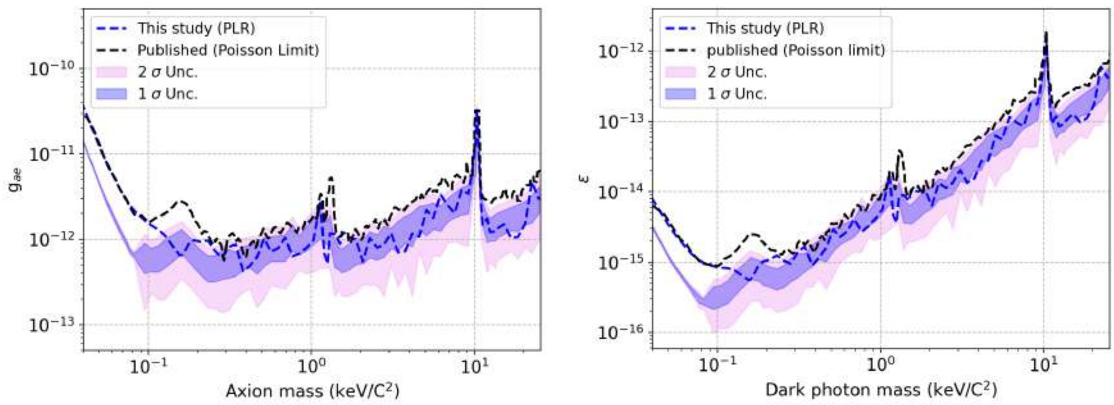

FIGURE 4.19: 90% upper limits on the axio-electric coupling for ALPs (left) and the kinetic mixing parameter for dark photons (right), derived using the PLR method. The colored bands represent the 1σ and 2σ sensitivity ranges expected from pseudo-datasets under the background-only hypothesis.

4.13 Summary and Conclusions

We have presented 90% upper limits on the axio-electric coupling constants for ALPs and the kinetic mixing parameters for dark photons, derived using the PLR method. This approach incorporates detailed, data-driven background models, enabling us to probe regions of parameter space that were previously inaccessible in SuperCDMS analyses.

Our results demonstrate an overall improvement of nearly a factor of two over the previously published SuperCDMS dark absorption limits using CDMSlite data. Notably, in energy regions near the L- and M-shell peaks of germanium, we achieve up to a five-fold enhancement in sensitivity. The use of the PLR method allows for a more rigorous treatment of systematic uncertainties through the profiling of nuisance parameters, further strengthening the robustness of our constraints.

At low energies, around and below 100 eV/c^2, the presence of unmodeled low-frequency noise (LFN) causes the PLR-derived limits to converge with earlier results that did not employ background modeling. However, at higher energies, where previous analyses

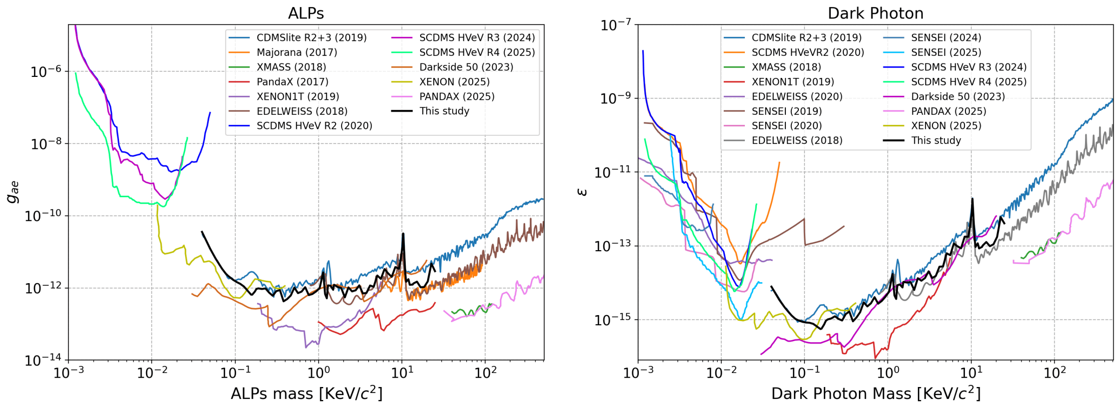

FIGURE 4.20: 90% upper limits on the axio-electric coupling for axion-like particles (left) and on the kinetic mixing parameter for dark photons (right), derived using the PLR method. Results from this work are compared with the latest 90% UL limits from other studies SuperCDMS [8, 34, 35], EDELWEISS [36], Majorana [37], DarkSide [38], XENON [39], PandaX [40], XMASS [41], and SENSEI [42, 43].

combined CDMSlite and iZIP data totaling approximately 440 kg-days of exposure, our PLR-based limits are competitive, and in some cases superior, to those obtained using simpler Poisson-based upper-limit methods.

A comparison of our PLR-based results with the latest constraints from other dark matter experiments is shown in Fig. 4.20. While many of the excluded regions are also constrained by other leading experiments, our study demonstrates that improved statistical techniques and detailed background modeling can extract meaningful and competitive results from existing data. This work highlights the importance of advanced analysis methods and sets a strong precedent for future searches in the low-mass dark matter regime, particularly with next-generation detectors such as SuperCDMS SNOLAB.

Furthermore, the developments presented in this work, including the development of axion-like particle and dark photon signal models with in-medium effects, as well as the construction of a PLR analysis framework for dark matter absorption processes—can be directly applied to future analyses in the SuperCDMS SNOLAB experiment.

Bibliography

[1] Gary Steigman and Michael S. Turner. "Cosmological Constraints on the Properties of Weakly Interacting Massive Particles". *Nucl. Phys. B* 253 (1985), pp. 375–386.

[2] Gerard Jungman, Marc Kamionkowski, and Kim Griest. "Supersymmetric dark matter". *Phys. Rept.* 267 (1996), pp. 195–373. arXiv: hep-ph/9506380.

[3] Peter Svrcek and Edward Witten. "Axions in string theory". *JHEP* 2006.06 (2006), p. 051.

[4] Markus Kuster, Georg Raffelt, and Berta Beltrán. *Axions: Theory, cosmology, and experimental searches*. Vol. 741. Springer Science & Business Media, 2007.

[5] Bob Holdom. "Two U(1)'s and Epsilon Charge Shifts". *Phys. Lett. B* 166 (1986), pp. 196–198.

[6] Marco Battaglieri, Alberto Belloni, Aaron Chou, Priscilla Cushman, Bertrand Echenard, Rouven Essig, Juan Estrada, Jonathan L Feng, Brenna Flaugher, Patrick J Fox, et al. "US cosmic visions: new ideas in dark matter 2017: community report". *arXiv preprint arXiv:1707.04591* (2017).

[7] Jim Alexander, Marco Battaglieri, Bertrand Echenard, Rouven Essig, Matthew Graham, Eder Izaguirre, John Jaros, Gordan Krnjaic, Jeremy Mardon, David Morrissey, et al. "Dark sectors 2016 workshop: community report". *arXiv preprint arXiv:1608.08632* (2016).

[8] T Aralis, T Aramaki, Isaac J Arnquist, Elham Azadbakht, W Baker, Samir Banik, D Barker, Corey Bathurst, DA Bauer, LVS Bezerra, et al. "Constraints on dark photons and axionlike particles from the SuperCDMS Soudan experiment". *Phys. Rev. D* 101.5 (2020), p. 052008.

[9] R Agnese, T Aralis, T Aramaki, IJ Arnquist, E Azadbakht, W Baker, S Banik, D Barker, DA Bauer, T Binder, et al. "First dark matter constraints from a SuperCDMS single-charge sensitive detector". *Phys. Rev. Lett.* 121.5 (2018), p. 051301.

[10] DW Amaral, T Aralis, T Aramaki, IJ Arnquist, E Azadbakht, S Banik, D Barker, C Bathurst, DA Bauer, LVS Bezerra, et al. "Constraints on low-mass, relic dark matter candidates from a surface-operated SuperCDMS single-charge sensitive detector". *Phys. Rev. D* 102.9 (2020), p. 091101.

[11] D. S. Akerib et al. "Exclusion Limits on the WIMP-Nucleon Cross Section from the First Run of the Cryogenic Dark Matter Search in the Soudan Underground Laboratory". *Phys. Rev. D* 72 (2005), p. 052009. arXiv: astro-ph/0507190.

[12] Z. Ahmed et al. "Dark Matter Search Results from the CDMS II Experiment". *Science* 327 (2010), pp. 1619–1621. arXiv: 0912.3592 [astro-ph.CO].

[13] E. Aprile et al. "WIMP Dark Matter Search Using a 3.1 Tonne-Year Exposure of the XENONnT Experiment". *Phys. Rev. Lett.* 135.22 (2025), p. 221003. arXiv: 2502.18005 [hep-ex].

[14] J. Aalbers et al. "First Dark Matter Search Results from the LUX-ZEPLIN (LZ) Experiment". *Phys. Rev. Lett.* 131.4 (2023), p. 041002. arXiv: 2207.03764 [hep-ex].

[15] Zihao Bo et al. "Dark Matter Search Results from 1.54 Tonne·Year Exposure of PandaX-4T". *Phys. Rev. Lett.* 134.1 (2025), p. 011805. arXiv: 2408.00664 [hep-ex].

[16] Roberto D Peccei. "The Strong CP problem and axions". In: *Axions: Theory, Cosmology, and Experimental Searches*. Springer, 2008, pp. 3–17.

[17] R. D. Peccei and H. R. Quinn. "CP Conservation in the Presence of Instantons". *Phys. Rev. Lett.* 38 (1977), pp. 1440–1443.

[18] Steven Weinberg. "A New Light Boson?" *Phys. Rev. Lett.* 40 (1978), pp. 223–226.

[19] Frank Wilczek. "Problem of Strong P and T Invariance in the Presence of Instantons". *Phys. Rev. Lett.* 40 (1978), pp. 279–282.

[20] Jihn E. Kim and Gianpaolo Carosi. "Axions and the Strong CP Problem". *Rev. Mod. Phys.* 82 (2010), pp. 557–602.

[21] Particle Data Group. "Review of Particle Physics". *Prog. Theor. Exp. Phys.* 2024.8 (2024), p. 083C01.

[22] Georg G. Raffelt. "Astrophysical Axion Bounds". *Lect. Notes Phys.* 741 (2008), pp. 51–71.

[23] Joerg Jaeckel and Andreas Ringwald. "The Low-Energy Frontier of Particle Physics". *Annu. Rev. Nucl. Part. Sci.* 60 (2010), pp. 405–437.

[24] M. F. Albakry et al. “Search for low-mass dark matter via bremsstrahlung radiation and the Migdal effect in SuperCDMS”. *Phys. Rev. D* 107.11 (2023), p. 112013. arXiv: 2302.09115 [hep-ex].

[25] Yonit Hochberg, Belina von Krosigk, Eric Kuflik, and To Chin Yu. “Impact of Dark Compton Scattering on Direct Dark Matter Absorption Searches”. *Phys. Rev. Lett.* 128.19 (2022), p. 191801.

[26] R. Agnese et al. “New Results from the Search for Low-Mass Weakly Interacting Massive Particles with the CDMS Low Ionization Threshold Experiment”. *Phys. Rev. Lett.* 116.7 (2016), p. 071301. arXiv: 1509.02448 [astro-ph.CO].

[27] R. Agnese et al. “Search for Low-Mass Dark Matter with CDMSlite Using a Profile Likelihood Fit”. *Phys. Rev. D* 99.6 (2019), p. 062001. arXiv: 1808.09098 [astro-ph.CO].

[28] Yonit Hochberg, Tongyan Lin, and Kathryn M Zurek. “Absorption of light dark matter in semiconductors”. *Phys. Rev. D* 95.2 (2017), p. 023013.

[29] Roy F. Potter. “Germanium (Ge)”. In: *Handbook of Optical Constants of Solids*. Ed. by Edward D. Palik. Burlington: Academic Press, 1997, pp. 465 –478.

[30] B.L. Henke, E.M. Gullikson, and J.C. Davis. “X-Ray Interactions: Photoabsorption, Scattering, Transmission, and Reflection at E = 50-30,000 eV, Z = 1-92”. *Atomic Data and Nuclear Data Tables* 54.2 (1993), pp. 181 –342.

[31] M. J. Berger, J. H. Hubbell, S. M. Seltzer, J. Chang, Coursey, R. Sukumar, D. S. Zucker, and K. Olsen. *XCOM: Photon Cross Section Database (version 1.5)*. 2010.

[32] Daniel Jardin. “A Likelihood Search for Low-mass Dark Matter via Inelastic Scattering in SuperCDMS”. PhD Thesis. Southern Methodist University, 2019.

[33] Glen Cowan, Kyle Cranmer, Eilam Gross, and Ofer Vitells. “Asymptotic formulae for likelihood-based tests of new physics”. *Eur. Phys. J. C* 71 (2011). [Erratum: Eur.Phys.J.C 73, 2501 (2013)], p. 1554. arXiv: 1007.1727 [physics.data-an].

[34] D. W. Amaral et al. “Constraints on low-mass, relic dark matter candidates from a surface-operated SuperCDMS single-charge sensitive detector”. *Phys. Rev. D* 102.9 (2020), p. 091101. arXiv: 2005.14067 [hep-ex].

[35] M. F. Albakry et al. "Light dark matter constraints from SuperCDMS HVeV detectors operated underground with an anticoincidence event selection". *Phys. Rev. D* 111.1 (2025), p. 012006. arXiv: 2407.08085 [hep-ex].

[36] E. Armengaud et al. "Searches for electron interactions induced by new physics in the EDELWEISS-III Germanium bolometers". *Phys. Rev. D* 98.8 (2018), p. 082004. arXiv: 1808.02340 [hep-ex].

[37] N. Abgrall et al. "New limits on Bosonic Dark Matter, Solar Axions, Pauli Exclusion Principle Violation, and Electron Decay from the Majorana Demonstrator". *Phys. Rev. Lett.* 118.16 (2017), p. 161801. arXiv: 1612.00886 [nucl-ex].

[38] P. Agnes et al. "Search for Dark Matter Particle Interactions with Electron Final States with DarkSide-50". *Phys. Rev. Lett.* 130.10 (2023), p. 101002. arXiv: 2207.11968 [hep-ex].

[39] E. Aprile et al. "Light Dark Matter Search with Ionization Signals in XENON1T". *Phys. Rev. Lett.* 123.25 (2019), p. 251801. arXiv: 1907.11485 [hep-ex].

[40] Changbo Fu et al. "Limits on Axion Couplings from the First 80 Days of Data of the PandaX-II Experiment". *Phys. Rev. Lett.* 119.18 (2017), p. 181806. arXiv: 1707.07921 [hep-ex].

[41] K. Abe et al. "Search for dark matter in the form of hidden photons and axion-like particles in the XMASS detector". *Phys. Lett. B* 787 (2018), pp. 153–158. arXiv: 1807.08516 [astro-ph.CO].

[42] Orr Abramoff et al. "SENSEI: Direct-Detection Constraints on Sub-GeV Dark Matter from a Shallow Underground Run Using a Prototype Skipper-CCD". *Phys. Rev. Lett.* 122.16 (2019), p. 161801. arXiv: 1901.10478 [hep-ex].

[43] Liron Barak et al. "SENSEI: Direct-Detection Results on sub-GeV Dark Matter from a New Skipper-CCD". *Phys. Rev. Lett.* 125.17 (2020), p. 171802. arXiv: 2004.11378 [astro-ph.CO].

Chapter 5

Reactor anti-neutrinos impact on the Neutrino floor

Contents

Weakly Interacting Massive Particles (WIMPs) are another theoretically well motivated dark matter candidates, arising naturally in extensions of the Standard Model such as supersymmetry and extra-dimensional frameworks [1–3]. Direct detection experiments aim to observe nuclear recoils induced by the elastic scattering of WIMPs off detector nuclei. These searches probe the WIMP mass (M_χ) and WIMP–nucleon cross section ($\sigma_{\chi-n}$) over a wide parameter space, spanning approximately 10^{-40} to 10^{-50} cm^2 in cross section and from sub-GeV/c^2 to TeV/c^2 in mass [4–8].

As experiments strive to probe ever smaller cross sections using detectors with larger masses and improved energy resolution, they encounter an irreducible background arising from neutrino interactions via coherent elastic neutrino–nucleus scattering (CEνNS) [9]. In CEνNS, low-energy neutrinos scatter coherently off entire nuclei, producing nuclear recoils that are indistinguishable from those induced by WIMPs. The presence of this background defines a practical sensitivity limit for the achievable cross-section, commonly referred to as the *neutrino floor*, below which WIMP signals can no longer be distinguished with high statistical significance [10–12].

The neutrino floor is not a sharp boundary but rather a sensitivity threshold that depends on both experimental and theoretical inputs. Key factors include:

- the understanding of CEνNS cross sections, which are well defined within the Standard Model, although experimental confirmation at high significance ($> 5\sigma$) is still ongoing,
- the knowledge of neutrino fluxes and their uncertainties from multiple sources, including solar, atmospheric, diffuse supernova neutrino background (DSNB), and geoneutrinos, and
- the detector target material, exposure, and energy threshold.

To emphasize the diffuse, site-dependent, and exposure-dependent nature of this sensitivity limit, the term *neutrino fog* has been introduced [13, 14]. It denotes the region of parameter space (in $\sigma_{\chi-n}$ vs M_χ) where the WIMP signal becomes statistically indistinguishable from the neutrino background. In this convention, the neutrino floor represents the upper boundary of the neutrino fog.

While CEνNS measurements from various experiments to date are consistent with Standard Model predictions [15–17], systematic uncertainties in neutrino fluxes, reaching up to $\sim 50\%$, remain the dominant limitation in precisely defining the neutrino floor. In more recent formulations based on the concepts of neutrino fog and opacity, the neutrino floor becomes largely independent of detector exposure and energy threshold, while the choice of target material continues to play a significant role. Consequently, the neutrino floor must be determined for the detector target material of interest. In this work, we focus on a SuperCDMS-like high-voltage (HV) germanium (Ge) detector and therefore evaluate the neutrino floor for a Ge target.

Neutrinos arise from both naturally occurring processes and human-made sources. Natural neutrino backgrounds originate from several environments, including the Sun, the Earth's interior, supernova activity throughout the universe, and cosmic-ray interactions in the atmosphere. Solar neutrinos provide the dominant contribution at low recoil energies, while atmospheric neutrinos become increasingly relevant at higher energies. Additional components arise from geoneutrinos produced in terrestrial radioactive decay chains and from the DSNB, which represents the cumulative emission from past stellar explosions in the universe [10, 11].

In addition to these natural sources, artificial neutrino backgrounds can also play an important role in certain experimental environments. Nuclear reactors produce intense fluxes of electron antineutrinos ($\bar{\nu}_e$) through the beta decays of fission products generated during reactor operation. For detectors located near reactor facilities, this flux can significantly contribute to the neutrino-induced recoil spectrum, thereby impacting the neutrino floor [18].

While the impact of solar, atmospheric, and DSNB neutrinos on dark matter searches has been studied extensively, the role of reactor antineutrinos has received comparatively less attention in neutrino-floor calculations [10, 13]. Their contribution depends sensitively on the relative positioning of the experiment with respect to nearby nuclear reactors, introducing a strong site dependence unlike the dominant components from solar and atmospheric neutrinos. This effect becomes particularly significant for low-mass WIMP searches in the sub-10 GeV/c^2 regime, rendering the neutrino floor highly dynamic.

5.1 Motivation

The influence of reactor neutrinos becomes particularly important when exploring the low-mass WIMP regime, spanning roughly from sub-GeV/c^2 to a few GeV/c^2. In this mass range, the nuclear recoils generated by CEνNS interactions of reactor antineutrinos fall within the same energy region expected from WIMP scattering events. As a result, the reactor-induced recoil spectrum can mimic the signal of low-mass dark matter, potentially elevating the neutrino floor by several orders of magnitude depending on the distance between the detector and the reactor source. Reliable sensitivity projections in this regime therefore require careful modeling of reactor antineutrino fluxes, including their energy spectra, total thermal power, and the geometric dependence of the flux with distance.

Phonon-sensitive germanium detectors operated at high bias voltage and optimized for extremely low energy thresholds provide a powerful platform for probing this parameter space. Experiments such as SuperCDMS employ such detectors to achieve sensitivity to nuclear recoils at the sub-keV scale [4, 19, 20]. This capability enables searches for WIMPs with masses approaching sub-GeV/c^2, but it also increases the experiment's sensitivity to neutrino-induced recoils originating from reactor antineutrinos. Consequently, reactor neutrino backgrounds must be carefully quantified when evaluating the ultimate sensitivity of these detectors.

In this work, we investigate how reactor-generated $\bar{\nu}_e$ fluxes influence the neutrino floor for germanium-based dark matter detectors. Detailed spectral models for a gigawatt-scale thermal reactor (GW_{th}) are employed to compute the CEνNS recoil spectrum expected in germanium, while detector effects such as quenching are incorporated to translate nuclear recoil energies into measurable signals. The resulting event rates are evaluated for different reactor–detector separations in order to quantify the dependence of the background on experimental location.

To characterize the resulting limitations on dark matter sensitivity, we consider two complementary definitions of the neutrino floor. The first follows the discovery-limit formalism, which defines the smallest WIMP–nucleon cross section that can be detected with 3σ significance at a 90% power across an ensemble of simulated experiments, taking into account statistical fluctuations and systematic uncertainties in the neutrino fluxes [10, 11]. The second approach adopts the opacity-based framework, often referred to as the neutrino fog, in which the degradation of experimental sensitivity is described through a dimensionless opacity parameter that captures the transition of WIMP discovery cross-section from a statistics-limited to a systematics-limited regime as neutrino backgrounds increase [13, 14].

Earlier investigations introduced these methodologies independently but did not provide a comprehensive study of how reactor antineutrinos modify the neutrino floor as a function of detector location. For example, the discovery-limit analysis by Billard *et al.* [10], later extended by Ruppin *et al.* [11], evaluated neutrino floors for several detector targets without including contributions from reactor or geoneutrinos. The opacity-based framework proposed by O'Hare [13] incorporated reactor neutrinos, but only for a specific experimental site at Gran Sasso. Similarly, subsequent studies, such as that by Fan *et al.* [14], examined the opacity floor for the CJPL laboratory without explicitly modeling the distance dependence of reactor fluxes. Other recent analyses have investigated reactor antineutrino spectra at various underground laboratories, but did not propagate these effects into WIMP sensitivity calculations, and therefore did not assess their impact on the neutrino floor [18].

A detailed study of how the neutrino floor varies with reactor–detector distance is therefore essential. Such an analysis is important not only for accurately assessing the impact of reactor antineutrinos on current low-mass WIMP search experiments, but also for guiding experimental planning and site selection for future dark matter experiments, where the effect strongly depends on the local antineutrino flux.

The analysis presented here addresses this gap by systematically evaluating how reactor antineutrino fluxes modify both definitions of the neutrino floor, the discovery-limit and opacity-based frameworks, for germanium detectors across a range of reactor-detector distances. Our results show that detectors located within approximately $\sim$ 10 km of a gigawatt-scale reactor can experience a substantial increase in the neutrino floor in the few-GeV/c^2 WIMP mass region, leading to potential degradations in discovery sensitivity by several orders of magnitude. In contrast, at distances exceeding $\sim$ 100 km, the contribution from reactor antineutrinos becomes negligible compared to natural neutrino backgrounds.

These findings underscore the importance of experimental siting and accurate background modeling for future low-threshold dark matter experiments. By explicitly incorporating reactor antineutrino contributions, this study provides a more realistic assessment of the neutrino floor and offers valuable guidance for the design and interpretation of next-generation searches for low-mass WIMPs.

5.2 WIMP Signal Rate Modeling

5.2.1 Differential Event Rate

Direct detection experiments aim to observe the tiny nuclear recoil energies produced when dark matter particles scatter elastically from atomic nuclei inside a detector. In the widely studied Weakly Interacting Massive Particle framework, the interaction probability is extremely small and the resulting recoil energies are correspondingly low. For low-mass WIMPs, particularly those with masses below approximately 10 GeV/c^2, the expected nuclear recoil energies fall in the sub-keV to few-keV range. Detecting such small energy depositions requires detectors with exceptionally low thresholds and excellent control over backgrounds, making this region of parameter space experimentally challenging [4, 5].

The predicted nuclear recoil spectrum from WIMP interactions is typically expressed in terms of the differential event rate per unit detector mass and recoil energy. The rate can be written as [21]

$$\frac{dR}{dE_R} = \frac{N_A\,\rho_0}{A}\,\frac{\sigma_N}{2M_\chi\,\mu_N^2}F^2(E_R)\,\eta(v_{\min}), \tag{5.1}$$

where E_R denotes the nuclear recoil energy. In this expression, N_A is Avogadro's number and ρ_0 represents the local dark matter density in the solar neighborhood, commonly taken to be approximately 0.3 $\mathrm{GeV/cm^3}$ [22]. The quantity A corresponds to the atomic mass number of the detector target nucleus, while M_χ is the mass of the WIMP particle.

The parameter μ_N denotes the reduced mass of the WIMP–nucleus system,

$$\mu_N = \frac{M_\chi M_N}{M_\chi + M_N},$$

where M_N is the nuclear mass. The term σ_N represents the WIMP–nucleus scattering cross section evaluated at zero momentum transfer. The factor $F(E_R)$ is the nuclear form factor, which accounts for the loss of coherence in the scattering process when the momentum transfer becomes comparable to the inverse nuclear size.

The astrophysical properties of the Galactic dark matter halo enter the recoil rate through the quantity $\eta(v_{\rm min})$, commonly referred to as the mean inverse speed. This factor encapsulates the fraction of WIMPs in the local halo that possess sufficient velocity to produce a recoil of energy E_R in the detector. It is defined as

$$\eta(v_{\rm min}) = \int_{v_{\rm min}}^{v_{\rm esc}} \frac{f(\mathbf{v}+\mathbf{v}_E)}{v}\, d^3v, \tag{5.2}$$

where $f(\mathbf{v})$ denotes the WIMP velocity distribution in the Galactic rest frame. The vector $\mathbf{v}_E$ represents the velocity of the Earth relative to the Galactic halo, and $v_{\rm esc}$ corresponds to the Galactic escape velocity beyond which particles are no longer gravitationally bound to the Milky Way.

Within the commonly adopted Standard Halo Model (SHM) [23], the dark matter velocity distribution is approximated by a Maxwell–Boltzmann distribution truncated at the escape velocity. Typical parameter values used in calculations are $v_{\rm esc} = 544$ km/s and $v_E = 232$ km/s. Under these assumptions, analytic expressions for the mean inverse speed can be derived, greatly simplifying the computation of recoil spectra for different detector materials and WIMP masses [21].

The lower limit of the velocity integral is determined by the minimum WIMP velocity required to produce a recoil of energy E_R in the target nucleus. This threshold velocity is given by

$$v_{\rm min} = \sqrt{\frac{M_N E_R}{2\mu_N^2}}. \tag{5.3}$$

This relation illustrates an important feature of WIMP kinematics: lighter WIMPs of a given velocity generate lower recoil energy compared to heavier particles. Consequently, experiments searching for low-mass WIMPs require detectors with very low energy thresholds. At the same time, this energy region could overlap with nuclear recoils generated by CEνNS, which can produce backgrounds that mimic the WIMP signal.

5.2.2 Spin-Independent WIMP–Nucleon Scattering in Germanium

Germanium-based detectors have become a leading technology for probing the low-mass WIMP parameter space ($\sigma_{\chi-n}$ vs M_χ) due to their excellent energy resolution and ability to achieve extremely low detection thresholds. These characteristics make them particularly suitable for detecting the small nuclear recoils expected from light dark matter particles.

An additional advantage arises from the nuclear structure of germanium. Most naturally occurring germanium isotopes possess even numbers of both protons and neutrons, resulting in nuclei with nearly zero total spin. Because of this nuclear configuration, spin-dependent (SD) interactions between WIMPs and nuclei are strongly suppressed in germanium targets. As a result, the dominant interaction channel is spin-independent (SI) scattering, which proceeds coherently across all nucleons in the nucleus. For this reason, the modeling of WIMP signals in germanium detectors generally focuses on the SI interaction channel.

The relationship between the SI WIMP–nucleus cross section σ_N and the fundamental WIMP–nucleon cross section $\sigma^{\mathrm{SI}}_{\chi-n}$ is given by

$$\sigma_N = \sigma^{\mathrm{SI}}_{\chi-n} A^2 \left(\frac{\mu_N}{\mu_n}\right)^2 , \tag{5.4}$$

where μ_n represents the reduced mass of the WIMP–nucleon system,

$$\mu_n = \frac{M_\chi m_n}{M_\chi + m_n},$$

and m_n is the nucleon mass.

The factor A^2 reflects the coherent enhancement of the scattering amplitude when the WIMP interacts with all nucleons in the nucleus simultaneously. This coherence effect significantly increases the expected event rate for heavier target nuclei. The ratio $(\mu_N/\mu_n)^2$ accounts for the difference in kinematic scaling between the WIMP–nucleus and WIMP–nucleon systems.

Substituting Eq. (5.4) into the general recoil rate expression of Eq. (5.1) yields the differential recoil rate for SI WIMP interactions in germanium:

$$\frac{dR}{dE_R} = \frac{N_A\, \rho_0\, \sigma^{\mathrm{SI}}_{\chi-n}}{2AM_\chi\, \mu_n^2} A^2 F^2(E_R)\, \eta(v_{\min}). \tag{5.5}$$

The nuclear form factor $F(E_R)$ describes the suppression of coherent scattering when the momentum transfer becomes comparable to the nuclear size. In this work, the Helm parameterization is adopted [21]:

$$F^2(E_R) = \left[\frac{3j_1(qr_n)}{qr_n}\right]^2 \exp(-q^2s^2), \tag{5.6}$$

where $j_1(x) = (\sin x/x^2 - \cos x/x)$ is the spherical Bessel function of order one. The momentum transfer is defined as $q = \sqrt{2M_N E_R}$. The parameter $s = 0.9$ fm represents the nuclear skin thickness, while the effective nuclear radius r_n is given by

$$r_n = \sqrt{c^2 + \frac{7}{3}\pi^2 a^2 - 5s^2},$$

with $c = 1.23A^{1/3} - 0.60$ fm and $a = 0.52$ fm. This parameterization provides an accurate description of the nuclear charge distribution and the associated loss of coherence at higher momentum transfer.

5.2.3 Quenching and the Measured WIMP Energy Spectrum

In addition to the theoretical recoil spectrum, it is necessary to account for detector-specific effects that influence how nuclear recoils are observed experimentally. Germanium detectors operated under high bias voltage conditions, such as those used in the SuperCDMS experiment, utilize the Neganov–Trofimov–Luke (NTL) effect to amplify phonon signals generated by ionization [24, 25]. This mechanism enhances the sensitivity of the detector to very small energy depositions, as low as $O(\text{eV})$.

However, nuclear recoils do not produce ionization as efficiently as electron recoils of the same deposited energy. Consequently, the observable signal associated with a nuclear recoil is reduced relative to the true recoil energy. This effect is known as quenching and is described by the ionization yield $Y(E_R)$, defined as the fraction of the recoil energy that is converted into ionization.

The ionization yield is commonly modeled using the Lindhard theory:

$$Y(E_R) = \frac{k\,g(\epsilon)}{1 + k\,g(\epsilon)}, \quad g(\epsilon) = 3\epsilon^{0.15} + 0.7\epsilon^{0.6} + \epsilon, \quad \epsilon = 11.5 E_R Z^{-7/3}. \tag{5.7}$$

Here Z is the atomic number of the target material and k is a material-dependent parameter that controls the shape and magnitude of the ionization yield. For germanium ($Z = 32$), recent measurements performed by the CONUS+ Collaboration indicate that $k \approx 0.162$ provides a good description of the ionization response down to recoil energies of approximately 150 eV_{ee} [26].

Because experimental measurements are typically reported in terms of electron-equivalent energy rather than nuclear recoil energy, the two quantities must be related through the ionization yield. The measured electron-equivalent energy is given by

$$E_{\mathrm{ee}} = Y(E_R)\, E_R. \tag{5.8}$$

To convert the recoil spectrum into the experimentally observable spectrum, the differential rate must be transformed accordingly:

$$\frac{dR}{dE_{\mathrm{ee}}} = \frac{dR}{dE_R}\frac{dE_R}{dE_{\mathrm{ee}}}. \tag{5.9}$$

This procedure ensures that theoretical predictions for WIMP-induced recoil spectra are expressed in the same energy scale as the measured detector response, allowing direct comparison with experimental data.

Figure 5.1 illustrates the expected recoil spectra in terms of nuclear recoil energy (top panel) and electron-equivalent energy (bottom panel). The results are shown for a benchmark WIMP with mass 6 GeV/c^2 and spin-independent cross section $\sigma_{\chi-n} = 4.4 \times 10^{-45}$ cm^2. Also included are the predicted CEνNS contributions from solar, atmospheric, geoneutrino, and reactor neutrino sources. A detailed description of these CEνNS components is provided in Sec. 5.3.

The comparison indicates that the recoil spectrum from ^{8}B solar neutrinos closely tracks that expected from low-mass WIMP interactions within the energy range of interest. This overlap highlights a key limitation for next-generation dark matter searches: neutrino-induced recoils can effectively mimic a WIMP signal. Consequently, a precise understanding and characterization of such backgrounds are crucial for accurately determining the discovery reach of direct detection experiments. This challenge motivates the detailed investigation of neutrino-induced backgrounds and the concept of the neutrino floor discussed in the following sections.

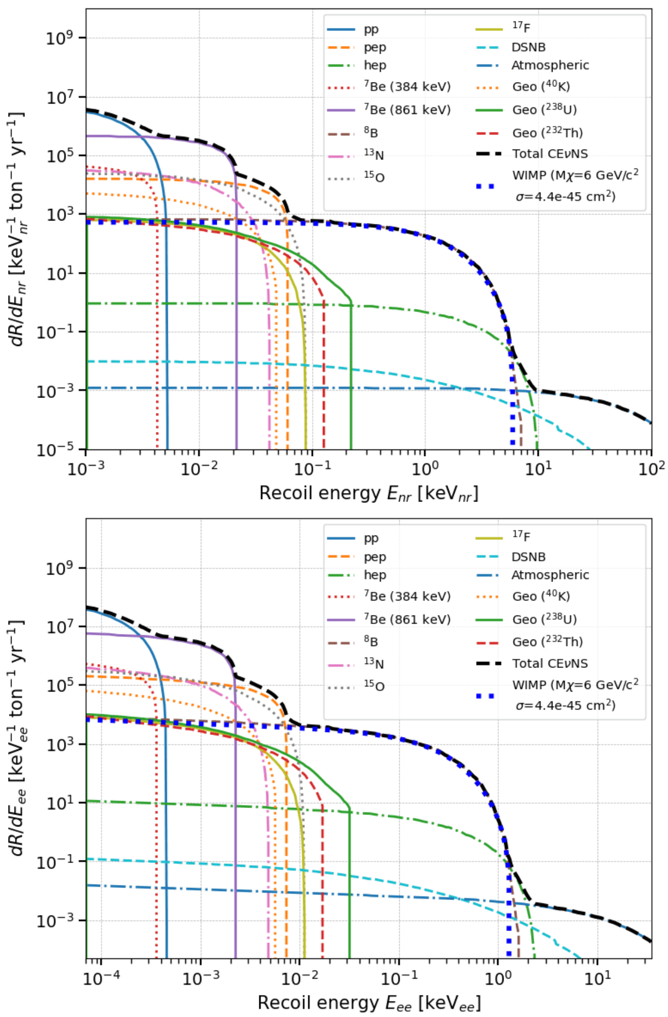

FIGURE 5.1: Nuclear-recoil (**top**) and corresponding electron-equivalent (**bottom**) energy spectra for different CEνNS components, shown for a low-threshold detector. The electron-equivalent spectrum is obtained using the Lindhard quenching model. A representative WIMP signal (6 GeV/c^2, $\sigma_{\chi\text{-}n} = 4.4 \times 10^{-45}$ cm^2) is included for comparison. The ^{8}B solar-neutrino-induced recoil spectrum closely follows the shape of the WIMP signal over the relevant energy range, illustrating the intrinsic degeneracy that limits discrimination in low-mass WIMP searches. Only the mean spectra are shown. Adapted from Ref. [18].

5.3 CEνNS-Induced Background Modeling

5.3.1 Differential Scattering Cross Section

CEνNS is a Standard Model neutral-current interaction in which a neutrino scatters elastically from an entire atomic nucleus. Unlike charged-current processes, CEνNS does not depend on neutrino flavor because the interaction proceeds via the exchange of a neutral Z boson. As a result, neutrinos of all flavors contribute to this process with equal coupling strength within the Standard Model framework [9].

A distinctive feature of CEνNS is the coherent enhancement of the scattering amplitude at sufficiently low momentum transfer. In this regime, the wavelengths associated with the exchanged momentum are comparable to or larger than the nuclear radius, allowing the scattering amplitudes from individual nucleons to add constructively. This coherence results in a cross section that approximately scales with the square of the weak nuclear charge. Because the weak charge receives its dominant contribution from neutrons, CEνNS interactions are particularly sensitive to the neutron content of the nucleus.

For a neutrino with energy E_ν scattering from a nucleus of mass M and producing a nuclear recoil with energy E_R, the differential CEνNS cross section can be expressed as [27]

$$\frac{d\sigma(E_\nu, E_R)}{dE_R} = \frac{G_F^2 M}{4\pi} Q_W^2 \left(1 - \frac{M E_R}{2E_\nu^2}\right) F^2(E_R), \tag{5.10}$$

where G_F is the Fermi constant and $F(E_R)$ represents the nuclear form factor that accounts for the loss of coherence at larger momentum transfers. The weak nuclear charge Q_W is given by

$$Q_W = N - (1 - 4\sin^2\theta_W)Z,$$

where N and Z denote the neutron and proton numbers of the target nucleus, respectively, and θ_W is the weak mixing angle. Because the factor $(1 - 4\sin^2\theta_W)$ is numerically close to zero, the proton contribution is strongly suppressed. Consequently, the CEνNS cross section is largely determined by the number of neutrons, leading to the characteristic scaling proportional to N^2.

For a given neutrino energy, the recoil energy imparted to the nucleus is kinematically limited. The maximum possible recoil energy is

$$E_R^{\max} = \frac{2E_\nu^2}{M + 2E_\nu}. \tag{5.11}$$

This relation illustrates that neutrinos with energies in the MeV range typically generate nuclear recoils at keV scale and below in heavy nuclei such as germanium. As a result, CEνNS signals are particularly relevant for detectors designed to probe extremely low-energy nuclear recoils.

5.3.2 Quenching and Observable CEνNS Spectrum

To determine the expected CEνNS event rate in a detector, the scattering cross section must be folded with the flux of neutrinos arriving at the detector from all relevant sources. The differential interaction rate per unit detector mass can therefore be written as

$$\frac{dR}{dE_R} = \frac{N_A}{A} \sum_j \int_{E_\nu^{\min}(E_R)}^{E_\nu^{\text{max,j}}} \phi_j(E_\nu) \frac{d\sigma(E_\nu, E_R)}{dE_R}\, dE_\nu, \tag{5.12}$$

where N_A is Avogadro's number and A is the atomic mass number of the detector material. The summation index j labels the different neutrino sources contributing to the background. The function $\phi_j(E_\nu)$ represents the neutrino flux spectrum associated with source j.

The lower limit of the integration corresponds to the minimum neutrino energy required to produce a nuclear recoil of energy E_R, which is given by

$$E_\nu^{\min}(E_R) = \sqrt{\frac{ME_R}{2}}.$$

The upper limit $E_\nu^{\text{max,j}}$ depends on the endpoint energy of the specific neutrino source under consideration. In this analysis, detector efficiency is assumed to be unity above the experimental threshold, allowing the theoretical recoil spectrum to be directly interpreted as the observable interaction rate.

For germanium detectors operated in HV mode, the conversion between nuclear recoil energy and measured signal requires accounting for quenching effects. As discussed in Sec. 5.2, only a fraction of the recoil energy is converted into ionization and subsequently amplified through the NTL effect. Consequently, the experimentally measured energy scale corresponds to electron-equivalent energy rather than true nuclear recoil energy.

The same quenching model applied to WIMP-induced recoils is therefore used to convert CEνNS recoil spectra into the electron-equivalent energy scale. This ensures that the predicted CEνNS background spectra are expressed in the same observable units as the detector response and can be directly compared with WIMP signal models.

5.3.3 Neutrino Sources Contributing to CEνNS Backgrounds

CEνNS interactions can be induced by neutrinos originating from a variety of astrophysical and terrestrial processes. These neutrino backgrounds can be broadly classified into natural sources and anthropogenic sources, both of which must be considered when evaluating the sensitivity of direct dark matter searches.

Non-Reactor Neutrinos

Solar Neutrinos Solar neutrinos constitute the largest neutrino flux reaching Earth and therefore represent the dominant CEνNS background for low-energy nuclear recoil experiments. These neutrinos are produced primarily through nuclear fusion reactions occurring in the Sun's core, with the pp chain and the CNO cycle providing the principal production mechanisms.

Solar neutrinos dominate the neutrino flux for energies below approximately 18 MeV and are particularly relevant for dark matter searches targeting low-mass WIMPs with masses below about 10 GeV$/c^2$. In the present analysis, we include the major components of the solar neutrino spectrum: pp, pep, hep, ^{7}Be, ^{8}B, ^{13}N, ^{15}O, and ^{17}F neutrinos. The corresponding nuclear recoil spectra in germanium are adopted from the calculations presented in Ref. [10].

Atmospheric Neutrinos Atmospheric neutrinos originate from the decay of secondary particles produced when high-energy cosmic rays interact with nuclei in the Earth's atmosphere. These interactions generate neutrinos over a broad energy range extending up to the TeV scale. Although the overall flux of atmospheric neutrinos is significantly lower than that of solar neutrinos, their higher energies allow them to produce larger nuclear recoils.

Consequently, atmospheric neutrinos become increasingly relevant for dark matter searches probing higher WIMP masses, typically above $\sim$ 100 GeV$/c^2$. However, as the neutrino energy increases, the coherence condition for CEνNS scattering gradually breaks down due to the larger momentum transfer involved. This loss of coherence suppresses the CEνNS rate. Following the approach of Ref. [10], atmospheric neutrinos with energies up to 1 GeV are included in the calculation of the recoil spectrum.

Geoneutrinos Geoneutrinos are electron antineutrinos produced through the β-decay chains of naturally occurring radioactive isotopes within the Earth, primarily ^{238}U, ^{232}Th, and ^{40}K. These isotopes are distributed throughout the Earth's crust and mantle, and their relative abundances, along with variations in crustal thickness and composition, lead to site-dependent differences in the observed geoneutrino flux. In general, locations with thicker continental crust exhibit higher fluxes compared to oceanic or shield regions.

Despite this spatial variability, the overall geoneutrino flux remains significantly lower than that of solar neutrinos, typically by about two orders of magnitude. Consequently, their contribution to the CEνNS-induced background in direct detection experiments is subdominant over most of the WIMP parameter space. Owing to their relatively low endpoint energies (of order a few MeV), geoneutrinos predominantly induce very low-energy nuclear recoils, making their impact most relevant for searches targeting WIMP masses near the sub-GeV to $\sim$1–2 GeV/c^2 range.

For the present study, we adopt a representative geoneutrino-induced differential recoil spectrum in germanium based on calculations performed for the China Jinping Underground Laboratory (CJPL) [28]. While the absolute normalization of the geoneutrino flux varies across experimental sites, its effect on the neutrino floor is relatively modest. As discussed in Sec. 5.4.2, a reduction of the flux by a factor of two, approximately corresponding to levels expected at SNOLAB, results in changes of at most $\sim$10% in the neutrino floor in the absence of reactor contributions, and only in a narrow WIMP mass region around $M_\chi \simeq 1.7$ GeV/c^2.

In comparison, reactor antineutrinos introduce a much stronger and rapidly varying site dependence, as their flux scales inversely with the square of the reactor–detector distance. As a result, variations in reactor proximity dominate over geoneutrino-induced differences when assessing site-dependent neutrino backgrounds. This justifies the use of a single representative geoneutrino model in this work without compromising the robustness of the overall conclusions.

Supernova Neutrinos The diffuse supernova neutrino background represents the integrated flux of neutrinos emitted by all past core-collapse supernovae throughout the history of the universe. These neutrinos typically have energies up to $\mathcal{O}(10\text{ MeV})$ and form a faint but persistent neutrino background.

Although the DSNB flux is relatively small, the resulting CEνNS recoils occur at energies relevant for dark matter searches targeting intermediate WIMP masses around 20 GeV$/c^2$. The corresponding recoil spectra in germanium are taken from Ref. [10].

For all non-reactor neutrino sources described above, the calculated nuclear recoil spectra are converted into electron-equivalent energy using the same quenching model applied to WIMP-induced recoils. Figure 5.1 compares the differential recoil spectra from the individual CEνNS components with the predicted spectrum for a representative WIMP signal. In particular, the recoil spectrum generated by ^{8}B solar neutrinos closely resembles that expected from low-mass WIMP interactions, illustrating the difficulty of distinguishing these two contributions experimentally.

The relative contributions of different neutrino sources vary significantly across the WIMP mass range of interest. In the low-mass regime ($m_\chi \lesssim 10\,\text{GeV}/c^2$), the CE$\nu$NS background is primarily driven by solar neutrinos, while at higher masses ($m_\chi \gtrsim 100\,\text{GeV}/c^2$), atmospheric neutrinos become the dominant contribution. The adopted uncertainties associated with each neutrino flux component are listed in Table 5.1. The likelihood analysis treats the flux normalization parameters as independent Gaussian nuisance parameters, neglecting correlations between their uncertainties.

The quenching parameter measured by the CONUS+ experiment, $k = 0.162 \pm 0.004$ [16],

TABLE 5.1: Systematic uncertainties (σ_j) on the normalization of CEνNS neutrino/anti-neutrino flux components considered in this analysis.

Flux component	**Uncertainty (σ_j)**
pp	0.6% [12]
pep	1% [12]
hep	30% [12]
^{7}Be I (384 keV)	6% [12]
^{7}Be II (861 keV)	6% [12]
^{8}B	2% [12]
^{13}N	15% [12]
^{15}O	17% [12]
^{17}F	20% [12]
DSNB	50% [12]
Atmospheric	25% [12]
Geo (^{40}K)	6% [28]
Geo (^{238}U)	30% [28]
Geo (^{232}Th)	30% [28]
Reactor	8% [12]

corresponds to a relative uncertainty of about 1%, which is small compared to the overall systematic uncertainties in flux normalisations affecting the CEνNS event rate. Moreover, since both neutrino-induced and WIMP-induced recoil spectra are modified by quenching in a similar manner, its impact on the determination of the neutrino floor is expected to be limited. We quantified this effect in Sec. 5.4.2, where we varied the quenching parameter within its 3σ uncertainty range and observed no significant change in the resulting neutrino floor. Based on this, the uncertainty associated with the quenching parameter is not propagated in the primary analysis.

Other detector-related uncertainties, such as those arising from signal efficiency and energy thresholds, are not included; an idealized detector response is assumed. These assumptions are consistent with those adopted in previous studies of the neutrino floor.

Reactor Antineutrinos

In addition to natural neutrino sources, nuclear reactors produce intense fluxes of electron antineutrinos through the beta decay of neutron-rich fission fragments. The dominant fission isotopes contributing to reactor antineutrino production are ^{235}U, ^{238}U, ^{239}Pu, and ^{241}Pu. The resulting antineutrino spectrum extends to energies of several MeV and can induce nuclear recoils through CEνNS interactions in nearby detectors.

For detectors located near nuclear reactor facilities, the reactor antineutrino flux can become a significant source of CEνNS background. Because the recoil energies generated by these neutrinos lie in the sub-keV range, they overlap directly with the signal region relevant for low-mass WIMP searches in germanium detectors.

The differential reactor antineutrino flux at a detector located a distance L from a reactor with thermal power P_{th} can be written as

$$\phi_{\bar{\nu}_e}(E_\nu) = \frac{P_{\text{th}}}{4\pi L^2 \langle E_f \rangle} \sum_i f_i S_i(E_\nu), \tag{5.13}$$

where $\langle E_f \rangle \approx 202.5$ MeV represents the average energy released per fission [29]. The quantities f_i denote the fractional contributions of the individual fissile isotopes, and $S_i(E_\nu)$ represents the antineutrino spectrum emitted per fission for isotope i. Typical fission fractions for a gigawatt-scale reactor, such as the KKL power plant used in CONUS+ experiment, are summarized in Table 5.2.

TABLE 5.2: Representative fission fractions (f_i) assumed for a gigawatt-scale nuclear reactor, based on typical operating conditions of the KKL reactor [30].

Isotope	**Fission fraction (f_i)**
^{235}U	53%
^{239}Pu	32%
^{238}U	8%
^{241}Pu	7%

The reactor antineutrino spectrum used in this work is constructed by combining an analytic description at higher energies with tabulated results at lower energies. For neutrino energies above 2 MeV, the spectra corresponding to individual fission isotopes are modeled using an exponential parameterization [31, 32]

$$\frac{dN_{\bar{\nu}_e}}{dE_{\bar{\nu}_e}} = a \exp\left(a_0 + a_1 E_{\bar{\nu}_e} + a_2 E_{\bar{\nu}_e}^2\right), \tag{5.14}$$

where the isotope-dependent coefficients are provided in Table 5.3.

TABLE 5.3: Coefficients for the parameterized $\bar{\nu}_e$ spectra (ν_e/MeV/fission) applicable for $E_\nu >$ 2 MeV.

Isotope	a	a_0	a_1	a_2
^{235}U	1.0461	0.870	−0.160	−0.0910
^{238}U	1.0719	0.976	−0.162	−0.0790
^{239}Pu	1.0527	0.896	−0.239	−0.0981
^{241}Pu	1.0818	0.793	−0.080	−0.1085

For energies below 2 MeV, we adopt tabulated spectra derived from detailed reactor calculations [32], as listed in Table 5.4.

TABLE 5.4: Tabulated $\bar{\nu}_e$ spectra below 2 MeV (in units of $\bar{\nu}_e$/MeV/fission) [32].

E_ν **[MeV]**	^{235}**U**	^{239}**Pu**	^{238}**U**	^{241}**Pu**
0.008	0.024	0.140	0.089	0.200
0.016	0.092	0.560	0.350	0.790
0.031	0.350	2.130	1.320	3.000
0.062	0.610	0.640	0.650	0.590
0.125	1.980	1.990	2.020	1.850
0.250	2.160	2.080	2.180	2.140
0.500	2.660	2.630	2.910	2.820
0.750	2.660	2.580	2.960	2.900
1.000	2.410	2.320	2.750	2.630
1.500	1.690	1.480	1.970	1.750
2.000	1.260	1.080	1.500	1.320

At low energies ($E_\nu \lesssim 1$ MeV), an additional contribution arises from neutron capture

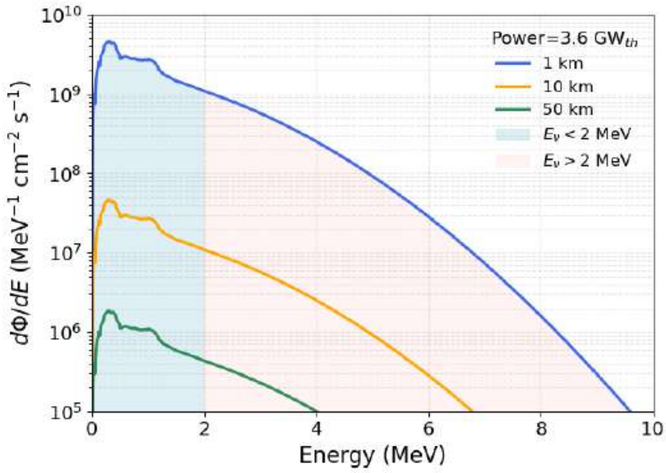

FIGURE 5.2: Reactor antineutrino flux spectra (mean values) at distances of 1, 10, and 50 km from a 3.6 GW_{th} reactor core, assuming an isotropic point-like source. The spectrum is constructed by combining an analytic parameterization above 2 MeV with tabulated data at lower energies (see Sec. 5.3.3). The overall normalization decreases with distance following the expected inverse-square ($1/L^2$) scaling, illustrating the rapid suppression of reactor antineutrino flux with increasing baseline. Only central values are shown; uncertainties from reactor fuel composition, spectral modeling, and normalization are not included. Adapted from Ref. [18].

on ^{238}U. The corresponding antineutrino spectrum is taken from Ref. [33] and normalized using an average yield of 1.2 antineutrinos per fission [32].

The total reactor antineutrino spectrum is obtained by summing the isotope-weighted contributions and scaling with the reactor power and detector distance. The resulting spectra for different reactor–detector separations are shown in Fig. 5.2. Following Ref. [12], we adopt a representative flux normalization uncertainty of 8% for the reactor antineutrino flux. This value reflects the current level of modeling uncertainty and is consistent with the ∼7.8% deficit observed by the Daya Bay experiment in the measured ^{235}U antineutrino yield relative to theoretical predictions [34]. Both KKL (CONUS+) and Daya Bay Nuclear Power Plant operate with low-enriched uranium (LEU) fuel and therefore exhibit broadly similar fuel compositions and fission fraction evolution over the reactor cycle. The adopted

8% value should thus be interpreted as a realistic reference rather than a universal site-independent constant. The impact of varying reactor systematic uncertainty on the neutrino floor is further studied in Sec. 5.4.

Reactor antineutrinos can form a significant component of the CEνNS background in direct detection experiments, particularly for detector sites located in close proximity to nuclear power plants. Their contribution is highly sensitive to the reactor–detector separation, resulting in substantial variations in the expected event rates across different locations. As illustrated in Fig. 5.3, the CEνNS rate from reactor antineutrinos can change by several orders of magnitude for baselines within ~50 km, and begins to exceed the solar neutrino contribution at distances below approximately ~10 km. This strong distance dependence makes an accurate, site-specific modeling of reactor fluxes essential for reliable neutrino floor predictions and for evaluating the discovery potential of future low-threshold dark matter experiments. The nuclear recoil spectrum from reactor induced CEνNS is converted into measurable electron-equivalent energy using the same Lindhard quenching model with $k = 0.162$.

To ensure the reliability of the reactor antineutrino modeling, we validated our predicted CEνNS recoil spectrum against experimental observations from the CONUS+ experiment [35]. CONUS+ employs kilogram-scale high-purity germanium detectors with sub-keV ionization thresholds and is located at a distance of 20.7 m from the KKL reactor core. It has reported the first observation of reactor antineutrino-induced CEνNS interactions with a significance of 3.7σ.

For this validation, we calculated the expected differential CEνNS event rate for a germanium detector at the same baseline. A comparison between the predicted spectrum and the measured CONUS+ data is shown in Fig. 5.4. The agreement between the two demonstrates that the reactor flux model and the CEνNS rate calculation accurately reproduce the

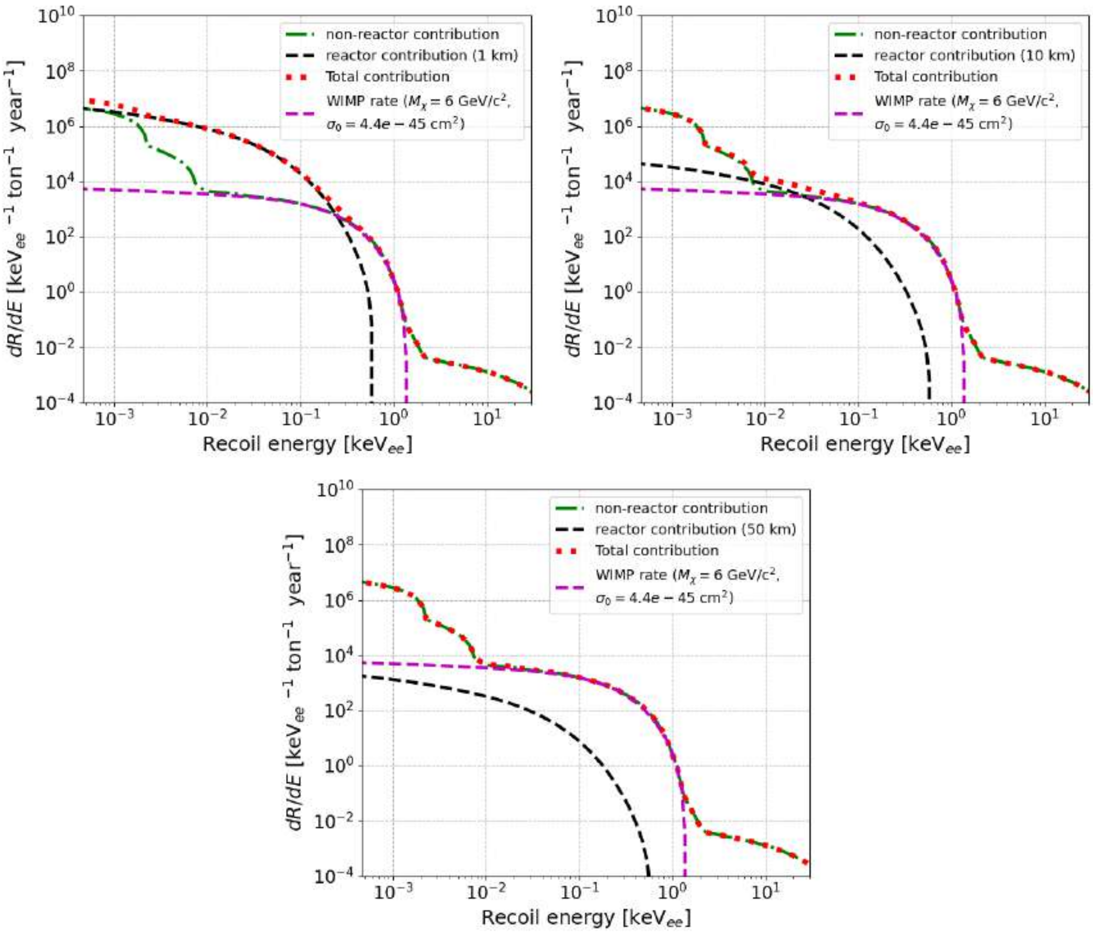

FIGURE 5.3: Differential CEνNS event rates (mean values) induced by reactor antineutrinos, compared with non-reactor sources (solar, atmospheric, DSNB, and geoneutrinos). Results are shown for detector locations at 1 km (upper left), 10 km (upper right), and 50 km (bottom) from a 3.6 GW_{th} reactor core. At distances below ∼10 km, reactor-induced CEνNS events become comparable to or exceed the combined non-reactor background. Adapted from Ref. [18].

experimentally observed signal.

Since the primary focus of this work is on the variation of reactor-induced backgrounds with distance (from a few kilometers up to ∼100 km), all non-reactor neutrino components are assumed to remain unchanged with detector location. Under this assumption, the observed variation in the total CEνNS background is driven predominantly by the reactor

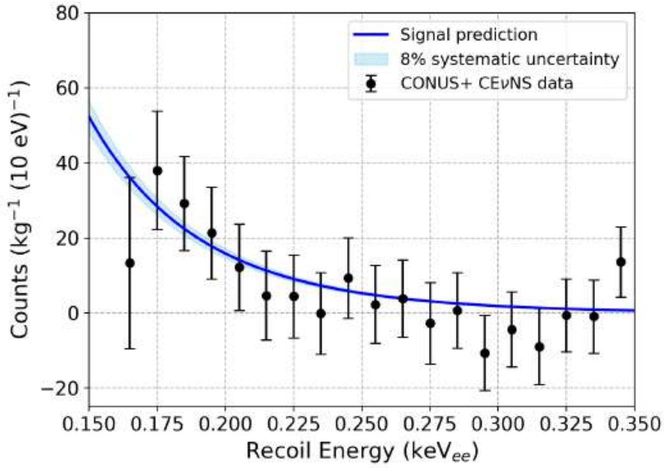

FIGURE 5.4: Comparison of the predicted CEνNS differential spectrum with CONUS+ measurements at a baseline of 20.7 m from the KKL reactor. The prediction includes quenching effects using the Lindhard model ($k = 0.162$), and the blue shaded band represents an assumed 8% systematic uncertainty in the reactor flux normalization. Adapted from Ref. [18].

antineutrino contribution.

5.4 Reactor Antineutrinos and Their Influence on the Neutrino Floor

We studied the impact of reactor-origin antineutrinos on the neutrino floor for low-threshold germanium-based dark matter detectors. To quantify this effect, we adopt two complementary and widely used definitions of the neutrino floor, each based on a distinct statistical framework. The first approach is the conventional *discovery-limit* formalism introduced by Billard *et al.* [10], which defines the minimum WIMP–nucleon cross section that can be identified with a statistical significance of at least 3σ in 90% of repeated hypothetical experiments.

The second approach follows the *opacity-based* framework developed by O'Hare [13]. In this picture, the so-called neutrino fog represents the region where neutrino-induced backgrounds increasingly obscure a potential dark matter signal. The neutrino floor is then identified as the boundary at which the sensitivity transitions from being dominated by statistical fluctuations to being limited by systematic uncertainties associated with the neutrino background.

Figure 5.5 presents the analysis flowchart used in this work to determine the neutrino floor. The primary objective is to study the impact of reactor antineutrinos on the neutrino floor for different reactor-to-detector distances. The figure shows both the discovery limit–based approach and the opacity-based approach, highlighting the key steps involved in each method as well as the differences between them.

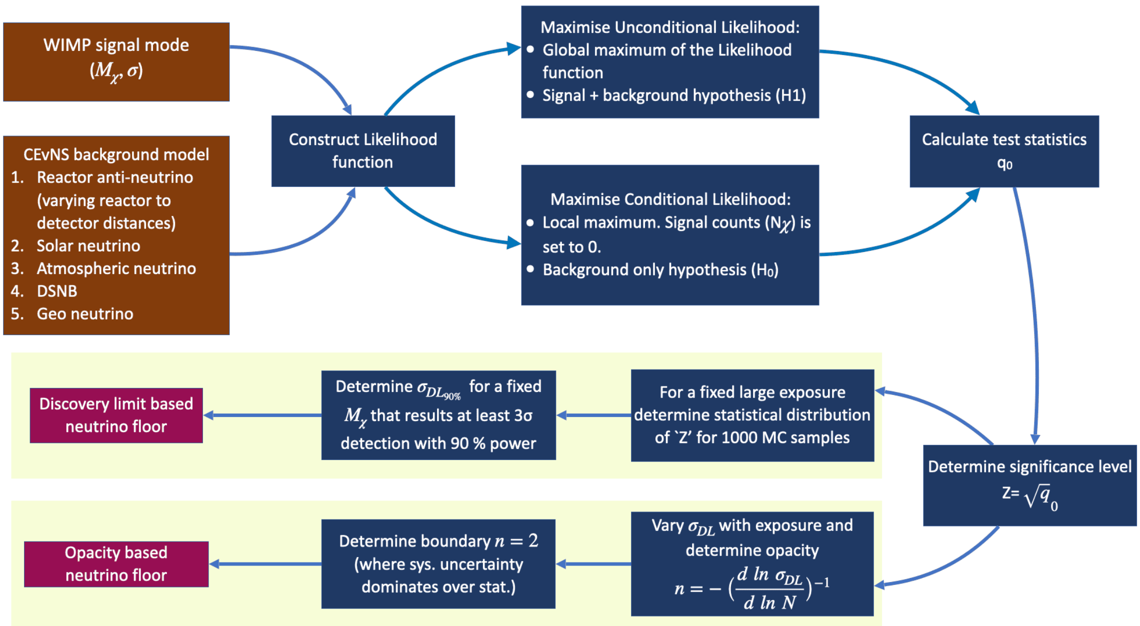

FIGURE 5.5: Analysis flowchart illustrating the procedures for determining the neutrino floor using the discovery limit–based approach and the opacity-based approach.

5.4.1 Discovery-Limit based definition of Neutrino floor

Within the discovery-limit formalism [10], the neutrino floor is determined by evaluating the smallest WIMP–nucleon cross section that can be identified as a signal in presence of the CEνNS backgrounds with a significance of at least 3σ in 90% of repeated realizations of the experiment, corresponding to a power of 0.9. This definition explicitly incorporates the statistical fluctuations of CEνNS backgrounds and the uncertainties associated with neutrino fluxes.

We employ a binned profile-likelihood approach, where the number of observed events in each energy bin is modeled as an independent Poisson-distributed variable. Systematic uncertainties in the neutrino flux normalizations are incorporated through independent Gaussian-distributed nuisance parameters. Correlations between different flux components are neglected. The statistical significance of a potential signal is evaluated using the profile likelihood ratio test, following the standard formalism for searches of new physics [36]. The corresponding likelihood function is defined as

$$\mathcal{L}(\boldsymbol{\alpha}) = \prod_{i=1}^{N_{\text{bins}}} \frac{\left(\sum_j \alpha_j B_{ij} + S_i\right)^{n_i}}{n_i!} e^{-\sum_j \alpha_j B_{ij} - S_i} \times \prod_j \exp\left[-\frac{(\alpha_j - 1)^2}{2\sigma_j^2}\right], \tag{5.15}$$

where n_i denotes the number of observed events in energy bin i, S_i is the predicted WIMP signal contribution, and B_{ij} corresponds to the CEνNS background from neutrino source j. The parameter α_j scales the normalization of each background component, and σ_j represents the corresponding fractional uncertainty (see Table 5.1). For sensitivity projections, the expected median sensitivity is obtained using the Asimov dataset, in which the observed counts in each bin are fixed to their expectation values under the signal-plus-background hypothesis,

$$n_i = S_i + \sum_j B_{ij},$$

i.e. in the absence of statistical fluctuations. The profile likelihood ratio evaluated with this Asimov dataset provides the median expected discovery significance.

To evaluate the presence of a signal, we construct the profile-likelihood ratio comparing the signal-plus-background (alternate hypothesis) and background-only hypotheses (null hypothesis). The corresponding conditional and unconditional log-likelihoods are

$$\ln \mathcal{L}_{\rm cond} = \sum_i n_i \ln\left(\sum_j \alpha_j B_{ij}\right) - \sum_i \sum_j \alpha_j B_{ij} - \sum_j \frac{(\alpha_j - 1)^2}{2\sigma_j^2}, \tag{5.16}$$

$$\ln \mathcal{L}_{\rm uncond} = \sum_i n_i \ln\left(S_i + \sum_j \alpha_j B_{ij}\right) - \sum_i \left(S_i + \sum_j \alpha_j B_{ij}\right) - \sum_j \frac{(\alpha_j - 1)^2}{2\sigma_j^2}. \tag{5.17}$$

The test statistic used to quantify the preference for the signal hypothesis is defined as

$$q_0 = 2\left[\ln \mathcal{L}_{\rm uncond}\Big|_{\alpha_j=\hat{\alpha}_j} - \ln \mathcal{L}_{\rm cond}\Big|_{\alpha_j=\hat{\hat{\alpha}}_j}\right], \tag{5.18}$$

where $\hat{\alpha}_j$ and$\hat{\hat{\alpha}}_j$ denote the unconditional and conditional maximum-likelihood estimators, respectively. Under the asymptotic approximation, the discovery significance in Gaussian units is given by

$$Z = \sqrt{q_0}, \tag{5.19}$$

which quantifies the statistical significance for rejecting the background-only hypothesis.

To determine the discovery-limit cross section, we perform Monte Carlo simulations using 1000 pseudo-experiments for each assumed WIMP mass and cross section. In each realization, event counts are generated by applying Poisson fluctuations to the expected signal-plus-background model in every energy bin. The profile-likelihood test statistic is then evaluated for each pseudo-dataset, yielding a distribution of significances that reflects statistical variability between experiments.

The discovery-limit cross section, $\sigma_{\chi-n}^{\rm disc}$, is defined as the smallest cross section for which at least 90% of pseudo-experiments achieve a significance of $Z \geq 3$. This criterion corresponds to a statistical power of 90% for detecting a WIMP signal at the 3σ level, providing a robust and experimentally meaningful sensitivity threshold. By performing the same methodology across a range of WIMP masses, the discovery-limit curve is obtained, which defines the neutrino floor in this framework.

To cover a broad WIMP mass range, we adopt two detector configurations with different energy thresholds, following Ref. [10]. A low-threshold setup (5.3 $\mathrm{eV_{nr}}$, corresponding to 0.46 $\mathrm{eV_{ee}}$ under the Lindhard model) is optimized for low-mass WIMP searches and captures the dominant contribution from solar neutrinos. A higher-threshold configuration (7.2 $\mathrm{keV_{nr}}$ or 1.65 $\mathrm{keV_{ee}}$) suppresses solar backgrounds and enhances sensitivity to DSNB and atmospheric neutrinos, which are relevant at higher WIMP masses. The most stringent sensitivity obtained from these two configurations at each mass point defines the overall neutrino floor.

The exposures used in the pseudo-experiments are chosen such that the statistical uncertainty on the neutrino background remains subdominant compared to systematic uncertainties. For the low-threshold configuration, the exposure corresponds to approximately 200 expected ^{8}B solar neutrino events, while the high-threshold setup yields around 500 total neutrino events [10, 11]. These correspond to exposures of ~0.4 ton-year and 1.43×10^4 ton-year, respectively. Although these values exceed current experimental capabilities, they serve as idealized benchmarks to probe the asymptotic regime where systematic uncertainties dominate.

All calculations incorporate the systematic uncertainties in neutrino fluxes listed in Table 5.1 as Gaussian priors and include contributions from solar, atmospheric, DSNB, geoneutrino, and reactor-induced CEνNS backgrounds. This ensures a realistic treatment of both statistical and systematic effects in the sensitivity projections.

Figure 5.6 shows the influence of reactor antineutrinos on the neutrino floor as a function

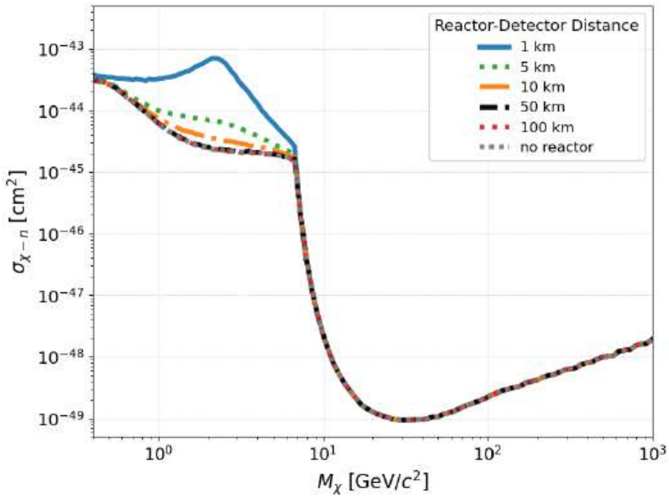

FIGURE 5.6: Dependence of the discovery-limit neutrino floor on reactor–detector distance for low-mass WIMPs. Results are shown for separations of 1, 5, 10, 50, and 100 km from a 3.6 $\mathrm{GW_{th}}$ reactor core, along with the no-reactor baseline. Adapted from Ref. [18].

of distance. The impact is most significant in the low-mass regime ($M_\chi \lesssim 10$ GeV$/c^2$), with the largest deviation occurring around $M_\chi \sim 2.5$–3 GeV/c^2. At short baselines, the enhanced reactor-induced CEνNS rate substantially raises the neutrino floor, degrading the discovery sensitivity by orders of magnitude. As the distance increases, the reactor contribution decreases following the inverse-square scaling, and the neutrino floor gradually approaches the baseline case without reactor contributions.

We further examine the role of systematic uncertainties in the reactor antineutrino flux. As shown in Fig. 5.7, reducing the flux uncertainty significantly improves the sensitivity at short distances (e.g., 1 km), where reactor backgrounds dominate. In contrast, at larger distances (e.g., 10 km), the impact of flux uncertainty is less pronounced due to the reduced reactor contribution.

Finally, Fig. 5.8 demonstrates the dependence of sensitivity on exposure. Increasing exposure enhances both signal and background statistics, reducing statistical uncertainties and improving the discrimination power. However, once systematic uncertainties dominate,

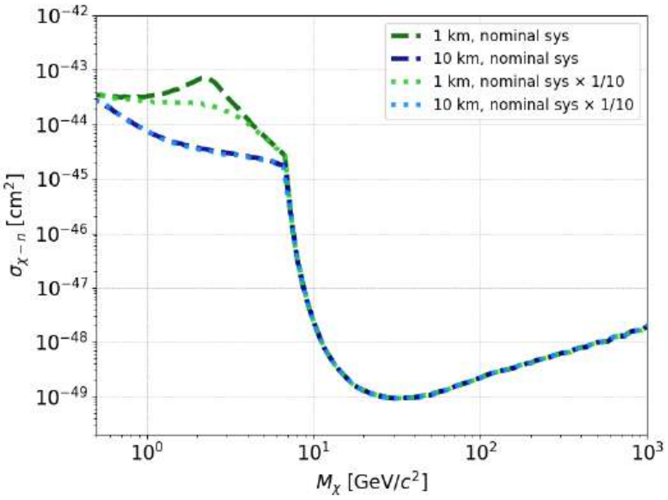

FIGURE 5.7: Impact of reactor flux uncertainty on the discovery-limit neutrino floor for detector distances of 1 km and 10 km. The nominal case assumes an 8% uncertainty, while the dashed curves correspond to a tenfold reduction. Adapted from Ref. [18].

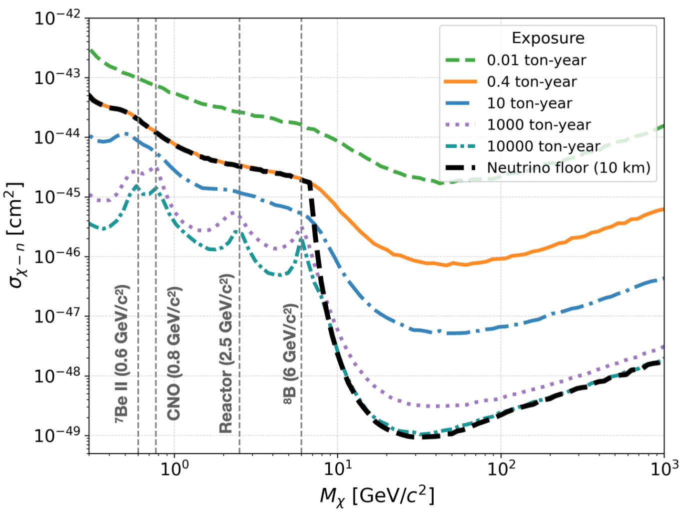

FIGURE 5.8: Dependence of the discovery limit on exposure for a detector with a nuclear-recoil threshold of 5.3 eV$_{\mathrm{nr}}$ (0.46 eV$_{\mathrm{ee}}$). A reactor–detector distance of 10 km is assumed. Increasing exposure improves sensitivity, but the gain saturates in regions where neutrino-induced recoils are spectrally indistinguishable from WIMP signals. Adapted from Ref. [18].

further increases in exposure yield diminishing returns. This effect is most evident in regions where the WIMP-induced recoil spectrum closely resembles that of neutrinos, such as near $M_\chi \sim 6$ GeV/c^2, where the signal is degenerate with the ^{8}B solar neutrino background. This behavior highlights the intrinsic sensitivity limit imposed by neutrino backgrounds.

To address the dependence of the discovery-limit framework on exposure and detector threshold, an alternative definition based on the concept of *opacity* is considered in the following subsection.

5.4.2 Opacity-Based Neutrino Floor

An alternative and more physically motivated definition of the neutrino floor has been developed in terms of the concept of *neutrino fog*, as introduced by O'Hare [13]. In this framework, the limitation imposed by neutrino backgrounds is not described as a sharp boundary, but rather as a gradual transition region in which the discrimination between WIMP-induced nuclear recoils and those arising from CEνNS becomes increasingly difficult. This degradation in sensitivity arises primarily from systematic uncertainties in the neutrino fluxes, rather than from statistical fluctuations alone.

Within this formalism, the neutrino floor is defined using the dimensionless *opacity parameter*, which quantifies how rapidly the discovery sensitivity deteriorates as the neutrino background increases. The opacity provides a direct measure of the relative importance of statistical versus systematic uncertainties, thereby offering a more nuanced characterization of the detector sensitivity across different regimes.

At low exposures, the sensitivity of a dark matter search improves with increasing exposure according to Poisson statistics, scaling approximately as the inverse square root of the number of events. In this regime, statistical fluctuations dominate the uncertainty,

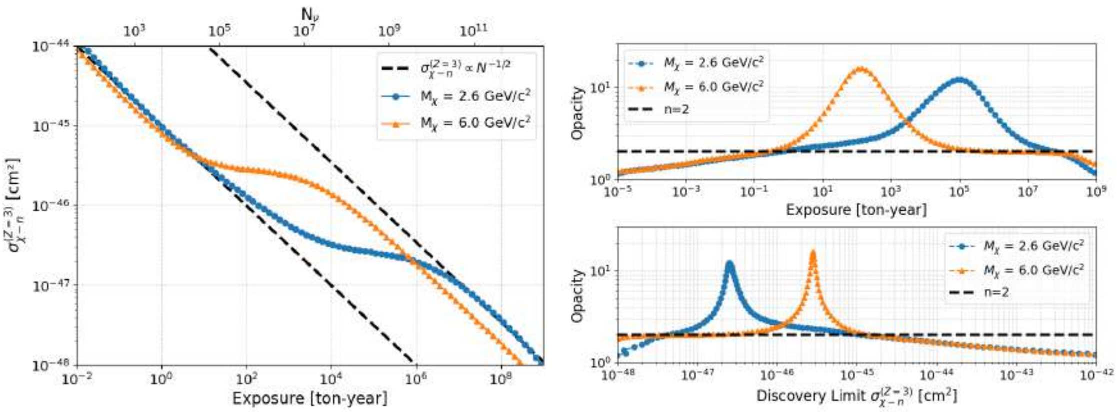

FIGURE 5.9: **Left**: WIMP discovery-limit cross section σ_χ vs. detector exposure for m_χ = 2.6 GeV$/c^2$ (solid) and 6 GeV$/c^2$ (dashed) at a 50 km reactor baseline. The two cases are dominated by reactor $\bar{\nu}_e$ CEνNS and the ^{8}B solar neutrino floor, respectively. **Right**: Evolution of the opacity parameter α with exposure, and discovery limits, at the same 50 km baseline, showing the onset of neutrino–signal degeneracy. Adapted from Ref. [18].

and increasing exposure leads to significant improvements in the minimum detectable WIMP–nucleon cross section. However, as the exposure grows, the number of neutrino-induced events increases proportionally, and uncertainties in their flux normalization begin to play a dominant role. This results in a gradual saturation of the discovery sensitivity, as illustrated in Fig. 5.8. Beyond this point, further increases in exposure yield diminishing improvements in sensitivity.

To quantify this transition, we follow the methodology outlined in Ref. [13]. For a fixed detection significance of $Z = 3$, the discovery-limit cross section, denoted $\sigma^{(Z=3)}_{\chi-n}$, is computed over a grid of WIMP masses M_χ and detector exposures. For each exposure, the total CEνNS background, N_ν, is obtained by summing contributions from all relevant neutrino sources, including solar, reactor, DSNB, geoneutrinos, and atmospheric neutrinos.

The opacity parameter, n, is defined in terms of the logarithmic response of the discovery-limit cross section to changes in the total neutrino background:

$$n = -\left(\frac{d \ln \sigma^{(Z=3)}_{\chi-n}}{d \ln N_\nu} \right)^{-1} . \tag{5.20}$$

This definition captures the scaling behavior of the sensitivity. In the statistics-dominated regime, the discovery limit scales as $\sigma_{\chi-n} \propto N_\nu^{-1/2}$, corresponding to $n \approx 1$. In contrast, when systematic uncertainties dominate, the sensitivity becomes weakly dependent on exposure, leading to $n \gg 1$.

Figure 5.9 (left) illustrates the dependence of the discovery-limit cross section on the total neutrino background for two representative WIMP masses. The first case, $M_\chi = 2.6$ GeV$/c^2$, corresponds to a scenario in which reactor antineutrinos provide a dominant CEνNS background, particularly for a reactor–detector distance of 50 km. The second case, $M_\chi = 6.0$ GeV$/c^2$, highlights the regime where ^{8}B solar neutrinos dominate the background and produce recoil spectra similar to those expected from WIMPs.

At low neutrino event counts (or equivalently low exposure), the expected $N_\nu^{-1/2}$ scaling is clearly observed, reflecting the Poisson-limited regime. As the exposure increases, the improvement in sensitivity slows down and approaches a plateau, indicating the onset of a systematics-dominated regime where uncertainties in neutrino flux normalization limit further gains. Interestingly, at very high exposures, the scaling behavior can partially revert toward the Poisson-like regime. This occurs because the spectral shapes of WIMP and CEνNS signals are not perfectly identical, and with sufficient statistics, these differences can be exploited to regain some discrimination power [12, 13].

The opacity-based neutrino floor is defined as the contour in the $(M_\chi, \sigma_{\chi-n})$ parameter space where the opacity parameter satisfies $n = 2$. This choice marks the transition between the statistics-limited regime ($n \lesssim 2$) and the systematics-limited regime ($n \gtrsim 2$). Above this opacity value, the sensitivity improvement from increasing exposure becomes significantly suppressed, and the detector operates within the neutrino fog region.

The evolution of the opacity parameter with exposure and discovery sensitivity is shown in Fig. 5.9 (right). The top panel illustrates how n increases with exposure, reflecting the transition from statistical to systematic dominance. The bottom panel presents the corresponding dependence on the discovery-limit cross section, providing a complementary view of the same transition.

The impact of reactor antineutrinos on the opacity-based neutrino floor is summarized in Fig. 5.10, which shows results for multiple reactor–detector baselines ranging from 1 km to 100 km, along with a no-reactor reference scenario. In the absence of reactor contributions, the low-mass sensitivity is primarily limited by solar neutrinos, particularly the ^{8}B component.

When reactor antineutrinos are included, an additional region of increased opacity emerges around $M_\chi \sim 2.5$–3 GeV/c^2, where the reactor-induced CEνNS spectrum closely resembles that of low-mass WIMPs. As the detector is placed closer to the reactor core, the flux increases significantly due to the $1/L^2$ dependence, leading to a substantial upward shift of the neutrino floor in this mass range. For baselines shorter than approximately 10 km, the reactor contribution can exceed that from solar neutrinos, becoming the dominant background in the low-energy regime.

This behavior contrasts with the discovery-limit-based definition, where the neutrino floor can depend explicitly on the choice of detector exposure and energy threshold used in pseudo-experiments. In the opacity-based framework, the definition is inherently less sensitive to these choices, as it is based on the scaling properties of the sensitivity rather than on a fixed statistical criterion. Consequently, the opacity-based neutrino floor provides a more robust and physically transparent characterization of the ultimate limitations imposed by neutrino backgrounds.

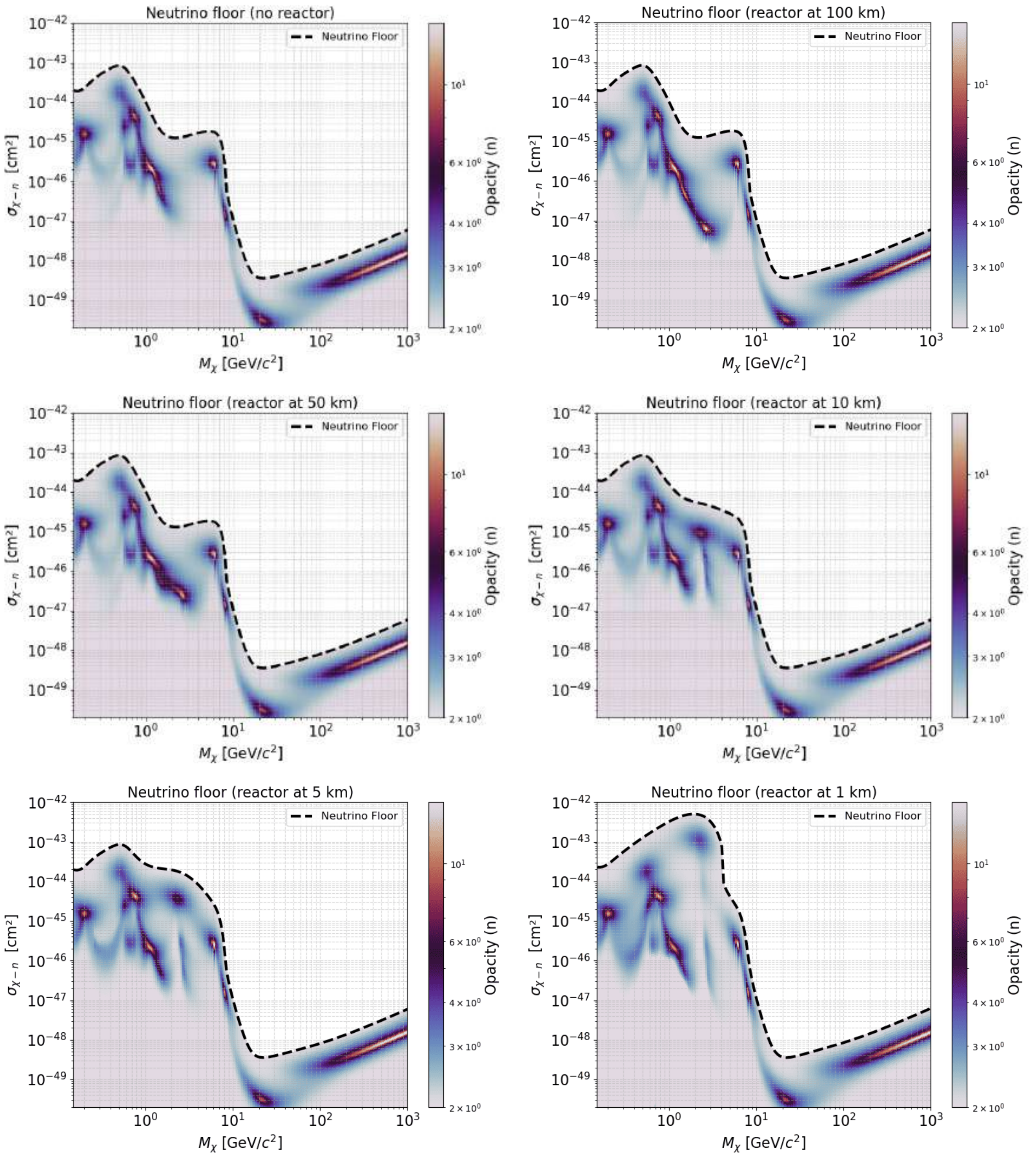

FIGURE 5.10: Impact of reactor $\bar{\nu}_e$ flux on the opacity-based neutrino floor (median expected sensitivity) for reactor–detector baselines of 1, 5, 10, 50, and 100 km, along with a no-reactor scenario. Reactor antineutrinos predominantly affect WIMP searches around $M_\chi \sim 2.5$–3 GeV/c^2. As the baseline decreases, the neutrino "fog" region shifts upward, with reactor-induced backgrounds overtaking the solar-neutrino contribution for distances $\lesssim 10$ km. Adapted from [18].

Overall, these results demonstrate that reactor antineutrinos constitute a significant and site-dependent background for dark matter searches targeting WIMP masses below ~ 10 GeV$/c^2$. Even at moderate distances, their contribution can substantially degrade sensitivity in the low-mass region, emphasizing the importance of careful site selection and background modeling for next-generation low-threshold experiments.

As an important validation of our analysis framework, we compare the baseline neutrino floor obtained in this work, defined as the neutrino floor in the absence of reactor antineutrino contributions, with previously published results for germanium-based detectors. This comparison serves as a consistency check for both the statistical treatment and the implementation of neutrino-induced backgrounds.

The comparison is performed for two commonly used definitions of the neutrino floor: the discovery-limit–based approach [37] and the opacity-based approach [13]. The results are presented in Fig. 5.11, where our calculations are shown alongside the corresponding curves reported in the literature.

For the discovery-limit–based neutrino floor, our results are in good agreement with those reported in the APPEC Committee Report (2021) [37] over most of the WIMP mass range. In particular, the overall shape and normalization of the neutrino floor at low masses are well reproduced. However a noticeable deviation is observed, in the region around a WIMP mass of $M_\chi \sim 6$ GeV$/c^2$. This mass range corresponds to the transition where the neutrino floor is primarily governed by recoils induced by ^{8}B solar neutrinos. The origin of this discrepancy can be traced to the different assumptions made regarding the systematic uncertainty associated with the ^{8}B neutrino flux. In the present work, we adopt a significantly reduced systematic uncertainty of 2% for the ^{8}B flux (see Table 5.1), reflecting recent improvements in solar-neutrino flux determinations. In contrast, the APPEC report assumes a much larger uncertainty of 16%. As discussed in Fig. 5.7, neutrino floor is sensitive to such normalization uncertainties, since the statistical discrimination between signal and background depends explicitly on the assumed level of background uncertainty. A reduction in the systematic uncertainty effectively enhances the ability to distinguish a potential WIMP signal from the neutrino background, thereby lowering the inferred neutrino floor and extending the accessible parameter space for dark matter discovery. To confirm this interpretation, we have repeated the calculation using a 16% uncertainty for the ^{8}B flux. Under this assumption, the resulting neutrino floor shifts upward and becomes consistent with the APPEC result, demonstrating that the observed difference arises entirely from the choice of input systematic uncertainties rather than from any methodological inconsistency. For the opacity-based neutrino floor, we find good agreement with the results presented in Ref. [13] across the full WIMP mass range.

Overall, this comparison demonstrates that the analysis framework employed in this work reliably reproduces established neutrino floor calculations in the reactor-free limit. The remaining differences are fully understood in terms of differing assumptions about background systematic uncertainties, providing confidence in both the implementation and the interpretation of the results.

Systematic Robustness Check of the Analysis

To quantify the stability of the inferred neutrino floor, we perform a series of controlled variation studies in which key physical inputs and detector-related parameters are systematically modified. These tests are designed to probe the sensitivity of the results to environmental conditions, detector response modeling, and reactor-related assumptions. In particular, they allow us to identify which effects produce meaningful shifts in the neutrino floor and which remain subdominant.

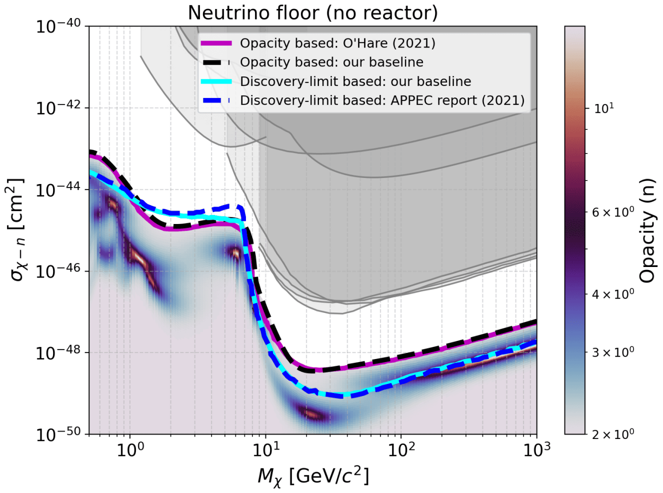

FIGURE 5.11: Comparison of the baseline neutrino floor (no-reactor case) with published discovery-limit–based [37] and opacity-based [13] results for a germanium detector. Overall, the results presented in this work successfully reproduce the established trends in the literature. The lower neutrino floor observed in the discovery-limit case near a WIMP mass of 6 GeV$/c^2$ arises from the smaller (2%) systematic uncertainty assumed for the ^{8}B solar-neutrino flux in this analysis, compared to the 16% uncertainty adopted in Ref. [37]. The grey shaded regions indicate parameter space excluded by leading direct-detection experiments, including SuperCDMS [4, 38], EDELWEISS [39], PICO [40], DarkSide [41], CRESST [5, 42], LZ [6], PandaX [7], and XENON [8]. Adapted from Ref. [18].

Impact of Geoneutrino Flux Variations: The geoneutrino flux originates from radioactive decays of uranium and thorium chains within the Earth's crust and mantle. Its magnitude depends on the geological composition surrounding the detector and can vary significantly between experimental sites. To account for this uncertainty, we consider a factor-of-two variation in the geoneutrino flux, spanning the range expected between locations such as CJPL and SNOLAB.

The impact of this variation on the neutrino floor is shown in Fig. 5.12. The effect is localized in the low-mass region, with the largest deviation occurring near $M_\chi \sim 1.7$ GeV$/c^2$, where the recoil spectrum from geoneutrinos overlaps with that expected from low-mass WIMPs. Even in this region, the change in the neutrino floor remains at the level of

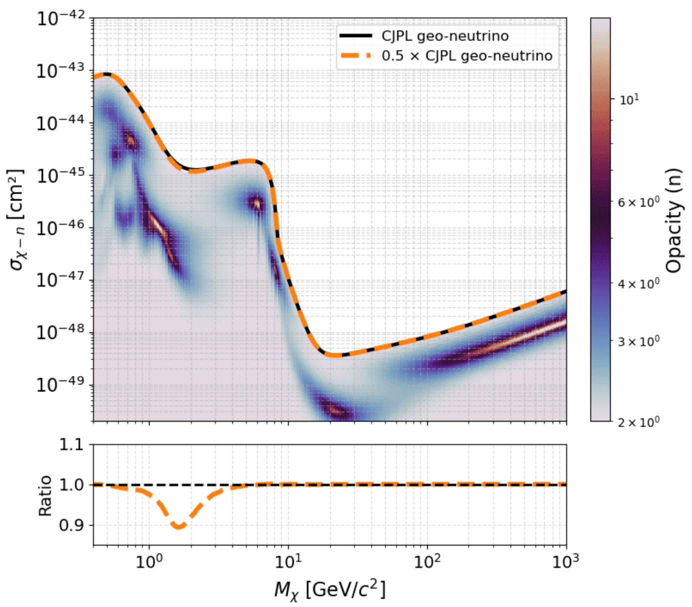

FIGURE 5.12: Effect of a factor-of-two variation in the geoneutrino flux on the opacity-based neutrino floor in the absence of reactor contributions, assuming a representative detector configuration. The impact is minimal ($\lesssim$10%), with the largest deviation occurring near $M_\chi \sim 1.7$ GeV$/c^2$. Only central values are shown; uncertainties beyond the flux variation are not included. Adapted from Ref. [18].

$O(10\%)$. At higher masses, the contribution becomes negligible due to the rapidly falling geoneutrino recoil spectrum.

When reactor antineutrinos are included at baselines of $O(10\,\text{km})$ or smaller, the CEνNS rate from reactor neutrinos dominates the low-energy recoil spectrum. In this regime, the relative contribution of geoneutrinos becomes negligible, indicating that geoneutrino-induced backgrounds do not play a significant role in near-reactor configurations.

Influence of Quenching-Model Uncertainties: The mapping between nuclear recoil energy and the observable detector response is governed by the quenching model. To assess the associated uncertainty, we vary the Lindhard quenching parameter within its experimentally allowed range, adopting the CONUS+ value $k = 0.162 \pm 0.004$. This variation modifies both the recoil-energy scale and the effective event rate.

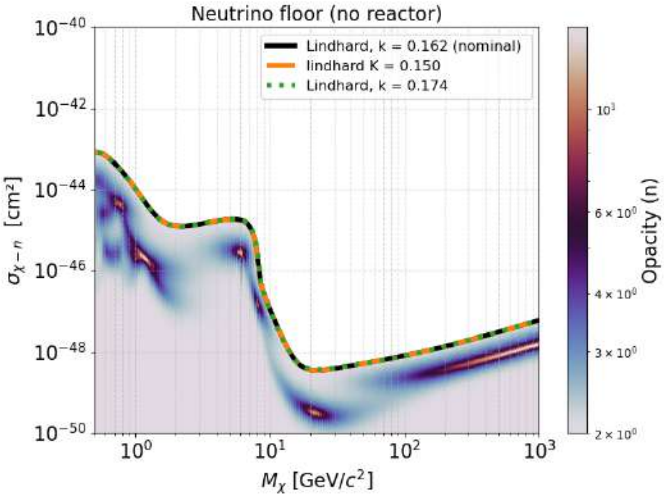

FIGURE 5.13: Opacity-based neutrino floor obtained under variations of the Lindhard quenching parameter within its 3σ uncertainty range. The resulting curves are nearly indistinguishable. Adapted from Ref. [18].

The resulting neutrino floors are shown in Fig. 5.13. Across the full WIMP mass range, the curves remain nearly identical, indicating that the effect of quenching uncertainty is negligible. This can be understood from the fact that both WIMP-induced and CEνNS-induced recoil spectra are modified in a similar manner under changes in the quenching model. As a result, the relative spectral degeneracy between signal and background remains essentially unchanged, leading to minimal impact on the inferred neutrino floor.

Effect of Multiple Reactor Sources: In realistic experimental environments, detectors may receive contributions from multiple nuclear reactors located at different distances and operating with different thermal powers. To evaluate this scenario, we consider a configuration consisting of three reactors with distinct baselines and compute the combined CEνNS spectrum.

The resulting neutrino floor, shown in Fig. 5.14, is found to be nearly indistinguishable from that obtained using an effective single-reactor description with an appropriately

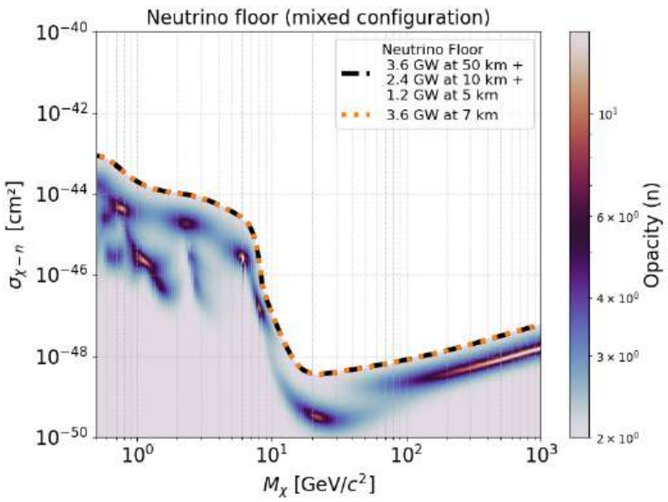

FIGURE 5.14: Neutrino floor for a multi-reactor configuration compared to an equivalent single-reactor approximation. The two cases show identical behavior. Adapted from Ref. [18].

weighted flux normalization. This indicates that the combined contribution of multiple reactors can be accurately captured by a simplified effective model, without requiring detailed treatment of each individual source. Such an approximation is particularly useful for studying detector sites influenced by complex reactor networks.

Reactor Spectrum Shape Variations: The antineutrino spectrum emitted by a reactor depends on its fuel composition, which determines the relative contributions from different fissile isotopes. To quantify the impact of this effect, we compare a nominal commercial reactor spectrum with a highly enriched ^{235}U configuration, representative of research reactors.

As shown in Fig. 5.15, the resulting change in the neutrino floor is at the level of $\sim 10\%$. This variation is small compared to the much larger shifts induced by changes in reactor baseline, which directly affect the overall flux normalization. Therefore, uncertainties associated with reactor fuel composition and spectral shape do not constitute a dominant

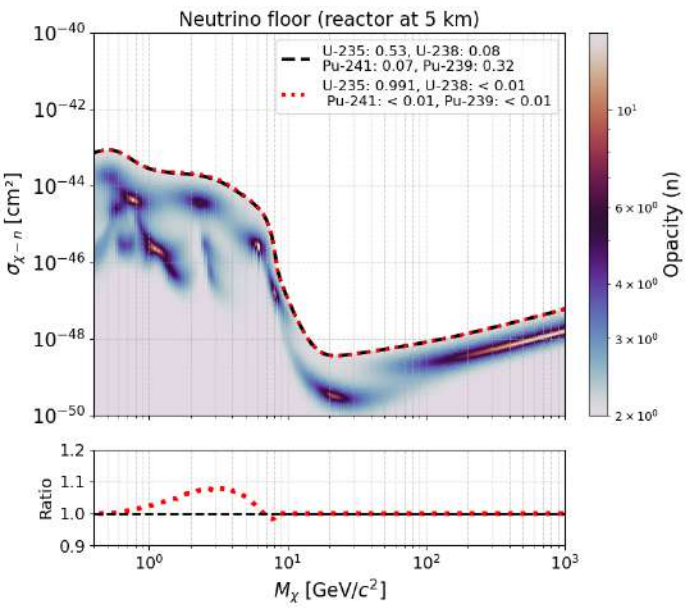

FIGURE 5.15: Comparison of neutrino floors obtained for different reactor fuel compositions at a fixed baseline. The fission fraction can change both the shape and normalisation of the reactor anti-neutrino flux. The variation remains at the ~ 10% level. Adapted from Ref. [18].

limitation in determining the neutrino floor.

Effect of Solar Neutrino Uncertainty Variations: The sensitivity of the neutrino floor is strongly influenced by the precision with which the solar neutrino fluxes are known. For dark matter masses of $O(\mathrm{GeV}/c^2)$, the dominant irreducible background arises from solar ^{8}B neutrinos. Early neutrino floor studies adopted a relatively large uncertainty of approximately 16% on the ^{8}B solar neutrino flux [10], reflecting the precision available at that time. More recent global analyses of solar neutrino fluxes have substantially improved the determination of the ^{8}B flux, reducing its uncertainty to about 2% [43], which is the value adopted throughout this study. To quantify the impact of this improvement, we compare the neutrino floor obtained using the current 2% uncertainty with that obtained using the earlier 16% assumption. As shown in Fig. 5.16, increasing the ^{8}B solar neutrino flux uncertainty from 2% to 16% raises the neutrino floor by approximately one order of magnitude for dark matter masses around 6 GeV/c^2. This demonstrates that reducing the uncertainty on the solar ^{8}B neutrino flux significantly lowers the neutrino floor, thereby improving the sensitivity of future direct detection experiments to weaker dark matter–nucleon cross sections.

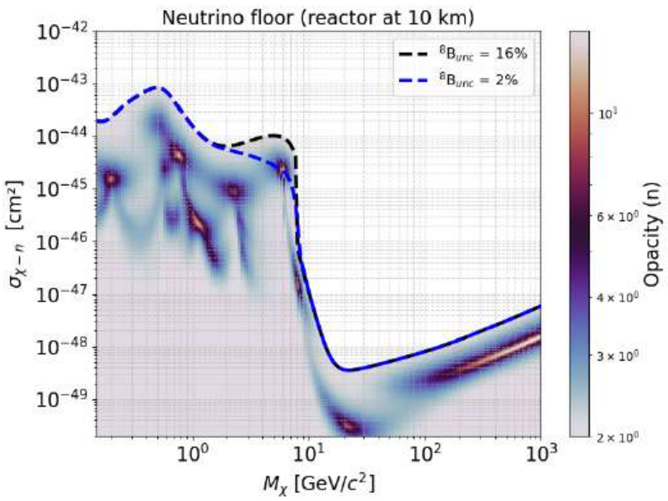

FIGURE 5.16: Comparison of the neutrino floor for two assumed uncertainties in the solar ^{8}B neutrino flux (2% and 16%) at a reactor-to-detector distance of 10 km. Increasing the solar ^{8}B flux uncertainty from 2% to 16% raises the neutrino floor by approximately one order of magnitude for dark matter around 6 GeV/c^2.

Taken together, these variation studies demonstrate that the inferred neutrino floor is robust against most of the systematic variations considered in this work. Variations in the geoneutrino flux, quenching model, reactor configuration, and reactor fuel composition produce only minor changes, generally at the level of $O(10\%)$ or less. In contrast, uncertainties in the flux of a dominant neutrino background can have a substantially larger impact on the neutrino floor. The solar ^{8}B neutrino flux provides a clear example: increasing its assumed uncertainty from 2% to 16% results in approximately an order-of-magnitude increase in the neutrino floor around $M_\chi \sim 6$ GeV$/c^2$. This highlights the importance of accurately determining the fluxes of the neutrino sources that contribute significantly to the background when assessing the ultimate sensitivity of direct dark matter detection experiments. Thus, while the opacity-based framework remains robust against the other systematic variations investigated here, its sensitivity to uncertainties in dominant neutrino fluxes reflects the importance of our knowledge of the underlying neutrino backgrounds.

5.5 Implications for Next-Generation Dark Matter Searches

Next-generation direct-detection experiments designed to probe WIMP masses below approximately 10 GeV/c^2 rely on detectors with extremely low energy thresholds. While such detectors significantly enhance sensitivity to low-mass dark matter, they also become increasingly susceptible to backgrounds arising from CEνNS. Among these backgrounds, antineutrinos emitted by nuclear reactors can play an important role when detectors are located within relatively short distances of reactor facilities.

Reactor antineutrinos generate nuclear recoils with energies comparable to those expected from low-mass WIMP interactions. As a result, their presence can effectively raise the neutrino floor and reduce the achievable discovery sensitivity of future experiments. Understanding the magnitude of this effect is therefore essential when assessing the realistic reach of upcoming low-threshold detectors.

Figure 5.17 compares the influence of reactor-induced CEνNS backgrounds on the neutrino floor using both the discovery-limit and opacity-based definitions. Although both approaches predict a similar qualitative behavior, quantitative differences of up to an order of magnitude can arise because the two methods characterize the neutrino background limitation in fundamentally different ways [13].

When a detector is located close to a nuclear reactor, the resulting antineutrino flux can become a dominant contributor to the low-energy recoil spectrum. This leads to a significant upward shift of the neutrino floor in the low-mass WIMP region. The magnitude of this shift depends strongly on the reactor–detector separation. Table 5.5 summarizes the calculated neutrino floor values for a representative WIMP mass of $M_\chi = 2.6$ GeV/c^2.

For baselines shorter than approximately 10 km, the neutrino floor can increase by several orders of magnitude compared to the baseline scenario without reactor contributions, with an enhancement of about two orders of magnitude around 2.6 GeV/c^2 at a reactor–detector distance of 1 km. In contrast, at distances of tens to hundreds of kilometers, the impact of reactor antineutrinos becomes progressively less significant.

The opacity-based definition shows a stronger sensitivity to variations in the reactor antineutrino flux compared to the discovery-limit approach. This behavior arises because the opacity formalism explicitly quantifies how systematic uncertainties in the neutrino background degrade experimental sensitivity. Consequently, detectors aiming to probe WIMP masses below ~10 GeV/c^2 would ideally be located at distances exceeding approximately 100 km from large gigawatt-scale reactor complexes. At such distances, reactor-induced CEνNS events contribute only a small fraction of the total neutrino background. These findings emphasize the importance of incorporating site-specific neutrino backgrounds into sensitivity forecasts for future dark matter experiments.

Finally, several experimental strategies may help mitigate neutrino-induced limitations in future detectors. One promising approach involves the use of directional detection techniques [44, 45], which exploit the anisotropic distribution of incoming neutrinos and dark matter particles to enhance signal discrimination.

TABLE 5.5: Neutrino floor cross sections for a WIMP mass $M_\chi = 2.6\ \mathrm{GeV}/c^2$, evaluated at different reactor–detector baselines. The table compares discovery-limit-based and opacity-based neutrino floors, normalized to the no-reactor baseline and quoted as percentage enhancements. At a 1 km reactor baseline, reactor antineutrinos can raise the low-mass neutrino floor by approximately two orders of magnitude compared to the reactor-free case.

Reactor–detector	Discovery-limit-based			Opacity-based		
	$\sigma_{\chi-n}$ [cm^2]	$\sigma/\sigma_{\mathrm{baseline}}$	Δ [%]	$\sigma_{\chi-n}$ [cm^2]	$\sigma/\sigma_{\mathrm{baseline}}$	Δ [%]
1 km	5.57×10^{-44}	25.79	2479	4.23×10^{-43}	326.15	32515
5 km	6.28×10^{-45}	2.91	191	1.66×10^{-44}	12.77	1177
10 km	3.32×10^{-45}	1.54	54	4.78×10^{-45}	3.68	268
50 km	2.27×10^{-45}	1.05	5	1.34×10^{-45}	1.03	3
100 km	2.20×10^{-45}	1.02	2	1.30×10^{-45}	1.00	0
no reactor (baseline)	2.16×10^{-45}	1.00	–	1.30×10^{-45}	1.00	–

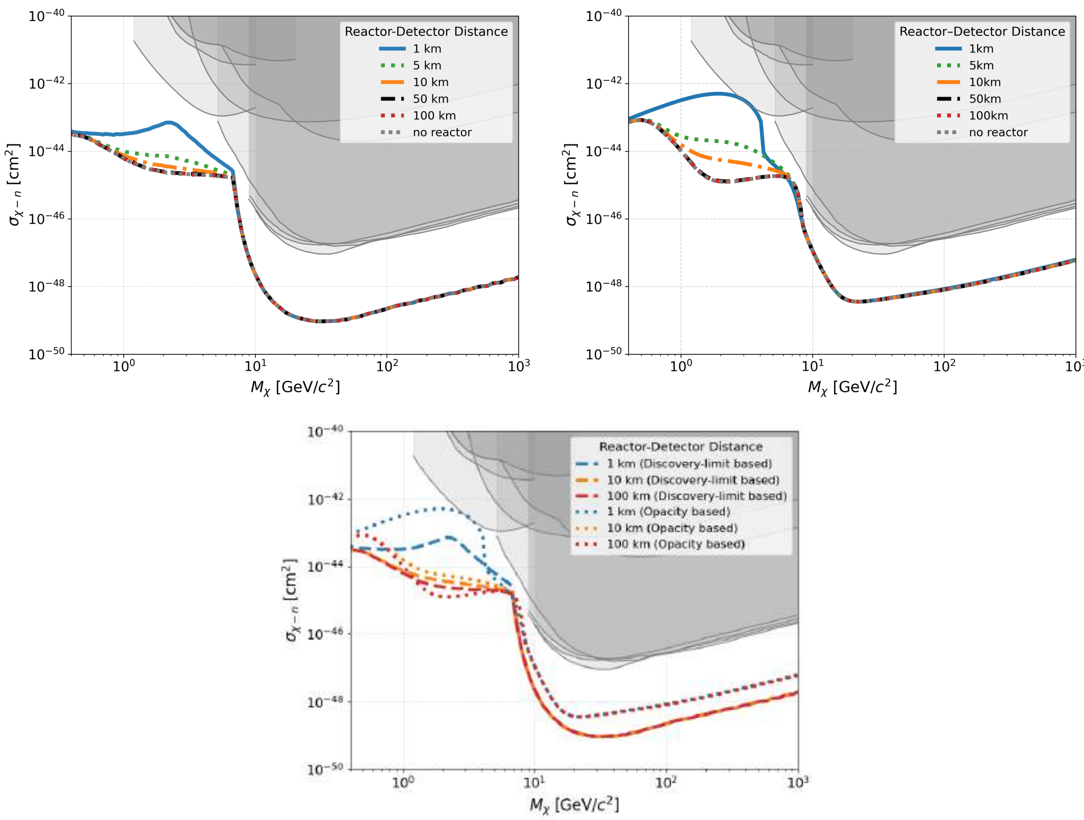

FIGURE 5.17: Impact of reactor proximity on low-mass WIMP sensitivity. **Upper Left:** discovery-limit–based neutrino floor. **Upper Right:** opacity-based neutrino floor. **Bottom:** discovery-limit versus opacity-based neutrino floor. The opacity-based definition exhibits stronger sensitivity to reactor antineutrino flux variations. Grey shaded regions indicate parameter space excluded by leading experiments, including SuperCDMS [4, 38], EDELWEISS [39], PICO [40], DarkSide [41], CRESST [5, 42], LZ [6], PandaX [7], and XENON [8]. The region between current experimental bounds and the neutrino floor defines the accessible discovery window for future WIMP searches. Adapted from Ref. [18].

5.6 Summary and Outlook

In this chapter, we studied the impact of antineutrinos from GW_{th}-scale nuclear reactors on the sensitivity of future low-threshold dark matter experiments targeting WIMPs with masses below $\sim$ 10 GeV/c^2. The analysis was performed for a detector configuration inspired by high-voltage germanium devices used in the SuperCDMS program, with the detector response modeled using Lindhard quenching to account for the conversion between nuclear-recoil and electron-equivalent energies. To quantify neutrino-induced backgrounds, the neutrino floor was evaluated using two complementary statistical approaches: the discovery-limit formalism and the opacity-based framework, allowing a consistent comparison of reactor effects across methods.

The main results of this work can be summarized as follows:

- The impact of reactor antineutrinos is most significant in the low-mass WIMP region, particularly around $M_\chi \sim 2.5$–3 GeV/c^2, where CEνNS recoil spectra overlap strongly with WIMP-induced signals.
- For reactor–detector separations below $\sim$ 10 km, reactor-induced CEνNS events substantially elevate the neutrino floor. At distances of order $\sim$ 1 km, the neutrino floor can increase by up to $\mathcal{O}(10^2)$ in the most affected mass region.
- The reactor antineutrino flux follows an approximate $1/L^2$ scaling with distance, causing its contribution to decrease rapidly and become negligible beyond $\mathcal{O}(100)$ km.
- Both the discovery-limit and opacity-based formalisms yield consistent qualitative trends, with reactor antineutrinos producing a similar upward shift in the neutrino floor. The opacity-based approach exhibits a stronger sensitivity to variations in the reactor antineutrino flux, while the overall conclusions remain robust.

- Additional studies considering uncertainties in detector response and background modeling (including quenching factor, geoneutrinos, and reactor flux uncertainties) show that geometric flux scaling with distance is the dominant factor governing the reactor-induced background.

The strong distance dependence of reactor antineutrino flux implies that site selection is a critical factor in the design of next-generation direct detection experiments. Facilities located in close proximity to nuclear reactors may experience a significant irreducible neutrino background that elevates the neutrino floor and reduces sensitivity to low-mass WIMPs. Therefore, experimental sites situated at distances well beyond $\sim$ 100 km from major reactor complexes are preferred for probing this parameter space. Complementary mitigation strategies, such as directional detection techniques or improved background discrimination, may further help in partially alleviating neutrino-induced limitations.

Overall, this analysis underscores the necessity of accounting for reactor antineutrino backgrounds in precision sensitivity studies for future dark matter searches, particularly in the low-mass WIMP regime. It also motivates further work exploring advanced detection techniques and background mitigation strategies to preserve sensitivity in neutrino-limited scenarios.

Bibliography

[1] Gary Steigman and Michael S. Turner. “Cosmological Constraints on the Properties of Weakly Interacting Massive Particles”. *Nucl. Phys. B* 253 (1985), pp. 375–386.

[2] Gerard Jungman, Marc Kamionkowski, and Kim Griest. “Supersymmetric dark matter”. *Phys. Rept.* 267 (1996), pp. 195–373. arXiv: hep-ph/9506380.

[3] Gary Steigman, Basudeb Dasgupta, and John F. Beacom. “Precise Relic WIMP Abundance and its Impact on Searches for Dark Matter Annihilation”. *Phys. Rev. D* 86 (2012), p. 023506. arXiv: 1204.3622 [hep-ph].

[4] R. Agnese et al. “Search for Low-Mass Dark Matter with CDMSlite Using a Profile Likelihood Fit”. *Phys. Rev. D* 99.6 (2019), p. 062001. arXiv: 1808.09098 [astro-ph.CO].

[5] G. Angloher et al. “First observation of single photons in a CRESST detector and new dark matter exclusion limits”. *Phys. Rev. D* 110.8 (2024), p. 083038. arXiv: 2405.06527 [astro-ph.CO].

[6] J. Aalbers et al. “First Dark Matter Search Results from the LUX-ZEPLIN (LZ) Experiment”. *Phys. Rev. Lett.* 131.4 (2023), p. 041002. arXiv: 2207.03764 [hep-ex].

[7] Zihao Bo et al. “Dark Matter Search Results from 1.54 Tonne·Year Exposure of PandaX-4T”. *Phys. Rev. Lett.* 134.1 (2025), p. 011805. arXiv: 2408.00664 [hep-ex].

[8] E. Aprile et al. “WIMP Dark Matter Search Using a 3.1 Tonne-Year Exposure of the XENONnT Experiment”. *Phys. Rev. Lett.* 135.22 (2025), p. 221003. arXiv: 2502.18005 [hep-ex].

[9] Daniel Z. Freedman. “Coherent effects of a weak neutral current”. *Phys. Rev. D* 9 (5 1974), pp. 1389–1392.

[10] J. Billard, L. Strigari, and E. Figueroa-Feliciano. “Implication of neutrino backgrounds on the reach of next generation dark matter direct detection experiments”. *Phys. Rev. D* 89.2 (2014), p. 023524. arXiv: 1307.5458 [hep-ph].

[11] F. Ruppin, J. Billard, E. Figueroa-Feliciano, and L. Strigari. “Complementarity of dark matter detectors in light of the neutrino background”. *Phys. Rev. D* 90.8 (2014), p. 083510. arXiv: 1408.3581 [hep-ph].

[12] Ciaran A. J. O’Hare. “Can we overcome the neutrino floor at high masses?” *Phys. Rev. D* 102.6 (2020), p. 063024. arXiv: 2002.07499 [astro-ph.CO].

[13] Ciaran A. J. O’Hare. “New Definition of the Neutrino Floor for Direct Dark Matter Searches”. *Phys. Rev. Lett.* 127.25 (2021), p. 251802. arXiv: 2109.03116 [hep-ph].

[14] Yingjie Fan, Xuewen Liu, and Ning Zhou. "Characterizing the CJPL's site-specific neutrino floor as the neutrino fog boundary". *Chin. Phys.* 49.10 (2025), p. 103001. arXiv: 2503.22155 [hep-ph].

[15] D. Akimov et.al and COHERENT Collaboration. "Observation of coherent elastic neutrino-nucleus scattering". *Science* 357.6356 (2017), pp. 1123–1126. eprint: https://www.science.org/doi/pdf/10.1126/science.aao0990.

[16] N. Ackermann et al. "Direct observation of coherent elastic antineutrino-nucleus scattering". *Nature* 643 (2025), pp. 1229–1233. arXiv: 2501.05206 [hep-ex].

[17] S. Adamski et al. "Evidence of Coherent Elastic Neutrino-Nucleus Scattering with COHERENT's Germanium Array". *Phys. Rev. Lett.* 134.23 (2025), p. 231801.

[18] D. Aristizabal Sierra, Valentina De Romeri, and Christoph A. Ternes. "Reactor neutrino background in next-generation dark matter detectors". *Phys. Rev. D* 109.11 (2024), p. 115026. arXiv: 2402.06416 [hep-ph].

[19] R Agnese et al. "First dark matter constraints from a SuperCDMS single-charge sensitive detector". *Physical Review Letters* 121.5 (2018), p. 051301.

[20] M. F. Albakry et al. "Search for low-mass electron-recoil dark matter using a single-charge sensitive SuperCDMS-HVeV Detector" (Sept. 2025). arXiv: 2509.03608 [hep-ex].

[21] J. D. Lewin and P. F. Smith. "Review of mathematics, numerical factors, and corrections for dark matter experiments based on elastic nuclear recoil". *Astropart. Phys.* 6 (1996), pp. 87–112.

[22] P. A. R. Ade et al. "Planck 2015 results. XIII. Cosmological parameters". *Astron. Astrophys.* 594 (2016), A13. arXiv: 1502.01589 [astro-ph.CO].

[23] J. D. Lewin and P. F. Smith. "Review of mathematics, numerical factors, and corrections for dark matter experiments based on elastic nuclear recoil". *Astropart. Phys.* 6 (1996), pp. 87–112.

[24] P.N. Luke, J. Beeman, F.S. Goulding, S.E. Labov, and E.H. Silver. "Calorimetric ionization detector". *Nuclear Instruments and Methods in Physics Research Section A: Accelerators, Spectrometers, Detectors and Associated Equipment* 289.3 (1990), pp. 406–409.

[25] P. N. Luke. "Voltage-assisted calorimetric ionization detector". *Journal of Applied Physics* 64.12 (Dec. 1988), pp. 6858–6860.

[26] N. Ackermann et al. "Direct observation of coherent elastic antineutrino–nucleus scattering". *Nature* 643.8074 (2025), pp. 1229–1233. arXiv: 2501.05206 [hep-ex].

[27] Kate Scholberg. "Prospects for measuring coherent neutrino-nucleus elastic scattering at a stopped-pion neutrino source". *Phys. Rev. D* 73 (2006), p. 033005. arXiv: hep-ex/0511042.

[28] Graciela B. Gelmini, Volodymyr Takhistov, and Samuel J. Witte. "Geoneutrinos in Large Direct Detection Experiments". *Phys. Rev. D* 99.9 (2019), p. 093009. arXiv: 1812.05550 [hep-ph].

[29] Chao Zhang, Xin Qian, and Muriel Fallot. "Reactor antineutrino flux and anomaly". *Prog. Part. Nucl. Phys.* 136 (2024), p. 104106. arXiv: 2310.13070 [hep-ph].

[30] N Ackermann, S Armbruster, H Bonet, C Buck, K Fülber, J Hakenmüller, J Hempfling, G Heusser, M Lindner, W Maneschg, et al. "CONUS+ experiment". *The European Physical Journal C* 84.12 (2024), p. 1265.

[31] Patrick Huber. "Determination of antineutrino spectra from nuclear reactors". *Phys. Rev. C* 84 (2 2011), p. 024617.

[32] Alexis Aguilar-Arevalo et al. "Search for light mediators in the low-energy data of the CONNIE reactor neutrino experiment". *JHEP* 04 (2020), p. 054. arXiv: 1910.04951 [hep-ex].

[33] H. T. Wong et al. "A Search of Neutrino Magnetic Moments with a High-Purity Germanium Detector at the Kuo-Sheng Nuclear Power Station". *Phys. Rev. D* 75 (2007), p. 012001. arXiv: hep-ex/0605006.

[34] F. P. An et al. "Evolution of the Reactor Antineutrino Flux and Spectrum at Daya Bay". *Phys. Rev. Lett.* 118.25 (2017), p. 251801. arXiv: 1704.01082 [hep-ex].

[35] N. Ackermann et al. "Direct observation of coherent elastic antineutrino–nucleus scattering". *Nature* 643.8074 (2025), pp. 1229–1233. arXiv: 2501.05206 [hep-ex].

[36] Glen Cowan, Kyle Cranmer, Eilam Gross, and Ofer Vitells. "Asymptotic formulae for likelihood-based tests of new physics". *The European Physical Journal C* 71.2 (2011), p. 1554.

[37] Julien Billard et al. "Direct detection of dark matter—APPEC committee report*". *Rept. Prog. Phys.* 85.5 (2022), p. 056201. arXiv: 2104.07634 [hep-ex].

[38] R. Agnese et al. "New Results from the Search for Low-Mass Weakly Interacting Massive Particles with the CDMS Low Ionization Threshold Experiment". *Phys. Rev. Lett.* 116.7 (2016), p. 071301. arXiv: 1509.02448 [astro-ph.CO].

[39] E. Armengaud et al. "Searching for low-mass dark matter particles with a massive Ge bolometer operated above-ground". *Phys. Rev. D* 99.8 (2019), p. 082003. arXiv: 1901.03588 [astro-ph.GA].

[40] C. Amole et al. "Dark Matter Search Results from the Complete Exposure of the PICO-60 C_3F_8 Bubble Chamber". *Phys. Rev. D* 100.2 (2019), p. 022001. arXiv: 1902.04031 [astro-ph.CO].

[41] P. Agnes et al. "Search for low-mass dark matter WIMPs with 12 ton-day exposure of DarkSide-50". *Phys. Rev. D* 107.6 (2023), p. 063001. arXiv: 2207.11966 [hep-ex].

[42] A. H. Abdelhameed et al. "First results from the CRESST-III low-mass dark matter program". *Phys. Rev. D* 100.10 (2019), p. 102002. arXiv: 1904.00498 [astro-ph.CO].

[43] Johannes Bergstrom, M. C. Gonzalez-Garcia, Michele Maltoni, Carlos Pena-Garay, Aldo M. Serenelli, and Ningqiang Song. "Updated determination of the solar neutrino fluxes from solar neutrino data". *JHEP* 03 (2016), p. 132. arXiv: 1601.00972 [hep-ph].

[44] Ciaran A. J. O'Hare, Anne M. Green, Julien Billard, Enectali Figueroa-Feliciano, and Louis E. Strigari. "Readout strategies for directional dark matter detection beyond the neutrino background". *Phys. Rev. D* 92.6 (2015), p. 063518. arXiv: 1505.08061 [astro-ph.CO].

[45] Philipp Grothaus, Malcolm Fairbairn, and Jocelyn Monroe. "Directional Dark Matter Detection Beyond the Neutrino Bound". *Phys. Rev. D* 90.5 (2014), p. 055018. arXiv: 1406.5047 [hep-ph].

CHAPTER 6

Calibration of EJ-301 Liquid Scintillation Detectors and Fast Neutron Measurements

Contents

6.1 Motivation

Fast neutrons constitute one of the most critical sources of background in rare event search experiments based on nuclear recoil detection, such as WIMP-like dark matter searches and coherent elastic neutrino-nucleus scattering (CEνNS) experiments. In these studies, the signal of interest arises from low-energy nuclear recoils, which can be closely mimicked by neutron-induced interactions in detector materials. This similarity makes fast neutrons (MeV scale kinetic energy) a particularly challenging and largely irreducible background, necessitating their precise characterization for reliable signal identification and background discrimination.

To reduce external backgrounds, rare event experiments are typically performed in deep underground laboratories, where the overburden significantly suppresses cosmic-ray-induced radiation. However, even in such environments, fast neutrons with energies of the order of MeV may persist as a significant background component. These neutrons are primarily produced through spontaneous fission of trace radioactive isotopes such as uranium and thorium present in the surrounding rock, (α, n) reactions induced by alpha particles from natural decay chains, and residual interactions of cosmic-ray muons with surrounding materials.

Owing to their electrically neutral nature, neutrons do not ionize directly but interact via nuclear processes, often producing recoil nuclei in detector materials. Consequently, accurate measurement of fast neutron energy spectra is of considerable importance in a broad range of nuclear and astroparticle physics applications.

Organic liquid scintillation detectors are widely employed for fast neutron detection due to their high detection efficiency, excellent timing characteristics, and PSD capability. In these detectors, fast neutrons predominantly interact through elastic scattering with hydrogen nuclei, producing recoil protons. These recoil protons deposit energy in the scintillator medium, leading to excitation of molecular states and subsequent emission of scintillation photons [1]. The emitted optical photons are collected by a PMT, where they are converted into electrical signals via photoelectron emission followed by amplification through dynode stages.

Among organic scintillators, EJ-301 [2] is particularly well-suited for neutron measurements due to its excellent PSD performance. The detector response is approximately linear for electron recoils, such as those arising from gamma-ray interactions, with slight deviations at low energies [3]. In contrast, nuclear recoils produced by neutron interactions exhibit significant non-linearity in the scintillation response due to quenching effects [4–6]. This non-proportional behavior complicates the direct interpretation of the measured pulse height spectrum in terms of the incident neutron energy.

A further challenge in neutron energy calibration arises from the lack of mono-energetic neutron sources. Commonly used neutron emitters, such as ^{252}Cf and ^{241}Am–^{9}Be, produce continuous energy spectra. As a result, conventional calibration techniques based on discrete energy deposition signatures are not applicable, necessitating the use of spectral unfolding techniques to reconstruct the incident neutron energy distribution from the measured detector response.

The unfolding procedure relies on the construction of a detector response matrix, which establishes the relationship between the incident neutron energy and the corresponding light output in the detector. This response matrix is typically obtained through detailed Monte Carlo simulations that incorporate neutron interactions, scintillation photon production, quenching effects described by Birks' law, and detector resolution. The reliability of the reconstructed neutron spectrum therefore depends critically on realistic modeling of the detector response.

Previous studies on neutron spectrum unfolding using organic scintillators such as NE213 and BC501A have often relied on simplified response models that do not explicitly include optical photon transport or detailed detector effects [7, 8]. Although some recent works have incorporated optical processes in simulations, they lack direct validation with experimental data [9]. This highlights the need for a comprehensive approach that combines detailed simulations with experimental calibration to achieve reliable neutron spectroscopy.

Motivated by these considerations, the primary objective of this chapter is to establish a robust and experimentally validated framework for fast neutron spectroscopy using an organic liquid scintillation detector. Specifically, this work aims to (a) determine the detector energy resolution scale, (b) extract the Birks' constant to account for scintillation quenching in nuclear recoils, (c) construct a detailed detector response matrix using Monte Carlo simulations, (d) validate different spectral unfolding methods, and (e) reconstruct and calibrate the incident neutron energy spectrum using detector response through unfolding techniques. These deliverables collectively enable a consistent and reliable approach for neutron energy reconstruction in low-background experiments.

In the following section, we discuss the working principle of scintillation detectors.

6.2 Working Principle of Scintillation Detectors

6.2.1 Scintillation Detector

A scintillation detector is a radiation detection device that converts the energy deposited by incident radiation into detectable light. When a particle traverses the scintillator medium, it loses energy through interactions with the material, resulting in excitation of electrons from lower to higher energy states. The subsequent de-excitation of these electrons leads to the emission of photons, typically in the ultraviolet or visible region of the electromagnetic spectrum. The intensity of emitted light is proportional to the energy deposited by the incident particle, making scintillators suitable for energy measurement.

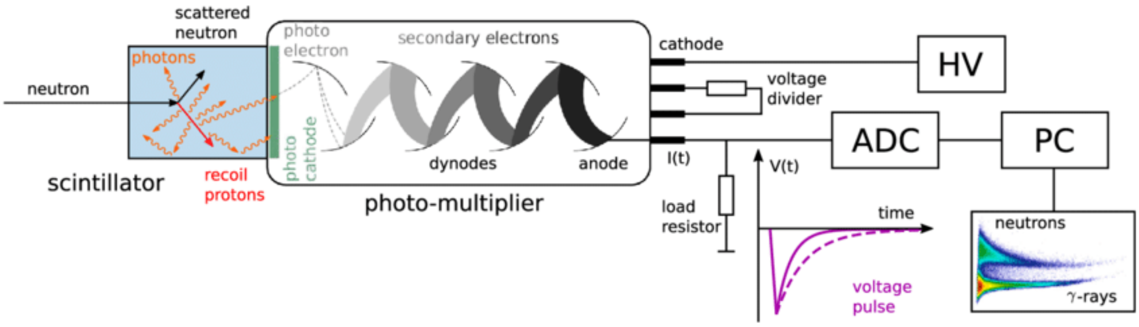

FIGURE 6.1: Schematic of a liquid scintillation detector illustrating the detection principle: incident radiation deposits energy in the scintillator, producing optical photons that are collected and converted into electrical signals by a PMT. This highlights the conversion of deposited energy into a measurable electronic response. Adapted from [10].

The scintillation photons are subsequently collected and converted into an electrical signal using a photosensitive device, typically a PMT. This conversion process forms the basis of radiation detection in scintillation-based systems.

6.2.2 Photomultiplier Tube

A PMT is a highly sensitive device used to convert low-intensity light signals into measurable electrical pulses. It consists of three main components: a photocathode, a series of dynodes, and an anode.

The photocathode is coated with a photosensitive material, such as bialkali compounds, which emits electrons when incident photons are absorbed. The efficiency of this conversion is characterized by the quantum efficiency (QE), typically $\sim$30% for commonly used photocathodes. The emitted photoelectrons are accelerated towards a sequence of dynodes maintained at progressively higher electric potentials using a voltage divider network.

At each dynode stage, secondary electron emission occurs, leading to a cascade multiplication process. This results in a substantial amplification of the initial signal, with the total gain by several orders of magnitude. The amplified electron cloud is finally collected at the anode, producing an electrical pulse whose amplitude is proportional to the number of initial photoelectrons, and hence to the energy deposited in the scintillator.

6.2.3 Properties and Types of Scintillators

An ideal scintillator should satisfy several key requirements:

- High scintillation efficiency to convert deposited energy into detectable light,
- Linear relationship between deposited energy and light output,
- Optical transparency to its own emitted photons,
- Fast decay time to enable good timing resolution.

Scintillators are broadly classified into two categories based on their composition:

- **Inorganic scintillators:** These are typically high-Z, high-density crystalline materials, making them suitable for gamma-ray detection due to their high stopping power.
- **Organic scintillators:** These are composed of low-Z materials and are particularly suitable for fast neutron detection and beta spectroscopy. Their low atomic number favors interactions with light charged particles such as recoil protons.

In this work, an organic liquid scintillator (EJ-301) is used due to its excellent performance in fast neutron detection.

6.3 Organic Scintillation Mechanism

In organic scintillators, scintillation light is produced through molecular excitation and de-excitation processes. The mechanism is governed by the π-electron structure of organic molecules, which gives rise to discrete energy levels.

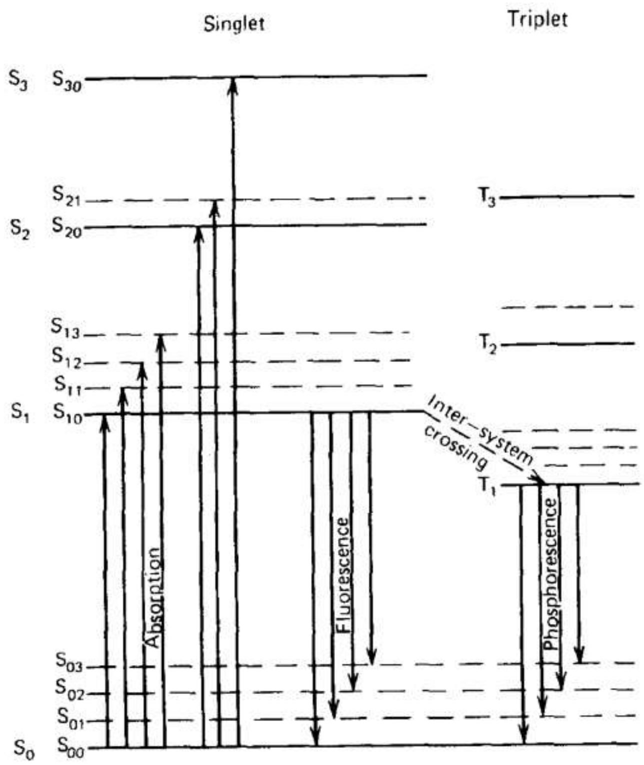

11

FIGURE 6.2: Molecular energy level structure in an organic scintillator showing singlet (S_i) and triplet (T_i) states, and the radiative transitions governing prompt (fluorescence) and delayed (phosphorescence) scintillation components. This shows the origin of the scintillation light. Adapted from [1].

These energy levels are categorized into singlet (S_i) and triplet (T_i) states. When energy is deposited in the scintillator, electrons are excited from the ground state (S_0) to higher excited singlet states (S_i). These excited states rapidly relax to the lowest excited singlet state (S_1), followed by radiative transitions back to the ground state. This process produces prompt scintillation light.

The time dependence of this prompt fluorescence can be described by an exponential decay:

$$I(t) = I_0 e^{-t/\tau}, \tag{6.1}$$

where τ is the decay constant, typically of the order of a few nanoseconds.

In addition to prompt fluorescence, a fraction of excited molecules undergo inter-system crossing to the triplet state (T_1). The de-excitation from the triplet state occurs over much longer timescales (microseconds to milliseconds), resulting in delayed fluorescence. The coexistence of prompt and delayed components forms the basis for pulse shape discrimination (PSD), which allows separation of neutron- and gamma-induced events.

6.3.1 Optical Properties and Practical Considerations

The emission spectrum of organic scintillators lies predominantly in the ultraviolet to visible region. Importantly, the emission spectrum is shifted relative to the absorption spectrum, ensuring that the scintillator medium remains largely transparent to its own emitted light. This property minimizes self-absorption and enhances light collection efficiency.

In practical applications, the performance of organic scintillators can be affected by environmental factors. Exposure to oxygen leads to quenching of scintillation light, reducing the overall light yield. Additionally, prolonged exposure to ultraviolet radiation and elevated temperatures can degrade the scintillator material. To mitigate these effects, scintillators are often sealed in airtight containers or maintained in an inert atmosphere using nitrogen or argon purging.

We next describe the experimental setup used in this analysis.

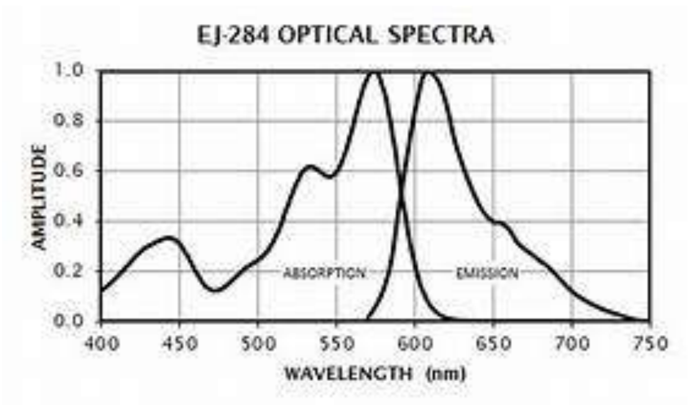

FIGURE 6.3: Emission and absorption spectra of a typical organic scintillator, showing the spectral separation between absorption and emission wavelengths. This separation ensures transparency to self-emitted scintillation light and thereby enhances photon transport and collection efficiency. Adapted from https://eljentechnology.com/17-products.

6.4 Experimental Setup

A schematic representation of the experimental setup is shown in Fig. 6.4. The overall configuration consists of an EJ-301 liquid scintillation detector, associated signal processing electronics, and a data acquisition system. The experimental methodology and analysis framework are explained below Ref. [11].

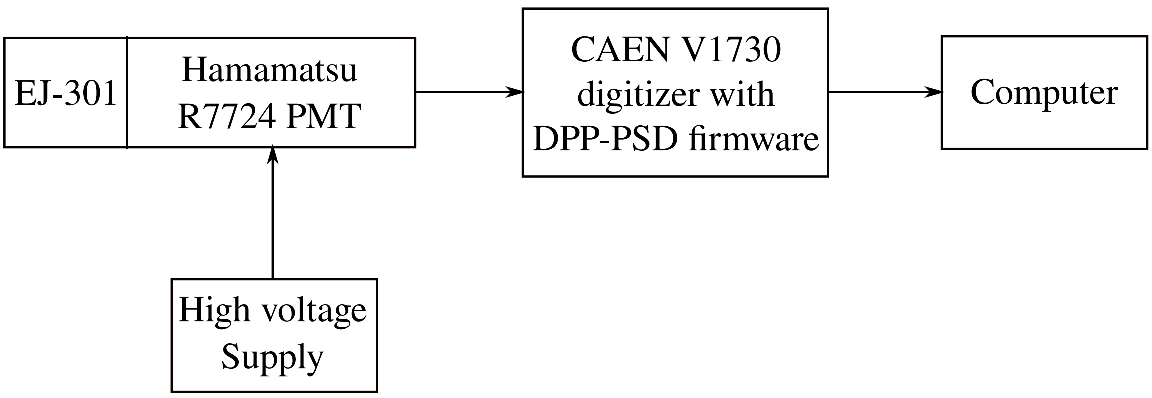

FIGURE 6.4: Block diagram of the experimental setup. Adapted from Ref. [11].

The detector used in this study is a 2″ × 2″ EJ-301 organic liquid scintillator, manufactured by Eljen Technology [2]. The scintillator is optically coupled to a photomultiplier tube (PMT), model R7724, developed by Hamamatsu [12]. This PMT provides fast timing response and high gain, which are essential for resolving scintillation pulses and performing pulse shape discrimination.

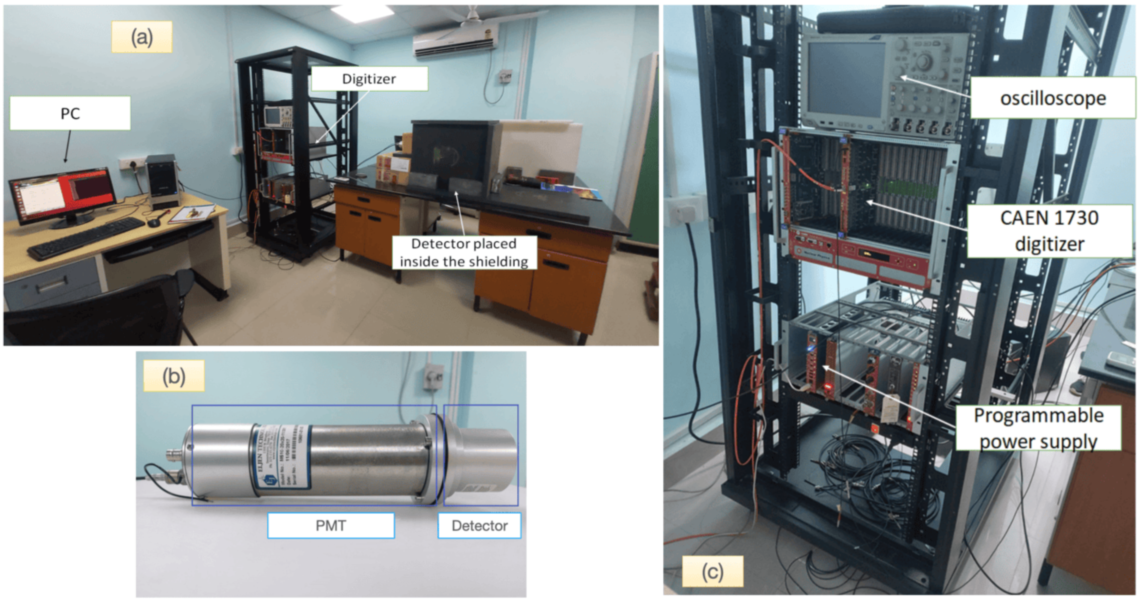

FIGURE 6.5: (a) Overview of the full experimental setup, with the detector placed inside the shielding. (b) EJ-301 liquid scintillation detector coupled to a PMT. (c) Electronics system comprising the power supply, digitizer, and oscilloscope.

When ionizing radiation interacts within the scintillator volume, it produces scintillation photons through excitation and de-excitation of molecular states. These optical photons are incident on the PMT photocathode, resulting in the emission of photoelectrons. The photoelectrons are subsequently amplified through a cascade of dynodes, producing a measurable electrical pulse at the anode. The amplitude and shape of this pulse carry information about the deposited energy and the type of interacting particle.

The analog signal from the PMT anode is digitized using a CAEN V1730 digitizer with 14-bit resolution. The digitizer operates in Digital Pulse Processing (DPP) mode, which enables real-time pulse shape analysis. PSD is performed using the charge integration method, where two integration gates are defined over the pulse waveform: a short gate (Q_S) that captures the prompt component of the scintillation signal, and a long gate (Q_L) that includes both prompt and delayed components.

The PSD parameter is defined as

$$\text{PSD} = 1 - \frac{Q_S}{Q_L}, \tag{6.2}$$

where Q_S and Q_L denote the integrated charges within the short and long gates, respectively [13]. Due to differences in scintillation decay profiles, neutron- and gamma-induced events occupy distinct regions in the PSD parameter space, allowing for effective event discrimination.

In the present work, the short and long integration gates are optimized to 30 ns and 280 ns, respectively, to achieve optimal neutron-gamma separation. The digitized signals are recorded and transferred to a computer for offline analysis. The PMT is operated at an anode voltage of +750 V. The operating conditions, including the applied high voltage and integration gate widths, are optimized to maximize the pulse shape discrimination performance. This performance is quantified using the Figure of Merit (FOM), which characterizes the separation between neutron and gamma distributions in the PSD parameter space [14]. A FOM value of approximately 1.14 is achieved for an energy threshold of 275 keV_{ee} in the present setup.

A photograph of the experimental setup is shown in Fig. 6.5.

6.5 Analysis Flowchart

The objective of this study is to establish a robust calibration of neutron energy for an EJ-301 liquid scintillation detector using a well-characterized Am-Be neutron source. To achieve this, a comprehensive simulation and analysis framework is developed, beginning with an accurate geometrical modeling of the detector system.

The initial stage focuses on characterizing the detector response to gamma radiation, as gamma-induced interactions produce electron recoils that define the electron-equivalent energy scale. Simulated gamma spectra are generated based on energy deposition arising primarily from Compton scattering. Optical photon transport is subsequently incorporated to model scintillation light production and collection, enabling a realistic description of the detector response, including finite resolution effects. The generated optical signals are then converted into electrical signals and digitized in terms of ADC channels to closely replicate experimental conditions.

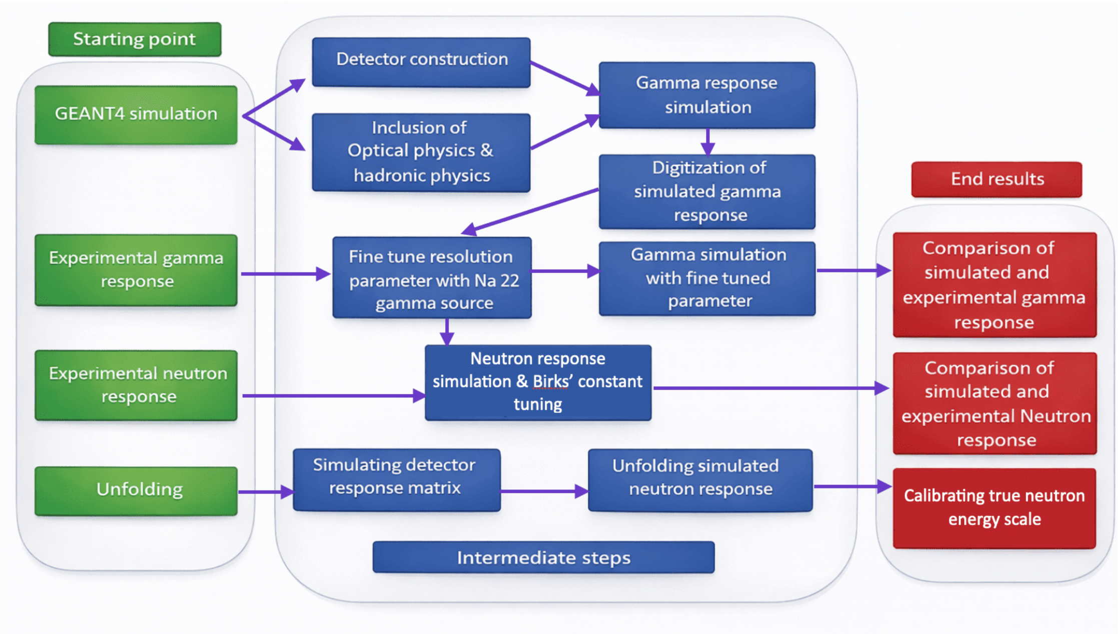

FIGURE 6.6: Analysis flowchart illustrating the simulation and data analysis framework for calibrating the EJ-301 liquid scintillation detector response to gamma rays and neutrons, including detector modeling, optical photon generation, signal digitization, parameter optimization, and neutron energy unfolding.

A key aspect of the calibration involves determining the intrinsic resolution scale of the scintillator, which is not readily available in the literature. This is achieved by comparing simulated and experimentally measured spectra from a ^{22}Na gamma source. The extracted resolution parameter is further validated through consistency checks using additional gamma sources such as ^{60}Co and ^{137}Cs.

Following the gamma calibration, the framework is extended to neutron interactions by incorporating hadronic processes along with high-precision neutron physics. The detector response to both mono-energetic neutrons and the continuous spectrum from the Am-Be source is modeled. Since the Am-Be source emits both gamma rays and neutrons, an essential step involves isolating neutron-induced events from gamma-induced backgrounds in experimental data. A comparison between simulated and measured neutron responses enables the determination of the quenching parameter, specifically Birks' constant, which governs the non-linear light yield for heavily ionizing particles.

After fine-tuning the resolution scale, Birks' constant, and the digitization procedure of the electron-equivalent response in terms of ADC channels, the detector response matrix for fast neutrons is constructed using simulations.

In the final stage, true fast neutron energy is calibrated through spectral unfolding techniques. The reliability of the unfolding methods is first validated using simulated data, demonstrating the effectiveness of both RooUnfold and GRAVEL algorithms. These methods are subsequently applied to experimental data obtained from the Am-Be source, enabling reconstruction of the incident neutron energy spectrum. This establishes a calibrated relationship between the detector response and neutron energy.

The overall workflow of the simulation and analysis procedure is summarized in Fig. 6.6.

The following section describes the Unfolding Methodology used in this analysis.

6.6 Unfolding Methodology

6.6.1 Overview of the Unfolding Problem

The primary objective of the unfolding procedure is to reconstruct the true energy spectrum of incident neutrons from the experimentally measured detector response. In scintillation-based neutron detectors, the measured signal does not directly represent the incident neutron energy spectrum. Instead, it corresponds to a convolution of the true spectrum with the detector response, which includes effects such as non-linear light yield, energy resolution, and statistical fluctuations.

Mathematically, this inverse problem can be expressed as a linear transformation, where the measured detector response is related to the true neutron energy distribution through the detector response function. The unfolding process aims to invert this relationship and recover the incident spectrum from the measured data.

The unfolding requires two essential inputs:

- The detector response matrix, typically obtained from detailed Monte Carlo simulations.
- The experimentally measured detector response (pulse height or light output spectrum),

6.6.2 Detector Response Matrix

The detector response matrix encodes the relationship between the incident neutron energy and the corresponding light output in the detector. The response matrix **R** can be expressed as:

$$\mathbf{R} = \begin{pmatrix} R_{L_1E_1} & R_{L_1E_2} & R_{L_1E_3} & \cdots & R_{L_1E_m} \\ R_{L_2E_1} & R_{L_2E_2} & R_{L_2E_3} & \cdots & R_{L_2E_m} \\ R_{L_3E_1} & R_{L_3E_2} & R_{L_3E_3} & \cdots & R_{L_3E_m} \\ \vdots & \vdots & \vdots & \ddots & \vdots \\ R_{L_nE_1} & R_{L_nE_2} & R_{L_nE_3} & \cdots & R_{L_nE_m} \end{pmatrix}. \tag{6.3}$$

Here, $R_{L_iE_j}$ represents the probability that an incident neutron with energy E_j produces a detector response in the i^{th} light output bin L_i. Each column of the response matrix corresponds to a normalized response function, representing the probability distribution of the collected optical photon signal (at the photocathode) over the light output bins for a given incident neutron energy.

Due to the lack of mono-energetic neutron sources, the response matrix is constructed using Monte Carlo simulations. In the present work, 240 mono-energetic neutron response functions are simulated over the energy range from 0.05 MeV to 12 MeV with uniform energy binning. This ensures adequate coverage of the fast neutron energy region relevant for the measurements.

6.6.3 Forward Model of Detector Response

The relationship between the incident neutron spectrum and the measured detector response can be written in matrix form as:

$$\mathbf{N} = \mathbf{R} \times \boldsymbol{\phi}, \tag{6.4}$$

where:

- **N** represents the measured detector response (light output spectrum),

- $\boldsymbol{\phi}$ is the incident neutron energy spectrum,

- $\mathbf{R}$ is the detector response matrix [8].

In expanded form, Eq. (6.4) can be written as:

$$\begin{pmatrix} N_1 \\ N_2 \\ \vdots \\ N_n \end{pmatrix} = \begin{pmatrix} R_{L_1E_1} & R_{L_1E_2} & \cdots & R_{L_1E_m} \\ R_{L_2E_1} & R_{L_2E_2} & \cdots & R_{L_2E_m} \\ \vdots & \vdots & \ddots & \vdots \\ R_{L_nE_1} & R_{L_nE_2} & \cdots & R_{L_nE_m} \end{pmatrix} \begin{pmatrix} \phi_1 \\ \phi_2 \\ \vdots \\ \phi_m \end{pmatrix}. \tag{6.5}$$

Here, N_i, ϕ_j, and $R_{L_iE_j}$ denote the individual elements of the detector response vector, incident spectrum vector, and response matrix, respectively.

The unfolding problem involves solving Eq. (6.4) for $\boldsymbol{\phi}$, which is an ill-posed inverse problem due to statistical fluctuations and finite detector resolution.

6.6.4 Unfolding Algorithms

Several unfolding techniques have been developed to address this inverse problem. In this work, two widely used methods are employed: the GRAVEL iterative method and the Bayesian unfolding approach implemented in the RooUnfold framework.

GRAVEL Iterative Method

The GRAVEL method is an iterative unfolding technique that updates the estimated spectrum at each iteration based on the agreement between measured and reconstructed detector responses. The update equation is given by [8]:

$$\phi_j^{k+1} = \phi_j^k \times \exp\left(\frac{\sum_i W_{ij}^k \ln\left(\frac{N_i}{\sum_j R_{L_i E_j}\phi_j^k}\right)}{\sum_i W_{ij}^k}\right), \tag{6.6}$$

where k denotes the iteration number. The weight factor W_{ij}^k is defined as:

$$W_{ij}^k = \frac{R_{L_i E_j}\phi_j^k}{\sum_{j'} R_{L_i E_{j'}}\phi_{j'}^k} \cdot \frac{N_i^2}{\sigma_i^2}. \tag{6.7}$$

Here, ϕ_j^k represents the unfolded spectrum at the j^{th} energy bin after the k^{th} iteration, and σ_i is the statistical uncertainty associated with the measured data, approximated as $\sqrt{N_i}$. The iteration is initialized with a uniform spectrum, ϕ^0, and proceeds until convergence is achieved.

Bayesian Unfolding (RooUnfold)

In addition to the GRAVEL method, the unfolding is also performed using the Bayesian approach implemented in the RooUnfold framework [15]. Specifically, the `RooUnfoldBayes` algorithm is used, which iteratively updates the estimated spectrum based on Bayes' theorem.

The initial prior distribution is taken as a uniform spectrum, $\phi_0 = 1/M$, where M is the total number of energy bins. At each iteration, the posterior distribution is updated using the detector response matrix and the measured data. This method naturally incorporates regularization through the number of iterations, which controls the level of smoothing in the unfolded spectrum.

6.6.5 Convergence and Goodness of Fit

To evaluate the quality of the unfolding and monitor convergence, the reduced chi-square statistic is calculated at each iteration:

$$\frac{\chi^2}{n.d.f} = \frac{1}{n.d.f} \sum_i \frac{\left(\sum_j R_{ij}\phi_j - N_i\right)^2}{\sigma_i^2}. \tag{6.8}$$

A value of $\chi^2/n.d.f$ close to unity indicates that the reconstructed detector response is consistent with the measured data within statistical uncertainties. This criterion is used to determine the optimal number of iterations for both unfolding methods. It is found (detailed in Sec. 6.10) that 150 iterations are sufficient for the χ^2/ndf to reach a stable value in the unfolding of both Monte Carlo simulated and experimental spectra, indicating that the results are insensitive to variations in the iteration number within this region. Therefore, this value is chosen as the cutoff for the iterative procedure.

We next describe the detector construction and material definition in GEANT4 used in this analysis.

6.7 Detector Construction and Material Description in GEANT4

A detailed Monte Carlo simulation of the EJ-301 detector has been developed using the GEANT4 toolkit to accurately model the detector response to incident radiation. The simulation incorporates realistic detector geometry, material composition, and optical photon processes to reproduce the experimental conditions as closely as possible. The overall methodology follows the framework presented in Ref. [11], with additional implementation details described in this section.

6.7.1 Detector Geometry

The geometrical parameters of the detector and its constituent components are obtained from the manufacturer specifications [2]. The detector consists of a cylindrical volume filled with liquid scintillator. The inner radius of the detector is 25.5 mm, while the outer radius is 27 mm, corresponding to the aluminium housing. The height of the detector is 50.8 mm.

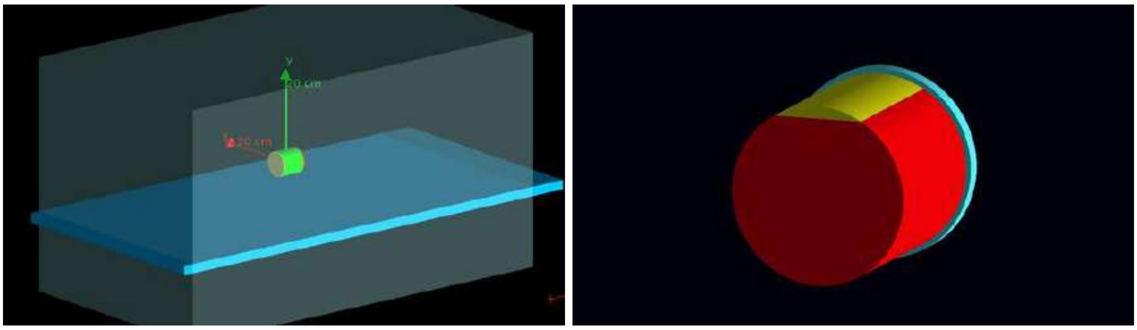

FIGURE 6.7: Simulated detector geometry: (left) external view showing the detector positioned above a granite base and surrounded by air; (right) internal view illustrating the active scintillator volume (red, 97%) and enclosed inert gas region (yellow, 3%) by volume. Adapted from Ref. [11].

A front cap of thickness 1.5 mm encloses the scintillator volume, while the rear side of the detector is coupled to a glass window of thickness 4.8 mm, which serves as an optical interface between the scintillator and the photomultiplier tube. The detector housing is modeled using aluminium, ensuring realistic treatment of particle interactions and optical boundary conditions.

The internal structure of the detector is composed of approximately 97% organic liquid scintillator and 3% inert gas. In the present simulation, argon is used to represent the inert gas component. Additionally, the inner walls of the detector are coated with TiO_2, which acts as a diffuse reflector with a reflectivity of approximately 90%. This coating enhances light collection efficiency by redirecting scintillation photons toward the PMT.

The simulated detector geometry is shown in Fig. 6.7. In order to replicate the experimental conditions, the detector is placed on a granite base within the simulation. This is included since secondary radiation produced from interactions of primary particles with surrounding materials can contribute to the measured detector response. The entire setup is enclosed within a world volume filled with air, representing the laboratory environment. The dimensions of the world volume are chosen to be sufficiently large to avoid boundary effects on particle transport.

Radioactive sources are positioned along the negative Z-axis at a distance of 10 cm from the front face of the detector.

6.7.2 Optical Physics and Scintillation Properties

In experiments, the energy deposited by gamma interactions is not directly observable. Instead, the deposited energy is converted into optical photons through the scintillation process, which are subsequently detected by the PMT and converted into an electrical signal. Therefore, the observable quantity is the number of optical photons produced in scintillator and subsequently detected in the PMT. This process involves the excitation of π-electrons in molecular energy levels, followed by photon emission (as discussed in Section 6.2).

To accurately simulate this process, the `G4OpticalPhysics` package in GEANT4 is employed [16]. This enables the generation, transport, and interaction of optical photons within the detector volume. The primary optical photon processes considered in the scintillation detector include absorption and transmission within the scintillator, absorption in the reflector (TiO_2 coating), reflection from the reflector and at the glass window, refraction at the interface between the scintillator and the window, and transmission through the glass window followed by collection at the photocathode.

The relevant optical and scintillation properties of the EJ-301 detector are implemented based on the manufacturer datasheet [2]. These include refractive index, absorption length, emission spectrum, scintillation yield, decay time components, and Birks' constant. The key properties used in the simulation are summarized in Table 6.1.

Scintillator properties	values
Light output (% w.r.t. Anthracene)	78
scintillation efficiency	12000/MeV
Wavelength of max emission (nm)	425
Decay time (ns)	3.2
Mean decay time of first 3 components (ns)	3.16 32.3 270
Attenuation length (m)	2.5-3
Specific gravity	0.874
Refractive index	1.505
H atoms / cm^3 ($\times 10^{22}$)	4.82
C atoms / cm^3 ($\times 10^{22}$)	3.98

TABLE 6.1: Key scintillation properties of EJ-301 used in our Geant4 simulation [2].

Their transport of optical photons is governed by processes such as absorption, scattering, reflection, and refraction. The attenuation length defines the distance over which the photon intensity reduces to $1/e$ of its initial value.

The inclusion of optical physics significantly alters the detector response. In the absence of optical processes, the simulation records only the deposited energy through ionization using electromagnetic physics. However, once scintillation and optical photon transport are included, the response becomes smeared due to photon statistics and absorption losses resulting detector resolution effect.

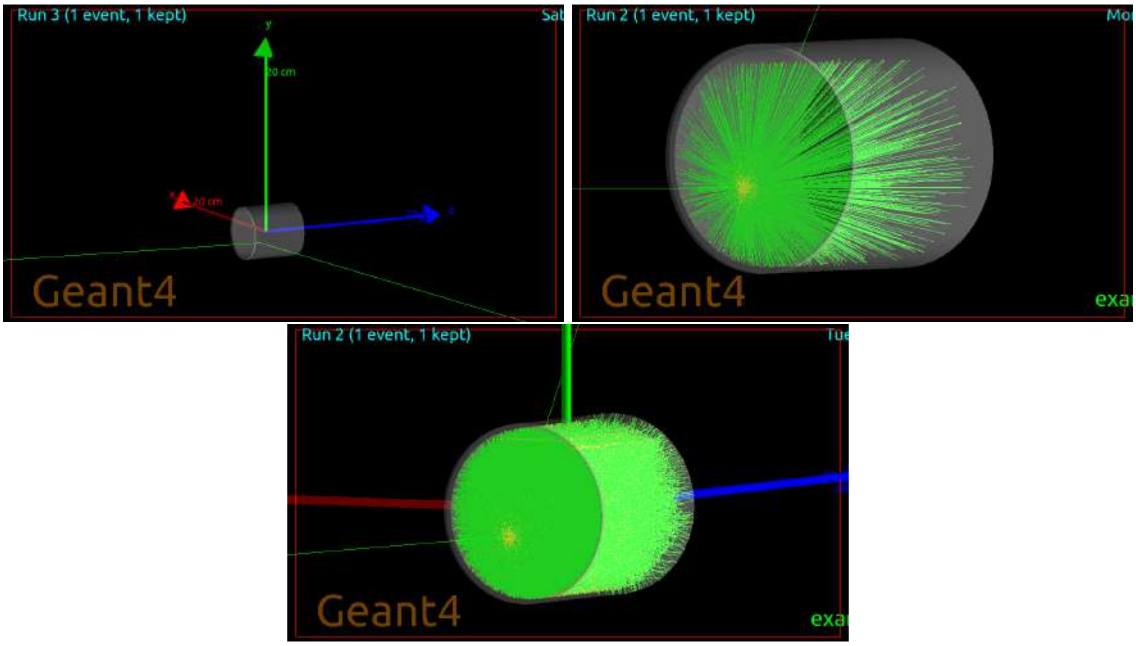

FIGURE 6.8: Simulated detector response to 662 keV gamma-rays under optical modeling conditions. **Top left:** Energy deposition without optical physics, representing only the raw deposited energy. **Top right:** Optical physics included without surface (boundary) properties, showing scintillation photon production without realistic transport. **Bottom:** Optical physics with boundary conditions, demonstrating realistic photon transport and detector response.

In addition to bulk material properties, optical boundary conditions are defined for all relevant interfaces in the detector. These include:

- Scintillator–glass boundary (dielectric–dielectric),
- Scintillator–aluminium boundary (dielectric–metal),
- Scintillator–argon boundary (dielectric–dielectric),
- Aluminium–argon boundary (metal–dielectric).

These interfaces govern the reflection, refraction, and absorption of optical photons, and are essential for accurately modeling light transport within the detector. The impact of including scintillation and optical physics in the GEANT4 simulation is illustrated in Fig. 6.8.

After implementing the optical properties, the simulated emission spectrum of optical photons is evaluated and compared with the reference spectrum provided by the manufacturer [2].

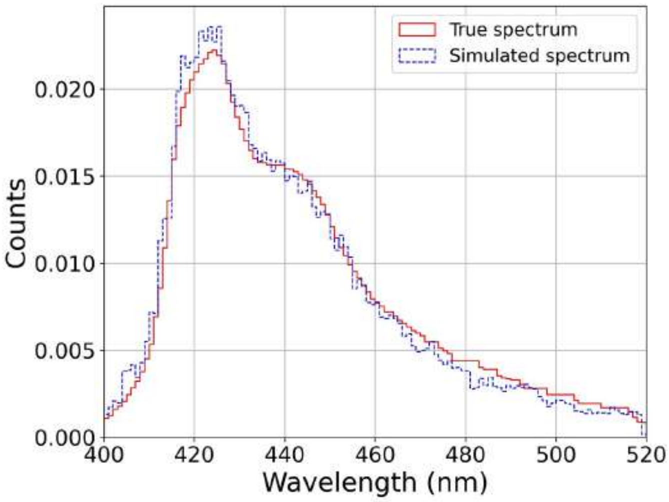

FIGURE 6.9: Simulated optical photon emission spectrum compared with the EJ-301 reference spectrum. The peak around 425 nm confirms correct implementation of scintillation properties. Adapted from Ref. [11].

The agreement between simulated and reference spectra confirms the correct implementation of scintillation emission, absorption, and transport processes.

6.7.3 Quenching Effect and Birks' Law

The non-linear response of the scintillator to charged particles is modeled using Birks' law:

$$\frac{dL}{dx} = \frac{S\frac{dE}{dx}}{1 + k_B\frac{dE}{dx}}. \tag{6.9}$$

Here, S denotes the scintillation efficiency, corresponding to the light yield per unit deposited energy in the linear (electron-equivalent) regime, and is fixed by the measured light yield of the EJ-301 scintillator. The parameter $k_B = 0.1065$ mm MeV^{-1} is the Birks' constant, whose value is obtained by tuning the simulation to reproduce the measured neutron response of EJ-301 to an Am–Be source through data–Monte Carlo comparison (see Sec. 6.9).

Quenching refers to any process that decreases the fluorescence intensity of a given material. While factors such as material impurities and insufficient solvent concentration can also contribute to quenching, these effects are not included in the present simulation, as they are expected to be negligible compared to the Birks' quenching effect.

Quenching becomes significant for particles with large stopping power (dE/dx). Electrons produced in gamma-ray interactions have relatively low dE/dx, resulting in an approximately linear light output that is only weakly affected by quenching. In contrast, recoil protons generated by neutron interactions possess much higher dE/dx, leading to strong quenching and consequently reduced light output.

This difference in quenching behavior is the primary reason why neutron-induced signals appear at lower light output compared to gamma rays depositing the same amount of energy in the scintillator.

The following sections present the simulated gamma-ray and neutron responses in GEANT4 and their comparison with experimental results.

6.8 Simulated Gamma Response and Comparison with Experiment

The gamma response of the EJ-301 liquid scintillation detector is primarily studied to tune the resolution parameter of the scintillator using Data-MC comparison.

6.8.1 Simulated Detector Response to Experimental Sources

In this work, gamma-rays from three standard radioactive sources (^{22}Na, ^{137}Cs, and ^{60}Co) are simulated to validate the detector response. The relevant gamma-ray energies, branching ratios, and corresponding Compton edge values are summarized in Table 6.2.

TABLE 6.2: Gamma-ray energies, branching ratios, and corresponding Compton edge energies for the sources used in the simulation.

Source	E_γ (MeV)	Branching Ratio (%)	Compton Edge (MeV)
^{22}Na	0.511	178	0.340
	1.275	99.84	1.062
^{137}Cs	0.662	85	0.477
^{60}Co	1.173	99.85	0.963
	1.332	99.98	1.117

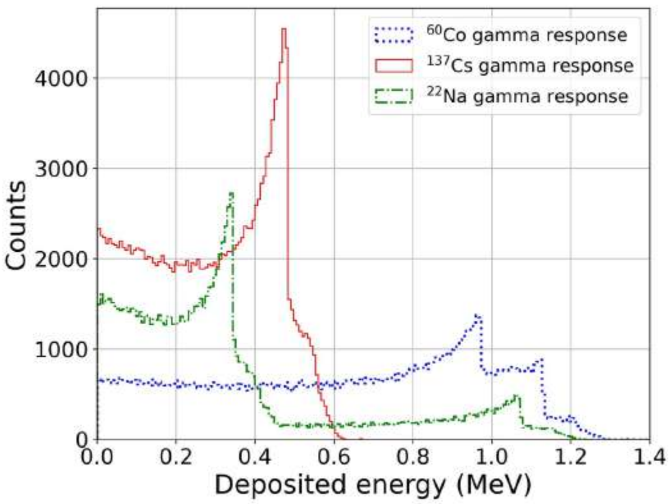

FIGURE 6.10: Simulated gamma-ray response in terms of deposited energy within the scintillator for ^{60}Co, ^{137}Cs, and ^{22}Na sources. Distinct Compton edges corresponding to each gamma-ray energy are visible, representing the maximum energy transfer in a single Compton scattering event, while events beyond the edge arise from multiple scattering within the detector volume. Adapted from Ref. [11].

To simulate gamma-ray interactions, the `G4EmStandardPhysics` electromagnetic physics list is implemented in GEANT4, which accurately models processes such as Compton scattering, photoelectric absorption, and pair production within the scintillator medium.

The simulated gamma responses, expressed in terms of deposited energy, are shown in Fig. 6.10.

In organic scintillators, gamma-ray interactions in the energy range of $O(100\,\mathrm{keV–MeV})$ are dominated by Compton scattering. Consequently, the energy deposition spectra exhibit characteristic Compton edges corresponding to the maximum energy transfer in a single scattering event. Events beyond the Compton edge arise from multiple scattering processes within the detector volume.

6.8.2 Optical Photon Generation in gamma interaction

After incorporating optical photon generation and transport in the simulation, the detector response is expressed in terms of scintillation light output rather than deposited energy. The inclusion of optical processes introduces statistical fluctuations in photon production and collection, leading to a broadening of spectral features.

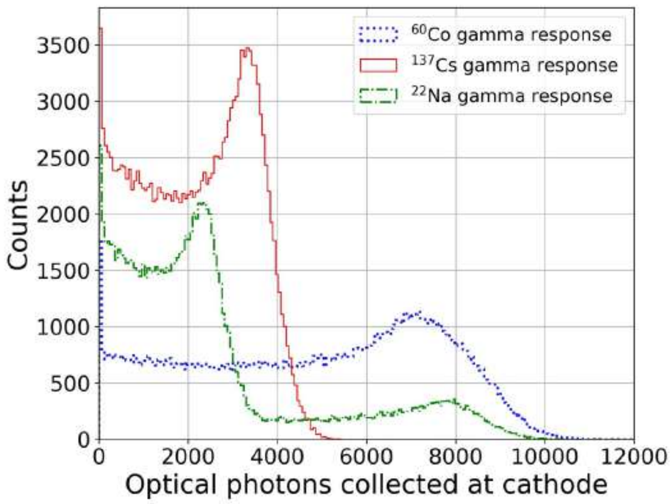

FIGURE 6.11: Simulated gamma-ray spectra including optical photon processes. The inclusion of optical photon physics results in a smearing of the Compton edges due to detector resolution effects. Adapted from Ref. [11].

The resulting smeared spectra for the gamma sources are shown in Fig. 6.11. The sharp Compton edges are now smeared due to the finite resolution effect of the scintillator primarily arising from optical photon generation statistics. The excess counts near the threshold in the experimental data are arising due to the electronic noise.

6.8.3 Digitization of Simulated Signals

To enable direct comparison between simulation and experiment, the simulated light output must be converted into digitized signals corresponding to the readout electronics. In the experiment, the digitizer operates with a charge sensitivity of 5 fC per Least Significant Bit (LSB) and a 14-bit resolution.

If N optical photons are incident on the photocathode in a given event, the corresponding ADC channel can be calculated as:

$$\begin{aligned}
\text{ADC channel} &= \frac{N \times \text{QE} \times \text{PMT gain} \times e}{\text{digitizer sensitivity}} \\
&= \frac{N \times 0.26 \times 4.44 \times 10^{4} \times 1.602 \times 10^{-19}}{5 \times 10^{-15}} \\
&= N \times 0.37, \qquad (6.10)
\end{aligned}$$

Here, for our PMT, the photocathode quantum efficiency (QE) is taken to be 26%, and the gain is taken to be 4.44×10^{4} [12]. This relation enables the conversion of simulated optical photon counts into the ADC scale used in the experiment.

6.8.4 Determination of Resolution Scale using data-MC comparison

The resolution scale parameter is tuned by comparing simulated and experimental gamma-ray spectra. In scintillation detectors, the finite energy resolution arises from statistical fluctuations in the number of generated optical photons. In Geant4, this effect is incorporated through a resolution scale parameter, which controls the width of the photon yield distribution. The spread in the number of produced optical photons is given by

$$\texttt{Spread} = \texttt{Resolution scale} \times \sqrt{\texttt{Scintillation yield}}, \tag{6.11}$$

[16]

where the scintillation yield represents the average number of optical photons produced per unit deposited energy. For the EJ-301 scintillator, this is approximately 12,000 optical photons per 1 $\mathrm{MeV_{ee}}$, where "ee" denotes electron-equivalent energy deposition.

The ^{22}Na source is chosen as the primary reference for tuning the resolution scale due to the presence of two well-separated gamma-ray peaks, which provide a sensitive probe of the detector resolution.

Simulations are performed for different values of the resolution scale, and the resulting spectra are compared with experimental data. The best agreement is obtained for a resolution scale value of 5. This value is subsequently validated using ^{137}Cs and ^{60}Co spectra.

The comparison between simulated and experimental spectra is shown in Fig. 6.12, along with ratio plots that demonstrate good agreement across the full energy range. Based on this study, the resolution scale is fixed at 5 for all subsequent simulations.

6.8.5 Energy Dependence of Light Yield for gamma

The relation between deposited energy and optical photon yield is investigated using mono-energetic gamma rays over a broad energy range. Gamma rays interact predominantly through electron recoil. These electrons deposit energy in the medium via ionization and excitation processes, which subsequently lead to the emission of scintillation photons.

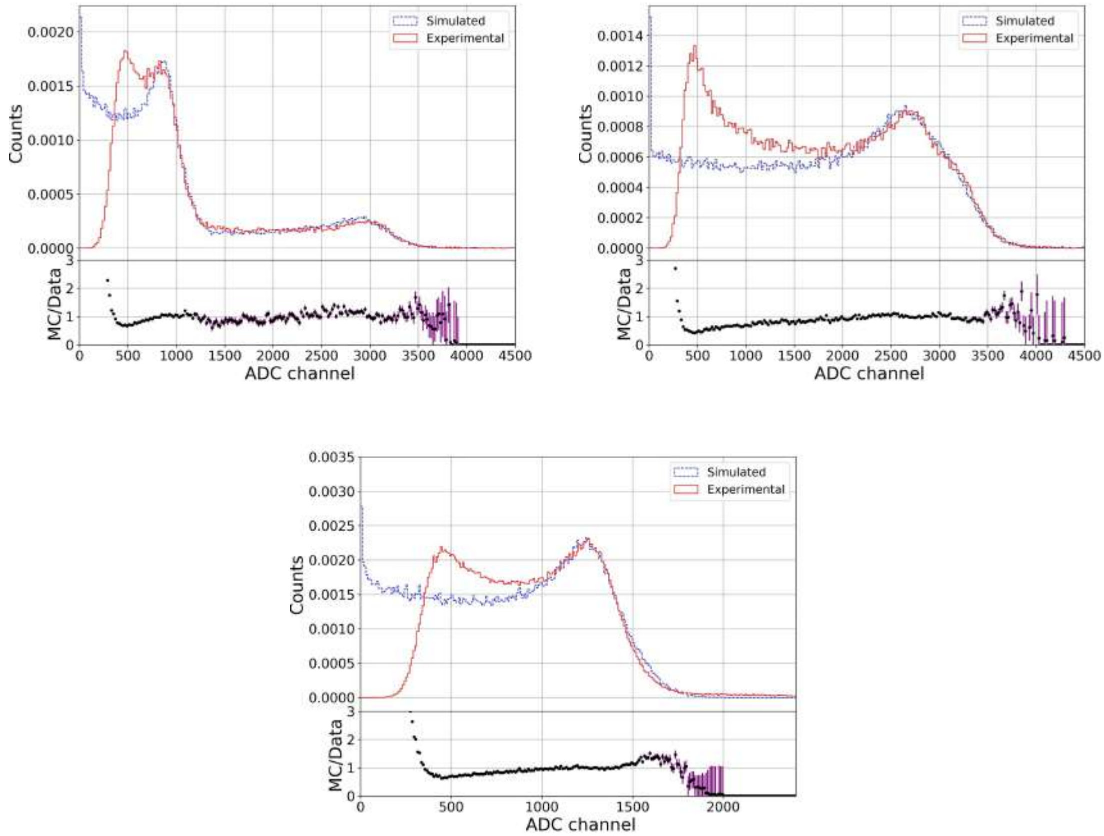

FIGURE 6.12: Comparison of simulated and experimental gamma-ray spectra for ^{22}Na (top left), ^{60}Co (top right), and ^{137}Cs (bottom). The overall agreement in spectral shape and Compton features validates the detector modeling, while excess counts near the threshold in the experimental data are attributed to electronic noise. Adapted from Ref. [11].

For a fixed gamma-ray energy, the number of scintillation photons produced is approximately proportional to the energy deposited by the secondary electrons. This results in an approximately linear relationship between deposited energy and optical photon yield, as observed in the top panels for 0.5 MeV and 1 MeV gamma rays. The linearity arises from the relatively low stopping power (dE/dx) of electrons, for which Birks' quenching remains weak.

Deviations from perfect linearity become more pronounced at lower gamma energies.

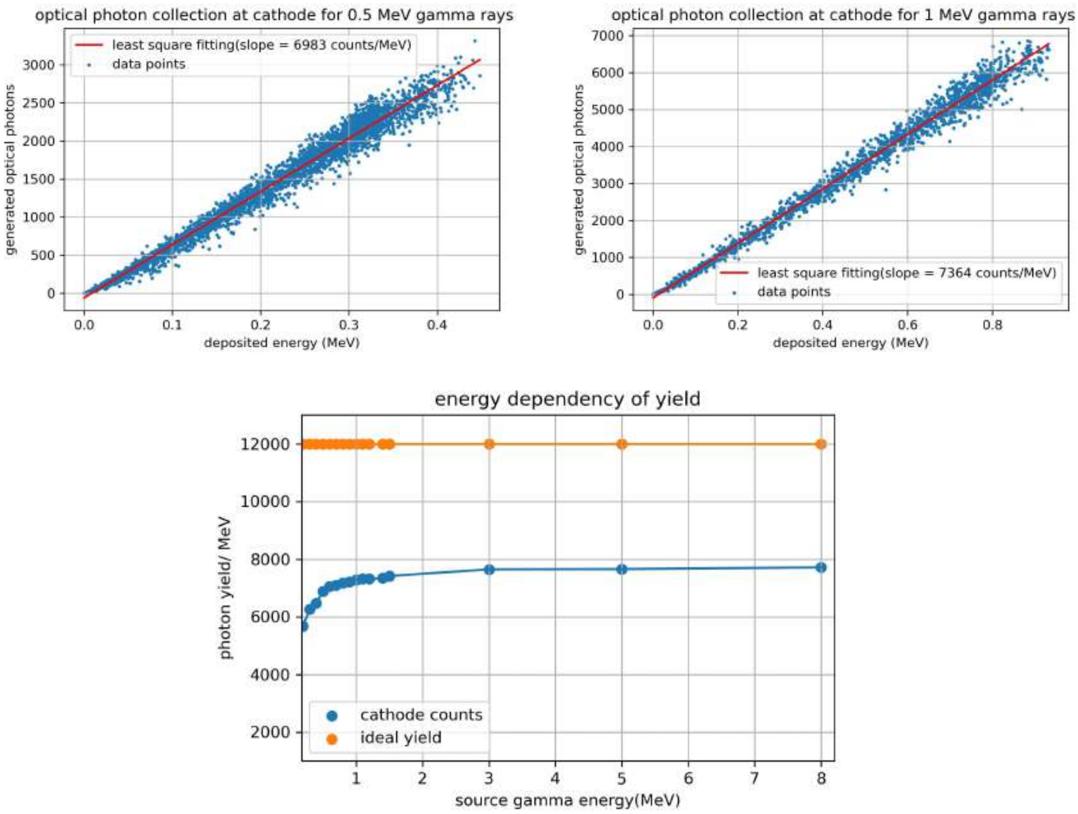

FIGURE 6.13: **Top:** Optical photon yield versus deposited energy for mono-energetic gamma rays of 0.5 MeV (left) and 1 MeV (right), showing an approximately linear response. **Bottom:** Energy dependence of optical photon yield up to 8 MeV, where the ideal scintillation yield (12000 photons/MeV$_{ee}$, orange) is compared with collected photons at the photocathode (blue). The reduced light yield at low energies reflects quenching effects from higher dE/dx of secondary electrons.

In this regime, the Compton-scattered electrons have lower kinetic energies and therefore higher average stopping power. According to Birks' law, an increase in dE/dx enhances non-radiative recombination processes, reducing the scintillation efficiency. This leads to a suppression of light yield relative to the intrinsic expectation.

At higher gamma energies, the secondary electrons possess higher kinetic energies and correspondingly lower stopping power. As a result, the influence of Birks' quenching is reduced, and the light yield approaches a linear dependence on deposited energy. In this regime, the scintillation response approaches the intrinsic light yield of the material.

The intrinsic scintillation yield of 12000 photons/MeV$_{ee}$ of EJ-301 represents the number of optical photons produced per unit electron-equivalent deposited energy under ideal conditions. However, the number of photons detected at the photocathode is lower than this value (Fig. 6.13). This difference arises from several factors, including optical photon absorption within the scintillator, scattering processes, reflections at material boundaries, finite geometrical acceptance.

Overall, the observed energy dependence of the light yield reflects the combined effects of charged-particle stopping power, non-linear quenching described by Birks' law, and optical photon transport and detection efficiencies within the detector system.

6.9 Simulated Neutron Response and Comparison with Experiment

6.9.1 Neutron Interaction in Scintillator

Unlike gamma rays, neutrons interact with the scintillator via nuclear processes rather than electromagnetic interactions. In hydrogen-rich organic scintillators such as EJ-301, the dominant mechanism is elastic scattering with hydrogen nuclei, producing recoil protons. Interactions with carbon nuclei, including both elastic and inelastic scattering, also occur, particularly at higher neutron energies, and neutrons may undergo multiple scattering events before fully losing their energy.

The resulting charged particles (primarily recoil protons, along with a smaller contribution from carbon ions) deposit energy in the medium through ionization and excitation. This leads to the formation of excited molecular states, whose de-excitation through singlet and triplet channels produces scintillation photons.

Neutron detection in such detectors can therefore be viewed as a two-stage process: (i) neutron interactions with nuclei generating recoil charged particles, and (ii) subsequent energy deposition by these particles, resulting in scintillation light emission.

In addition, inelastic scattering on carbon can produce excited nuclear states that de-excite via gamma emission. These secondary gamma rays further contribute to the total deposited energy through electron production.

It is important to note that the scintillation light yield is not linearly proportional to the deposited energy for heavily ionizing particles such as recoil protons. This nonlinearity arises from quenching effects, which are commonly described by Birks' law.

To simulate neutron interactions, the `G4HPNeutron` physics list is employed [16]. This model provides a high-precision, data-driven description based on evaluated nuclear data libraries, and is well suited for accurately modeling neutron interactions over a wide energy range.

6.9.2 Optical Photon Generation in Neutron Interaction

Neutron interactions produce more complex detector responses compared to gamma rays due to the stochastic nature of nuclear scattering processes and the involvement of multiple interaction channels.

In elastic scattering, the incident neutron transfers a fraction of its energy to a recoil proton. Due to the large stopping power (dE/dx) of these protons, the resulting scintillation light output is strongly quenched, leading to relatively low light yield per unit deposited energy. Such neutron response is also highly non-linear, as shown in Fig. 6.14. In contrast, inelastic scattering processes produce secondary gamma rays, which subsequently generate recoil electrons with lower dE/dx. These electrons produce comparatively higher light output. The coexistence of these processes results in characteristic band-like structures in

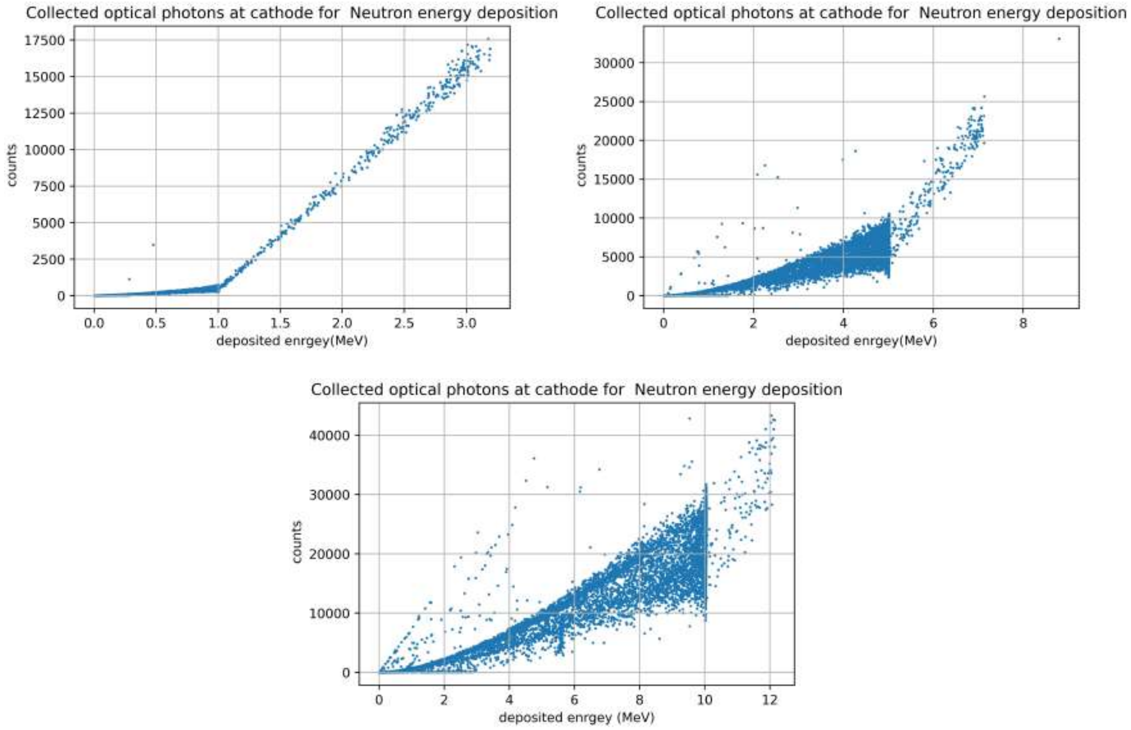

FIGURE 6.14: Optical photon yield versus deposited energy for mono-energetic neutrons of 1 MeV (top left), 5 MeV (top right), and 10 MeV (bottom). The non-linear response reflects energy deposition via recoil nuclei (primarily protons) with high dE/dx, leading to significant quenching.

the light output versus deposited energy distributions.

Furthermore, neutron-induced scintillation signals exhibit different temporal characteristics compared to gamma-induced signals. Recoil protons preferentially excite triplet states in the scintillator molecules, leading to a larger slow component in the scintillation decay. This results in longer pulse tails for neutron events, forming the basis for PSD between neutron and gamma interactions.

The response functions i.e. the detector response to mono-energetic sources exhibit significant broadening with increasing neutron energy. A few examples of response functions are shown in Fig. 6.15. This behaviour arises from the increasing contribution of multiple

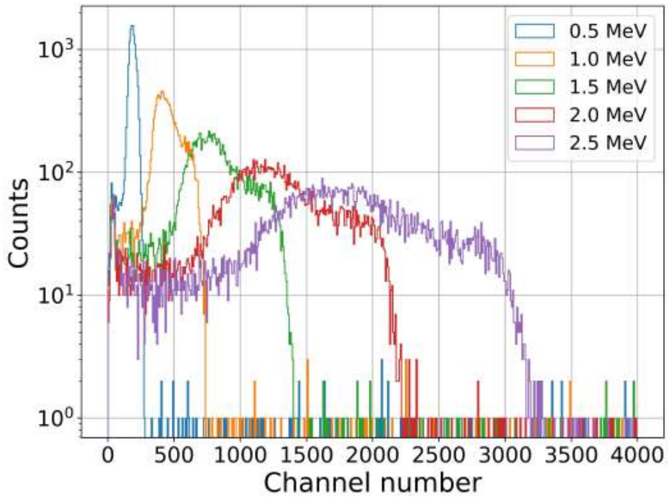

FIGURE 6.15: Response functions of the EJ-301 detector for mono-energetic neutrons, showing the broadening of the energy deposition spectrum with increasing neutron energy.

scattering events, wider kinematic distributions of recoil energies, and the presence of additional interaction channels such as inelastic scattering. These effects collectively lead to a broad and non-Gaussian detector response.

6.9.3 Electron-Equivalent Energy Calibration and Need for Unfolding

The detector is typically calibrated using gamma-ray sources, providing a response in terms of electron-equivalent energy ($\mathrm{MeV_{ee}}$). However, due to the non-linear scintillation response arising from quenching, neutron-induced signals cannot be directly interpreted on this energy scale.

A mapping between nuclear recoil energy and electron-equivalent energy is obtained using detailed Monte Carlo simulations. The resulting relation, as shown in Fig 6.16, exhibits strong non-linearity, primarily due to the enhanced quenching associated with high-dE/dx recoil protons. As a result, a given nuclear recoil energy corresponds to a significantly lower electron-equivalent energy. Direct experimental validation of this

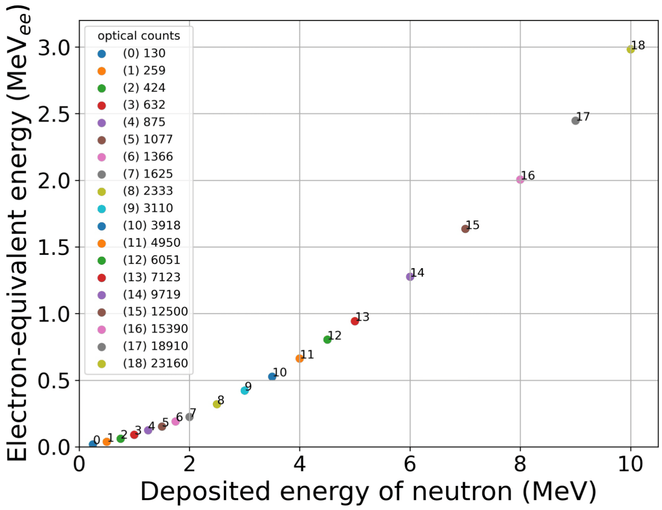

FIGURE 6.16: Relation between nuclear recoil energy and electron-equivalent energy. Each point corresponds to a optical photon yield. The observed non-linearity reflects the effect of quenching in the scintillator.

mapping is challenging due to the limited availability of mono-energetic neutron sources over a wide energy range.

Unfolding techniques provide a powerful approach to address this limitation. By comparing the unfolded neutron energy spectra with known reference spectra (e.g., Am–Be sources), the accuracy of the detector response matrix and the associated calibration can be assessed.

6.9.4 Response Matrix Construction

The detector response to mono-energetic neutrons is simulated over an energy range from 0.05 MeV to 12 MeV. This range is divided into 240 bins, corresponding to an energy bin width of 0.05 MeV. For each incident neutron energy, the corresponding light output distribution is recorded, and these distributions collectively form the detector response matrix.

The nature of the response functions evolves significantly with increasing neutron

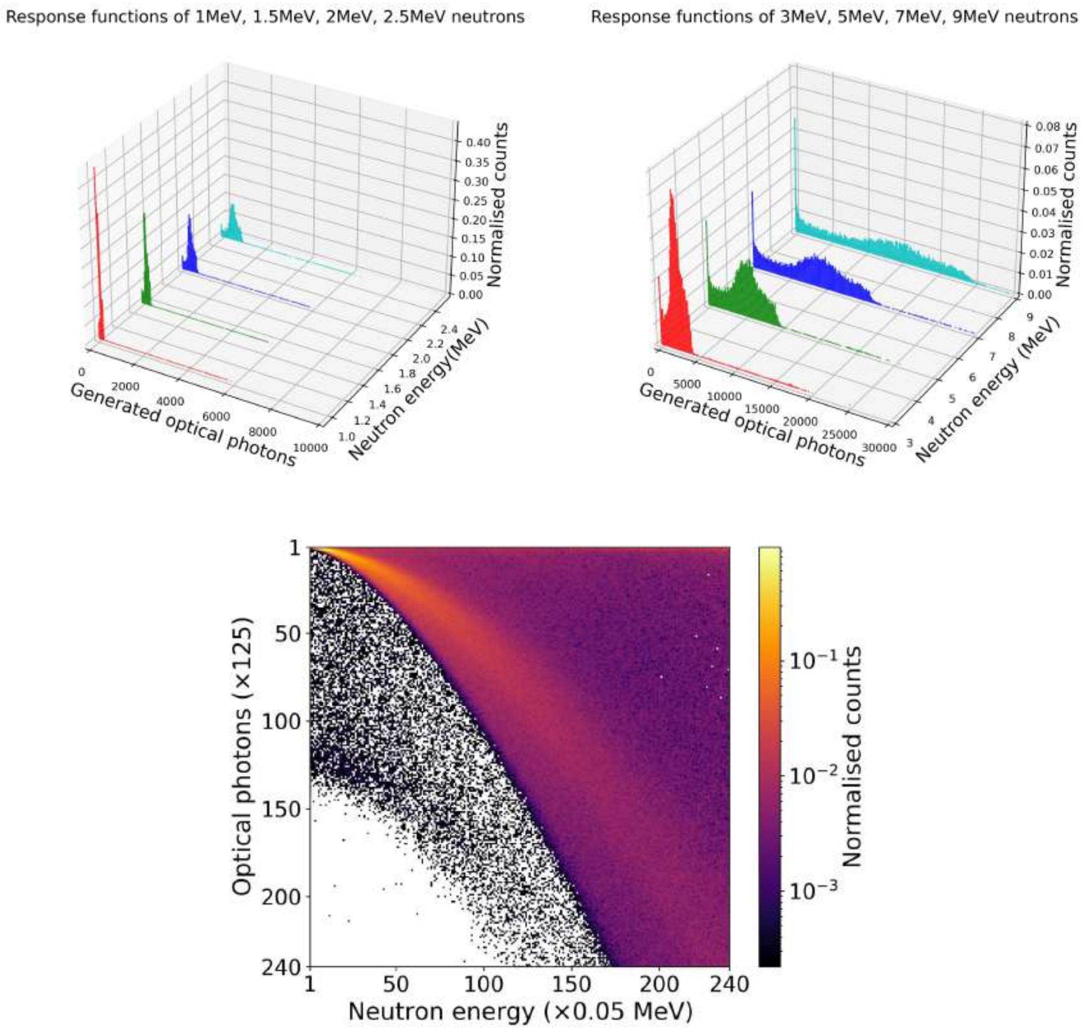

FIGURE 6.17: **Top:** Variation of detector response functions with incident neutron energy, illustrating the broadening and shifting of the spectra. **Bottom:** Simulated neutron response matrix (240 × 240) for the EJ-301 detector. Adapted from Ref. [11].

energy. At lower energies, the response is relatively localized, whereas at higher energies, the response functions become broader and flatter. This behavior arises due to the increasing contribution of multiple interaction channels and energy transfer mechanisms. Additionally, the peak of the light output distribution shifts towards higher energies with increasing incident neutron energy.

Due to the complex and non-linear nature of neutron interactions in the scintillator, the response functions do not follow a simple analytical form. As a result, the detector response matrix cannot be described using a closed-form expression and is instead represented numerically in the form of tabulated data or histograms.

The simulated neutron response functions and the corresponding response matrix are shown in Fig. 6.17.

6.9.5 Simulation of Am-Be Neutron Source

The neutron spectrum from an Am-Be source follows a continuous energy distribution, as defined by the ISO standard [17]. This spectrum is used as input in the simulation to generate neutrons incident on the detector.

The presence of the granite base slightly modifies the neutron spectrum due to scattering effects, particularly at low energies. This effect is included in the simulation to ensure consistency with experimental conditions.

The simulated detector responses to the Am-Be source are shown in Fig. 6.18, both in terms of deposited energy and optical photon counts.

6.9.6 Neutron–Gamma event Discrimination using PSD

Since the Am-Be source emits both neutrons and gamma rays, it is essential to separate their respective contributions in the experimental data. This discrimination is achieved using PSD, a well-established technique in organic scintillators that exploits differences in scintillation decay characteristics for neutron- and gamma-induced events.

Gamma rays primarily interact via Compton scattering, producing fast electron recoils that result in prompt scintillation (fluorescence). In contrast, neutrons interact predominantly through elastic scattering with hydrogen nuclei, producing recoil protons that induce

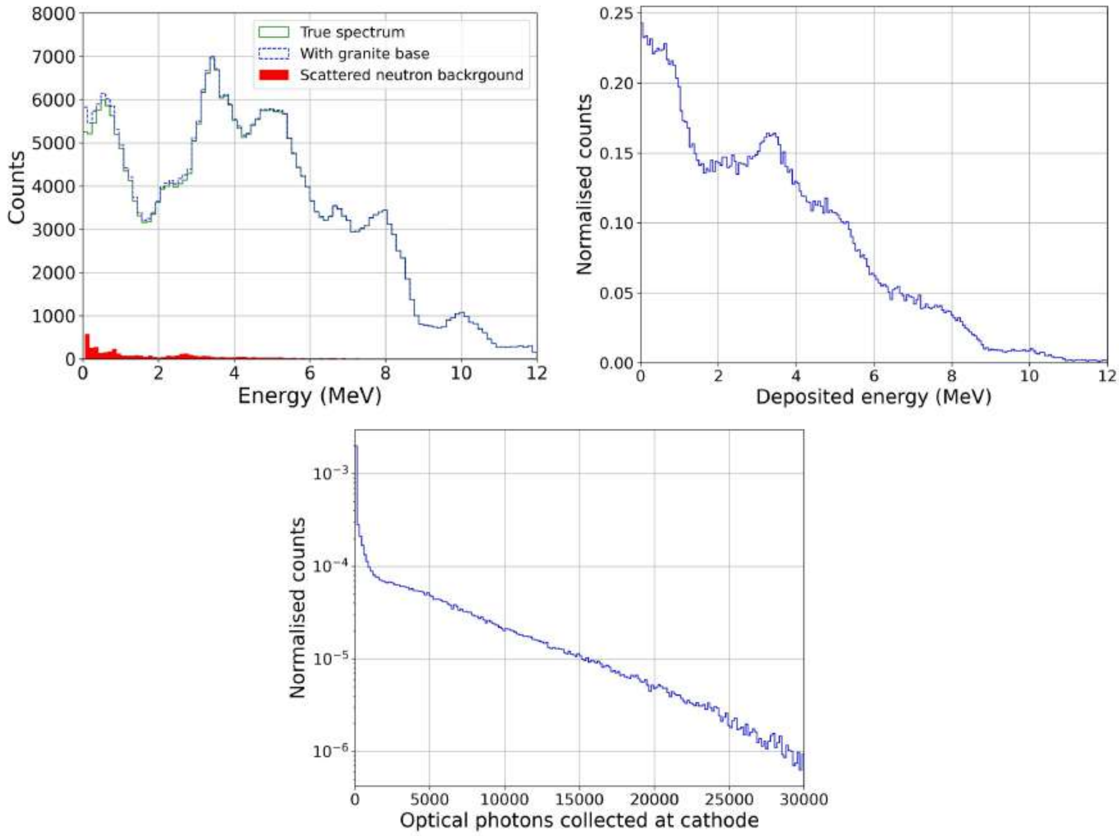

FIGURE 6.18: Simulated Am–Be neutron spectrum and corresponding detector response. **Top left:** Input neutron spectrum, showing negligible modification due to scattering from the granite base. **Top right:** Deposited energy spectrum in the scintillator. **Bottom:** Resulting optical photon yield. The figures links the incident neutron spectrum to the measurable detector response. Adapted from Ref. [11].

a larger fraction of delayed scintillation (delayed fluorescence). As a result, neutron-induced pulses exhibit a longer tail compared to gamma-induced pulses, as illustrated in Fig. 6.19.

The discrimination is performed using the charge integration method, where the pulse is integrated over two time windows: a short gate and a long gate. The PSD parameter is defined in Eq. 6.2.

The quality of neutron–gamma separation is quantified using the Figure of Merit, defined as:

$$FOM = \frac{\mu_n - \mu_\gamma}{\mathrm{FWHM}_n + \mathrm{FWHM}_\gamma}, \tag{6.12}$$

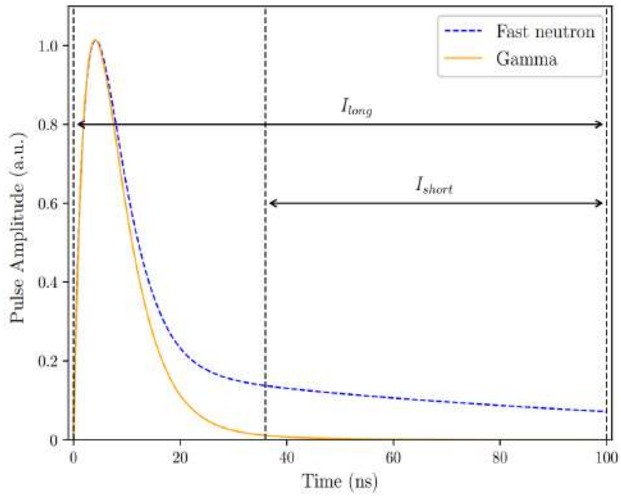

FIGURE 6.19: Pulse shape discrimination using the charge integration method. Representative neutron and gamma pulses are shown, with neutron-induced events exhibiting a longer tail. Short (I_{short}) and long (I_{long}) integration gates quantify this difference, enabling event separation based on pulse shape. Adapted from [18].

where μ_n and μ_γ are the mean PSD values for neutron and gamma distributions obtained from a Gaussian fit to the PSD distribution, and FWHM_n and FWHM_γ are their corresponding full widths at half maximum. A higher FOM indicates better separation.

To optimize the discrimination performance, the FOM is evaluated as a function of detector operating parameters. The anode voltage and integration gate widths are varied to identify optimal conditions. The maximum FOM is achieved at an anode voltage of 750 V, with a short gate of 30 ns and a long gate of 280 ns, which are adopted for the analysis. The corresponding FOM achieved is 1.14 for an energy threshold of 275 keV_{ee}.

An example of a typical raw pulse recorded from the Am-Be source is shown in Fig. 6.20, illustrating the waveform used for charge integration.

Using the optimized PSD parameters, neutron and gamma events form distinct bands in the PSD distribution, as shown in Fig. 6.21. Events within the mean $\pm 3\sigma$ region are identified for each class. Neutron events are selected by subtracting the gamma contribution

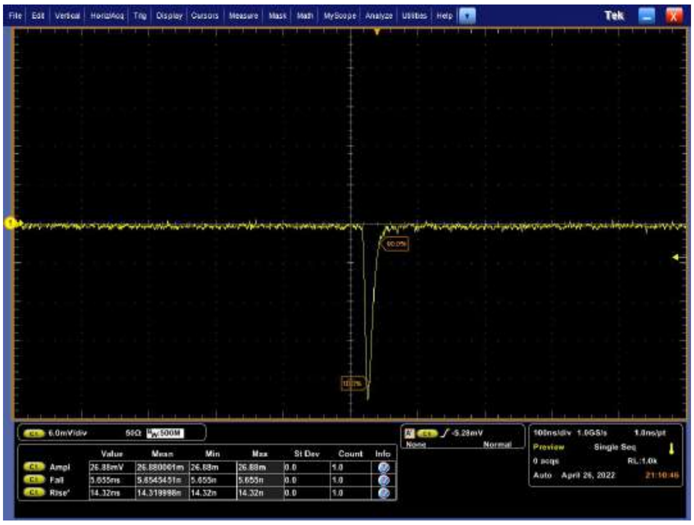

FIGURE 6.20: Example of a raw pulse recorded using an oscilloscope for an Am-Be source.

from the total spectrum, enabling efficient separation of neutron-induced events from gamma backgrounds for further analysis. An additional cut at 740 ADC channels is applied to suppress gamma leakage into the neutron band. Above this threshold, the fraction of misidentified gamma events is negligible. Therefore, no explicit PSD efficiency correction is applied in the analysis.

This negligible contribution of gamma in neutron band is further supported by the PSD distribution obtained from background data, shown in Fig. 6.21 (right), where the contribution of ambient gamma events in the neutron band is found to be negligible. The fraction of such misidentified events is estimated to be ~0.17% of the total Am–Be neutron event rate.

Following the selection of neutron-induced events, the simulated detector response is compared with the corresponding experimental data to determine the Birks' constant governing scintillation quenching. The results of this comparison are presented in Fig. 6.22. The nominal value of the Birks' constant is found to be $k_B = 0.1065\ \mathrm{mm\,MeV^{-1}}$. Although the exact scintillating composition of the commercial EJ-301 detector is not explicitly

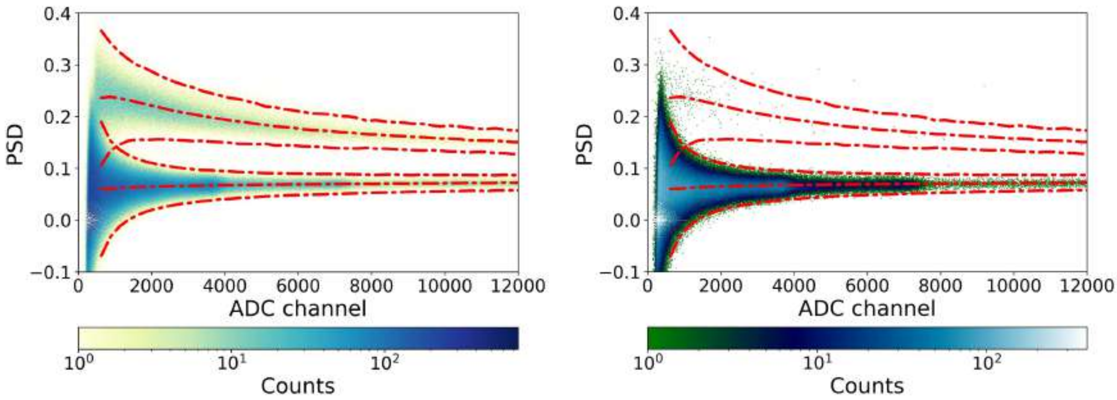

FIGURE 6.21: (left) PSD distribution for the Am–Be source showing clear separation between neutron and gamma events. Events within the mean $\pm 3\sigma$ region are identified used for further analysis. Adapted from Ref. [11]. (right) PSD distribution for background data, demonstrating negligible leakage of ambient gamma events into the neutron band. The misidentified fraction is ~0.17% relative to the Am–Be neutron event rate, indicating a negligible impact on the analysis.

specified, this value is consistent with those reported for pseudocumene-based organic scintillators. To study the effect of variation of k_B on the simulated spectrum, it is varied within ±10% of its nominal value. This variation results in only a minimal change in the simulated detector response, indicating that the unfolding results are largely insensitive to the exact value of the Birks' constant within this range. Therefore, the systematic uncertainty arising from the choice of the Birks' constant is considered to be negligible.

Overall, the simulated and experimental spectra show good agreement. However, a noticeable deviation is observed in the high-energy region above approximately 8000 ADC channels. Although the event statistics are relatively low in this region, the ratio of the simulated spectrum to the experimental data remains systematically below unity, with uncertainties that do not overlap with unity. This indicates that the observed discrepancy cannot be attributed solely to statistical fluctuations.

This deviation corresponds to energies above $(8000/0.37) \approx 2.2\times10^4$ cathode-collected optical photons. To investigate the origin of this discrepancy, several checks were per-

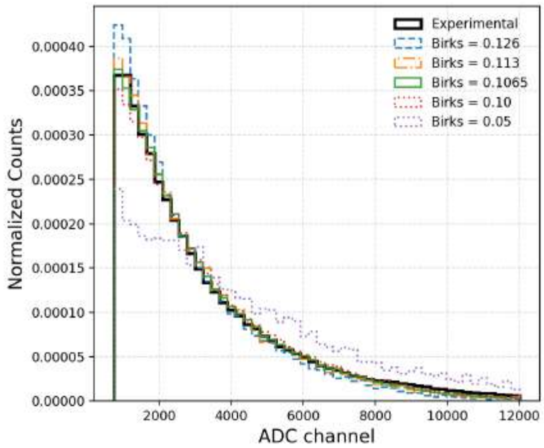

FIGURE 6.22: Comparison of simulated detector response for different values of the Birks' constant. The nominal value $k_B = 0.1065$ mm MeV^{-1} provides the best agreement with the experiment. Variations within ±10% of this value produce only minor changes in the spectrum, indicating a negligible systematic uncertainty associated with the Birks' constant.

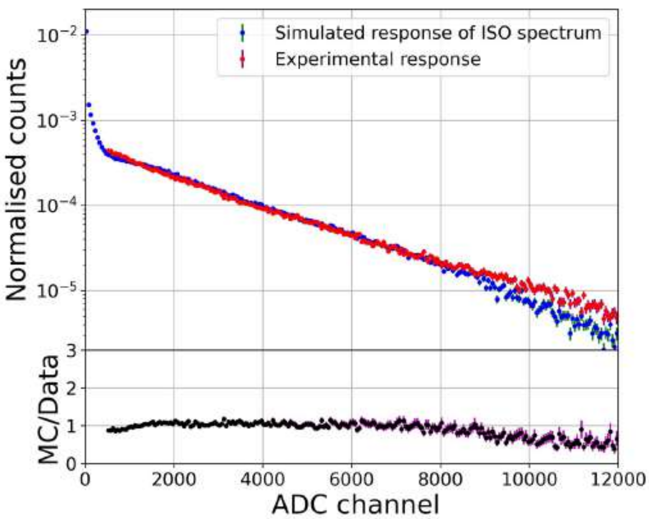

FIGURE 6.23: Comparison of simulated detector response to the Am–Be ISO neutron spectrum with experimental data, where neutron events are selected using PSD. The overall agreement validates the simulation, with deviations at higher energies. The possible reasons for these difference are discussed in the text. Adapted from Ref. [11].

formed.

First, three different Geant4 physics lists (*FTFP*, *QBBC*, and *QGSP*) were implemented in the simulation, all of which produce consistent detector responses. This demonstrates that the observed discrepancy is not driven by the choice of physics list, and that the associated systematic uncertainty from the Geant4 physics modeling is negligible. The comparison is shown in Fig. 6.24.

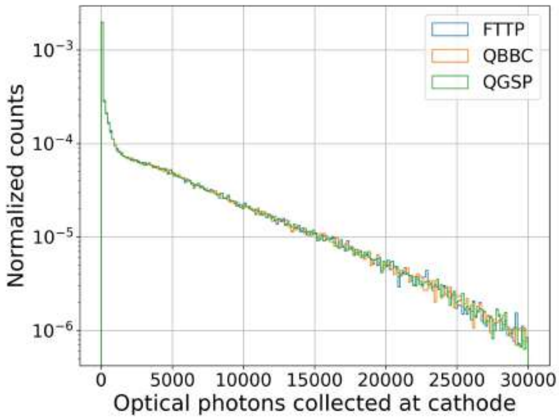

Figure 6.24: Comparison of simulated detector responses using different Geant4 physics lists (*FTFP*, *QBBC*, and *QGSP*). The consistency among the spectra indicates that the systematic uncertainty associated with the choice of physics list is negligible. The horizontal axis represents the number of optical photons collected at the photocathode, which can be converted to ADC channels using a conversion factor of 0.37.

Second, the resolution scale parameter used in the simulation was varied and examined. The comparison of spectral broadening between simulation and experiment indicates no significant energy dependence, implying that the resolution model does not account for the observed difference.

Third, possible contributions from external neutron backgrounds not fully accounted for in the simulation were investigated. For instance, neutrons produced by cosmic muon interactions with surrounding materials, such as nearby lead shielding or the concrete structure of the laboratory, could enhance the high-energy component of the measured spectrum. However, this effect was found to be negligible based on background data (without the Am–Be source). Neutron-like events selected using PSD were observed to lie below channel 2000 and constitute only ~ 0.17% of the total neutron event rate, indicating an insignificant contribution to the high-energy region.

Finally, the effect of environmental neutron scattering was considered. In particular, the experimental setup was placed on a granite base, which was included in the simulation to account for possible scattered neutron backgrounds. The results show that this contribution primarily affects the low-energy region and has a negligible impact on the high-energy part of the spectrum.

After accounting for these factors, two primary explanations remain. One possibility is that the neutron energy spectrum of the Am-Be source used in the experiment deviates slightly from the standard ISO spectrum, particularly in the high-energy region. Since Am-Be is a composite source, variations in its composition can lead to changes in the emitted neutron spectrum.

Another possible explanation is related to limitations in the nuclear data used in the simulation. As neutron interactions are modeled using evaluated cross-section libraries, incomplete or insufficient data for certain isotopes, particularly hydrogen and carbon, may contribute to the observed discrepancy.

These factors are likely responsible for the differences observed between the simulated and experimental spectra in the high-energy region.

In the following section, we describe the unfolding of the detector response to the Am–Be neutron spectrum.

6.10 Unfolding of Detector Response to Am-Be Neutron Spectrum

6.10.1 Validation of Unfolding Methods Using Simulated Data

As a first step, the unfolding procedure is validated using simulated detector responses. A Monte Carlo Am-Be neutron spectrum based on ISO reference data [17] is used as the input spectrum. The corresponding detector response is generated using the GEANT4 simulation framework described in previous sections.

The purpose of this validation is to assess the capability of the unfolding algorithms, namely the GRAVEL iterative method and the Bayesian unfolding method implemented in RooUnfold, to accurately reconstruct the true neutron energy spectrum from the detector response.

The GRAVEL unfolding algorithm is implemented in Python, while the RooUnfold method is applied using the PyROOT interface [15]. The unfolded spectra obtained from both methods are shown in the upper left panel of Fig. 6.25. The corresponding evolution of the goodness-of-fit parameter, $\chi^2/n.d.f$, as a function of iteration number is presented in the upper right panel.

Both unfolding methods successfully reconstruct the input ISO spectrum with good accuracy. The agreement between the unfolded and true spectra demonstrates the robustness of the response matrix and validates the unfolding procedure.

6.10.2 Efficiency Correction

The detection efficiency of the scintillation detector is energy-dependent, particularly for neutrons. High-energy neutrons have a lower probability of interacting within the detector volume due to their longer mean free path, resulting in reduced detection efficiency at

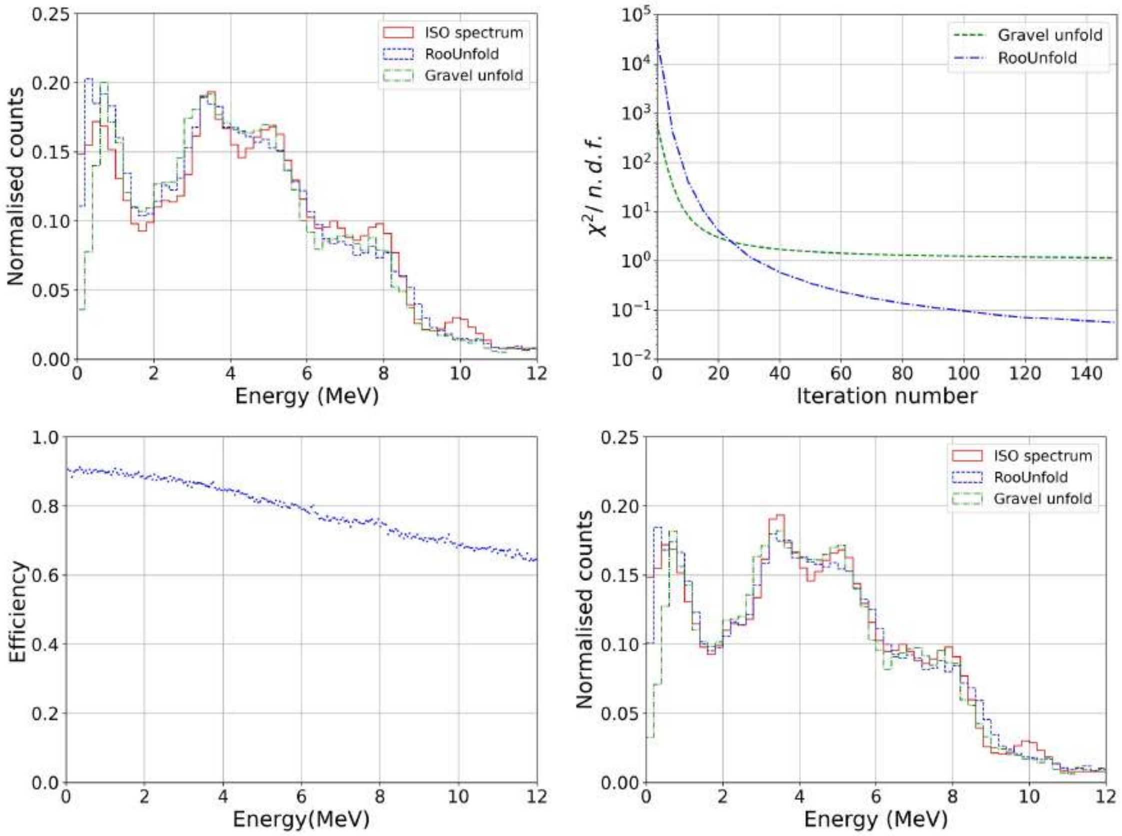

FIGURE 6.25: Unfolding results for the simulated Am–Be detector response: (upper left) reconstructed neutron spectrum; (upper right) variation of χ^2/n.d.f. with iteration number; (lower left) neutron detection efficiency as a function of energy; (lower right) efficiency-corrected reconstructed spectrum. This demonstrates the convergence and performance of the unfolding procedure. Adapted from Ref. [11].

higher energies.

To account for this effect, an efficiency correction is applied to the unfolded spectra. The neutron detection efficiency is estimated from simulation as the ratio of detected events to the number of incident neutrons for each energy bin. The efficiency curve is shown in the lower left panel of Fig. 6.25.

After applying the efficiency correction, the reconstructed spectra (lower right panel of Fig. 6.25) show improved agreement with the true ISO spectrum across the entire energy range.

A comparison between the GRAVEL and RooUnfold methods reveals that both approaches yield consistent results within statistical uncertainties. However, the RooUnfold method exhibits faster convergence and improved stability, as reflected in the behavior of the $\chi^2/n.d.f$ metric. This makes the Bayesian unfolding approach computationally more efficient for practical applications.

6.10.3 Unfolding of Experimental Data

Following validation with simulated data, the unfolding procedure is applied to the experimentally measured detector response obtained from the Am-Be neutron source.

The unfolded spectra from experimental data are shown in the upper left panel of Fig. 6.26, along with the variation of $\chi^2/n.d.f$ in the upper right panel. The differences between the unfolded spectra give an estimate of the systematic uncertainties between the unfolding algorithm.

In the experimental setup, a threshold is applied in terms of ADC channels (740 channels, corresponding to ∼2 MeV). Due to the intrinsic resolution of the detector, this threshold does not correspond to a sharp cutoff in neutron energy. Instead, it introduces a gradual suppression of low-energy events.

As a result, the detection efficiency is significantly reduced below this threshold, as shown in the lower left panel of Fig. 6.26. Additionally, events observed below 2 MeV arise from inelastic scattering processes and detector resolution effects.

6.10.4 Efficiency-Corrected Experimental Spectrum

After applying the efficiency correction, the unfolded experimental spectrum is shown in the lower right panel of Fig. 6.26. While the overall shape of the reconstructed spectrum

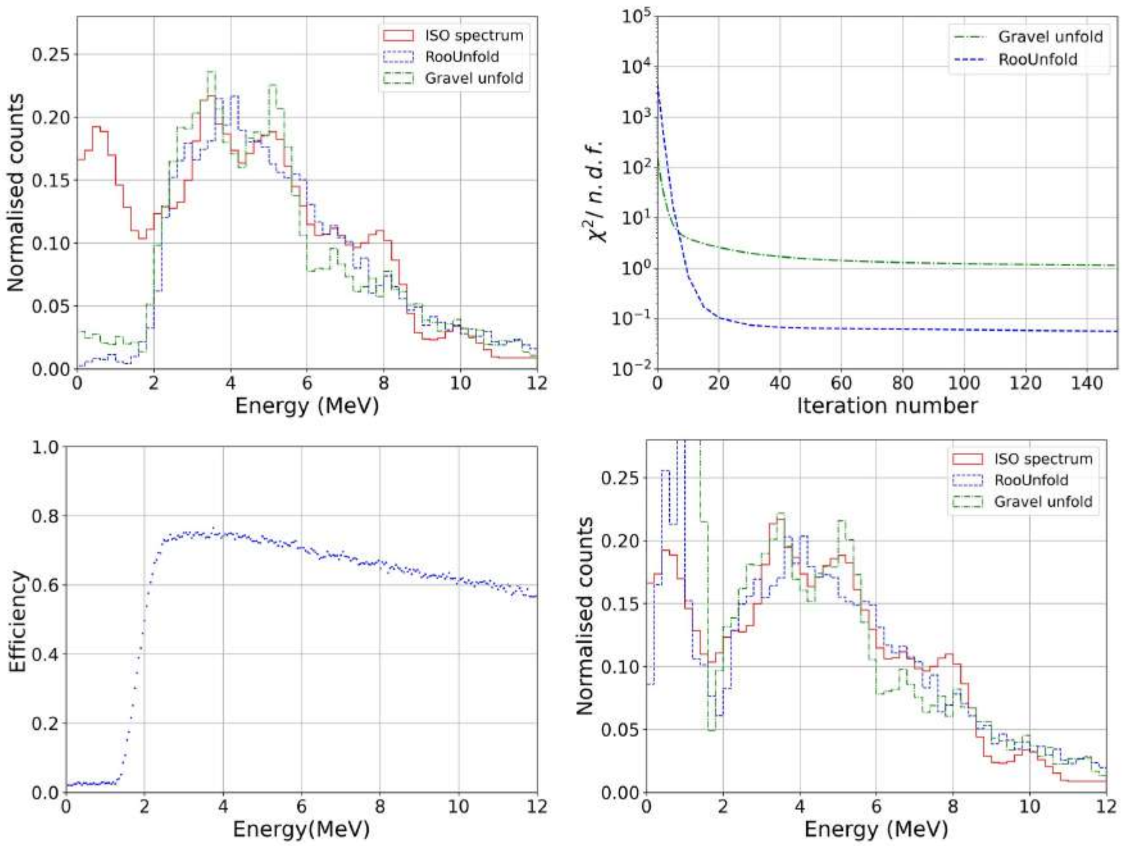

FIGURE 6.26: Unfolding results for experimental data: (upper left) reconstructed neutron spectrum; (upper right) variation of χ^2/n.d.f. with iteration; (lower left) neutron detection efficiency including threshold effects; (lower right) efficiency-corrected reconstructed spectrum. Adapted from Ref. [11].

is consistent with the ISO reference, some deviations are observed, particularly at low and high energies.

At energies below 2 MeV, the efficiency correction leads to an overestimation of the spectrum due to large uncertainties associated with threshold effects and inelastic scattering contributions. Therefore, the reconstructed spectrum in this region should be interpreted with caution.

The deviations observed at higher energies may arise from several sources:

- Variations in the actual Am-Be source spectrum compared to the ISO reference, due to differences in isotope composition and source fabrication.

- Limitations in the GEANT4 neutron cross-section data at higher energies, which may affect the accuracy of the simulated response matrix.

- Residual uncertainties in detector modeling, including optical properties and Birks' constant.

Despite these limitations, the overall agreement between the unfolded and reference spectra demonstrates the reliability of the unfolding methodology and validates the use of the EJ-301 detector for fast neutron spectroscopy.

6.11 Discussion of Uncertainties in Unfolding

The uncertainties in the reconstructed neutron spectrum arise from both statistical and systematic sources. These can be broadly categorized into (i) experimental uncertainties, (ii) uncertainties associated with the unfolding methodology, and (iii) detector and simulation modeling uncertainties. These are summarized and discussed below.

Statistical Uncertainty: The statistical uncertainty in the experimental spectrum, both before and after efficiency correction, is shown in Fig. 6.27. The detector threshold at 740 ADC channels corresponds to an incident neutron energy of approximately 2 MeV. Due to the finite detector resolution and contributions from inelastic neutron interactions, a small fraction of neutrons with energies below this threshold can still produce sufficient light output to cross the threshold. As a result, statistical fluctuations are higher in this region due to limited statistics. After applying the efficiency correction, these fluctuations are scaled up, leading to larger uncertainties in the reconstructed spectrum below ~2 MeV.

Therefore, the unfolded spectrum in this region is associated with significant statistical uncertainty and should be interpreted with caution.

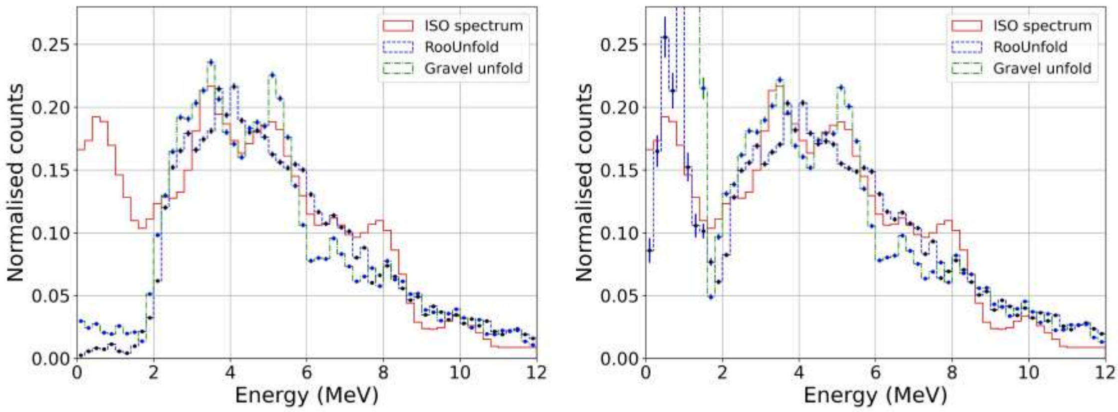

FIGURE 6.27: Unfolded neutron spectrum with statistical uncertainties: (left) without efficiency correction and (right) with efficiency correction. The increase in uncertainty at low energies reflects the combined effects of detector threshold and efficiency scaling.

Unfolding Methodology: A source of systematic uncertainty arises from the unfolding procedure itself. This is evaluated by comparing results obtained using the iterative GRAVEL algorithm and the Bayesian unfolding approach implemented in RooUnfold. Regularization is used to stabilize the ill-posed inversion of the detector response matrix by suppressing statistical fluctuations. In both methods, it is implemented through controlled iteration, with the number of iterations acting as the effective regularization parameter. Differences in the update rules used in the iterative procedures lead to small variations in the unfolded spectra. The difference between the unfolded spectra is an estimate of the associated systematic uncertainty.

Detector and Simulation Modeling: Additional systematic uncertainties arise from the detector modeling in the simulation. These include uncertainties associated with the choice of physics list, optical photon transport, and scintillation quenching.

The Birks' constant governing scintillation quenching is determined by comparing simulated and experimental detector responses. Varying the Birks' constant within ±10% of its nominal value results in only a minimal change in the simulated spectrum (Fig. 6.22), indicating that the unfolded results are mostly insensitive to this parameter within the considered range.

Similarly, the impact of different GEANT4 physics lists on the detector response is evaluated (Fig. 6.24). The resulting spectra are consistent, indicating that the systematic uncertainty associated with the choice of physics list is negligible.

Overall, the dominant uncertainties arise from statistical fluctuations, particularly in the low-energy region below ~2 MeV, as well as from systematic effects associated with the unfolding methodology. Systematic uncertainties related to detector and simulation modeling, including the choice of Birks' constant and physics list, are found to be small within the explored parameter variations.

6.12 Conclusion

In this work, a comprehensive study of the response of a $2'' \times 2''$ EJ-301 liquid scintillation detector to gamma rays and fast neutrons has been carried out using a combination of detailed GEANT4 simulations and experimental measurements. A realistic detector model, including geometry, material composition, optical photon processes, and quenching effects, has been implemented to accurately reproduce the detector response.

The simulated gamma-ray responses were used to calibrate the detector in the electron-equivalent energy scale and to determine the resolution scale parameter by comparison with experimental data. A consistent agreement between simulated and measured spectra for multiple gamma sources demonstrates the validity of the detector modeling. In addition, the Birks' constant for the EJ-301 scintillator has been estimated through tuning of the simulated neutron response, yielding a value consistent with those reported for similar organic scintillators.

A detailed neutron response matrix was constructed using mono-energetic neutron simulations over a wide energy range. This response matrix forms the basis for unfolding the experimentally measured detector response. Two different unfolding techniques, namely the GRAVEL iterative method and the Bayesian unfolding method implemented in the RooUnfold framework, have been applied to reconstruct the neutron energy spectrum from the measured Am-Be source data.

The unfolding methods were first validated using simulated data, where both approaches successfully reproduced the input neutron spectrum. When applied to experimental data, both methods yielded consistent results, demonstrating the robustness of the unfolding procedure. The RooUnfold method was found to be computationally more efficient.

An energy-dependent efficiency correction was applied to the unfolded spectra to account for the finite detection probability of neutrons within the scintillator volume. After correction, the reconstructed neutron spectrum shows good agreement with the reference ISO Am-Be spectrum, with some deviations at low and high energies attributed to threshold effects, detector resolution, and possible uncertainties in the source characteristics and simulation inputs.

The results of this work establish a reliable calibration of the EJ-301 detector for fast neutron energy measurements. The methodology developed here, combining detailed detector simulation with unfolding techniques, provides a robust framework for neutron spectroscopy using organic scintillation detectors.

This calibrated detector can be effectively deployed in low-background environments, such as underground laboratories, to measure fast neutron energy spectra. Such measurements are crucial for characterizing neutron-induced backgrounds in rare event search experiments, including dark matter searches and coherent elastic neutrino-nucleus scattering studies.

Future improvements may include refined modeling of neutron interaction cross-sections at higher energies, incorporation of more detailed detector response effects, and application of advanced regularization techniques in unfolding to further reduce systematic uncertainties. Additionally, extending this methodology to other detector geometries and materials can broaden its applicability in nuclear and astroparticle physics experiments.

Bibliography

[1] Glenn F Knoll. *Radiation detection and measurement*. 4th ed. John Wiley & Sons, 2010.

[2] Eljen Technology. *EJ-301, EJ-309 - Neutron/Gamma PSD Liquid Scintillators - Eljen Technology*. 2021.

[3] Antoni Nassalski, M Moszynski, A Syntfeld-Kazuch, L Swiderski, and T Szczeniak. “Non-proportionality of organic scintillators and BGO”. *IEEE Transactions on Nuclear Science* 55.3 (2008), pp. 1069–1072.

[4] Zachary S. Hartwig and Peter Gumplinger. “Simulating response functions and pulse shape discrimination for organic scintillation detectors with Geant4”. *Nuclear Instruments and Methods in Physics Research Section A: Accelerators, Spectrometers, Detectors and Associated Equipment* 737 (2014), pp. 155–162.

[5] Yanping Xu, Gerhard Randers-Pehrson, Stephen A Marino, Guy Garty, Andrew Harken, and David J Brenner. “Broad energy range neutron spectroscopy using a liquid scintillator and a proportional counter: Application to a neutron spectrum similar to that from an improvised nuclear device”. *Nuclear Instruments and Methods in Physics Research Section A: Accelerators, Spectrometers, Detectors and Associated Equipment* 794 (2015), pp. 234–239.

[6] R Batchelor, WB Gilboy, JB Parker, and JH Towle. "The response of organic scintillators to fast neutrons". *Nuclear Instruments and Methods* 13 (1961), pp. 70–82.

[7] W.R. Burrus and V.V. Verbinski. "Fast-neutron spectroscopy with thick organic scintillators". *Nuclear Instruments and Methods* 67.2 (1969), pp. 181–196.

[8] YongHao Chen, XiMeng Chen, JiaRong Lei, Li An, XiaoDong Zhang, JianXiong Shao, Pu Zheng, and XinHua Wang. "Unfolding the fast neutron spectra of a BC501A liquid scintillation detector using GRAVEL method". *Science China Physics, Mechanics & Astronomy* 57.10 (2014), pp. 1885–1890.

[9] Bin Liu, Huanwen Lv, Hu Xu, Lan Li, Wei Li, Futing Jing, Yirui Wu, et al. "Study on neutron spectrum unfolding method of organic scintillation measurement based on iterative regularization". *Annals of Nuclear Energy* 162 (2021), p. 108504.

[10] M. Cecconello. "Liquid Scintillators Neutron Response Function: A Tutorial". *Journal of Fusion Energy* 38 (Aug. 2019).

[11] S. Das, V.K.S. Kashyap, and B. Mohanty. "Energy calibration of EJ-301 scintillation detector using unfolding methods for fast neutron measurement". *Nuclear Instruments and Methods in Physics Research Section A: Accelerators, Spectrometers, Detectors and Associated Equipment* 1042 (2022), p. 167405.

[12] Hamamatsu Photonics K.K. and its affiliates. *Photomultiplier tube R7724, Hamamatsu Photonics*. 2021.

[13] CAEN. *User Manual UM5960 CoMPASS Multiparametric DAQ Software for Physics Applications*. 2022.

[14] Willem GJ Langeveld, Michael J King, John Kwong, and Daniel T Wakeford. "Pulse shape discrimination algorithms, figures of merit, and gamma-rejection for liquid and solid scintillators". *IEEE Transactions on Nuclear Science* 64.7 (2017), pp. 1801–1809.

[15] ATLAS Collaboration. *Introduction to Unfolding with RooUnfold — StatisticalMethods documentation*. 2019.

[16] Geant Collaboration. "Geant4 User's Guide for Application Developers". *Accessible from the GEANT4 web page [1] Version geant4* 9 (2012).

[17] Hermann Kluge. *Irradiation facility with radioactive reference neutron sources: basic principles*. Tech. rep. Physikalisch-Technische Bundesanstalt, 1998.

[18] MJ Cieślak, Kelum AA Gamage, Robert Glover, and C James Taylor. “Pulse shape discrimination performance of a pixelated plastic scintillator (EJ-299-34) for a coded-aperture based dual particle imaging system”. *Journal of Instrumentation* 14.07 (2019), P07017–P07017.

CHAPTER 7

Conclusion and Outlook

Contents

7.1 Conclusion

This thesis presents a comprehensive investigation of key experimental and phenomenological challenges in the search for low-mass dark matter, with particular emphasis on sub-keV detector calibration, statistically robust signal extraction, and the characterization of irreducible backgrounds. The work is motivated by the growing shift of direct detection experiments toward the sub-GeV/c^2 dark matter regime, where traditional assumptions regarding detector response, background rejection, and statistical inference require significant refinement.

The central objective of this thesis has been to develop and validate a coherent framework for rare-event searches that integrates:

- Precision detector calibration at sub-keV energy scales using ultra-sensitive cryogenic silicon calorimeters, together with studies of their bias-dependent detector response.
- Advanced statistical inference methods for low-count spectral analyses, enabling signal extraction and upper-limit setting on coupling strengths, particularly in the context of axion-like particle and dark photon searches.
- Quantitative understanding of irreducible neutrino backgrounds through coherent elastic neutrino–nucleus scattering (CEνNS) in low-mass WIMP dark matter search experiments.
- Experimental characterization and modeling of fast neutron backgrounds relevant to nuclear-recoil-based rare-event searches, such as WIMP-like dark matter and CEνNS searches.

These components are inherently interconnected. As detector thresholds approach the O(eV) scale and experimental exposure increases, sensitivity becomes progressively limited not only by statistical fluctuations but also by systematic uncertainties associated with detector response and background modeling. The contributions presented in this thesis explicitly address this transition, establishing a framework for precision-driven rare-event searches in the low-mass dark matter regime.

Precision Sub-keV Calibration and Detector Response study in Cryogenic Detectors

A major experimental achievement of this work is the development of a sub-keV calibration framework for SuperCDMS silicon HVeV detectors based on Compton-step features arising from bound-electron scattering. Using controlled ^{137}Cs gamma irradiation, distinct spectral features corresponding to the L-shell (∼100–150 eV) and K-shell (∼1.8 keV) binding energies were resolved. The detectors achieved an energy resolution of approximately 3 eV and thresholds near 30 eV, demonstrating dark matter signal sensitivity to the sub-keV scale.

The calibration methodology incorporated FEFF-based modeling of bound-electron Compton scattering, Geant4 simulations for validation at higher energies, and a data-driven treatment of low-energy excess backgrounds. This framework enabled a continuous and consistent energy calibration from the sub-keV regime up to ∼2 keV, providing a robust mapping between deposited energy and detector response in the region of interest for low-mass dark matter searches.

An independent calibration using optical photon injection under high-voltage operation (150 V) yields well-defined energy signatures for absorbed photons, consistent with Neganov–Trofimov–Luke (NTL) amplification. A key result is that the detector response at zero bias is approximately 30% lower than under high-voltage operation. This difference reflects the underlying phonon production mechanisms and underscores the importance of bias-dependent response modeling. Such effects introduce a non-negligible systematic uncertainty, directly impacting energy reconstruction, signal efficiency estimation, and the interpretation of low-energy spectral features.

Overall, this work establishes a robust and experimentally validated calibration framework that significantly reduces one of the dominant uncertainties in sub-keV dark matter searches.

Searches for Axion-Like Particles and Dark Photons Using Advanced Statistical Tools

This thesis presents a statistically rigorous search for axion-like particles and dark photons using a profile likelihood ratio (PLR) framework applied to SuperCDMS CDMSlite data. The analysis utilizes an exposure of approximately 110 kg·days, with an energy resolution at the level of $\mathcal{O}(10\ \mathrm{eV_{ee}})$, and performs a spectral analysis over the mass range from ~40 eV/c^2 to 25 keV/c^2.

Unlike earlier analyses based on Poisson counting or optimum interval methods, the PLR approach:

- Incorporates detector response, signal efficiency, background parameterization, and systematic uncertainties through nuisance parameters.
- Exploits the full spectral information and enables simultaneous signal–background fitting to data.
- Provides well-defined statistical coverage within a unified likelihood framework.
- Naturally includes systematic uncertainties in the analysis.
- Supports both exclusion limits and discovery-oriented analyses for weak signals.

In contrast, conventional Poisson counting and OI methods are primarily limited to upper-limit setting and constraining coupling parameters, and do not provide a general framework for discovery-based hypothesis testing.

No statistically significant excess consistent with dark matter absorption was observed in the analysis. The resulting 90% confidence level limits on the axion-electron coupling (g_{ae}) and the dark photon kinetic mixing parameter (ϵ) improve upon previous SuperCDMS analyses of the same datasets by up to a factor of ∼5. Although these constraints are not yet competitive with those from leading liquid noble gas detector experiments (e.g., XENONnT, PandaX, and DarkSide), this work demonstrates the strength of semiconductor-based detectors as complementary probes and establishes a methodologically robust framework for future analyses with larger exposures.

Importantly, this study highlights that statistical methodology itself is a limiting factor in rare-event searches, and that likelihood-based approaches are essential for maximizing sensitivity in the low-energy regime.

Reactor CEνNS Backgrounds and the Neutrino Floor

Another key conceptual contribution of this thesis is the systematic evaluation of reactor antineutrino-induced coherent elastic neutrino–nucleus scattering (CEνNS) backgrounds and their impact on the neutrino floor for low-mass WIMP searches. This work addresses an important gap in the literature by explicitly quantifying the site dependence of neutrino backgrounds arising from nearby nuclear reactors.

Reactor antineutrino fluxes were modeled for a typical 3.6 GW_{th} reactor, with baselines ranging from ∼1 km to ∼100 km. The flux modeling incorporates fission fractions from ^{235}U, ^{239}Pu, ^{238}U, and ^{241}Pu, combined with hybrid spectral models, and is validated against the CONUS+ CEνNS measurement, which shows agreement with the Standard Model prediction at approximately the 3.7σ level.

The key physical findings of this analysis are:

- Reactor CEνNS produces nuclear recoils predominantly in the sub-keV energy regime.

- The spectral overlap with WIMP-induced recoils is most significant for WIMP masses around 2–3 GeV/c^2.
- At distances $\lesssim$ 10 km, reactor antineutrinos from a $\mathrm{GW_{th}}$-scale reactor can increase the neutrino floor by a few orders of magnitude.
- At distances $\gtrsim$ 100 km, the reactor contribution becomes negligible.

These results demonstrate that the neutrino floor is not a universal limit, but instead depends on experimental site, exposure, and associated systematic uncertainties.

Two complementary statistical frameworks were developed. The first is a discovery-limit approach, based on achieving a 3σ detection in 90% of pseudo-experiments. The second is an opacity (neutrino fog) framework, which characterizes the transition of the CEνNS background from a statistics-limited regime to one dominated by systematic uncertainties. The main conclusions are consistent under both definitions of the neutrino floor and remain robust against reasonable variations in detector quenching, site-dependent geoneutrino contributions, and reactor antineutrino flux uncertainties.

These findings have direct implications for experimental design, including site selection, detector threshold optimization, and the interpretation of future low-mass dark matter searches.

Experimental Characterization and Modeling of Fast Neutron Backgrounds

Another key contribution of this thesis is the experimental characterization and modeling of fast neutron backgrounds using EJ-301 liquid scintillation detectors. Fast neutrons represent a critical background for nuclear-recoil-based rare-event searches, as they produce signals that closely mimic WIMP and CEνNS interactions. Their neutral nature and high penetration through shielding materials make accurate measurement and modeling essential for reliable background estimation.

The detector response is studied using a 2”×2” cylindrical EJ-301 detector coupled to a photomultiplier tube and exposed to an Am–Be neutron source. Owing to its hydrogen-rich composition and pulse-shape discrimination capability, the EJ-301 detector efficiently separates neutron-induced nuclear recoils from gamma-induced electron recoils. A detailed GEANT4 simulation framework models neutron and gamma interactions, scintillation light production, and optical photon transport.

The detector energy response is calibrated using Compton spectra from standard gamma-ray sources, including ^{22}Na, ^{60}Co, and ^{137}Cs, allowing precise tuning of the energy resolution based on optical photon statistics. The scintillation response to nuclear recoils is described using Birks’ law, capturing the non-linear light yield and strong quenching of proton recoils. The Birks’ constant is determined by comparing simulated and measured proton-recoil spectra, ensuring consistency between data and the detector model.

Using the validated model, a neutron response matrix is constructed for mono-energetic neutrons. This matrix is used to reconstruct the incident neutron spectrum from measured data through unfolding techniques such as `Gravel` and `RooUnfold`. The unfolded spectrum agrees well with the reference ISO Am–Be neutron spectrum, demonstrating the reliability of both the detector modeling and the unfolding procedure.

Overall, this work establishes a robust framework for fast neutron measurements, providing a direct mapping between detector signals and incident neutron energies. This is essential for background characterization in rare-event searches, validating simulations, and reducing systematic uncertainties. The methods developed here are directly applicable to neutron background studies in current and next-generation dark matter and CEνNS experiments.

7.2 Outlook

The results of this thesis are directly relevant to next-generation experiments, particularly: SuperCDMS SNOLAB and Low-threshold cryogenic semiconductor detectors worldwide. Future extensions of this work may include the application of the PLR framework to larger exposures and multi-detector datasets, improved modeling of low-energy backgrounds and detector non-linearities, and further reduction of systematic uncertainties associated with neutrino fluxes and detector calibration.

Additional directions include the exploration of advanced background discrimination techniques beyond spectral analysis, as well as the development of novel detection strategies such as directionality. As experiments approach and potentially reach the neutrino floor, progress will increasingly depend on precision modeling, cross-experiment comparisons, and innovative analysis techniques that go beyond traditional rate-based approaches.

In summary, this thesis establishes a precision-driven and experimentally validated framework for low-mass dark matter searches by integrating sub-keV detector calibration, statistically rigorous data analysis, and quantitative background modeling. These contributions enhance the reliability, interpretability, and future sensitivity of rare-event searches, and provide a strong foundation for ongoing and future efforts to probe the particle nature of dark matter.